

# Clays, Clay Minerals and Ceramic Materials Based on Clay Minerals

Edited by  
Gustavo Morari do Nascimento

---

# Clays, Clay Minerals and Ceramic Materials Based on Clay Minerals

---

Edited by Gustavo Morari do Nascimento

# **Clays, Clay Minerals and Ceramic Materials Based on Clay Minerals**

Edited by Gustavo Morari do Nascimento

**Published by ExLi4EvA**

Copyright © 2016

All chapters are Open Access distributed under the Creative Commons Attribution 3.0 license, which allows users to download, copy and build upon published articles even for commercial purposes, as long as the author and publisher are properly credited, which ensures maximum dissemination and a wider impact of our publications. After this work has been published, authors have the right to republish it, in whole or part, in any publication of which they are the author, and to make other personal use of the work. Any republication, referencing or personal use of the work must explicitly identify the original source.

As for readers, this license allows users to download, copy and build upon published chapters even for commercial purposes, as long as the author and publisher are properly credited, which ensures maximum dissemination and a wider impact of our publications.

## **Notice**

Statements and opinions expressed in the chapters are those of the individual contributors and not necessarily those of the editors or publisher. No responsibility is accepted for the accuracy of information contained in the published chapters. The publisher assumes no responsibility for any damage or injury to persons or property arising out of the use of any materials, instructions, methods or ideas contained in the book.

**Publishing Process Manager**

**Technical Editor**

**Cover Designer**

AvE4EvA MuViMix Records

First published March 11, 2016

ISBN-10: 953-51-2259-2

ISBN-13: 978-953-51-2259-3



---

## Contents

---

### Preface

Chapter 1 Structure of Clays and Polymer–Clay Composites Studied by X-ray Absorption Spectroscopies

by Gustavo M. Do Nascimento

Chapter 2 Clay Minerals and Clay Mineral Water Dispersions — Properties and Applications

by Guadalupe Sanchez-Olivares, Fausto Calderas, Luis Medina-Torres, Antonio Sanchez-Solis, Alejandro Rivera-Gonzaga and Octavio Manero

Chapter 3 Charging Behavior of Clays and Clay Minerals in Aqueous Electrolyte Solutions — Experimental Methods for Measuring the Charge and Interpreting the Results

by Tajana Preocanin, Ahmed Abdelmonem, Gilles Montavon and Johannes Luetzenkirchen

Chapter 4 Adsorption of Industrial Pollutants by Natural and Modified Aluminosilicates

by Liudmila Novikova and Larisa Belchinskaya

Chapter 5 Structural and Electrochemical Properties of Cementitious and Hybrid Materials Based on Nacrite

by Nouha Jaafar, Hafisia Ben Rhaiem and Abdesslem Ben Haj Amara

Chapter 6 Clay/Biopolymer Composite and Electrorheological Properties

by Mehmet Cabuk

Chapter 7 Ceramic Materials Based on Clay Minerals in Cultural Heritage Study

by Rodica-Mariana Ion, Radu-Claudiu Fierăscu, Sofia Teodorescu, Irina Fierăscu, Ioana-Raluca Bunghez, Daniela Turcanu-Caruțiu and Mihaela-Lucia Ion



---

## Preface

---

This book presents the state-of-the-art results of characterization of clays, clay minerals and ceramic materials based on clay minerals.

The main goal of this work is to contribute to the rationalization of some important results obtained in the open area of clays and clay materials characterization.

Moreover, this book also provides a comprehensive account on polymer and biopolymer-clay nanocomposites, use of clay as adsorption materials for industrial pollutants, ceramic materials in cultural heritage and physical-chemistry aspects of clay and clay minerals aqueous dispersions.

This book will be beneficial for students, teachers and researchers of many areas who are interested to expand their knowledge about clays and its derivates in the fields of Nanotechnology, Biotechnology, Environmental Science, Industrial Remediation, Cultural Heritage, etc.



---

# Structure of Clays and Polymer–Clay Composites Studied by X-ray Absorption Spectroscopies

---

Gustavo M. Do Nascimento

Additional information is available at the end of the chapter

<http://dx.doi.org/10.5772/61788>

---

## Abstract

A wide range of spectroscopic techniques employ higher-energy electromagnetic radiation, ranging from vacuum UV ( $\approx$ 10–40 eV, 125–31 nm), including soft X-rays (40–1500 eV, 31–0.8 nm), and going to hard X-rays (1500– $10^5$  eV, 0.8–0.01 nm) for elucidating molecular structures of chemical and biological interest. A typical X-ray absorption (XAS) spectrum has a large absorption near the edge followed by serial oscillations that gradually fade away. This set of oscillations extends over a wide energy range and can be divided into two regions: the absorption near the edge is called XANES (X-ray absorption near-edge structure) and the second region is the so-called EXAFS (extended X-ray absorption fine structure). The XAS data enables the determination of crystallographic parameters and also the signal intensity contains information of the oxidation state and the chemical bond in the solid. For instance, theoretical calculations were essential to verify the differences between the oxygen and silicon sites in clays. Experimental and theoretical EXAFS studies of clays with Cu(II) show that Cu(II) has interchangeable octahedral, tetragonal, and square planar coordinations in the clay interlayer, depending on Cu(II) loading and degree of hydration. XANES data of intercalated poly(aniline) show new bands at 398.8 eV and 405–406 eV, which were assigned to new chromophoric segments formed within the galleries of the Montmorillonite clay. Hence, in this chapter, this amazing new area will be reviewed concerning the state-of-the-art results of characterization of their structural features. Previous and new results of the X-ray absorption spectroscopy of clays and polymer–clay materials obtained by our group will be considered. The main goal of this work is to contribute to the rationalization of some important results obtained in the open area of clays and clay materials characterization.

**Keywords:** XANES, Clays, Ceramics, EXAFS

## 1. Introduction

### 1.1. Clays, clay minerals, and ceramics

The term clay can assume different meanings for different groups of people. For the farmer, clays are the mechanical and chemical environment where most plants grow. For the ceramist, it is the raw material of his works for over 4000 years. To the editor, it gives softness to the paper's surface in high-quality prints. In the medical area, it may be for the relief of diarrhea and so on. In fact, there is no uniform nomenclature for clay and clay materials [1, 2]. Georgius Agricola (1494–1555), the founder of geology, was apparently the first to propose a definition for clay [3]. The last definition is that the term clay can be considered as natural fine-grained minerals with plastic behavior at appropriate water contents that will harden when dried or fired. Generally, in the area of geology, clays are considered as particles with a size dimension of  $<4\text{ }\mu\text{m}$ , while in colloid science, a value of  $<1\text{ }\mu\text{m}$  is more acceptable [4, 5]. Likewise, the term "clay mineral" is difficult to define. As a first approximation, the term signifies a class of hydrate phyllosilicates making up the fine-grained fraction of rocks, sediments, and soils. The definition that the JNCs have proposed is "...phyllosilicate minerals and minerals which impart plasticity to clay and which harden upon drying or firing" [3] Since the origin of the mineral is not part of the definition, clay mineral (unlike clay) may be synthetic.

Hence, clay minerals are extremely fine materials that can only be studied in detail by using X-ray techniques or sophisticated microscopic techniques, such as the electron scanning microscope [6]. They are primarily hydrated aluminosilicates in which the magnesium and iron can replace the aluminum wholly or partly with alkaline or alkaline earth elements. Thus, its chemical composition is variable, such as the nature of the interlayer cations and water content. The different clay minerals have different dehydration properties, structural failure limits, decomposition products, cation exchange capacity (CEC), and other useful properties of economic interest.

Clays layers are formed from tetrahedral sheets in which a silicon atom is surrounded by four oxygen atoms and octahedral sheets in which a metal such as aluminum or magnesium is surrounded by eight oxygen atoms [1-3, 7]. The tetrahedral (T) and octahedral (O) sheets are bonded by the oxygen atoms. Unshared oxygen atoms are present in hydroxyl form. Two main arrangements of T and O layers are observed in major parts of clays. One tetrahedral fused to one octahedral (1:1) is known as the kaolin group, with a general composition of  $\text{Al}_2\text{Si}_2\text{O}_5(\text{OH})_5$  and a layer thickness of ~0.7 nm. Phyllosilicates are formed by one octahedral sheet bonded between two tetrahedral sheets (2:1) with a total thickness of 0.94 nm. When the aluminum cations in the octahedral layers are partially substituted by divalent magnesium or iron cations, the smectite clay group is formed, whose structure consists of a central sheet containing groups  $\text{MO}_4(\text{OH})_2$  of octahedral symmetry associated with two tetrahedral sheets ( $\text{MO}_4$ ) producing layers designated as T:O:T (see Figure 1.) [7]. The octahedral sites are occupied by ions of aluminum, iron and magnesium, while the centers accommodate tetrahedrons of silicon and aluminum ions. The negative charges from the T:O:T lamellae are neutralized by hydrated alkaline cations that can be exchanged with any other cationic species. Mainly, smectite clays exhibit surface adsorption and catalytic activity in organic reactions.

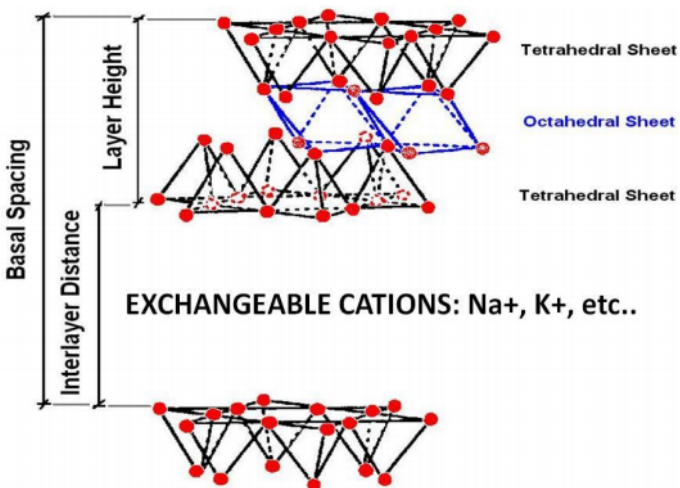


Figure 1. Schematic representation of montmorillonite clay (MMT)

Finally, the ceramics are defined [8-10] as the art and science of making products and articles (a) chiefly or entirely from "earthy" raw materials, that is, from the so-called nonmetallics excepting fuels and ores of metals; and (b) with a high-temperature treatment involved, either in manufacturing or in service. The technology of clays in the field of ceramics includes consideration of both the room-temperature properties and the behavior at elevated temperatures. When clays are used in ceramics, one of several functions is generally served. Most clays, alone or in mixtures, are used for their contribution to the working properties, drying strength of the ceramic masses which they comprise or to which they have been added. Some clays, however, are used more because they offer an inexpensive body constituent or filler of the desired chemical composition, already subdivided by nature to a convenient grain size.

## 1.2. Polymer-clay materials

A polymer-clay material is made by the combination of a polymer and synthetic or natural clay. The presence of clay can improve the mechanical, thermal, barrier and fire retardancy properties of the polymer. If the polymer-clay material has at least one phase with organization in the nanometer scale, the material is called a nanocomposite. It is important to emphasize that the main characteristics of the polymer-clay materials are strongly related to the physical and chemical peculiarities of each component and also due to the nano size aspect and interfacial adhesion between the nanocomposite parts [11, 12].

Polymer nanocomposites are formed at least with one part in the nanometer scale (<100 nm). Despite the term nanocomposite being very recent, in fact, has been possible to recognize in the nature a diverse range of materials, such as bones, shells and wood that can be considered nanocomposites because they are formed by carbohydrates, lipids and proteins organized in the nanometer regime [13]. In recent years, the characterization and control of structures at the

nanoscale level have been studied, investigated and exploited. Consequently, the nanocomposite technology has emerged as an efficient and powerful strategy to upgrade the structural and functional properties of synthetic polymers. Polymer nanocomposites have attracted great attention due to the exhibition of superior properties such as strength, toughness and fire barrier far from those of conventional microcomposites and comparable with those of metals. The presence of one nanoscale phase leads to tremendous interfacial contacts between the polymer and clay and, as a consequence, the improvement of the polymer bulk phase, such as mechanical, thermal, barrier, durability, chemical stability, flame retardancy, scratch/wear resistance, biodegradability as well as optical, magnetic and electrical properties [14-17]. The increased performance of the mechanical properties of nanocomposites is related to the clay content and the aspect ratio of the clay [18].

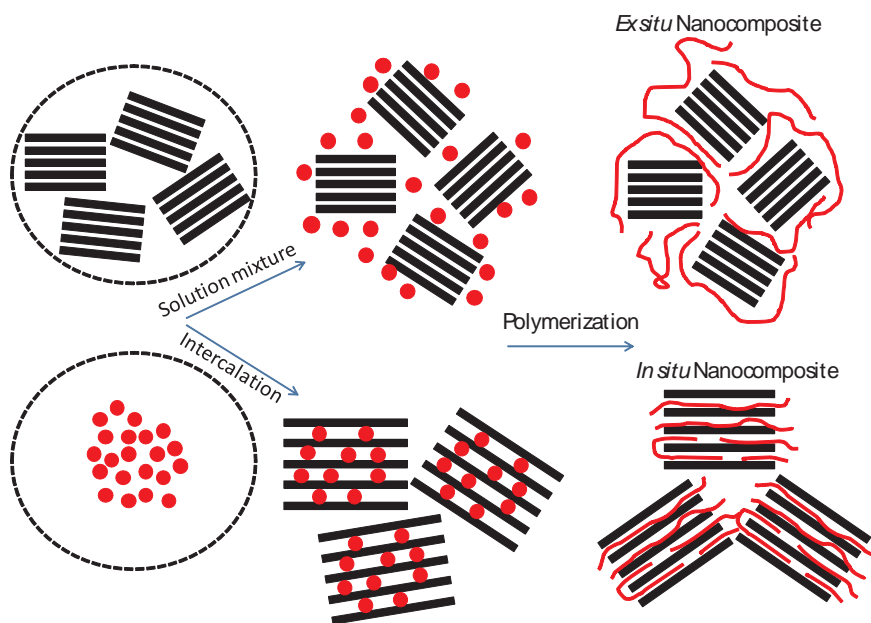


Figure 2. Schematic representation of two types of preparations of polymer–clay nanocomposites

Clays have been widely used for the preparation of polymer nanocomposites. Recently, there has been a growing interest for the development of polymer–clay nanocomposites due to their dramatically improved properties compared to conventional polymer composites in a very low fraction [19, 20]. Polymer–clay nanocomposites can be prepared by direct mixture of two aqueous solutions containing the monomer and the clay suspension (see Figure 2.); afterward, the polymer can be formed by adding a polymerization agent, or induced by thermal or light exposition. The resulting material is called an *ex situ* nanocomposite because the major part of the polymer if found outside the interspaces of the clay. It is important to mention that the initial clay concentration can be modulated and, in some cases, the clay layers are completely

separated, as a consequence, the resulting material is known as exfoliated polymer–clay nanocomposite. In a second method (see Figure 2.), the monomer is intercalated in the interlayer space of the clays by charge exchange or by diffusion inside the clay galleries previously modified with an organic salt. Afterward, the intercalated polymer can be polymerized and the resulting material is known as an *in situ* nanocomposite because the major part of the polymeric content is inside the clay interspaces.

### 1.2.1. Nonconducting polymer–clay materials

In this chapter, we will only provide a summary of the main characteristics found in the polymer–clay nanocomposites. Here, we divide the section between polymer–clay nanocomposites formed by intrinsic nonconducting polymers or by conducting polymers. Traditionally, the clay layers must be previously treated with an organic agent (this point was not explicitly discussed in Figure 2.) to ensure good dispersion of clay layers within the polymer matrix. The dispersion of clay plates into the polymeric matrix is very difficult, mainly by stacking forces between the clay layers and its hydrophilic character. Hence, it is necessary to modify the clay layers in order to increase the chemical compatibility with hydrophobic polymer chains. Only a few hydrophilic polymers such as polyethylene oxide and polyvinyl alcohol can be miscible with clay layers [21].

The origin of polymer–clay hybrids starts with the creation of nylon-6-clay hybrid (NCH) developed in 1986 under Toyota Central Research and Development Laboratories. Afterward, the use of modified clays as precursors to nanocomposite formation was extended into various polymer systems including epoxies, polyurethanes, polyimides, nitrile rubber, polyesters, polypropylene, polystyrene and polysiloxanes, among others. For true nanocomposites, the clay nanolayers must be uniformly dispersed and exfoliated in the polymer matrix. The presence of aggregated tactoids in conventional polymer–clay composites improves rigidity but sacrifices strength, elongation and toughness. However, exfoliated clay nanocomposites, such as NCH, show enhancement in all aspects of their mechanical performance.

### 1.2.2. Conducting polymer–clay materials

The intrinsically conducting polymers (ICPs), or simply synthetic metals, form one of the largest classes of molecular conductors [22]. The preparation of stable poly(acetylene) (PA) films was achieved in the 1970s by Shirakawa and Ikeda [23, 24]. However, it was only in 1977 that the possibility of doping PA using Lewis's acid (or base) was discovered [25]. During the process of doping [26, 27], the conductivity typically ranges from  $10^{-10}$  to  $10^{-5}$  S cm $^{-1}$ , and the polymer is converted into a "metallic" regime. The addition of nonstoichiometric chemical species in quantities that are commonly low ( $\leq 10\%$ ) results in dramatic changes in the electronic, electrical, magnetic, optical and structural properties of the polymer. The doping is reversible, and the polymer can return to its original state without major changes in its structure. In the doped state, the presence of counterions stabilizes the doped state. All conductive polymers, for example, poly(para-phenylene) (a), poly(*p*-phenylene-vinylene) (b), poly(pyrrole) (c), poly(thiophene) (d), poly(furan) (e), poly(heteroaromatic vinylene) (f), (where Y=NH, NR, S, O), poly(aniline) (g), poly(para-phenylenediamine) (h), poly(benzidine)

(i), poly(ortho-phenylenediamine) (j), among others (see Figure 3.), may be doped by p (oxidation) or n (reduction) through chemical and/or electrochemical process.

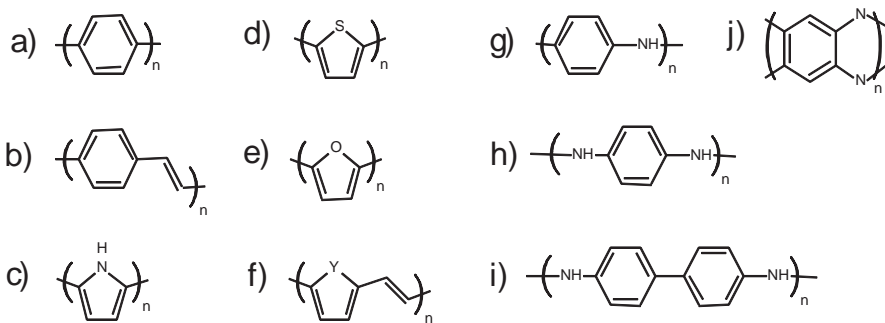


Figure 3. Schematic representation of the chemical structures of the most common conducting polymers

In this chapter, we will give special attention to the polymer–clay nanocomposites formed by polyaniline (PANI) and its derivates. Among the different types of hosts used in the formation of nanocomposites with PANI, lamellar materials are undoubtedly the most widely employed. The main reason is that the distance between the layers can be modified, facilitating the intercalation of various chemical species. Hosts, such as MoO<sub>3</sub> [28], V<sub>2</sub>O<sub>5</sub> [29, 30],  $\alpha$ -Zr(HPO<sub>4</sub>)<sub>2</sub>H<sub>2</sub>O [31], HUO<sub>2</sub>PO<sub>4</sub>.4H<sub>2</sub>O [32], FeOCl [33], layered double hydroxide (LDH) [34] and MoS<sub>2</sub> [35], and most frequently, clays were used for intercalation of PANI [36-50].

The adsorption of aniline on MMT clay has been studied a long time ago, and since then, it has been well-known that clays have a property to generate colored species by the adsorption of aromatic amines. The best known case is the blue color generated by the adsorption of benzidine (4, 4'-diaminobiphenyl) in clay [37]. Among the earlier studies [38-40], it was reported that films of MMT containing metal ions become black after immersion in aniline; the authors suggest that this is due to the polymerization of monomers. Soma and Soma [41, 42] and Soma et al. [43-45] used resonance Raman spectroscopy (RR) in the study of oxidation of aromatic compounds (benzene and derivatives) adsorbed on clay, and showed that when the adsorption of aniline on Cu<sup>2+</sup> or Fe<sup>3+</sup>-MMT is made in the liquid phase, polymer formation occurs. Soma and Soma proposed that the polymer formed was equal to that generated electrochemically (PANI-ES), but with the presence of azo linkages (—N=N—). Also, Mehrotra and Giannelis [46] synthesized PANI intercalated in a synthetic hectorite containing Cu<sup>2+</sup> ions, the UV-vis-NIR spectrum was very similar to that observed for PANI-EB, and the polymer was converted to conductive PANI-ES form, simply by exposing the material to HCl vapors. Other work done by Chang et al. [47] reported the polymerization of PANI into MMT clay galleries. The intercalation was confirmed by measures of X-ray diffraction, and the interlayer distance obtained was changed from 1.47 to 0.36 nm after the polymerization of aniline. Absorption bands of the PANI-ES form were observed at 420 and 800 nm in the UV-vis-NIR

spectrum of the material. In addition, the IR bands at 1568, 1505, 1311 and 1246  $\text{cm}^{-1}$  were upshifted in comparison to the free polymer, probably due to intercalation.

Wu et al. [48, 49] also obtained PANI-MMT using ammonium persulphate as an oxidizing agent, the electronic spectrum of the material obtained was very similar to that obtained for secondarily doped PANI-CSA, suggesting that the PANI was obtained in an extended conformation. The formation of PANI-ES was confirmed by the presence of bands at 1489, 1562 and 1311  $\text{cm}^{-1}$  in the FTIR spectrum of the material. Despite the high organization level of PANI chains into the MMT clay, the conductivity of the material, ca.  $10^{-3} \text{ S.cm}^{-1}$ , was not much higher than those obtained previously. The justification of the authors is that there are few polymeric connections between the particles of clay, which significantly reduces the conductivity observed for the material. Later, other authors reported the synthesis of PANI into MMT clay by the intercalation of anilinium ions into MMT followed by oxidation with ammonium persulphate as a standard method to obtain PANI-MMT nanocomposites [50-62].

Some studies were performed by varying the aniline/clay ratio during intercalation, and it was possible to show the increase of interlayer space and the amount of intercalated PANI as well as the increase of the conductivity of the material [63]. The synthesis of PANI with clay in a medium containing surfactants (dodecylbenzenesulfonic acid, DBSA, and camphorsulfonic acid, HCSA) was also used [56-58]. Intercalation was confirmed by X-ray diffraction data, with interlayer distances of ~1.5 nm and ~1.6 nm being obtained for composites of PANI-DBSA-MMT and PANI-CSA-MMT, respectively. DC conductivity values for PANI-DBSA-MMT and PANI-CSA-MMT at room temperature were near  $0.3 \text{ S.cm}^{-1}$  and  $1.0 \text{ S.cm}^{-1}$ , respectively. The intercalated PANI was also obtained by electrochemical polymerization of aniline, using modified clay electrodes [59], graphite electrode-modified clay [60], Pt electrode-modified clay [61] and electrode stainless steel [62]. Inoue and Yoneyama [59] used a clay-modified electrode and intercalation was performed by immersing the electrode in an aniline solution. An interlayer distance value of 0.54 nm was obtained for MMT clay after immersion. Another work using graphite or Pt electrode modified with clay also reported the formation of PANI, as confirmed by the voltammogram profile curves. The oxidation of a suspension of aniline containing MMT clay intercalated with stainless steel electrodes produced a polymer-MMT-valued interlayer distance of 0.51 nm. The FTIR spectrum of the material presented bands at 1579, 1490 and 1311  $\text{cm}^{-1}$ , similar to that obtained by Wu et al. [48] in the chemical polymerization of aniline with ammonium persulphate.

Using resonance Raman (RR) and X-ray absorption spectroscopy, it was possible to show that the structure of intercalated PANI was different from the free PANI structure [64-71]. At early polymerization stages, the presence of radical cations, dications and benzidine dications were observed in the RR spectra by head-to-tail and tail-to-tail coupling of aniline monomers. However, at the final stages, the RR spectra showed different bands, this indicates coupling between the initial segments with the formation of new chromophoric segments. In order to elucidate the structure of the intercalated polymer, the use of XANES spectroscopy was decisive. The XANES spectroscopy opens the possibility of investigating the chemical environments of both clays and polymers.

### 1.3. X-ray absorption process

A large number of spectroscopic techniques are routinely used in clay and clay materials science research in order to identify elemental, molecular, and crystalline aspects of the samples. Among them, X-ray spectroscopy has a unique capability to obtain atom-specific information as it measures the excitation of core electrons of selected atoms. An X-ray absorption spectrum (XAS) reflects the excitation of a core electron to unoccupied states. As a consequence, it reflects the electronic structure of unoccupied states of a specific atom in the sample; in fact, it is sensitive to the local environment of the selected element. The X-ray intensity ( $I$ ) is attenuated when it penetrates into a solid material. This decrease is analogous to the Beer–Lambert law [72], i.e., showing that  $I_{(x)}=I_0e^{(-\alpha x)}$  the light intensity decreases due to its penetration into the material ( $x$ ), since the argument ( $-\alpha x$ ) is a negative function. The decrease is higher when the magnitude of the absorption coefficient ( $\alpha$ ) is higher. The value of  $\alpha$  is a function of the material structure and also the wavelength of the electromagnetic field [73].

X-ray absorption occurs if the incident photon energy is transferred to an electron strongly bounded to the atom. Figure 4 schematically represents the absorption of a K shell electron (1s level) of an atom bonded in a solid material. The absorption coefficient decreases with increasing incident photon energy, but there are sudden changes. These variations correspond to different absorption edges present in the material.

Considering photons with energy lower than the ionization threshold ( $h\nu_1$ ), they are poorly absorbed by the material since there are no unoccupied states below this energy. However, when the energy of the photon reaches the  $h\nu_2$  value, there is a sharp increase in the absorption, corresponding to the K edge absorption, this energy is called the ionization threshold for the 1s electron. If the photon energy increases ( $h\nu_3$ ), the atom can be ionized; as a consequence, the absorption coefficient has the same magnitude as the cross-section of the photoelectric effect. If the value of the photon energy continues to increase, absorption begins to degrade, but there may be new sudden jumps, since there are other edges in the absorption material [74–76].

The detection of a chemical element in a material is only the simplest information that is available from the X-ray absorption spectra. In fact, the phenomenon of X-ray absorption is much more complex, and therefore carries much more information. Generally, the absorption spectra are complex; possessing a set of variations that extend over a wide range of energies (tens of units of eV). Figure 5 represents a typical X-ray absorption spectrum, which has a large absorption near the edge and a series of oscillations that will lose intensity as it moves away from the absorption edge. The region near the edge is called XANES (X-ray absorption near-edge structure) and the second one is known as EXAFS (near-edge X-ray absorption fine structure). The XANES region includes a range of energies before the absorption edge up to the beginning of the EXAFS region. The definition of the boundary between these two regions is arbitrary, but there is some consensus that the XANES region extends to 50 eV after the absorption edge. The EXAFS region can be defined as the point where the wavelength of ejected electrons is equal to the distance between the absorber atom and its neighbor atoms, this region can extend up to 1000 eV after the edge [77].

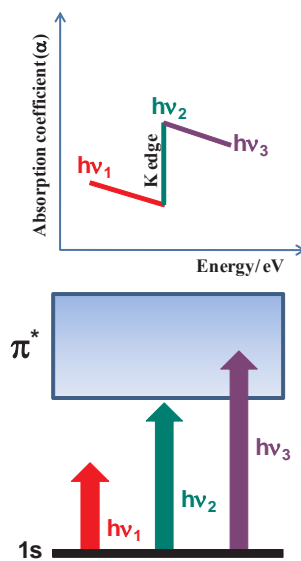


**Figure 4.** Schematic representation of photons with different energies compared in relation to the ionization threshold for a given material. The  $h\nu_1$  photon has low energy to produce ionization; the photon  $h\nu_2$  has the exact energy for ionization, so there is a sudden jump in the absorption coefficient that is the experimental characterization of the absorption edge, and finally the photon  $h\nu_3$  has much more energy than the edge.

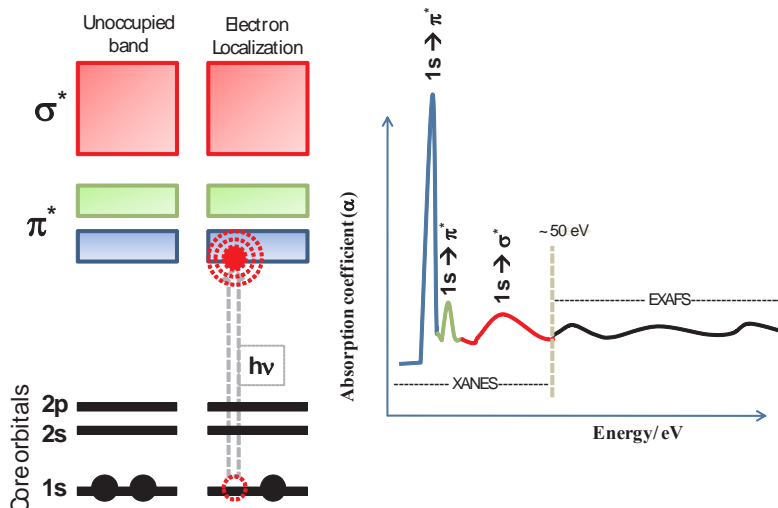


**Figure 5.** The oscillations in the absorption spectrum were caused by the different final states and contain information related to the structure around the atom that absorbed the radiation.

The EXAFS spectrum originates from interference effects between the excited atoms [77-79]. The wave function of the excited electron propagates beyond the atom and is partially reflected by neighboring atoms. The interference between the wave that spreads and reflected by neighboring atoms causes ripples in the absorption spectrum [78, 79]. The interference can be constructive or destructive, depending on the wavelength associated with the electron and with the interatomic distance. Figure 5 schematically illustrates the origin of the X-ray absorption spectrum. The process can also be visualized as an electronic transition from a core orbital to an unoccupied level with the formation of a core-hole configuration. Photoabsorption coefficient,  $\mu$ , or photoabsorption cross-section can be generally described by Fermi's "Golden Rule" as

$$\mu \propto \sum_f \left| \langle \psi_f | \exp(i\mathbf{N}r) \cdot \mathbf{e} \cdot \mathbf{P} | \psi_i \rangle \right|^2 \times \delta(\hbar\omega - E_f + E_i) \quad (1)$$

where  $\psi_f$  and  $\psi_i$  are multielectron wave functions at the final and initial states, respectively. The  $E_f$  and  $E_i$  are the total energy values of the corresponding states. The terms  $\hbar$ ,  $\omega$ ,  $\mathbf{N}$ ,  $\mathbf{e}$ , and  $\mathbf{r}$  are energy, wave number vector, the unit vector for the polarization direction of the X-ray and the position of the excited electron, respectively.  $\mathbf{P}$  is the sum of the linear momentum operators of electrons. In the XAS, the equation can be approximated using one electron wave functions of the core state  $\phi_i$ , and that of the excited electron,  $\phi_f$  as

$$\mu \propto \sum_f \left( \left| \langle \phi_f | e \cdot r | \phi_i \rangle \right|^2 + 1/4 \langle \phi_f | (e \cdot r)(\mathbf{N} \cdot \mathbf{r}) | \phi_i \rangle \right) \times \delta(\hbar\omega - E_f + E_i) \quad (2)$$

The core-hole configuration must be included in the one-electron approximation. The electronic relaxation associated with the presence of the core-hole and excited electron need to be accounted for if one wants to reproduce the experimental spectra by first principles calculations using Eq. (2). Under the dipole approximation, where  $\mathbf{N}r \ll 1$  and  $\exp(i\mathbf{N}r) \approx 1$ , Eq. (2) can be further simplified to

$$\mu \propto \sum_f \left| \langle \phi_f | e \cdot r | \phi_i \rangle \right|^2 \times \delta(\hbar\omega - E_f + E_i) \quad (3)$$

There are two different methods to resolve Eq. (2). The first way is called multiple scattering methods, and the second way is by band-structure methods under periodic boundary conditions.

Hence, through treatment with XANES/EXAFS data, it is possible to determine the interatomic distances between the atoms that have suffered excitation and its neighbor atoms [80-82]. The XANES spectrum contains information similar to the EXAFS spectrum, but the information is more difficult to extract from the math standpoint [80, 83, 84]. This is largely due to the different

possibilities of transitions that may occur in the solids in the XANES region, which in the language of scattering theory means that there is multiple scattering in the XANES region. The intensity of absorption is influenced by the number of electrons that occupy the initial state and may therefore participate in absorption, and it also depends on the density of the unoccupied states and the transition momentum. The unoccupied energy levels depend on the oxidation state and the nature of the chemical bond so that this atom, with its neighbors, makes it possible through the XANES spectra, to distinguish the different states of oxidation of this element. The observed modulations into the XANES spectra are also influenced by the oxidation state and nature of chemical bonds of the materials under study. In the following paragraphs, the focus will be on the analysis of XANES spectra at different edges in order to investigate the structure of clays and clay derivate materials. The absorption measurements are only possible in conditions of ultrahigh vacuum (the pressure inside the chamber is ca.  $10^{-7}$  mbar). What is measured is a signal that is directly proportional to the amount of photons absorbed [85]. Upon absorption, emissions occur from the electrons (photoelectrons, electrons Auger and secondary electrons) whose intensities are proportional to the amount of photons absorbed; to keep the sample electrically neutral, it grounds the sample compartment so that the current replacement of the electrons in the sample (typically, the current is of the order of  $10^{-12}$  A) is proportional to the intensity of photons absorbed. It can be described as:

$$I_{(\text{current of replacement of the electrons})} \propto I_{(\text{electrons emitted})} \propto A_{(\text{photons absorbed})}$$

Another concern is about the number of samples that can be placed at one time in the compartment because it takes between 3 and 5 h to reach the required pressure inside the chamber. The arrangement used in our experiments is displayed in Figure 6. Another grooved rod is placed over the main rod to delimit the area (ca.  $0.2\text{ cm}^2$ ) and prevent the mixing of the samples, since the measurements are made with the rod positioned vertically in the sample chamber.

## 2. Results and discussion

### 2.1. XANES data

XANES spectroscopy has been widely used for the investigation of clay structures, metal sites in the clays and also for polymer–clay nanocomposites. By selecting the appropriate energy in the X-ray source, it is possible to investigate the silicon, oxygen and aluminum sites in the clay layers; the metal ions incorporated into the clay layers; as well as the carbon, nitrogen, oxygen and other atoms in the polymer chains. In addition, it is possible to measure the absorption, emission and photoejection signals from the clay materials.

The XANES data supported by DFT calculations were essential to verify the differences into the oxygen sites observed for montmorillonite (MMT) and muscovite mica (MT) clays. The hydroxyl groups localized in these cavities and van der Waals forces contributed significantly to adsorption processes. In both clays, the oxygen surface sites are directly affected by the

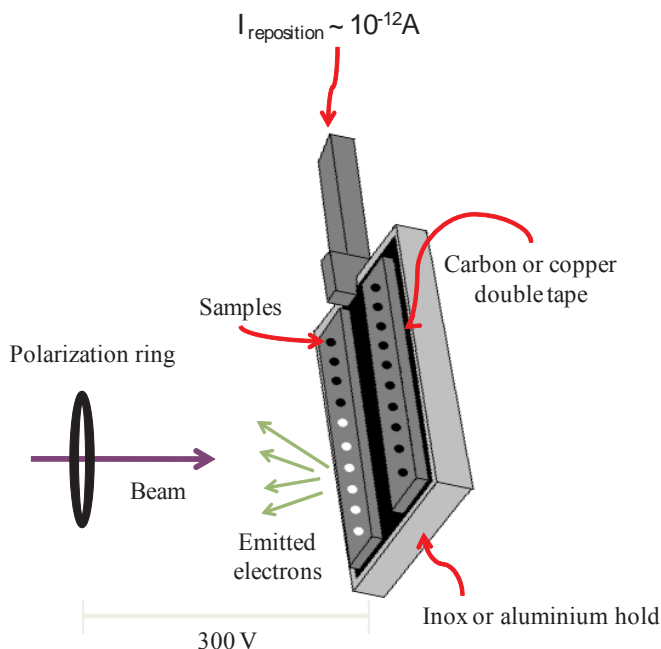
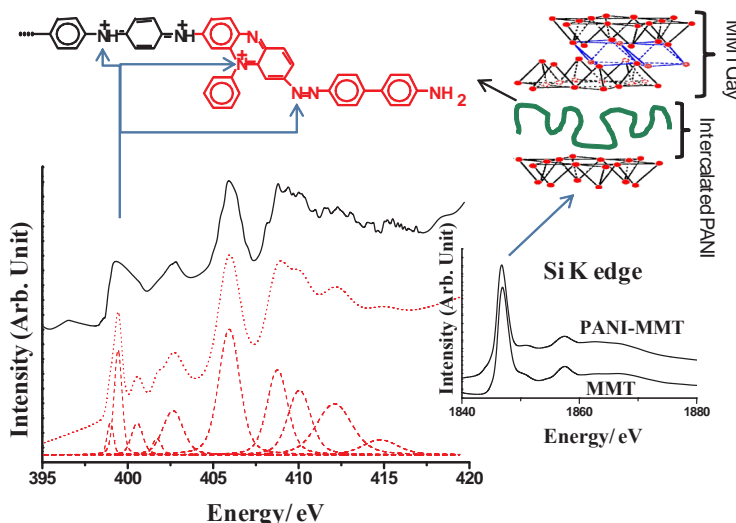


Figure 6. Experimental setup used for XANES measurements.

intralayer interaction through hydroxyl groups. The chemical environment of the hydroxyl groups is distinct in the MMT and MT structures. In fact, the oxygen atoms in the apical position in MT layers are less influenced by van der Waals forces. In addition, the silicon surfaces in MT are more sensitive to the Si-O apical-Al changes and have no disturbance on hydroxyl groups than in MMT clay (86). In another very recent work, the XAS data associated with DFT calculations were used to the study of the electronic structure of synthetic and natural kaolinite clay. This can serve as a model system for engineered and natural clay materials. It was possible to correlate the XANES features with the structural defects present in the clay layers. In both synthetic and natural kaolinite, oxygen replaces hydrogen in the Al (001)-hydroxyl groups on the kaolinite clay sheets. The energy levels associated with these defects are situated in the band gap, and its value decreases by about 3.2 eV as this defect is formed [87].

The presence of metals in clays has also been investigated. Many soils around the globe are contaminated with metals due to inputs from anthropogenic activities; however, the long-term processes that retain these metals in soils remain unclear. Changes in Mn K-edge XANES with soil depth were consistent with a mixing of different pools of Mn. In particular, the proportions of Mn(II)/Mn(III) present in the mineral soil increased relative to Mn(IV) with increasing depth. Mn can be preferentially retained in soils relative to other elements due to this process of uptake and immobilization. The Mn that is taken up into the plant's biomass exists mostly as aqueous and organic Mn(II) compounds that are immobilized as Mn(III)/(IV) oxides during decompo-

sition [88]. Another work studied the interaction of CO<sub>2</sub> and O<sub>2</sub> gases in volcanic soils containing different minerals and clays having Fe(II/III) ions, which was investigated by using the XANES spectroscopy at Fe K-edge. The authors also measured the Fe K-XANES spectra for a great number of reference materials, thus permitting the determination of Fe species during the cycle of CO<sub>2</sub> and O<sub>2</sub> interactions [89].



**Figure 7.** Top: N K XANES spectra of powered samples of PANI-MMT nanocomposites. Experimental spectra are represented by the black continuous line (—). The Voigt bands used in the deconvolution of the experimental spectrum are shown below the experimental data (dashed red line, ---). The sum spectrum of the Voigt bands is also displayed (dotted red line, ...). Deconvolution of the experimental N K XANES spectra was done using SPSS (1995) with Voigt bands (Voigt area mode with varying widths) and linear baseline (linear, D2 mode). The Si K XANES spectra of powdered samples of MMT and PANI-MMT are also shown inside the figure. Scheme of PANI-MMT nanocomposites and the intercalated PANI structure are also shown at the top of the figure. Bottom: Tentative assignments of bands observed in N K XANES of PANI-MMT, PBZ-MMT and PpPD-MMT nanocomposites. The band positions were calibrated using the first resonance band value for KNO<sub>3</sub> salt (the beam line has a resolution of 0.1 eV; the N K XANES were calibrated considering the value 405.5 eV, according to ref. [91]).

XANES permits the investigation of the confined polymer into clay galleries, differently from surface techniques, such as X-ray photoelectron spectroscopy. The N K XANES spectrum of polyaniline-montmorillonite prepared by in situ polymerization within the cavities of the MMT clay is displayed in Figure 7. The spectrum of PANI-MMT nanocomposites contains bands with different patterns than the spectra of “free” PANI forms [90]. It is interesting to observe that the structure of MMT clay is not changed because there is no modification of the XANES spectra of MMT at the Si K-edge after PANI formation (see Figure 7). Comparing the set of N K XANES spectra obtained for several organic molecules with nitrogen atoms in different electronic environments [67-69] it was possible to assign the observed bands. Table 1 summarizes the data obtained for PANI-MMT and displays the tentative assignments for the various transitions observed.

Samples			Tentative assignments	
PANI-MMT	PBZ-MMT	PpPD-MMT		
bands/cm <sup>-1</sup> (linewidths of the bands/cm <sup>-1</sup> )				
398.99 ± 0.05 (0.32)	398.8 ± 0.1 (1.3)	398.8 ± 0.1 (1.5)	1s → π*	—N= of phenazine-like rings and/or —N=N— of azo bonds
399.46 ± 0.05 (0.47)	—	399.64 ± 0.05 (0.88)	1s → π*	—H <sub>2</sub> N+= or =N+= of phenazine-like rings and/or dications of PANI
400.57 ± 0.05 (0.75)	400.18 ± 0.05 (1.4)	400.26 ± 0.05 (0.56)	1s → π*	π-Conjugated nitrogen
401.74 ± 0.05 (0.54)	401.75 ± 0.05 (0.66)	—	1s → π*	Amine nitrogen
402.7 ± 0.1 (1.4)	—	402.2 ± 0.1 (1.1)	1s → π*	Amine nitrogen
406.0 ± 0.1 (1.4)	405.1 ± 0.1 (1.0)	406.0 ± 0.1 (2.0)	1s → π*	—H <sub>2</sub> N+—NH <sub>2</sub> —
408.8 ± 0.1 (1.4)	408.7 ± 0.1 (2.4)	—	1s → σ*	—N=N—
410.1 ± 0.1 (1.6)	410.9 ± 0.1 (2.7)	409.2 ± 0.1 (4.8)	1s → σ*	—H <sub>2</sub> N+—NH <sub>2</sub> —
412.2 ± 0.1 (2.4)	—	412.7 ± 0.1 (2.7)	1s → σ*	—
414.8 ± 0.1 (2.4)	—	—	1s → σ*	—

**Table 1.** Data obtained for PANI-MMT and their tentative assignments

It should be mentioned that all N K XANES bands (for  $1s \rightarrow \pi^*$  and  $1s \rightarrow \sigma^*$  transitions) observed for intercalated PANI have lower linewidths than those observed for “free” PANI. Structural limitations of the polymer lead to an electronic reorganization and shorter electronic bands; as a consequence, the absorption bands are narrower than those for “free” PANI. The same behavior was observed for polybenzidine (PBZ) and poly(*p*-phenylenediamine) (PpPD) intercalated in the MMT clay. Hence, the N K XANES bands for intercalated PANI can be related to nitrogen atoms bonded in the phenazine-like rings and azo bonds; a similar behavior was also observed for intercalated PpPD. In the case of intercalated PBZ, the bands related to the azo bonds were more intense. The most intense band observed for all spectra of the nanocomposites is near 405–406 eV and can be assigned to protonated azo bonds (hydrazinium bonds); it also confirms the presence of new segments in the intercalated polymers. Finally, it was observed that the structure of confined polymers contains new segments in comparison to that observed for “free” polymers.

## 2.2. EXAFS data

Much fewer works deal with EXAFS of clays and its derivate materials compared to XANES data. However, it is possible to find studies on the experimental and theoretical determination of Cu(II) sites in clay surfaces and interlayer. Cu(II) in the fully hydrated, Cu-saturated MMT has a singlet 1st derivative XANES spectrum. FEFF calculations show that this singlet feature originates from a quasi-regular octahedral coordination of water molecules around the interlayer Cu(II) atom. All other samples and models have doublet 1st derivative XANES

spectra. FEFF calculations suggest that the doublet features arise from an axially elongated octahedral coordination under the Jahn–Teller effect or square planar coordination. FEFF calculations of the EXAFS spectra as a function of the axial oxygen bond length demonstrate that a destructive interference between backscattering from equatorial oxygen (O-eq) and that from axial oxygen (O-ax) atoms leads to an apparent coordination number (CN) less than six expected for the tetragonal coordination, with the farther, loosely bound axial oxygen atoms making a minor, yet negative, contribution to the CN determined by the EXAFS analysis. This study shows that Cu(II) has interchangeable octahedral, tetragonal and square planar coordination in the MMT interlayer, depending on Cu(II) loading and degree of hydration. The quasi-regular octahedral coordination of the interlayer Cu(II) in MMT is a new finding of this study [92]. In another work [93], the authors studied the sorption mechanism of Cu(II) on hectorite clay. The XAS spectra show an angular dependence between the Cu-O-eq atomic pair and the direction perpendicular to the clay layer plane. Based on the number of Mg/Al and Si nearest neighbors, the  $\text{Cu}(\text{O-eq})_4(\text{O-ax})_{1-2}$  polyhedron is attached to the clay surface by sharing one to three edges with the structural Al/Mg octahedral and zero to three corners with the Si/Al tetrahedral. Copper has an unusually high coordination on the two dioctahedral aluminous clays, as explained by the presence of distorted empty cavities at their surface, which can accommodate irregular coordination polyhedrals. The steric match between the distorted empty octahedral cavities and the Jahn–Teller distorted Cu polyhedral provides a rationale to explain the higher affinity of Cu(II) for Al octahedral sheets.

### 3. Perspectives

X-ray absorption spectroscopy is now a powerful tool for the investigation of clays and its derivates. However, their use in clay science is still in its infancy. In fact, there are plenty of investigation possibilities in clay science, since the studies of surface aspects about the Si, Fe, Al and O sites, where the specificity of the XAS signal can give atomic information around the absorbing atom and up to the characterization of intercalated metals, molecules, biomolecules, and polymers and so on. The XANES data, supported by DFT calculations, were essential to verify the differences in the oxygen sites observed in clays. The hydroxyl groups localized in these cavities and van der Waals forces contribute significantly to adsorption processes. The oxygen surface sites are directly affected by the interlayer interaction through hydroxyl groups. Experimental and theoretical EXAFS studies of clays with Cu(II) show that Cu(II) has interchangeable octahedral, tetragonal and square planar coordination in the clay interlayer, depending on Cu(II) loading and degree of hydration. The angular dependence between the Cu-O-eq atomic pair and the direction perpendicular to the clay layer plane was also observed and the consequences of different coordination sites where the Cu ions can be found. XANES data of intercalated PANI show new bands at 398.8 eV and 405–406 eV. These new bands were assigned to phenazine-like rings and azo bonds in the structure of the polymers (polyaniline, polybenzidine and poly(*p*-phenylenediamine) within the galleries of Montmorillonite clay. The investigation of the electronic structure of the conducting polymer–clay nanocomposites through XANES spectroscopy has been decisive in the determination of their structure and

also in the study of the interactions between the polymeric chains and the clay layers. The force of these interactions is responsible for guidance in the formation of a polymeric backbone with a distinct structure to that observed in the free polymer. We believe that the XANES/EXAFS studies of the structural pattern of the metal-clay, molecules-clay and polymer-clay nanocomposites will be decisive for their applications.

## Acknowledgements

This work is dedicated to my parents (Iara Ap. Morari do Nascimento and Romualdo J. do Nascimento). Many thanks to the National Synchrotron Light Laboratory (LNLS, Campinas-Brazil) for XANES measurements.

## Author details

Gustavo M. Do Nascimento\*

Address all correspondence to: morari@yahoo.com

Universidade Federal do ABC-CCNH, Campus SBC, Santo André, Brazil

## References

- [1] Bergaya, F. & Lagaly, G. (2006). General introduction: Clays, clay minerals, and clay science. In: *Handbook of Clay Science*, Bergaya, F. Theng, B. K. G. & Lagaly, G. (Eds.). 1–18 Elsevier, Amsterdam.
- [2] Hall, P. L. (1987). Clays: their significance, properties, origins and uses. In: *A Handbook of Determinative Methods in Clay Mineralogy*, Wilson, M.J. (Ed.). 1–25, Blackie, Glasgow.
- [3] Guggenheim, S. & Martin, R. T. (1995). Definition of clay and clay mineral: joint report of the AIPEA nomenclature and CMS nomenclature committees. *Clays and Clay Minerals* 43, 255–256 and *Clay Minerals* 30, 257–259.
- [4] Moore, D. M. & Reynolds, R. C. Jr. (1997). *X-ray Diffraction and the Identification and Analysis of Clay Minerals*, 2<sup>nd</sup> edition. Oxford University Press, Oxford.
- [5] Weaver, C. E. (1989). *Clays, Muds, and Shales*. Elsevier, Amsterdam.
- [6] Brown, G. (1980). Associated minerals. In: *Crystal Structures of Clay Minerals and their X-ray Identification*. Brindley, G.W. & Brown, G. (Eds.). 361–410, Mineralogy Society, London.

- [7] Yariv, S. (2002). Introduction to organo-clay complexes and interactions. In: *Organoclay Complexes and Interactions*. Yariv, S. & Cross, H. (Eds.). Marcel Dekker, Inc. New York.
- [8] Wilson, H. (1927). *Ceramics-Clay Technology*. McGraw-Hill Book Co. New York.
- [9] Reis, H. (1927). *Clays, Their Occurrence Properties and Uses*. John Wiley & Sons. Committee on Definition of the Term "Ceramics" (1920). Report of the committee. *Am. Ceramic Soc. Jour.*, 3, 7, 526.
- [10] Norton, F. H. (1952). *Elements of Ceramics*. Cambridge, MA., Addison-Wesley Press.
- [11] Zhang, R., Ni, Q. Q., Natsuki, T. & Iwamoto, M. (2007). Mechanical properties of composites filled with SMA particles and short fibers. *Composite Structures*, Vol. 79, 90–96.
- [12] Meneghetti, P. & Qutubuddin, S. (2006). Synthesis, thermal properties and applications of polymer–clay nanocomposites. *Thermochimica Acta*, Vol. 442, 74–77.
- [13] Hussain, F., Hojjati, M., Okamoto, M. & Gorga, R.E. (2006). Review article: Polymer-matrix nanocomposites, processing, manufacturing, and application: an overview. *Journal of Composite Materials*, Vol. 40, No. 17, 1511–1565.
- [14] Armentano, I., Dottori, M., Fortunati, E., Mattioli, S. & Kenny, J.M. (2010). Biodegradable polymer matrix nanocomposites for tissue engineering: A review. *Polym. Degrad. Stab.*, 95, 11, 2126–2146. 0141–3910.
- [15] Cosoli, P., Scocchi, G., Pricl, S. & Fermaglia, M. (2008). Many-scale molecular simulation for ABS-MMT nanocomposites: Upgrading of industrial scraps. *Micropor. Mesopor. Mat.*, Vol. 107, 169–179.
- [16] Ma, H., Xu, Z., Tong, L., Gu, A. & Fang, Z. (2006). Studies of ABS-graft-maleic anhydride/clay nanocomposites: Morphologies, thermal stability and flammability properties. *Polym. Degrad. Stab.*, Vol. 91, 2951–2959.
- [17] Pandey, J. K., Reddy, K. R., Kumar, A. P. & Singh, R. P. (2005). An overview on the degradability of polymer nanocomposites. *Polym. Degrad. Stab.*, Vol. 88, 234–250.
- [18] Sheng, N., Boyce, M. C., Parks, D.M., Rutledge, G. C., Abes, J. I. & Cohen R.E. (2004). Multiscale micromechanical modeling of polymer/clay nanocomposites and the effective clay particle. *Polymer*, Vol. 45, 487–506.
- [19] LeBaron, P. C., Wang, Z. & Pinnavaia, T. J. (1999). Polymer-layered silicate nanocomposites: an overview. *Appl. Clay Sci.*, Vol. 15, 11–29.
- [20] Thostenson, E. T., Li, C. & Chou, T. W. (2005). Nanocomposites in context. *Compos. Sci. Technol.*, Vol. 65, 491–516.
- [21] Pavlidou, S. & Papaspyrides, C. D. (2008). A review on polymer-layered silicate nanocomposites. *Prog. Polym. Sci.*, Vol. 32, 1119–1198.

- [22] Shirakawa, H. (2001). The discovery of polyacetylene film: the dawning of an era of conducting polymers (Nobel Lecture). *Angew. Chem. Int. Ed.* 40, 14, 2575–2580, 14337851.
- [23] Shirakawa, H. & Ikeda, S. (1971). Infrared spectra of poly(acetylene). *Polym. J.* 2, 2, 231–244, 0032–3896.
- [24] Shirakawa, H. & Ikeda, S. (1974). Cyclotrimerization of acetylene by tris(acetylacetato)titanium(III)-diethylaluminum chloride system. *J. Polym. Sci. Chem.*, 12, 5, 929–937, 0887–624X.
- [25] MacDiarmid, A. G. (2001). “Synthetic metals”: a novel role for organic polymers (Nobel Lecture). *Angew. Chem. Int. Ed.*, 40, 2581–2590.
- [26] Heeger, A. J. (2001). Semiconducting and metallic polymers: the fourth generation of polymeric materials (Nobel Lecture). *Angew. Chem. Int. Ed.*, 40, 2591–2611.
- [27] Do Nascimento, G. M. & Souza, M. A. (2010). Spectroscopy of nanostructured conducting polymers. In: *Nanostructured Conducting Polymers*. Eftekhari. A.; (Org.). Londres: Wiley and Sons, 341–375.
- [28] Bissessur, R., DeGroot, D. C., Schindler, J. L., Kannewurf, C. R. & Kanatzidis, M. G. (1993). Inclusion of poly(aniline) into MOO<sub>3</sub>. *J. Chem. Soc.: Chem. Commun.*, 8, 687–689. 0022–4936.
- [29] Liu, Y-J., DeGroot, D. C., Schindler, J. L., Kannewurf, C. R. & Kanatzidis, M. G. (1993). Stabilization of anilinium in vanadium(V) oxide xerogel and its post-intercalative polymerization to poly(aniline) in air. *J. Chem. Soc.: Chem. Commun.*, 7, 593–596. 0022–4936.
- [30] Wu, C-G., DeGroot, D. C., Marcy, H. O., Schindler, J. L., Kannewurf, C. R., Liu, Y-J., Hirpo, W. & Kanatzidis, M. G. (1996). Redox intercalative polymerization of aniline in V<sub>2</sub>O<sub>5</sub> xerogel. The postintercalative intralamellar polymer growth in polyaniline/metal oxide nanocomposites is facilitated by molecular oxygen. *Chem. Mater.*, 8, 1992–2004. 0897–4756.
- [31] Chang, T., Ho, S. & Chao, K. (1994). Polyaniline intercalated into zeolites, zirconium-phosphate and zirconium arsenate, *J. Phys. Org. Chem.*, 7, 371–376. 0894–3230.
- [32] Kanatzidis, M. G. & Liu, Y. (1993). Topotactic polymerization of aniline in layered uranyl phosphate. *Inorg. Chem.*, 32, 2989–2991. 0020–1669.
- [33] Wu, C-G., DeGroot, D. C., Marcy, H. O., Schindler, J. L., Kannewurf, C. R., Bakas, T., Papaefthymiou, V., Hirpo, W., Yesinowski, J. P., Liu, Y-J. & Kanatzidis, M. G. (1995). Reaction of aniline FEOCL—formation and ordering of conducting polyaniline in a crystalline layered host. *J. Am. Chem. Soc.*, 117, 9229–9242. 0002–7863.

- [34] Moujahid, E. M., Dubois, M., Besse, J-P. & Leroux, F. (2002). Role of atmospheric oxygen for the polymerization of interleaved aniline sulfonic acid in LDH. *Chem. Mater.*, 14, 3799–3807. 0897–4756.
- [35] Wypych, F., Seefeld, N. & Denicoló, I. (1997). Preparation of nanocomposites based on the encapsulation of conducting polymers into 2H-MoS<sub>2</sub> and 1T-TiS<sub>2</sub>. *Química Nova*, 20, 356–360. 0100–4042.
- [36] Yariv, S. & Michaelian, K. H. (2002). Structure and surface acidity of clay minerals. In *Organic-Clay Complexes and Interactions*. Yariv, S. & Cross, H., (Eds.). Marcel Dekker: New York, 1.
- [37] Hauser, E. A. & Leggett, M. B. (1940). Color reactions between clays and amines. *J. Am. Chem. Soc.*, 62, 1811–1814. 0002–7863.
- [38] Yariv, S., Heller, L. & Safer, Z. (1968). Sorption of aniline by montmorillonite, *Israel J. Chem.*, 6, 741–. 0021–2148.
- [39] Furukawa, T. & Brindley, G. W. (1973). Adsorption and oxidation of benzidine and aniline by montmorillonite and hectorite. *Clays and Clay Miner.*, 21, 279–288. 0009–8604.
- [40] Cloos, P., Moreale, A., Broers, C. & Badat, C. (1979). Adsorption and oxidation of aniline and p-chloroaniline by montmorillonite. *Clay Miner.*, 14, 307–321. 0009–8558.
- [41] Soma, Y. & Soma, M. (1988). Adsorption of benzidines and anilines on Cu-montmorillonites and Fe-montmorillonites studied by resonance Raman-spectroscopy. *Clay Miner.*, 23, 1–15. 0009–8558.
- [42] Soma, Y. & Soma, M. (1989). Chemical-reactions of organic-compounds on clay surfaces. *Environmental Health Perspectives*, 83, 205–214. 0091–6765.
- [43] Soma, Y., Soma, M. & Harada, I. (1983). Raman-spectroscopic evidence of formation of para-dimethoxybenzene cation on Cu-montmorillonite and Ru-montmorillonite. *Chem. Phys. Lett.*, 94, 475–478. 0009–2614.
- [44] Soma, Y., Soma, M. & Harada, I. (1984). The reaction of aromatic-molecules in the interlayer of transition-metal ion-exchanged montmorillonite studied by resonance Raman-spectroscopy. 1. Benzene and para-phenylenes. *J. Phys. Chem.*, 88, 3034–3038. 0022–3654.
- [45] Soma, Y., Soma, M. & Harada, I. (1985). Reactions of aromatic-molecules in the interlayer of transition-metal ion-exchanged montmorillonite studied by resonance Raman-spectroscopy. 2. 4, 4'-Disubstituted biphenyls. *J. Phys. Chem.*, 89, 738–742. 0022–3654.
- [46] Mehrotra, V. & Giannelis, E. P. (1991). Metal-insulator molecular multilayers of electroactive polymers-intercalation of polyaniline in mica-type layered silicates. *Solid State Commun.*, 77, 155–158. 0038–1098.

- [47] Chang, Te-C., Ho, S-Y. & Chao, K-J. (1992). Intercalation of polyaniline in monmorillonite and zeolite, *J. Chin. Chem. Soc.*, 39, 209–212. 0009–4536.
- [48] Wu, Q., Xue, Z., Qi, Z. & Wang, F. (1999). Synthesis and characterization of PAN/CLAY hybrid with extended chain conformation of polyaniline. *Acta Polym. Sin.*, 10, 551–556. 1000–3304.
- [49] Wu, Q., Xue, Z., Qi, Z. & Hung, F. (2000). Synthesis and characterization of PAn/clay nanocomposite with extended chain conformation of polyaniline. *Polymer*, 41, 2029–2032. 0032–3861.
- [50] Biswas, M. & Ray, S. S. (2000) Water-dispersible nanocomposites of polyaniline and montmorillonite, *J. Appl. Polym. Sci.*, 77, 2948–2956. 0021–8995.
- [51] Do Nascimento, G. M. (2013). Synthesis, characterization and applications of conducting polymer-clay nanocomposites. In: *Conducting Polymers: Synthesis, Properties and Applications*. Luiz Carlos Pimentel Almeida. (Org.). 3ed. New York: Nova Science Publishers, Inc., 155–178.
- [52] Lee, D. K., Lee, S. H., Char, K. & Kim, J. (2000). Expansion distribution of basal spacing of the silicate layers in polyaniline/Na<sup>+</sup>-montmorillonite nanocomposites monitored with X-ray diffraction. *Macromol. Rapid Commun.*, 21, 1136–1139. 1022–1336.
- [53] Lee, D., Char, K., Lee, S. W., Park, Y. W. (2003). Structural changes of polyaniline/montmorillonite nanocomposites and their effects on physical properties. *J. Mater. Chem.*, 13, 2942–2947. 0959–9428.
- [54] Yeh, J-M., Liou, S-J., Lai, C-Y., Wu, P-C. & Tsai, T-Y. (2001). Enhancement of corrosion protection effect in polyaniline via the formation of polyaniline-clay nanocomposite materials. *Chem. Mater.*, 13, 1131–1136. 0897–4756.
- [55] Zeng, Q. H., Wang, D. Z., Yu, A. B., Lu, G. Q. (2002). Synthesis of polymer–montmorillonite nanocomposites by in situ intercalative polymerization. *Nanotechnology*, 13, 549–553. 0957–4484.
- [56] Kim, B. H., Jung, J. H., Joo, J., Kim, J. W. & Choi, H. J. (2000). Charge transport and structure of nanocomposites of polyaniline and inorganic clay. *J. Korean Phys. Soc.*, 36, 366–370. 0374–4884.
- [57] Kim, B. H., Jung, J. H., Kim, J. W., Choi, H. J. & Joo, J. (2001). Effect of dopant and clay on nanocomposites of polyaniline (PAN) intercalated into Na<sup>+</sup>-montmorillonite (N<sup>+</sup>-MMT). *Synth. Met.*, 121, 1311–1312. 0379–6779.
- [58] Kim, B. H., Jung, J. H., Kim, J. W., Choi, H. J. & Joo, J. (2001). Physical characterization of polyaniline-Na<sup>+</sup>-montmorillonite nanocomposite intercalated by emulsion polymerization. *Synth. Met.*, 117, 115–118. 0379–6779.
- [59] Inoue, H. & Yoneyama, H. (1987). Electropolymerization of aniline intercalated in montmorillonite. *J. Electroanal. Chem.*, 233, 291–294. 0022–0728.

- [60] Orata, D. & David, S. K. (2000). A comparative study of the electrochemical/electro-degradation of polyaniline from aniline loaded in a clay-mineral/polyaniline composite matrix to that of the bulk solution. *React. Funct. Polym.*, *43*, 133–138. 1381–5148.
- [61] Feng, B., Su, Y., Song, J. H. & Kong, K. C. (2001). Electropolymerization of polyaniline/montmorillonite nanocomposite, *J. Mater. Sci. Lett.*, *20*, 293–294. 0261–8028.
- [62] Chen, K. H. & Yang, S. M. (2003). Synthesis of polyaniline-modified montmorillonite nanocomposite. *Synth. Met.*, *135*, 1–3, 51–52. 0379–6779.
- [63] Jara, P., Justiniani, M., Yutronic, N. & Sobrados, I. (1998). Syntheses and structural aspects of cyclodextrin/dialkylamine inclusion compounds. *J. Incl. Phenom.*, *32*, 1–8. 0923–0750.
- [64] Do Nascimento, G. M. & Temperini, M. L. A. (2008). Structure of polyaniline formed in different inorganic porous materials: A spectroscopic study. *Eur. Polym. J.*, *44*, 3501–3511.
- [65] Do Nascimento, G. M. & Temperini, M. L. A. (2011). Spectroscopic study of the polymerization of intercalated anilinium ions in different montmorillonite clays. *J. Mol. Struct.*, *1002*, 63–69.
- [66] Do Nascimento, G. M., Constantino, V. R. L. & Temperini, M. L. A. (2002). Spectroscopic characterization of a new type of conducting polymer–clay nanocomposite. *Macromolecules*, *35*, 7535–7537.
- [67] Do Nascimento, G. M., Landers, R., Constantino, V. R. L. & Temperini, M. L. A. (2004). Aniline polymerization into montmorillonite clay: a spectroscopic investigation of the intercalated conducting polymer. *Macromolecules*, *37*, 9373–9385.
- [68] Do Nascimento, G. M., Constantino, V. R. L. & Temperini, M. L. A. (2004) Spectroscopic characterization of doped poly(benzidine) and its nanocomposite with cationic clay. *J. Phys. Chem. B*, *108*, 5564–5571.
- [69] Do Nascimento, G. M., Landers, R., Constantino, V. R. L. & Temperini, M. L. A. (2006). Spectroscopic characterization of polyaniline formed in the presence of montmorillonite clay. *Polymer*, *47*, 6131–6139.
- [70] Do Nascimento, G. M., Barbosa, P. S. M., Constantino, V. R. L. & Temperini, M. L. A. (2006). Benzidine oxidation on cationic clay surfaces in aqueous suspension monitored by *in situ* resonance Raman spectroscopy. *Colloids Surf. A: Physicochem. Eng. Aspects*, *289*, 39–46.
- [71] Do Nascimento, G. M., Padilha, A. C. M., Constantino, V. R. L. & Temperini, M. L. A. (2008). Oxidation of anilinium ions intercalated in montmorillonite clay by electrochemical route. *Colloids Surf. A: Physicochem. Eng. Aspects*, *318*, 245–253.
- [72] Atkins, P. W. (1994). *Physical Chemistry*; Oxford University Press: Oxford-London, page 545.

- [73] Margaritondo, G. (2002). *Elements of Synchrotron Light for Biology, Chemistry and Medical Research*. Oxford University Press: New York, Chapter 3.
- [74] Margaritondo, G. (1988). *Introduction to Synchrotron Radiation*. Oxford University Press: New York, Chapter 2.
- [75] Durham, P. J. (1988). In *Chemical Analysis*; Koningsberger, D. C., Prins, R., Eds.; John Wiley & Sons: USA, 92, Chapter 2, page 53.
- [76] Thompson, A. C. & Vaughan, D. (2001). *X-ray Data Booklet Compiled and Edited by Lawrence Berkeley National Laboratory*; Lawrence Berkeley National Laboratory University of California Berkeley: California.
- [77] Bianconi, A. (1980). Surface x-ray absorption-spectroscopy—surface EXAFS and surface XANES. *Appl. Surf. Sci.*, 6, 392–418. 0169–4332.
- [78] Lee, P. A., Citrin, P. H., Eisenberger, P. & Kincaid, B. M. (1981). Extended x-ray absorption fine-structure—its strengths and limitations as a structural tool. *Rev. Mod. Phys.* 53, 769–806. 0034–6861.
- [79] Stern, E. A. (1988). In *Chemical Analysis*. Koningsberger, D. C. & Prins, R., Eds., John Wiley & Sons: USA, 92, Chapters 1 and 3.
- [80] Abruña, H. D. (1989). In *Modern Aspects of Electrochemistry*; Bockris, J. O'M., White, R. E. & Conway, B. E., Eds.; Plenum Press: New York, 20, Chapter 4, page 265.
- [81] Parsons, J. G., Aldrich, M. V. & Gardea-Torresdey, J. L. (2002). Environmental and biological applications of extended X-ray absorption fine structure (EXAFS) and X-ray absorption near edge structure (XANES) spectroscopies. *Appl. Spect. Rev.*, 37, 187–222. 0570–4928.
- [82] Bianconi, A. (1988). In *Chemical Analysis*; Koningsberger, D. C. & Prins, R., Eds.; John Wiley & Sons: USA, 92, Chapter 11, page 573.
- [83] Manne, R. & Åberg, T. (1970). Koopmans' theorem for inner-shell ionization. *Chem. Phys. Lett.*, 7, 282–284. 0009–2614.
- [84] Manne, R. & Åberg, T. (1978). In *Benchmark Papers in Physical Chemistry and Chemical Physics/2:X-ray Photoelectron Spectroscopy*. Carlson, T. A., Ed.; Dowden, Hutchinson & Ross, Inc.: Stroudsburg-Pennsylvania, Chapter 3, page 124.
- [85] Heald, S. M. (1988). In *Chemical Analysis*; Koningsberger, D. C. & Prins, R., Eds.; John Wiley & Sons: USA, 92, Chapter 3, page 87.
- [86] Alvim, R. S. & Miranda, C. R. (2015). First principles characterization of silicate sites in clay surfaces. *Phys. Chem. Chem. Phys.*, 17, 4952–4960. 1463–9076.
- [87] Pietzsch, A., Nisar, J., Jämstorp, E., Gråsjö, J., Arhammar, C., Ahuja, R., J-E. Rubensson, J. E. (2015). Kaolinite: Defect defined material properties – A soft X-ray and first principles study of the band gap. *J. Electron Spectrosc.*, 202, 11–15. 0368–2048.

- [88] Herndon, E. M., Martínez C. E. & Brantley, S. L. (2014). Spectroscopic (XANES/XRF) characterization of contaminant manganese cycling in a temperate watershed. *Biogeochemistry*, 121, 505–551. 0168–2563.
- [89] Rennert, T., Eusterhues, K., De Andrade, V., Totsche, K. U. (2012). Iron species in soils on a mofette site studied by Fe K-edge X-ray absorption near-edge spectroscopy. *Chem. Geology.*, 332–333, 116–123. 0009–2541.
- [90] Do Nascimento, G. M. (2013). X-ray absorption spectroscopy of nanostructured poly-anilines. *Chemical Papers*, 67, 8, 933–945. 0366–6352.
- [91] Vinogradov, A. S. & Akimov, V. N. (1998). X-ray absorption study of the spectrum of free electronic states in a KNO<sub>3</sub> crystal. *Opt. Spectrosc.*, 85, 53–59. 0030–400X.
- [92] Hyun, S. P. & Hayes, K. F. (2015). X-ray absorption spectroscopy study of Cu(II) coordination in the interlayer of montmorillonite. *Appl. Clay Sci.*, 107, 122–130. 0169–1317.
- [93] Schlegel, M. L. & Manceau, A. (2013). Binding mechanism of Cu(II) at the clay-water interface by powder and polarized EXAFS spectroscopy. *Geochim. Cosmochim. Acta*, 113, 113–124. 0016–7037.



# **Clay Minerals and Clay Mineral Water Dispersions — Properties and Applications**

---

Guadalupe Sanchez-Olivares, Fausto Calderas, Luis Medina-Torres,  
Antonio Sanchez-Solis, Alejandro Rivera-Gonzaga and Octavio Manero

Additional information is available at the end of the chapter

<http://dx.doi.org/10.5772/61588>

---

## **Abstract**

This chapter deals with the properties and applications of clay mineral water dispersions and clay minerals as flame retardant additives for polymers. Clay minerals, such as kaolinites, micas, and smectites, are the basic constituents of clay raw materials, which are classically employed in the ceramic industry to produce porcelain, fine ceramics, coarse ceramics, cements, electro-ceramics, tiles and refractories. These products are mainly used in sectors of economic importance, such as agriculture, civil engineering, and environment. A direct method to prepare clay mineral polymer composites is through dispersion in water. Water dispersions of clay exhibit some interesting flow phenomena such as yield stress; i.e., the material behaves as a solid until a critical force applied on the material forces it to flow. Water dispersions of clay have also been reported to be used to prepare materials with enhanced flame-retardant properties such as leather. On the other hand, direct melt compounding of clay mineral with different polymers as the composite matrix (HIPS, PP, and HDPE) to prepare a number of polymer composites with flame-retardant properties has also been reported.

**Keywords:** Clay minerals, ceramics, polymer nanocomposites, clay water suspensions, flame-retardant leather

---

## **1. Introduction**

Clay minerals have recently been one of the most used materials in many research and development areas. Clay minerals are excellent as clarifiers, absorption and adsorption materials. They are used in many industrial applications such as paper, paint, petroleum, ceramic, cement, adhesive, asphalt, and food and health-care industry due to their versatility, abundance, and low cost [1, 2].

Currently, clay minerals have been proved to have a wide range of new applications, specifically as reinforcing agents of polymers to produce nanocomposites. Nanocomposites are high-performance composite materials in which one of the phases that compose them has dimensions in the nanoscale ( $10^{-9}$  m). The surface area-to-volume ratio of the reinforcing materials contained in a nanocomposite is of paramount importance and plays a key role in the final properties of these materials [3]. Clay minerals, and specially smectites, are materials that offer a high area-to-volume ratio (layered silicates) to be used as reinforced agents in polymer matrices [3–9]. Smectites contain not only external surface but also internal surface, and after a certain treatment, this internal surface can absorb the hydrophobic molecules of organic compounds [10]. The high surface area-to-volume ratio is maximized when the individual platelets, naturally occurring as stacks, become delaminated (exfoliated), thus offering large-scale interactions as reinforcing materials. The thickness of individual platelets (layers) is about 1 nm. Other important reinforcing agents for preparing polymer nanocomposites are carbon nanotubes (CNTs) [11] and, more recently, graphene [12, 13].

Many of the properties that clay minerals impart on polymer nanocomposites are due to the exfoliation and good dispersion of clay platelets which are initially in stacks. A direct method to prepare clay mineral composites is dispersion in water which has been used as an initial approach to produce clay–polymer composites [14]. Water dispersions of clay also exhibit some interesting flow phenomena such as yield stress; i.e., material behaves as a solid until a critical force applied on the material forces it to flow. These clay dispersions have been used as model fluids to study complex flow phenomena and to test some rheological constitutive equations predictions [15]. Water dispersions of clay minerals have also been used to prepare materials with enhanced flame-retardant properties such as leather [16].

Clay–polymer nanocomposite properties mainly depend on the type of clay mineral, chemical modification, concentration, dispersion, structure, and process conditions. With respect to chemical modification of clay minerals, this step has been proven to be crucial in preparing flame-retardant polymer materials. Chemical modification of clay minerals can either produce an effective halogen-free flame-retardant material or, on the contrary, causes a negative effect and increases polymer flammability. In high-impact polystyrene (HIPS), both natural and modified sodium montmorillonite ( $\text{Na}^+\text{Mt}$ ) were used to study the burning rate of the nanocomposite produced. It was found that when natural  $\text{Na}^+\text{Mt}$  is added to HIPS, an antagonistic effect on the burning rate is observed: the burning rate increases with respect to virgin HIPS. However, when triphenyl phosphite-modified sodium montmorillonite is added (at a specific content) to HIPS, the burning rate is effectively reduced [17].

Process conditions have an important impact on polymer nanocomposites properties [18]. It is necessary to find the appropriate processing conditions in order to disperse clay minerals at the nanometric level. The effect of processing conditions on HIPS, polypropylene (PP) and high-density polyethylene (HDPE) using modified  $\text{Na}^+\text{Mt}$  and bentonite has been reported [19–21]. Two different extrusion processes were applied: twin extrusion and single extrusion adapted with a special static mixer die and with and without on-line ultrasound application. For HIPS composites, it was found that when the static mixer die is employed, the heat release rate of HIPS is reduced attributed to better clay dispersion. With regard to HDPE and PP, when

on-line ultrasound is applied, modified clay mineral (at specific content) is dispersed effectively (presumably at the nanometric level) and mechanical properties, Izod impact resistance, tensile strength, strain at break, and tenacity were also improved. It was also possible to optimize the content of flame-retardant additives with respect to traditional polymer composites; the materials were classified as V0 (burning stops within 10 seconds on a vertical position specimen; drips of particles allowed as long as they are not inflamed) in accordance with the UL94 standard (ASTM D3801).

To produce nanocomposites, not only polymer matrix materials are used but also metal and ceramic-based materials have been reported [3]. Traditional ceramics have good wear resistance and very high thermal and chemical stability properties. Their main disadvantage for many potential industrial applications is their brittleness. Ceramic-based nanocomposites have recently received attention to produce ceramics with higher performance as the incorporation of reinforcing agents in the form of whiskers, fibers, platelets, and particles to render ceramics with improved fracture toughness. Among the reported reinforced agents used for ceramics are CNTs [22, 23] and graphene [24].

Clay minerals, such as kaolinites, micas, and smectites, are the basic constituents of clay raw materials. The latter are classically employed in the ceramic industry to produce porcelain, fine ceramics, coarse ceramics, cements, electro-ceramics, tiles, and refractories [10, 25]. These products are mainly used in sectors of economic importance, such as agriculture, civil engineering, and environment.

This chapter deals with the properties and applications of clay mineral water dispersions (subchapter 2) and clay minerals as flame-retardant additives for polymers (subchapter 3). Subchapter 2 is divided into three sections: the first one is dedicated to discuss yield stress phenomena (subsection 2.1), the second one discusses the use of an unmodified clay mineral ( $\text{Na}^+\text{Mt}$ ) water dispersion as a precursor to prepare an epoxy resin-based composite (subsection 2.2), and the last one deals with the application of clay mineral dispersions to prepare leather with flame retardancy properties (subsection 2.3). Subchapter 3 is also divided into three sections to give examples of clay mineral polymer composites based on different polymers: HIPS (subsection 3.1), PP (subsection 3.2), and HDPE (subsection 3.3), where good dispersion of clay mineral and additives in the polymer matrix is proved to be a key issue in preparing this type of materials.

## 2. Clay mineral water dispersions

Clay mineral dispersions have a wide range of applications in the industry. For example, they are used as prominent excipients in the pharmaceutical industry to impart adequate semisolid formulations [26]. Rheology is very important in this type of materials, since a correct understanding of their flow properties allows improvement and optimization of the processing conditions and characteristics of the final products. Aguzzi et al. [27] studied the thixotropy in peloid systems (concentrated clay suspensions in mineral medicinal water). Cruz et al. [28] studied the rheological properties of bentonite and kaolinite dispersions in copper–gold

flotation systems. They also discuss the yield stress phenomena exhibited by kaolinite dispersions and how pH affects the Bingham yield stress of these systems and the diverse configurations that the kaolinite platelets adopt related to this phenomenon. The viscoelastic behavior and yield stress of clay mineral dispersions (smectites, beidellite, and montmorillonites) have also been reported by Paineau et al. [29]. Also aqueous clay mineral dispersions are employed as precursors to prepare composites and nanocomposites of which epoxy resin nanocomposites are of special interest here, specifically when the clay mineral used is not organically modified. More recently, clay minerals have been used for the preparation of materials with flame-retardant properties such as leather, which would allow direct incorporation of flame-retardant additives on-line, instead of treating the finished leather with spraying methods. Flame-retardant leather can be used as upholstery material in aeronautic and automotive applications.

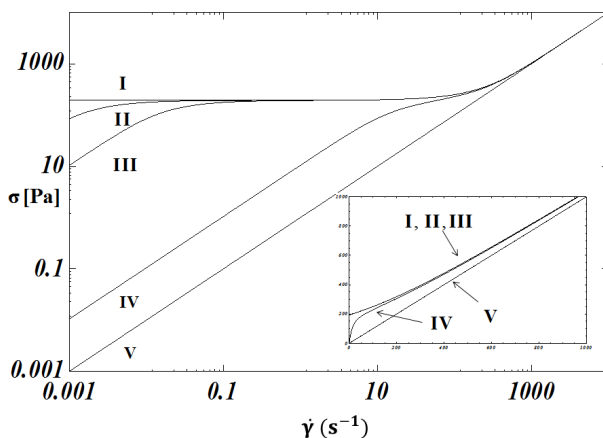
## 2.1. Yield stress in water clay dispersions

The yield stress of clay mineral water dispersions has received a lot of attention [15, 28, 29]. The yield stress phenomenon occurs when the shear stress does not depend on the shear strain (constant value). Under these circumstances, the system behaves as an elastic solid. However, upon increasing the strain rate, after a critical point is reached (yield stress), the material starts to flow. The “real” yield stress has been associated with the Bingham yield stress, i.e., an asymptotic nonzero value of the stress as the shear rate tends to zero. While the term “apparent yield stress” is associated with a very large zero-shear rate viscosity, which corresponds to a zero shear viscosity plateau. A viscoplastic material under strain exhibits little or no deformation up to a critical value of stress which is called the yield stress. Above this critical point, the material starts to flow. Concentrated dispersions of solid particles in Newtonian liquids (such as aqueous clay mineral suspensions) exhibit yield stress followed by nearly Newtonian behavior. These materials are often called Bingham plastics. Various other fluids of a practical interest, such as liquid foams, paints, droplet emulsions, or high cholesterol blood, possess such elastoviscoplastic behavior.

Cheng [30] reported that the stress becomes almost independent of the shear rate in an intermediate range of shear rates, while increasing shear rates results in Newtonian-like behavior. The presence of an essentially horizontal region in a double logarithmic plot of stress versus strain rate has been considered to be the most satisfactory criterion for the existence of a yield stress [31]. Regarding rheological models that predict yield stress at moderate shear rates, both the Bingham [32] and the Herschel–Bulkley [33, 34] models predict a flattening of the stress as a function of shear rate. One of the computational problems mentioned by Barnes [32] is that the behavior of a Bingham or similar materials at the yield stress is in no way smooth and differentiable in a mathematical sense. At stresses below the yield stress, the viscosity becomes indefinite (tending to infinite). At stresses above the yield stress, the viscosity is an asymptotically decreasing function of shear stress, usually tending to a constant value of viscosity as the stress becomes infinite. These problems can lead to inconsistencies in the numerical modeling of flow in complex geometries, and difficulties in properly defining the boundaries between nondeforming “solid” zones and flowing “liquid” zones.

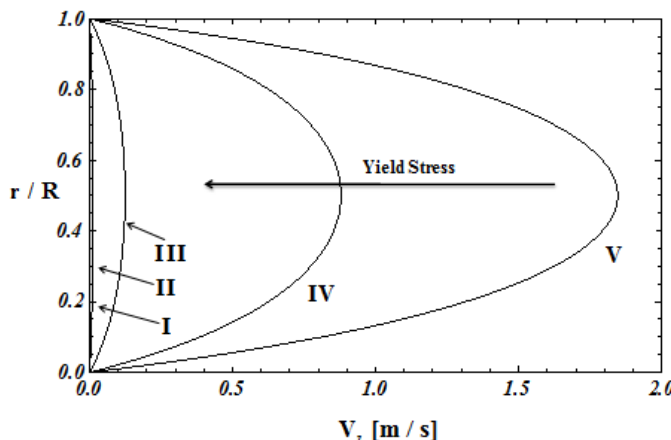
Several constitutive equations have been proposed to model yield stress phenomena: Papastasiou [35] proposed a slightly modified version of the Bingham plastic [33], containing three fitting parameters. Although this model is continuous and differentiable, it does not predict a real solid-like behavior. Alternative models have been proposed to account for the real solid case (Hookean behavior before yielding). Houlsby and Puzrin [36] and Isayev and Fan [36] proposed models which are based on the original Voigt-Kelvin or Maxwell-like behavior with added yield stress terms. The Houlsby and Puzrin [36] model predicts an elastic behavior before yielding, and a Kelvin-Voigt solid behavior at long times (after yield), while the Isayev model [37] predicts a Hookean elastic behavior before yielding and a viscous one after yielding. These models have the disadvantage that the solid-liquid transition is discontinuous. Saramito [38, 39] proposed a constitutive equation for elastoviscoplastic materials which is continuous and differentiable. Nevertheless, it does not predict a real solid-like behavior. To predict a solid behavior, a new version of the latter viscoplastic model was suggested, based on the Herschel-Bulkley one [34]. In summary, models that predict real solid behavior and a smooth transition to liquid-like behavior are mostly empirical. Bautista et al. [40] presented a model (Bautista-Montero-Puig [BMP] model) that predicts several rheological phenomena observed in complex materials. This model has been shown to describe the apparent and real yield stress behavior [15].

Fig. 1 shows a log-log plot of the stress versus shear rate for various values of the fluidity  $\varphi_0$  (inverse of the viscosity function  $1/\eta_0$ ). In the case of  $\varphi_0 > 0$ , the stress goes to zero as the applied shear rate goes to zero, except when  $\varphi_0 = 0$ ; in this case, Bingham behavior is observed, corresponding to a real yield stress. In the inset, the linear plot depicts the region of very small shear rates, showing that all the curves tend to zero, except curves I, II, and III. Although these curves show a real yield stress, only curve I fulfills the term "real," since curves II and III show an "apparent" yield. This is only observed in the linear plot (inset) where the stress reaches the true yield stress value at zero rate of deformation (y-intercept).



**Figure 1.** BMP model predictions of the shear stress as a function of shear rate (log-log plot) for various values of the zero shear-rate fluidity. As this parameter tends to zero, the real yield stress is reached. Inset: Linear plot.

Fig. 2 shows predictions of the BMP model for the velocity profile (radial position from lower pipe wall  $r/R = 0$  to upper pipe wall  $r/R = 1$  versus axial velocity  $V_z$ ) of a general fluid flowing in a pipe of normalized diameter (pipe of length  $z = L$  and radius  $r = R$ ), i.e., Poiseuille flow. In the simulations II–V, the shape of the velocity is parabolic. Under Poiseuille flow, when the flow becomes more and more dominated by the yield stress, the velocity profile becomes more plug-like (zero velocity case I, Fig. 1). This arises because the material deformation is restricted in the tube to just near the wall.



**Figure 2.** BMP model predictions for the velocity profile of pressure driven flow of a complex fluid with approximating from the no yield stress case (V) to the real yield stress case (I) in a circular pipe.

The BMP model possesses the capacity of predicting the rheological behavior of complex structural fluids such as wormlike micellar solutions, dispersions of lamellar liquid crystals, associative polymers, bentonite suspensions, polymer-like micellar solutions, and polymer nanocomposites [40–48]. In addition, the model reproduces the complete flow curve for a shear-thinning and shear-thickening fluid, i.e., Newtonian plateau at low and high shear rate, and the intermediate power law region for viscosity, and nonvanishing normal stress difference. The model also gives a reasonable description of the elongational and complex viscosity with finite asymptotic value and non-exponential stress relaxation and start-up curves, thixotropy, and shear-banding flow. Yield stress predictions for this model have been proved to be in very good agreement with rheological data at short times (steady and unsteady state measurements) for kaolin (a clay mineral) suspensions in water at 60% mass concentration and also for ketchup [15]. The one-mode model fails to predict the behavior for these materials at long times. A more recent version of the model has been proposed as a linear sum of modes. Such model is more effective in modeling the behavior of complex materials at long times [49].

Fig. 3 shows a comparison of different model predictions in the yield stress region. The “real” yield stress models in Fig. 3 predict an asymptotic region independent of the shear rate for shear rate tending to zero [33, 34, 40, 50]. In the insets, models that predict “apparent” yield

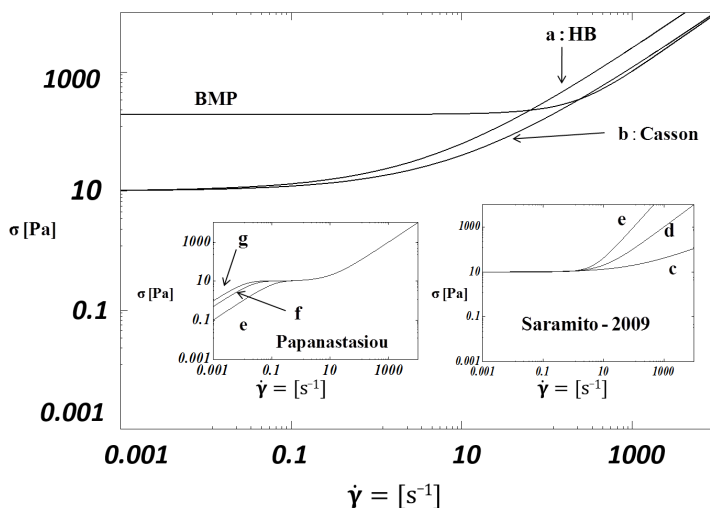


**Figure 3.** Shear stress versus shear rate showing various model predictions. Parameters for the simulations are as follows: Herschel–Bulkley,  $n = 0.5$ ,  $\sigma_y = 10$ . Saramito  $n = 0.5, 1.0, 1.5$ ,  $\sigma_y = 10$ . Casson,  $\sigma_y = 10$ . Bingham,  $\sigma_y = 10$ . Papanastasiou,  $n = 5, 10, 15$ ,  $\sigma_y = 10$ . BMP,  $\sigma_y = 26$ .

stresses illustrate the region at vanishing shear rates where the flow curves tend to a very high zero-shear rate viscosity [35, 38]. The BMP model predicts characteristic rigid solid behavior before yielding of the Bingham [33] or Herschel–Bulkley [34] models applicable for an elastic or viscoelastic solid behavior, as in the Houslsby and Puzrim [36], Isayev and Fan [37], or Saramito [38, 39] models. Finally, after yielding, it predicts either a shear thickening, a shear thinning, or a Newtonian behavior [40].

## 2.2. Composites with clay mineral water dispersion as precursor

There are a large number of reports about clay mineral thermostable resin nanocomposites. However, most of these studies deal with epoxy–silicate systems rather than sodium montmorillonite ( $\text{Na}^+\text{Mt}$ )–polyester systems. Furthermore, montmorillonite is organically modified in order to be used in epoxy- and polyester-based nanocomposites [51–55]. There are few studies regarding unmodified montmorillonite which is basically used to compare with the organically modified one. Unmodified montmorillonite is incompatible with the polymer due to its hydrophilic nature. Attempts to use suspensions of mineral clay as a precursor to prepare thermostable resin nanocomposites are even scarcer. For example, it has been reported that the hydrated form of the  $\text{Na}^+\text{Mt}$  facilitates the intercalation of an epoxy monomer in the clay interlaminar spacing. When hydration of clay occurs, the platelets of  $\text{Na}^+\text{Mt}$  separate from each other as the forces of layers attraction weaken due to water entering the interlaminar spaces [56]. Clay montmorillonite suspensions have been used to prepare exfoliated nanocomposites by mixing it with melt polymer (nylon 6). The high temperature of the melt polymer evaporates the water, leaving the final polymer matrix with regions of exfoliated clay as well as tactoids

of clay [57]. A slurry compounding method has also been reported.  $\text{Na}^+\text{Mt}$  is suspended first in water and then ketone or alcohol is added to form a binary system. Then, the montmorillonite is treated with xylene to obtain modified clay. This modified clay is used to produce epoxy-nanoclay systems [57–59].

A more recent attempt in the preparation of unsaturated polyester resin nanocomposites is based on an unmodified mineral clay suspension in water as a precursor [14].  $\text{Na}^+\text{Mt}$  is suspended in water ( $\text{Na}^+\text{Mt}/\text{H}_2\text{O}$ ) to incorporate this suspension in an isophthalic neopentyllic polyester resin (UP) which is then polymerized. Clay mineral individual layers are separated in the aqueous suspension and allows the resin molecules to intercalate in the interlayer spacing. The mixing method and clay mineral/water proportion are key features in the preparation of this nanocomposite. In this case, a 1:1.5 (water-to-clay) proportion was used, which is lower than what is reported in the literature.

UP nanocomposites obtained by this method (clay mineral water suspension) showed augmented mechanical properties in comparison with UP resin without clay and UP- $\text{Na}^+\text{Mt}$  resin with unsuspended clay mineral at a concentration of 5 phr mineral clay. Flexural strength and flexural modulus values showed increments of 13% and 120%, respectively, for the suspended clay–resin system as compared to the UP resin, see Table 1.

$\text{Na}^+\text{Mt}$ concentration [phr]	UP- $\text{Na}^+\text{Mt}$		UP- $\text{Na}^+\text{Mt}/\text{H}_2\text{O}$	
	Flexural strength [MPa]	Flexural modulus [MPa]	Flexural strength [MPa]	Flexural modulus [MPa]
0	31.3 ( $\pm 0.2$ )	830 ( $\pm 8$ )	31.3 ( $\pm 0.2$ )	830 ( $\pm 8$ )
1	33.4 ( $\pm 0.6$ )	884 ( $\pm 4$ )	41.3 ( $\pm 0.9$ )	1296 ( $\pm 93$ )
3	36.7 ( $\pm 1.1$ )	905 ( $\pm 66$ )	30.0 ( $\pm 1.1$ )	959 ( $\pm 10$ )
5	39.8 ( $\pm 0.9$ )	1189 ( $\pm 44$ )	35.5 ( $\pm 1.2$ )	1821 ( $\pm 15$ )

**Table 1.** Flexural strength and flexural modulus for samples UP- $\text{Na}^+\text{Mt}$  and UP- $\text{Na}^+\text{Mt}/\text{H}_2\text{O}$ .

These increased values are attributed to the intercalation of the resin in the interlayer space of the clay platelets. This intercalation enhances the polymer-clay interaction and the stress distribution, transferring the polymer matrix stresses to the nanoclay platelets, and improving the mechanical properties. Intercalation of the polymer in the clay platelets was evidenced by X-ray diffraction pattern, where the basal spacing of the platelets  $\text{Na}^+\text{Mt}$  (1.23 nm) was incremented at UP- $\text{Na}^+\text{Mt}/\text{H}_2\text{O}$  to 1.56 nm [14]. Clay mineral intercalation was further evidenced by transmission electron microscopy (TEM) and scanning electron microscopy (SEM) techniques. Fig. 4 shows a TEM micrograph of arrangements of three, five, and six intercalated platelets in the UP matrix; the platelets show no exfoliation at all. SEM micrographs in Fig. 5 shows the fractured surface of the nanocomposite (Fig. 5b), which is more rugged than the surface of the UP matrix alone (Fig. 5a), and indicates the existence of bonds between the clay mineral and the polymer matrix.

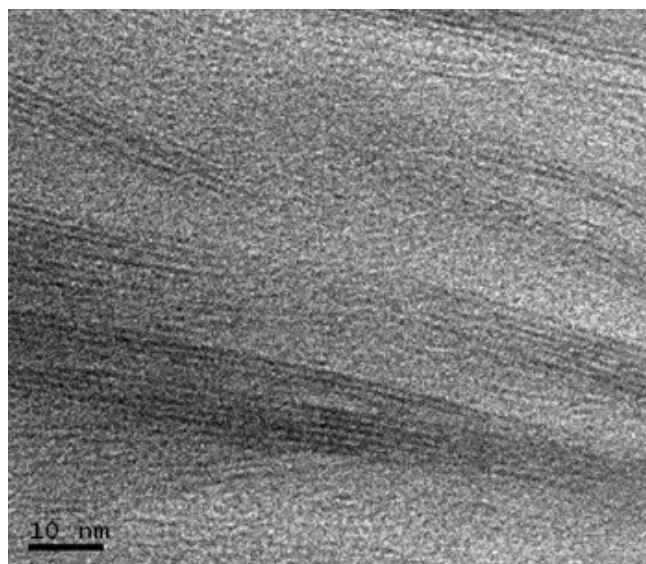


**Figure 4.** TEM micrograph showing sample UP-Na<sup>+</sup>Mt/H<sub>2</sub>O. The polymer matrix is intercalated in the interlaminar space of the clay platelets which preserve an ordered configuration.

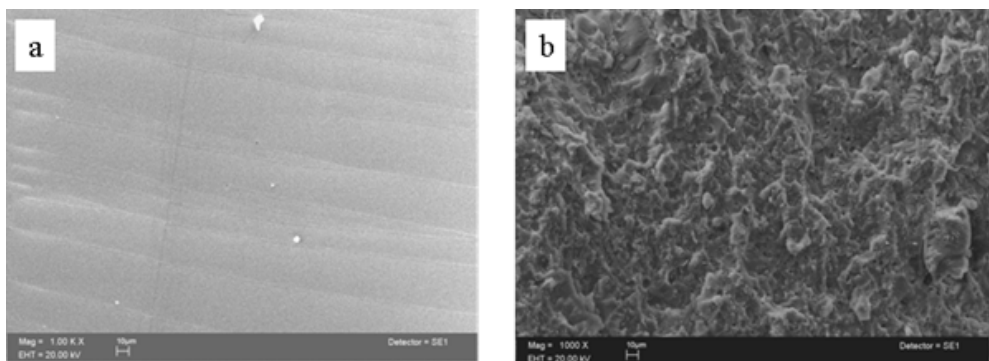


**Figure 5.** SEM micrographs for UP (a) and UP-Na<sup>+</sup>Mt/H<sub>2</sub>O at 5 phr clay content (b).

Thermogravimetric analysis (TGA) revealed that the nanocomposite UP-Na<sup>+</sup>Mt/H<sub>2</sub>O is more resistant to degradation than UP polymer (Fig. 6) with the unsuspended clay mineral sample (UP-Na<sup>+</sup>Mt) in the middle of them. This is attributed to the intercalated clay platelets which act as a thermal insulator and as a mass transport barrier.

Rheological analysis evidenced a shift in the gelation temperature toward higher temperatures, from 86°C for UP to 96°C for UP-Na<sup>+</sup>Mt/H<sub>2</sub>O sample (5 phr of suspended Na<sup>+</sup>Mt) (Fig. 7). Sample with non-suspended Na<sup>+</sup>Mt showed an intermediate gelation temperature (92°C).

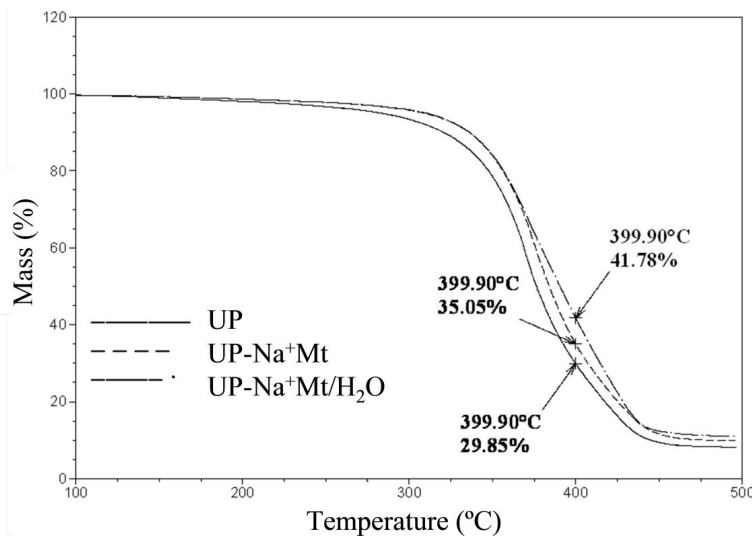


Figure 6. Mass loss from TGA analysis for UP, UP-Na<sup>+</sup>Mt/H<sub>2</sub>O 5 phr clay, and UP-Na<sup>+</sup>Mt 5 phr clay.

When Na<sup>+</sup>Mt acquires an intercalated structure within the polymer matrix, an interconnected network is formed which, in principle, is more thermally stable and caused an increase in the gelation temperature.

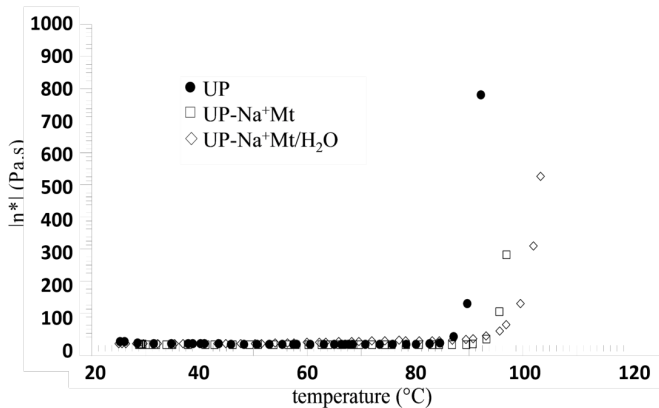


Figure 7. Complex viscosity versus temperature for samples UP, UP-Na<sup>+</sup>Mt 5 phr clay and UP-Na<sup>+</sup>Mt/H<sub>2</sub>O 5 phr clay mineral where gelation temperature is evidenced as a sudden increase in viscosity.

Regarding continuous shear flow, shear viscosity data revealed an increase for UP-Na<sup>+</sup>Mt/H<sub>2</sub>O of almost two decades in comparison with pure UP together with a shift from Newtonian to

a strong shear thinning behavior and a tendency towards a yield stress value at low shear rates. The interconnected network formed by the intercalated structure is destabilized by shear, which is evidenced by superimposed viscosity curves at high shear rate (Fig. 8). Unsuspended Na<sup>+</sup>Mt has little or almost no influence in the rheology of the system with the water added acting only as a lubricant by reducing the viscosity of the sample.

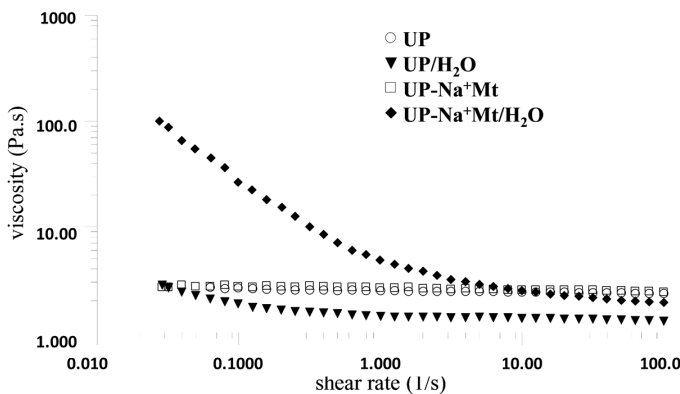


Figure 8. Shear viscosity for the systems UP, UP/H<sub>2</sub>O, UP-Na<sup>+</sup>Mt 5 phr clay, and UP-Na<sup>+</sup>Mt/H<sub>2</sub>O 5 phr clay.

Frequency sweep measurements in the linear viscoelastic regime performed on the uncured samples are presented in Fig. 9, the system UP-Na<sup>+</sup>Mt/H<sub>2</sub>O revealed characteristics of a weak gel with storage modulus ( $G'$ ) values independent of the frequency applied, while samples UP and UP-Na<sup>+</sup>Mt (unsuspended clay) showed a viscoelastic liquid behavior, i.e., slope values of ~1 and 2 for  $G'$  and  $G''$ , respectively, at low frequencies.

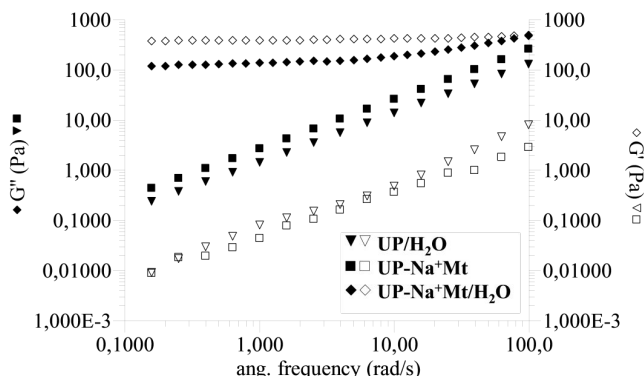


Figure 9. Storage and loss moduli versus frequency from linear viscoelastic measurements for samples UP, UP/H<sub>2</sub>O, UP-Na<sup>+</sup>Mt 5 phr clay, and UP-Na<sup>+</sup>Mt/H<sub>2</sub>O 5 phr of clay.

### 2.3. Clay mineral as flame retardant for leather

In recent years, the tannery industry has paid attention to clay minerals because of the potential advantages that these materials represent. Research works about the use of clay minerals on leather have reported better leather performance on processes such as tanning, coating, and, ultimately, in the final properties of the leather itself [60]. Nevertheless, reports on leather flame-retardant properties using clay minerals are still rare. In spite of this, clay minerals have shown very good synergistic effect on flame-retardant properties. A considerable reduction on the content (load) of flame-retardant additives (other than clay minerals) in polymer composites has been reported by using clay minerals [20, 21].

The effect of sodium montmorillonite ( $\text{Na}^+\text{Mt}$ ) on the morphology, thermal, flame-retardant, and mechanical properties of semi-finished leather was studied in order to obtain flame-retardant leather for upholstery uses in the aeronautic industry [16]. In this investigation,  $\text{Na}^+\text{Mt}$  particles were dispersed in hot water at 1:20 ratio ( $\text{Na}^+\text{Mt}$ :water), along with continuous stirring. This dispersion was incorporated into the leather during an ordinary retanning process in a drum, as it is commonly used in the tannery industry. Dispersion of  $\text{Na}^+\text{Mt}$  and leather was rotated for a specific time. Three samples with different  $\text{Na}^+\text{Mt}$  contents of 1, 3, and 6 wt.% were prepared.

Leather morphology was studied by scanning electron microscopy (SEM). Sample reference (leather without  $\text{Na}^+\text{Mt}$ ) showed a grain surface with different pore sizes (from 100  $\mu\text{m}$  to 400 nm). The cross section showed interstitial voids between fibers of leather. Based on the leather morphology, we can assume that the  $\text{Na}^+\text{Mt}$  particles penetrate inside the leather through the pores during the retanning process. Mapping of elements (Si, Al, and Mg) was carried out on the leather samples with the different contents of  $\text{Na}^+\text{Mt}$ . The elements mapping pointed out that  $\text{Na}^+\text{Mt}$  particles were well distributed and dispersed within the leather structure.

Thermal stability of the leather samples was studied by thermogravimetry. The test analysis in nitrogen atmosphere showed that leather degrades in a single stage, with a maximum degradation temperature of 327°C. However, when leather degrades in atmospheric air, the degradation mechanism presents two main stages. The first stage occurs at a maximum degradation temperature of 319°C and the second one at 459°C. The mass loss of the leather in both test analysis is attributed to the collagen, since it is the main component of leather [61, 62]. Clay mineral inside the leather changes the thermal degradation mechanism. According to test analysis, leather with  $\text{Na}^+\text{Mt}$  samples exhibited better thermal stability than the reference sample (without clay mineral). Particularly at the second stage, the maximum degradation temperature of the leather with  $\text{Na}^+\text{Mt}$  samples increased to 469, 463, and 463°C at 1, 3, and 6 wt.% of  $\text{Na}^+\text{Mt}$ .

Flame-retardant properties were evaluated through a 60-second vertical flammability test according to "14 C.F.R. (code of federal regulations) F part 25 title 14—aeronautics and space, published by United States of America transportation department." According to Table 2,  $\text{Na}^+\text{Mt}$  particles significantly improved the flame-retardant properties of semifinished leather. The burning length of leather was reduced from 16.4 cm to 13.3 and 13.4 cm for samples with 3 and 6  $\text{Na}^+\text{Mt}$  wt.%, respectively (Table 2). These results were attributed to the barrier

mechanism which has been observed and reported previously in flame-retardant polymer nanocomposites [63, 64]. According to “14 C.F.R. standard,” the average burn length must not exceed 15.2 cm. Therefore, leather with Na<sup>+</sup>Mt (3 and 6 wt.%) are suitable for upholstery uses in the aeronautic industry.

Mechanical properties, tensile strength, strain at break, and tear strength of reference leather and leather with Na<sup>+</sup>Mt samples were also evaluated. According to Table 3, tensile strength and tear strength were enhanced by using 1 and 3 wt.% of Na<sup>+</sup>Mt which evidences the reinforcing effect of Na<sup>+</sup>Mt interacting physically with the leather, even at these low contents.

Na <sup>+</sup> Mt content [wt.%]	Burning length [cm]
0	16.4 ( $\pm 0.9$ )
1	14.3 ( $\pm 0.7$ )
3	13.3 ( $\pm 0.5$ )
6	13.4 ( $\pm 1.1$ )

**Table 2.** Burning length of leather samples.

Na <sup>+</sup> Mt content [wt.%]	Tensile strength [MPa]	Tear strength [N]	Strain at break [%]
0	16.5 ( $\pm 0.7$ )	79 ( $\pm 3.0$ )	51 ( $\pm 1$ )
1	22.5 ( $\pm 0.4$ )	94 ( $\pm 1.0$ )	51 ( $\pm 2$ )
3	22.8 ( $\pm 0.8$ )	85 ( $\pm 5.0$ )	41 ( $\pm 1$ )
6	17.0 ( $\pm 0.8$ )	85 ( $\pm 5.0$ )	34 ( $\pm 1$ )

**Table 3.** Mechanical properties of leather samples.

In conclusion, morphology, thermal stability, and flame-retardant and mechanical properties were studied on semifinished leather using Na<sup>+</sup>Mt particles. It was found that by using 3 wt. % of Na<sup>+</sup>Mt present during retanning process of leather, flame-retardant, and mechanical properties are improved. A semifinished leather suitable for aeronautic industry as upholstery product was obtained.

### 3. Clay minerals as flame-retardant additives on polymer blends

In the last decades, clay minerals have demonstrated to be efficient nontoxic flame-retardant systems to produce polymer composites [63, 65]. Different mechanisms have been proposed on how clay minerals act as flame retardants, and these mechanisms mainly vary depending on the polymer matrix. In some cases, clay mineral may change the polymer thermal degradation process, causing cross-linking, or promote the formation of a carbonaceous char layer

on the surface of the burning material, which acts as an insulating barrier [66]. Currently, the flame-retardant properties of clay minerals have become a very common topic for industrial and academic research due to their versatility and advantages, such as efficiency, environment friendly, and good impact on mechanical properties, with respect to traditional flame-retardant additives [67].

### 3.1. High-impact polystyrene

High-impact polystyrene (HIPS) is a widely used polymer in different industry fields due to its high-impact resistance. However, this polymer is highly flammable when exposed to fire, since it shows a low char-forming tendency during combustion process due to its chemical structure: aliphatic groups connected to aromatic moieties [68]. To improve HIPS flame-retardant properties, agents formulated from halogenated compounds have been used traditionally [69, 70]. Unfortunately, these compounds form highly toxic vapors during the combustion process.

Sanchez-Olivares et al. [19] analyzed in detail the fire behavior of high-impact polystyrene (HIPS) using  $\text{Na}^+\text{Mt}$  intercalated with triphenyl phosphite (Tri-Ph) as halogen-free flame-retardant additive. Intercalated sodium montmorillonite ( $\text{Na}^+\text{Mt}/\text{Tri-Ph}$ ) was obtained by mixing  $\text{Na}^+\text{Mt}$  and Tri-Ph (viscous liquid) at 1:1 ratio, along with stirring at 90–105°C to render a homogenous slurry. Thermogravimetry analysis was carried out in order to evaluate the Tri-Ph intercalation in the  $\text{Na}^+\text{Mt}$  gallery.  $\text{Na}^+\text{Mt}$ , Tri-Ph, and  $\text{Na}^+\text{Mt}/\text{Tri-Ph}$  samples were evaluated. It was found that when Tri-Ph is intercalated in  $\text{Na}^+\text{Mt}$ , the thermal stability is higher than for pure Tri-Ph. A conical twin-screw intermeshing counter-rotating extruder (TS) and a single-screw extruder adapted with a static mixing die (SS-MD), which had conical compression and decompression sections to produce extensional flows, were employed in order to evaluate  $\text{Na}^+\text{Mt}/\text{Tri-Ph}$  dispersion effect on fire behavior of HIPS. About 5 phr of  $\text{Na}^+\text{Mt}/\text{Tri-Ph}$  were added to HIPS during TS and SS-MD extrusion process. The injection molding method was carried out to obtain HIPS- $\text{Na}^+\text{Mt}/\text{Tri-Ph}$  specimens to evaluate fire behavior. Intercalation degree of samples HIPS- $\text{Na}^+\text{Mt}/\text{Tri-Ph}_\text{TS}$ , and HIPS- $\text{Na}^+\text{Mt}/\text{Tri-Ph}_\text{SS-MD}$  was studied using X-ray diffraction analysis. The  $\text{Na}^+\text{Mt}/\text{Tri-Ph}$  X-ray pattern showed the characteristic peak of mineral clay in 2–10 degree at 2 theta scale diffraction ( $\text{Cu-K}_\alpha$ -X-raysource,  $\lambda = 1.540562 \text{ \AA}$ ). However, the HIPS- $\text{Na}^+\text{Mt}/\text{Tri-Ph}_\text{TS}$  and HIPS- $\text{Na}^+\text{Mt}/\text{Tri-Ph}_\text{SS-MD}$  patterns did not show that peak, which was attributed to the effect of clay mineral intercalation in the polymer matrix caused by the shear forces during mixing.

Combustion behavior of HIPS, HIPS- $\text{Na}^+\text{Mt}/\text{Tri-Ph}_\text{TS}$  and HIPS- $\text{Na}^+\text{Mt}/\text{Tri-Ph}_\text{SS-MD}$  samples was studied through limited oxygen index (LOI), UL94 vertical position, and cone calorimetric tests. According to limited oxygen index results, LOI was slightly increased for HIPS- $\text{Na}^+\text{Mt}/\text{Tri-Ph}_\text{SS-MD}$  sample, from 18.8% (HIPS) to 19.6% with respect to the LOI percent of HIPS- $\text{Na}^+\text{Mt}/\text{Tri-Ph}_\text{TS}$  sample, it was 19.2% which is very close to the HIPS value (18.8%). LOI results indicated that fire behavior HIPS- $\text{Na}^+\text{Mt}/\text{Tri-Ph}$  under controlled atmosphere is slightly improved using single-screw extruder/static mixing die (SS-MD); probably compression and decompression zones (extensional flow) contributed to improve  $\text{Na}^+\text{Mt}/\text{Tri-Ph}$  dispersion and distribution. With respect to UL94-V results, no differences on flammability of the HIPS- $\text{Na}^+\text{Mt}/\text{Tri-Ph}_\text{TS}$  and HIPS- $\text{Na}^+\text{Mt}/\text{Tri-Ph}_\text{SS-MD}$  samples were observed with

respect to HIPS. These results provide evidence that the extrusion process does not substantially influence the flammability properties of the sample HIPS-Na<sup>+</sup>Mt/Tri-Ph. Nevertheless, the fire behavior under forced combustion in cone calorimeter test showed differences depending on the extrusion process. Fig. 10 depicts the heat release rate versus time to ignition curves of HIPS, HIPS-Na<sup>+</sup>Mt/Tri-Ph\_TS, and HIPS-Na<sup>+</sup>Mt/Tri-Ph\_SS-MD samples. The peak heat release rate (pkHRR) is reduced about 13% with respect to that of HIPS when the single-screw process with the static mixing die (SS-MD) is used. On the contrary, when the twin-screw extrusion process (TS) is employed, the increase of pkHRR is about 3%. Good dispersion and distribution of clay mineral (Na<sup>+</sup>Mt) in the polymer matrix was achieved by the use of a static mixer die. When clay mineral is well dispersed and distributed in the polymer matrix, it probably acts as a barrier for the combustion process by forming a protective char layer and reducing the heat release rate. Good dispersion of particles in the polymer matrix is associated with significant changes in the pkHRR values. Actually, poor dispersion of particles at the micrometer level has been reported to be associated with an increase in the value of the pkHRR[17].

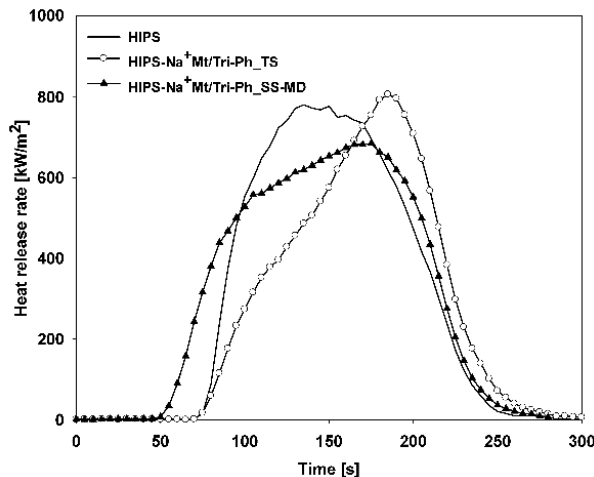


**Figure 10.** Heat release rate with respect to ignition time for the HIPS, HIPS-Na<sup>+</sup>Mt/Tri-Ph\_TS, and HIPS-Na<sup>+</sup>Mt/Tri-Ph\_SS-MD samples.

Finally, the use of a static mixing die placed at the end of a single-screw extruder improves clay minerals distribution and reduces the peak heat release rate according to the cone calorimeter test; the results are even better than those obtained by using a twin-screw extrusion process. An important relation for HIPS blends between clay dispersion and fire-retardant properties was found; i.e., the peak heat release decreases when good clay dispersion is achieved.

### 3.2. Polypropylene

The intumescence systems have been extensively studied as flame-retardant agents on polymers materials. The results have showed very good effectivity [71-72]. However, in order to achieve

these results, it is necessary to use a large amount of these additives (>30%). These high concentrations cause great problems during the processing of these materials and affect negatively their mechanical properties. A suggested technique for obtaining a good dispersion and distribution of the dispersed phase particles in polymer composites is the on-line application of ultrasonic waves during the extrusion process. Important advantages such as the distribution and dispersion of particles of carbon nanotubes and various clay minerals to the nanometric size have been achieved by using this process [73-76]. The processing of flame-retardant intumescence systems together with modified clay mineral was studied in detail. Extrusion processes, such as twin screw (TS) and single screw, adapted with a special static mixer die with ultrasound application (SS-MDU) were considered. It was found that process conditions influence clay mineral dispersion which has a remarkable impact on the flame-retardant and mechanical properties [20]. Sodium bentonite was modified by an ion exchange method, using a mono-chlorhydrated amino acid to obtain organically modified clay (organoclay, referred to as OCLAY). An intumescence system, composed of pentaerythritol, melamine, and ammonium polyphosphate, was used as a flame-retardant compound. Polypropylene, OCLAY, and the intumescence system were processed by both extrusion processes mentioned (TS and SS-MDU). Table 4 discloses the composition of the materials.

Sample identification	Extrusion process	IFR [phr]	OCLAY [phr]
PP-IFR 30	Twin screw	30	0
PP-IFR 21	Twin screw	21	0
PP-IFR 21_C1	Twin screw	21	1
PP-IFR 30-US	Single screw Ultrasound	30	0
PP-IFR 21-US	Single screw Ultrasound	21	0
PP-IFR 21_C1-US	Single screw Ultrasound	21	1

**Table 4.** Materials composition based on PP.

The morphological study by scanning electron microscopy (SEM) revealed that when the materials are processed by SS-MDU extrusion, an important improvement on IFR (Intumescence Flame Retardant) particles dispersion and distribution is achieved. All materials processed by TS extrusion, PP-IFR 30, PP-IFR 21, and PP-IFR 21\_C1, presented IFR agglomerates of about 10–30 µm. This confirms that by using the traditional extrusion process, it is difficult to disperse and distribute IFR particles. On the contrary, all the materials processed by the SS-MDU extrusion (PP-IFR 30-US, PP-IFR 21-US, and PP-IFR 21\_C1-US) presented better dispersion and distribution of IFR particles in comparison with those processed by the TS extrusion, since IFR particles of 1–3 µm were observed in the former systems.

According to flame-retardant properties evaluated by UL94 vertical position standard of the studied materials (Table 5), the addition of OCLAY shows an important effect, depending on

the extrusion process employed. When the materials are compounded with high IFR content (30 phr: parts per hundred parts of resin), V0 classification was achieved regardless of extrusion processes (TS or SS-MDU). However, when IFR content is reduced to 21 phr, no V0 classification was observed. These results confirm that traditional flame-retardant additives must be added at high contents in order to obtain the desired effect. Nevertheless, when 1 phr of OCLAY is added, even at low IFR content (21 phr), V0 classification was obtained by using the SS-MDU process. These results are related to an improved dispersion and distribution of IFR and also to the effect of OCLAY, which was probably exfoliated.

Sample identification	UL94-V rating
PP	Fail
PP-IFR 30	V0
PP-IFR 21	Fail
PP-IFR 21_C1	Fail
PP-IFR 30-US	V0
PP-IFR 21-US	Fail
PP-IFR 21_C1-US	V0

**Table 5.** Flame retardant properties of PP materials.

Table 6 discloses the mechanical properties of the PP materials. The results showed clearly that OCLAY and ultrasound applications have a good impact on the mechanical properties of the PP-IFR materials, since the PP-IFR 21\_C1-US sample showed better Izod impact resistance and strain at break with respect to traditional flame-retardant systems (PP-IFR 30). The Izod impact resistance increased from 73 to 89 J/m, and the strain at break from 17 to 115%, respectively. These results were attributed to an improved dispersion of particles (IFR and OCLAY), as small particles inhibit the fracture propagation by acting as stress concentrators.

Sample identification	Izod impact resistance	Strain at break
	[J/m]	[%]
PP	175	163
PP-IFR 30	73	17
PP-IFR 21	65	98
PP-IFR 21_C1	67	39
PP-IFR 30-US	84	34
PP-IFR 21-US	124	95
PP-IFR 21_C1-US	89	115

**Table 6.** Mechanical properties of PP materials.

To sum up, it has been demonstrated that clay mineral (OCLAY) has a remarkable effect on flame-retardant and mechanical properties in the PP matrix. With the use of clay mineral and a special extrusion process, the content of traditional flame retardant is reduced from 30 to 21 phr to obtain a V0 classification, according to the UL94 vertical position. Moreover, Izod impact resistance and strain at break were improved with respect to systems with high flame-retardant additives content (30 phr).

### 3.3. High-density polyethylene

The use of clay minerals as flame-retardant additives for industrial applications is highly attractive due to the synergistic effect on flame-retardant properties of polymer materials achieved by the combination of clay minerals and traditional flame-retardant additives. This combination allows obtaining the right properties for industrial applications with less flame-retardant additive contents (loads). Also, the cost of the final material may be cheaper than traditional flame-retardant systems [77]. The use of sodium bentonite (chemically modified) at specific content along with high-density polyethylene (HDPE) demonstrated an important reduction in aluminum trihydroxide content (lower about 40%) to reach the optimal V0 UL94 classification. Moreover, mechanical properties were improved with respect to common flame-retardant HDPE composite [21]. HDPE, modified bentonite (OCLAY), aluminum trihydroxide (ATH), and zinc borate (ZnB) were processed in a twin-screw counter-rotating extruder (TS). Alternatively, a single-screw extruder was coupled to a static mixer die, which promotes extensional flow, assisted by piezoelectric elements to generate ultrasonic waves (SS-US). Table 7 discloses the HDPE materials composition.

Sample identification	Extrusion process	ATH [phr]	ZnB [phr]	OCLAY [phr]
PE-50ATH	Twin screw	50	0	0
PE-30ATH-3ZnB	Twin screw	30	3	0
PE-30ATH-3ZnB-C1	Twin screw	30	3	1
PE-30ATH-3ZnB-C2	Twin screw	30	3	2
PE-30ATH-3ZnB/US	Single screw ultrasound	30	3	0
PE-30ATH-3ZnB-C1/US	Single screw ultrasound	30	3	1
PE-30ATH-3ZnB-C2/US	Single screw ultrasound	30	3	2

Table 7. Materials composition based on HDPE.

The morphological study by scanning electron microscopy (SEM) showed that the SS-US extrusion process is a very good method to improve the dispersion and distribution of ATH

particles. Agglomerates of the ATH particles (around 1–3 µm) were observed when the materials were processed by TS. It illustrates the problem to achieve an adequate level of dispersion and distribution of the additives with high ATH concentration. On the contrary, when the materials were processed by SS-US, the ATH particles were reduced in size and no agglomerates were observed. Aluminum elemental analysis was carried out in order to confirm the dispersion and distribution level of ATH.

Table 8 discloses flame-retardant properties evaluated by UL94-V. According to results, the materials obtained with high flame-retardant additive content (50 phr of ATH) render an optimum V0 classification. This result is not surprising considering that, at high concentrations, the flame-retardant additives are very effective. However, when the ATH additive content is reduced (from 50 phr to 30 phr), no V0 rating is reached, even with the additives combination of ZnB (3 phr) and the addition of different OCLAY content (1 and 2 phr). Nevertheless, when the same materials, PE-30ATH-3ZnB/US, PE-30ATH-3ZnB-C1/US, and PE-30ATH-3ZnB-C2/US, are processed under the SS-US extrusion, V2, V2 and V0 ratings, respectively, are obtained. These results demonstrated that a specific content of OCLAY (2 phr) and its good dispersion (probably at the nanometric scale), as well as an efficient dispersion and distribution of the additives (ATH and ZnB) with the help of an on-line ultrasound system (SS-US) rendered an optimized flame-retardant HDPE.

Sample identification	UL94-V rating
HDPE	Fail
PE-50ATH	V0
PE-30ATH-3ZnB	Fail
PE-30ATH-3ZnB-C1	Fail
PE-30ATH-3ZnB-C2	Fail
PE-30ATH-3ZnB/US	V2
PE-30ATH-3ZnB-C1/US	V2
PE-30ATH-3ZnB-C2/US	V0

**Table 8.** Flame retardant properties of HDPE materials.

Mechanical properties of the materials based on HDPE are disclosed in Table 9. One of the main problems in flame-retardant polymers is the negative effect on mechanical properties when a high load of additives is used. This is clearly observed in Table 9, where the material with highest additive content (50 phr) displayed poor mechanical properties: Izod impact resistance and strain at break. However, when the materials are extruded with the SS-US, the mechanical properties are greatly improved, in particular with the addition of OCLAY (samples PE-30ATH-3ZnB-C1/US and PE-30ATH-3ZnB-C2/US).

Sample identification	Izod impact resistance [J/m]	Strain at break [%]
HDPE	153	>500
PE-50ATH	53	43
PE-30ATH-3ZnB	52	200
PE-30ATH-3ZnB-C1	53	83
PE-30ATH-3ZnB-C2	49	52
PE-30ATH-3ZnB/US	63	191
PE-30ATH-3ZnB-C1/US	70	350
PE-30ATH-3ZnB-C2/US	85	210

**Table 9.** Mechanical properties of HDPE materials.

The use of on-line ultrasound application with a special mixer die, effectively reduced the size of ATH particles ( $<1\text{ }\mu\text{m}$ ) and improved the particle dispersion and distribution within the polymer matrix. The improvement of the dispersion of the flame-retardant additives attained by the combination of ultrasound and mixing die had a positive effect in the flame-retardant properties. Most of the obtained materials were classified as UL94-V2, and a V0 rating was achieved with the addition of 2 phr of OCLAY. Mechanical properties (Izod impact resistance and strain at break) were also improved. An optimal flame-retardant HDPE composite was obtained by reducing the ATH content from 50 phr (typical high concentration) to 30 phr (21.5 wt.%).

## Author details

Guadalupe Sanchez-Olivares<sup>1\*</sup>, Fausto Calderas<sup>1</sup>, Luis Medina-Torres<sup>2</sup>, Antonio Sanchez-Solis<sup>3</sup>, Alejandro Rivera-Gonzaga<sup>4</sup> and Octavio Manero<sup>3</sup>

\*Address all correspondence to: gsanchez@ciatec.mx, fcalderas@ciatec.mx

1 CIATEC, A. C., León, Gto., Mexico

2 Facultad de Química, Universidad Nacional Autónoma de México, Ciudad Universitaria, México D.F., Mexico

3 Instituto de Investigaciones en Materiales, Universidad Nacional Autónoma de México, Ciudad Universitaria, México D.F., Mexico

4 Instituto de Ciencias de la Salud, Universidad Autónoma del Estado de Hidalgo, San Agustín Tlaxiaca, Hgo., Mexico

## References

- [1] Murray H. Applied clay mineralogy today and tomorrow. *Clay Minerals*. 1999;34:39–49.
- [2] Bergaya, F., Lagaly, G. Chapter 1: Clays, Clay Minerals, and Clay Science, Developments in Clay Science. In: Bergaya et al., editor. *Handbook of clay science*. Amsterdam, The Netherlands: Elsevier; 2006. pp. 1–18
- [3] Camargo P., Satyanarayana K., Wypych F. Nanocomposites: Synthesis, Structure, Properties and New Application Opportunities. *Materials Research*. 2009;12:1–39.
- [4] Alateyah A., Dhakai H., Zhang Z. Processing, Properties, and Applications of Polymer Nanocomposites Based on Layer Silicates: A Review. *Advances in Polymer Technology*. 2013;32:21368.
- [5] Zare Y. Recent progress on preparation and properties of nanocomposites from recycled polymers: A review. *Waste Management*. 2013;33:598–604.
- [6] Mittal V. Polymer Layered Silicate Nanocomposites: A Review. *Materials*. 2009;2:992–1057.
- [7] Pavlidou S., Papaspyrides C. A review on polymer-layered silicate nanocomposites.. *Progress in Polymer Science*. 2008;33:1119–1198.
- [8] Ray S., Okamoto M. Polymer/layered silicate nanocomposites: a review from preparation to processing. *Progress Polymer Science*. 2003;28:1539–1641.
- [9] Alexandre M., Dubois P. Polymer-layered silicate nanocomposites: preparation, properties and uses of a new class of materials. *Materials Science and Engineering*. 2000;28:1–63.
- [10] Konta J. Clay and man: Clay raw materials in the service of man. *Applied Clay Science*. 1995;10:275–335.
- [11] Rahmat M., Hubert P. Carbon nanotube–polymer interactions in nanocomposites: A review. *Composites Science and Technology*. 2014;72:72–84.
- [12] Hu K., Kulkarni D., Choi I., Tsukruk V. Graphene-polymer nanocomposites for structural and functional applications. *Progress in Polymer Science..* 2014;39:1934–1972.
- [13] Mittal G., Dhand V., Rhee K., Park S., Lee W. A review on carbon nanotubes and graphene as fillers in reinforced polymer nanocomposites. *Journal of Industrial and Engineering Chemistry*. 2015;21:11–25.
- [14] Rivera-Gonzaga A., Sanchez-Solis A., Sanchez-Olivares G., Calderas F., Manero O. Unsaturated polyester-clay slurry nanocomposites. *Journal of Polymer Engineering*. 2012;32:1–5.

- [15] Calderas F., Herrera-Valencia E. E., Sanchez-Solis A., Manero O., Medina-Torres, L., Renteria A., Sanchez-Olivares G. On the yield stress of complex materials. *Korea-Australia Rheology Journal*. 2013;25:233–242.
- [16] Sanchez-Olivares G., Sanchez-Solis A., Calderas F., Medina-Torres L., Manero O., Di Blasio, A. Alongi J. Sodium montmorillonite effect on the morphology, thermal, flame retardant and mechanical properties of semi-finished leather. *Applied Clay Science*. 2014;102:254–260.
- [17] Sanchez-Olivares G. Sanchez-Solis A., Manero O. Effect of montmorillonite clay on the burning rate of high-impact polystyrene. *International Journal of Polymeric Materials and Polymeric Biomaterials*. 2008;57:245–257.
- [18] Calderas F., Sanchez-Olivares G., Herrera-Valencia E. E., Sanchez-Solis A., Manero O. Chapter 6: PET-MMT and PET-PEN-MMT Nanocomposites by Melt Extrusion. In: Boreaddy S. R. Reddy, editor. *Advances in Nanocomposites-Synthesis, Characterization and Industrial Applications*. Rijeka, Croatia: Intech; 2011. pp. 101–120.
- [19] Sanchez-Olivares G., Sanchez-Solis A., Manero O. Study on the combustion behavior of high impact polystyrene nanocomposites produced by different extrusion processes. *eXPRESS Polymer Letters*. 2008;2:569–578.
- [20] Sanchez-Olivares G., Sanchez-Solis A., Calderas F., Medina-Torres L., Herrera-Valencia E.E., Rivera-Gonzaga A., Manero O. Extrusión with ultrasound applied on intumescence flame retardant polypropylene. *Polymer Engineering and Science*. 2013;53[20]:2018–2026.
- [21] Sanchez-Olivares G., Sanchez-Solis A., Calderas F., Medina-Torres L., Herrera-Valencia E. E., Castro-Aranda J. I., Manero O., Di Blasio A., Alongi J. Flame retardant high density polyethylene optimized by on-line ultrasound extrusion. *Polymer Degradation and Stability*. 2013;98:2153–2160.
- [22] Ahmad K., Pan W. Microstructure-toughening relation in alumina based multiwall carbon nanotube ceramic composites. *Journal of the European Ceramic Society*. 2015;35:663–671.
- [23] Mukherjee S., Kundu B., Chanda A., Sen S. Effect of functionalisation of CNT in the preparation of HAp–CNT biocomposites. *Ceramics International*. 2015;41:3766–3774.
- [24] Fan Y., Igarashi G., Jiang W., Wang L., Kawasaki A. Highly strain tolerant and tough ceramic composite by incorporation of graphene. *Carbon*. 2015;90:274–283. DOI: 10.1016/j.carbon.2015.04.029
- [25] Harvey C., Murray H. Industrial clays in the 21st century: A perspective of exploration, technology and utilization. *Applied Clay Science*. 1997;11:285–310.
- [26] Viseras C., Aguzzi C., Lopez-galindo A. Uses of clay minerals in semisolid health care and therapeutic products. *Applied Clay Science*. 2007;36:37–50.

- [27] Aguzzi C., Sanchez-Espejo R., Cerezo P., Machado J., Bonferoni C., Rossi S., Salcedo I., Viseras C. Networking and rheology of concentrated clay suspensions “matured” in mineral medicinal water. *International Journal of Pharmaceutics*. 2013;453:473–479.
- [28] Cruz N., Peng Y., Farrokhpay S., Bradshaw D. Interactions of clay minerals in copper-gold flotation: Part 1 – Rheological properties of clay mineral suspensions in the presence of flotation reagents. *Minerals Engineering*. 2013;50–51:30–37.
- [29] Paineau E., Michot L., Bihannic I., Baravian C. Aqueous Suspensions of Natural Swelling Clay Minerals. 2. Rheological Characterization. *Langmuir*. 2011;27:7806–7819.
- [30] Cheng D.C.H. Yield stress: A time-dependent property and how to measure it. *Rheologica Acta*. 1986;25:542–554.
- [31] Evans I.D. Letter to the editor: On the nature of the yield stress. *Journal of Rheology*. 1992;36:1313–1316.
- [32] Barnes H.A. The yield stress—a review —everything flows?. *Journal of Non-Newtonian Fluid Mechanics*. 1999;81:133–178.
- [33] Bingham E.C. *Fluidity and Plasticity*. New York: McGraw-Hill; 1922.
- [34] Herschel W.H., Bulkley R. Konsistenzmessungen von Gummi-Benzol-Loesungen. *Kolloid Zeitschrift*. 1926;39:291–300.
- [35] Papanastasiou T.C. Flows of materials with yield. *Journal of Rheology*. 1987;31:385–404.
- [36] Housby G.T., Puzrin A. M. Rate-dependent plasticity models derived from potential functions. *Journal of Rheology*. 2002;46:113–126.
- [37] Isayev A., Fan X. Viscoelastic plastic constitutive equation for flow of particle filled polymers. *Journal of Rheology*. 1990;34:35–54.
- [38] SaramitoP. A new constitutive equations for elastoviscoplastic fluid flows. *Journal of Non-Newtonian Fluid Mechanics*. 2007;145:1–14.
- [39] Saramito P. A new elastoviscoplastic model based on the Herschel-Bulkley viscoplastic model. *J. Non-Newtonian Fluid Mech*. 2009;158:154–161.
- [40] Bautista F., De Santos J.M., Puig J.E., Manero O. Understanding thixotropic and anti-thixotropic behavior of viscoelastic micellar solutions and liquid crystalline dispersions. The model. *Journal of Non-Newtonian Fluid Mechanics*. 1999;80:93–113.
- [41] Soltero J., Puig J., Manero O. Rheology of Cetyltrimethylammonium p-Toluenesulfonate-Water System. 3, Nonlinear Viscoelasticity. *Langmuir*. 1999;15:1604–1612.

- [42] Bautista F., Soltero J.F.A., Macias E.R., Puig J.E., Manero O. Thermodynamics approach and modeling of Shear-Banding Flow of Wormlike Micelles. *Journal of Physical Chemistry B.* 2002;106:13018–13026.
- [43] Bautista F., Perez-Lopez J. H., Garcia J. P., Puig J.E., Manero O. Stability analysis of shear banding flow with the BMP model. *Journal of Non-Newtonian Fluid Mechanics.* 2007;144:160–169.
- [44] Herrera EE, Calderas F, Chávez AE, Manero O, Mena B. Effect of random longitudinal vibration pipe on the Poiseuille-flow of a complex liquid. *RheologicaActa.* 2009;48:779–800.
- [45] Herrera EE, Calderas F, Chavez AE, Manero O. Study of the pulsating flow of a worm-like micellar solution. *Journal of Non-Newtonian Fluid Mechanics.* 2010;165:174–183.
- [46] Manero O., Perez-Lopez J. H., Escalante J. I., Puig J.E., Bautista F. A thermodynamic approach to rheology of complex fluids: The generalized BMP model. *Journal of Non-Newtonian Fluid Mechanics.* 2007;146:22–29.
- [47] Escalante J.I., Macias E.R., Bautista F., Pérez-López J.H., Soltero J.F.A., Puig J.E., Manero O. Shear-banded flow and transient Rheology of cationic wormlike Micellar solutions. *Langmuir.* 2003;19:6620–6626.
- [48] Escalante J.I., Escobar D., Macias E.R., Perez-Lopez J.H., Bautista F., Mendizabal E., Puig J.E., Manero O. Effect of a hydrotope on the viscoelastic properties of polymer-like micellar solutions. *Rheologica Acta.* 2007;46:685–691.
- [49] Moreno L., Calderas F., Sanchez-Olivares G., Medina-Torres L., Sanchez-Solis A., Manero O. Effect of cholesterol and triglycerides levels on the rheological behavior of human blood. *Korea-Australia Rheology Journal.* 2015;27:1–10.
- [50] Casson N. A flow equation for pigment oil suspensions of printing type ink. In: Mill C. C, editor. *Rheology of disperse systems.* Oxford, U.K: Pergamon Press; 1959. pp. 84–104.
- [51] Fu X., Qutubuddin S. Synthesis of unsaturated polyester-clay nanocomposites using reactive organoclays. *Polymer Engineering and Science.* 2004;44:345–351.
- [52] Mironi-Harpaz I., Narkis M., Siegmann A. Nanocomposite system based on unsaturated polyester and organoclay. *Polymer Engineering and Science.* 2005;45:174–185.
- [53] Suh D.J., Lim Y.T., Park O.O. The property and formation of unsaturated polyester-layered silicate nanocomposites depending on fabrication methods. *Polymer.* 2000;41:8557–8563.
- [54] Inceoglu A.B., Yilmazer U. Synthesis and mechanical properties of unsaturated polyester based nanocomposites. *Polymer Engineering and Science.* 2003;43:661–669.

- [55] Salahuddin N.A. Layered silicate/epoxy nanocomposites: synthesis, characterization and properties. *Polymers for Advanced Technologies*. 2004;15:251–259.
- [56] Bongiovanni R., Mazza D., Ronchetti S., Turcato E.A. The influence of water on the intercalation of epoxy monomers in Na-montmorillonite. *Journal of Colloid and Interface Science*. 2006;296:515–519.
- [57] Hasegawa N., Okamoto H., Kato M., Usuki A., Sato N. Nylon 6/Na-montmorillonite nanocomposites prepared by compounding Nylon 6 with Na-montmorillonite slurry. *Polymer*. 2003;44:2933–2937.
- [58] Wang K., Wang L., Wu J. S., Chen L., He C. B. Preparation of exfoliated epoxy/clay nanocomposites by “slurry compounding”: process and mechanisms. *Langmuir*. 2005;21:3613–3618.
- [59] Wang K., Wu J. S., Chen L., Toh M.L., He C. B., Yee A.F. Epoxy nanocomposites with highly exfoliated clay: mechanical properties and fracture mechanisms. *Macromolecules*. 2005;38:788–800.
- [60] Chen Y., Fan H., Shi B. Nanotechnologies for leather manufacturing: a review. *Journal of the American Leather Chemists Association*. 2011;106:260–273.
- [61] Budrudeac P., Miu L., Bocu V., Wortman F.J., PopescuC. Thermal degradation of collagen-base materials that are supports of cultural and historical objects. *Journal of Thermal Analysis and Calorimetry*. 2003;72:1057–1064.
- [62] Kaminska A., Sionkowska A. The effect of UV radiation on the thermal parameters of collagen degradation. *Polymer Degradation and Stability*. 1993;51:15–18.
- [63] Gilman J.W. Flammability and thermal stability studies of polymer layered-silicate (clay) nanocomposites. *Applied Clay Science*. 1999;15:31–49.
- [64] Schartel B., Bartholmai M., KnollU. Some comments on the main fire retardancy mechanisms in polymer nanocomposites. *Polymers for Advanced Technologies*. 2006;17:772–777.
- [65] Kiliaris P., Papaspyrides C.D. Polymer/layered silicate (clay) nanocomposites: An overview of flame retardancy. *Progress in Polymer Science*. 2010;35:902–958.
- [66] Gilman J.W. Flame retardant mechanism of polymer-clay nanocomposites. In: Morgan, A. B. and Wilkie, C.A, editors. *Flame retardant polymer nanocomposites*. Hoboken, New Jersey: John Wiley and Sons; 2007. pp. 67–83.
- [67] Alongi J., Carosio F., Malucelli G. Current emerging techniques to impart flame retardancy to fabrics: An overview. *Polymer Degradation and Stability*. 2014;106:138–149.
- [68] Krevelen Van D. W., Nijenhuis te K. *Properties of Polymers*. 4th ed. Amsterdam: Elsevier; 2009. pp. 772–774.

- [69] Utevski L., Scheinker M., Georlette P., Lach S. Flame retardancy in UL-94 V-0 and in UL-94 5VA high impact polystyrene. *Journal of Fire Sciences*. 1997;15:375–389.
- [70] Chin-Ping Y., Biing-Shiou S. Effect of tetrabromobisphenol. A diallyl ether on flame retardancy of high impact strength polystyrene. *Journal of Applied Polymer Science*. 1989;37:3185–3194.
- [71] Camino G., Costa L., Martinasso G. Intumescent fire-retardant systems. *Polymer Degradation and Stability*. 1989;23:359–376.
- [72] Horacek H., Pieh S. The importance of intumescence systems for fire protection of plastic materials. *Polymer International*. 2000;49:1106–1114.
- [73] Peng B., Wu H., Bao W., Guo S., Chen Y., Huang H., Chen H., Lai S. Y., Jow J. Effects of ultrasound on the morphology and properties of propylene-based plastomer/nanosilica composites. *Polymer Journal*. 2011;43:91–96.
- [74] Isayev A. I., Kumar R., Lewins T. M. Ultrasound assisted twin screw extrusion of polymer-nanocomposites containing carbon nanotubes. *Polymer*. 2009;50:250–260.
- [75] Li J., Zhao L. J., Guo S. Y. Ultrasound assisted development of structure and properties of polyamide 6/montmorillonite nanocomposites. *Journal of Macromolecular Science, Part B: Physics*. 2007;46:423–439.
- [76] Lapshin S., Swain S. K., Isayev A. I. Ultrasound aided extrusion process for preparation of polyolefin-clay nanocomposites. *Polymer Engineering and Science*. 2008;48:1584–1591.
- [77] Beyer G. Flame retardant properties of organoclays and carbon nanotubes and their combination with alumina trihydrate. In: Morgan A. B., Wilkie C.A, editors. *Flame retardant polymer nanocomposites*. Hoboken, New Jersey: John Wiley and Sons, Inc; 2007. pp. 164–177.

---

# **Charging Behavior of Clays and Clay Minerals in Aqueous Electrolyte Solutions — Experimental Methods for Measuring the Charge and Interpreting the Results**

---

Tajana Preocanin, Ahmed Abdelmonem, Gilles Montavon and Johannes Luetzenkirchen

Additional information is available at the end of the chapter

<http://dx.doi.org/10.5772/62082>

---

## **Abstract**

We discuss the charging behavior of clays and clay minerals in aqueous electrolyte solutions. Clay platelets exhibit different charging mechanisms on the various surfaces they expose to the solution. Thus, the basal planes have a permanent charge that is typically considered to be independent of pH, whereas the edge surfaces exhibit the amphoteric behavior and pH-dependent charge that is typical of oxide minerals. Background electrolyte concentration and composition may affect these two different mechanisms of charging in different ways. To guide and to make use of these unique properties in technical application, it is necessary to understand the effects of the various master variables (i.e. pH and background salt composition and concentration). However, how to disentangle the various contributions to the charge that is macroscopically measurable via conventional approaches (i.e. electrokinetics, potentiometric titrations, etc.) remains a challenge. The problem is depicted by discussing in detail the literature data on kaolinite obtained with crystal face specificity. Some results from similar experiments on related substrates are also discussed. As an illustration of the complexity, we have carried out extensive potentiometric mass and electrolyte titrations on artificial clay samples (Na-, Ca-, and Mg-montmorillonite). A wide variety of salts was used, and it was found that the different electrolytes had different effects on the end point of mass titrations. In the case of a purified sample (i.e. no acid-base impurities), the end point of a mass titration (the plateau of pH achieved for the highest concentrations of solid), in principle, corresponds to the point of zero net proton and hydroxide consumption, at which in ideal systems, such as oxide minerals, the net proton surface charge density is zero. To such concentrated (dense) suspensions of clay particles, aliquots of salts can be added and the resulting pH indicates the specificity of a given salt for a given clay particle system. In the experimental data, some ambiguity remains, which calls for further detailed and comprehensive studies involving the application of all the available techniques to one system. Although, right now, the overall picture appears to be clear from a generic point of view (i.e. concerning the trends), clearly, in a quantitative sense, huge differences occur for nominally

identical systems and only such a comprehensive study will allow to proof the current phenomenological picture and allow the next step to be taken to understand the fine details of the complex clay-electrolyte solution interfaces.

**Keywords:** Mass titration, clay mineral, montmorillonite, smectite, adsorption, acid-base properties, surface charge

---

## 1. Introduction

The charging of clays and clay minerals (hereafter referred to as clays for simplicity) is of importance in various areas. One important property related to the charging is the so-called point of zero charge. We will not repeat the various definitions of points of zero charge in detail here, but rather refer to the literature (1-3). Only the points of zero charge used in the present chapter will be explicitly defined. The books summarizing published points of zero charge of minerals include thousands of experimental studies [4, 5]. Points of zero charge can be considered sample and system intrinsic properties. In the typical compilations, the given values will indicate under which conditions (usually in terms of pH) a particle is net uncharged subject to the definition of the respective point of zero charge cited. Or, to put it otherwise, the points of zero charge indicate for which conditions a mineral surface will bear a negative or positive charge. The charge is affecting the aggregation of the particles but also the uptake of contaminants on the clays from electrolyte solutions. Most of the data that are available have been collected under ambient conditions (room temperature and ambient pressure, though sometimes carbon dioxide is excluded). This is also true for the data discussed in the following.

Well-behaved particles of oxide minerals are rather well understood with respect to their charging properties [6-8]. This is partially due to the uniform charging properties of the different crystal planes of a given particle, the domination of one specific crystal plane or that of a specific surface functional group. Clay platelets expose various crystal faces with very different properties to the surrounding solutions, which result in significant anisotropy. This is shown in a very schematic way in Figure 1.

The basal plane is often considered as a permanently charged face, which is at the origin of the overall negative charge measured for many clay platelets over the usual pH range (between pH 2 and 12). The edge faces show pH-dependent behavior as shown in Figure 1, and this results in the anisotropy of the particles with respect to charging behavior and charge. Therefore, compared to the oxide minerals, a number of complications exist, which will be discussed in more detail in the following.

For the basal planes, the following can be generally stated:

- Basal planes exhibit permanent, negative charge that, in the common picture, arises from the isomorphic substitution within the particles and is typically not expected to depend on the proton concentration. At extreme pH values, some dependence on pH will occur if one believes in current models [9], but experimental data that will be discussed later also suggest effects in the usually studied pH range.

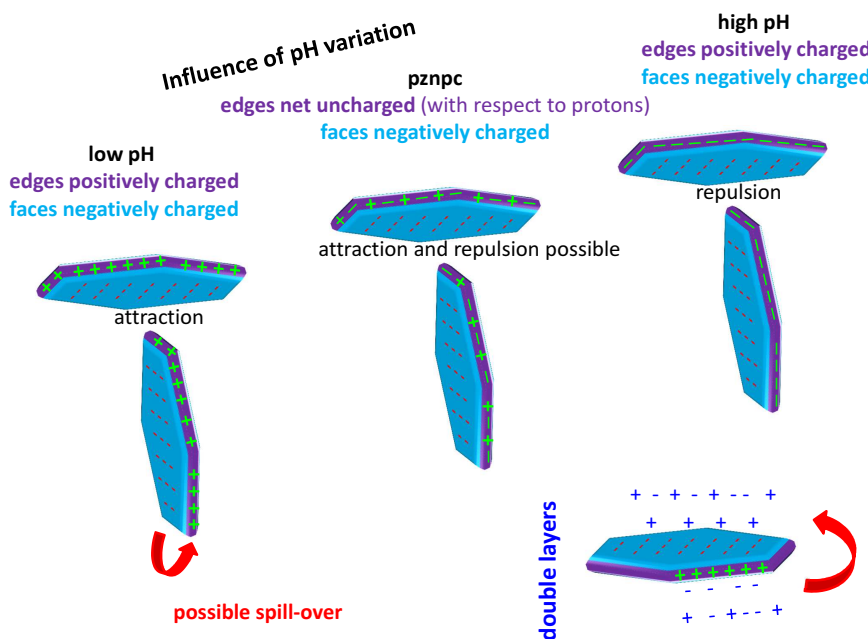


**Figure 1.** Schematic view of clay platelets and their anisotropic charging behavior. The faces (basal planes) exhibit permanent negative charge, whereas edge faces show amphoteric, pH-dependent behavior similar to oxide minerals. The anisotropy causes, depending on the pH and the concomitant charge of the edge faces, possible attraction (at low and intermediate pH values) or net repulsion (at high pH values). The respective charging conditions may cause aggregation (in some kind of card-house structure) and will involve spillover situations, which, in turn, affect the electrical double layers.

- There might be different basal planes (such as on kaolinite, with a gibbsite plane and a silica plane) with different charging properties.
- The permanently charged basal surfaces are affected by salt concentration.

For the edge surfaces, the generally accepted viewpoint is similar to that for oxide minerals and can be summarized as follows:

- The amphoteric clay edge surfaces expose hydroxyl groups to the solution, which may take up or release protons depending on the nature of these groups and on the proton concentration in solution. There is a specific pH at which the net charge on such surfaces is zero, which can be called the “point of zero net proton charge” [2] ( $\text{pH}_{\text{pznpc}}$ ) and has also been termed “point of zero net proton consumption” [10].<sup>1</sup>

<sup>1</sup> As indicated above, there is a somewhat confusing nomenclature within the literature, which requires to assign a clear definition to whatever point of zero charge is discussed; here, the definition would be that, on the specific surface that is being discussed, the net charge arising from proton adsorption and desorption in the plane of the surface hydroxyls is zero. Furthermore, it is inherently assumed that the adsorption/desorption of protons and hydroxide ions in other parts of the interface can be neglected.

- Again, the situation may be complicated by the occurrences of various clay edge surfaces with different properties on a given particles (i.e. different values of  $\text{pH}_{\text{pznc}}$  may appear on the edges of one clay particle).

Another yet distinct mechanism occurring on these particles is (cat)ion exchange.

- Whereas some clays (such as kaolinite) do not exhibit strong interlayer cation exchange, others (such as montmorillonite or illite) possess relatively high cation exchange capacities.
- Exposing the latter to strongly concentrated electrolyte solutions will cause an exchange of the interlayer ions (i.e. exposure of a sodium clay to a sufficiently concentrated calcium solution will transform the clay to the calcium form at equilibrium) and was shown to have repercussions on modeling metal ion adsorption [11].<sup>2</sup>
- At very low pH, the solid can be transformed to its H-form, which will involve a substantial buffering capacity.

The impact of the master variables pH and ionic strength on these particles becomes highly complex. The formation of the so-called electrical interfacial layer (EIL) of charged particles in aqueous solutions is one central aspect [12]. The more distinct properties a certain clay possesses, the more complex the overall behavior will be. We briefly discuss the effect of electrolyte concentration and composition before discussing the role of pH.

- The formation of the EIL on a single crystal plane is defined by the overall surface charge density (immobile, Stern layer) and the diffuse layer properties (electrolyte composition and concentration). The former arises from the specific adsorption of potential/charge-determining ions and/or the permanent charge due to isomorphic substitution. Electrolyte ions may have twofold effects. First, they may form ion pairs with the charged surface and thus screen the charge within the immobile layer. The higher the affinity of a given ion to a specific surface is, the more effective the screening will be. Sufficiently high affinity may lead to overcharging (i.e. charge inversion). Second, electrolyte ions will neutralize the net charge of the immobile layer in the diffuse part of the EIL. The higher the charge of an ion is, the more effective the screening will be. Increasing the electrolyte concentration will enhance screening.
- The ion-exchange properties are obviously also dependent on the salt concentration. Thus, studying the behavior of a Na-clay in high concentrations of calcium or some other cation different from sodium will transform the clay either partially or completely into another form, similar to what happens at low pH as discussed above.
- Protons are potential/charge-determining ions on the clay edge surfaces, where they adsorb or desorb from surface hydroxyl groups. They may also play a role in ion-exchange reactions if the pH is sufficiently low (i.e. the proton concentration is sufficiently high). Basal planes are, in many cases, not prone to reactions with protons in a wide range of pH. Model

---

<sup>2</sup> In this example with high relevance, the form of the given clay resulted in different properties with respect to contaminant adsorption, an issue that is presently not solved within an otherwise consistent model. As an unsatisfactory way out, the stability constants for Eu adsorption are different on Na- and Ca-montmorillonite for identical reactions, which causes problems for mixed Na/Ca systems.

calculations suggest such behavior from pH 3 to 10 for the gibbsite basal plane, which occurs as aluminol terminated face on kaolinite and therefore is quite relevant [13]. Unfortunately, experimental data for and consequently the interpretation of this seemingly simple surface are still quite diverging for unknown reasons [13-17]. However, there are some observations in the literature that would suggest additional effects of protons (or hydroxide ions) on such basal planes [18].

Various macroscopic measurements on the effects of electrolytes and protons on clay surface charging exist. The major techniques are titrations, electrokinetic experiments, measurements of the cation exchange capacities, or adsorption studies. These measurements test different chemical reactions. Among the titrations, various techniques can be used. For a detailed recent overview, we refer to the literature [19]. Electrokinetic techniques have also been reviewed frequently [20]. We will not discuss the two other techniques mentioned above, because they are only indirectly related to the charging.

- Classical potentiometric acid-base titrations both in terms of evaluation of the raw data and thermodynamic modeling involve proton balances. For an accurate treatment of the raw data, all the reactions occurring in a given system need to be known and their respective extents need to be quantified. Quite importantly for the interpretation of the measurements, secondary effects on pH may occur that also will affect the overall proton balance. This includes the dissolution of the particles and subsequent reactions of the freshly dissolved species in solution. As is the case when changing the electrolyte concentration, a multitude of reactions involving solutes may occur when changing the pH. Re-precipitation may occur (of primary or secondary phases). Dissolved species may adsorb, as has been discussed for aluminum ions on gibbsite-basal-plane-like surfaces [17]. Also, it becomes difficult, if not impossible, to disentangle the concomitant origins of a macroscopic scale observation, as all these processes have their own, sometimes unknown, pH dependencies.
- Mass and electrolyte titrations [21-23] are far less frequently applied, and we will therefore devote a part of this chapter to these kinds of experiments. They involve relatively high mass concentrations, which will suppress the relative importance of the secondary reactions (such as dissolution, precipitation, or (re)adsorption of previously dissolving clay components) in the overall proton balance. As a example, the dissolution of a given particle into a thick suspension will not cause the same effects as in a dilute suspension. In the latter, much more has to be dissolved (in absolute terms) to achieve a solubility equilibrium compared to the thick suspension.
- Electrokinetic measurements (such as electrokinetic mobility) test the movement of a particle in an applied electric field. The resulting mobility is caused by the behavior of the overall particle. This may be very complex. The available set-ups will produce a value for the electrophoretic mobility. The value typically used, however, is the so-called zeta-potential. The transition from the former to the latter is not simple for non-spherical particles. It may be even more complex for anisotropic particles such as clays.

The anisotropy has been alluded to above and is caused by the crystal face-specific properties of the overall particles. Only recently, more face-specific work has become available (see

Chapter 2) on anisotropic particles. Crystal face-specific effects have been acknowledged for a long time. Early examples of general importance [24] or specific work on oxides [25] can be consulted. The differences in charging on the different crystal planes may have significant consequences on the overall charging.

- Depending on the size of the surfaces with different properties that contribute to the overall exposed surface area, macroscopic observations can be described using various assumptions [26]. The approaches discussed in that reference and also in the literature cited therein consider a common diffuse part of the double layer.
- It is well conceivable that, with sufficiently large patches, distinct diffuse layers may evolve, resulting in repercussions on inner-layer equilibria and local effects. The consequences of these effects are not well established, although spillover effects have been discussed with respect to clays [27, 28]. Only more recently, an approach based on MD simulations and thermodynamic modeling has addressed montmorillonite [29, 30]. Interesting and challenging questions can be asked about the relevance of these double layers at the locations, where the transition from plate to edge occurs in such cases (i.e. whether and how the changes will affect the equilibria of adsorption and dissolution).
- Another issue would be how different surface potentials on one particles are related via the bulk of the solid [31] and how this may affect reactivity [32]. Probably, this is not a major issue for clays and more relevant to solids with sufficient electrical conductivity.
- Moreover, the effects of interfacial water molecules and water ions ( $H^+$  and  $OH^-$ ), especially on the basal plane, should be taken into account [33]. It is known that the physical and chemical properties of water change close to such interfaces, and for example, the ionization of water molecules becomes more pronounced [34].

The association of the various measurements with a specific property in the EIL is one of the challenges (i.e. what quantity is actually measured, what property is tested, and which interdependencies exist between the properties and quantities). Things are further complicated by the fact that the overall properties are finally relevant to processes such as aggregation (i.e. does aggregation of particles occur), the morphology of the aggregates formed (i.e. how do the particles interact with each other), the interaction of the particles with other surfaces (i.e. by which particle face is a clay particle attached to any kind of surface), or the interaction of solutes with a particle (i.e. on which particle face is a contaminant ion bound), to only name a few. Just to give an illustration of the potential difficulties, we can cite a study that has shown that heterogeneously charged particles may move in an applied electric field, although their net surface charge (relevant for electrokinetics) is zero [35]. Because such work is predominantly of theoretical nature, recent activities have turned towards experimental approaches. Surface plane-specific investigations are possible by the study of single crystals [exposing only one specific crystal plane, usually sufficiently large samples need to be available as was the case for gibbsite [14] or is the case for many single crystal samples of oxides including sapphire, hematite [36, 37], mica [38, 39], and others] or by exposing distinct crystal planes from small particles in an intelligent way to force probes [as recently published for gibbsite [40] and

extensively done with kaolinite [41-44]]; the major problem remains the edge part of the clays due to their small dimensions).

Overall, it appears that experimental techniques for studying the interfacial properties of clay particles have made a significant leap forward beyond the macroscopic approaches. The more sophisticated approaches that are plane specific require detailed technical knowledge and instrumentation, whereas the macroscopic approaches are more standard although not necessarily simple. Unfortunately, at present, a combined study involving the available experimental and theoretical approaches on the different scales on a defined sample has not been performed in a comprehensive way.

Here, we will describe in detail the case of kaolinite where the use of crystal face specificity has been driven quite far [42-44] and add some information on other minerals where the approaches have been applied as well before describing non-conventional but very simple titration methods in more detail. In the part dealing with macroscopic methods, a synthetic clay has been used to assure a well-controlled starting material, free of impurities that are associated with natural samples and that, in turn, require specific preparation protocols.

Although the advances in the experimental techniques allow the specific study of defined crystal planes with more (basal plane surfaces) or less (edge surfaces) confidence, the problem remains, for example, how to assemble the detailed information for the defined crystal planes in reconstructing the overall behavior such as the titration curve or the zeta-potentials. Early attempts on obtaining zeta-potentials for kaolinite in such a way exist [45, 46]. On the other extreme, the advent of modern theoretical approaches has allowed to calculate protonation constants for surface functional groups on ideal surfaces, some studies notably including phyllosilicates [47]. Such information is quite compatible with results from advanced surface complexation models [6] and can, in principle, be used to construct a model to predict the overall clay behavior involving the problems of how to couple the different planes. Using the crystal face-specific information obtained, protonation constants can be more directly tested in a first step. This is the goal of the following sections, where we also point to experimental problems. First, we will discuss in some detail the available experimental face-specific data on kaolinite and relate them to the theoretical results, complemented by similar data on talc. Second, we will discuss the basal plane of mica in some detail. The final chapter describes some experimental data from mass and electrolyte titrations showing the complexity that will have to be considered in constructing comprehensive models for clay particles that take into account the microscopic reactions and their associated stability constants and the various phenomena involved plus the “interactions” between the different facets.

## 2. Kaolinite as an example

### 2.1. Effect of pH

As indicated in the introduction, the most well-studied system from the point of view of interfacial charge is probably the kaolinite sample investigated by Miller and co-workers

[41-44, 48]. Here, we briefly review the outcome of that comprehensive study. The challenging steps in this study included the preparation of kaolinite particles, such that they would expose the silica or gibbsite basal faces to the atomic force microscopy (AFM) probe and design an experiment by which to measure the behavior of the edges. The dimension of the edge planes (below 50 nm) is a major obstacle. Compared to the edge surfaces, the basal surfaces have much larger extensions. Also, the basal planes can probably be considered smoother than the edge surfaces.

### 2.1.1. Basal plane surfaces

In the above-cited studies, the basal surfaces were attached to a larger single crystal surface (serving as a supporting material). One single crystal was a fused alumina surface that was expected to have a high isoelectric point and to exhibit positive charge over a wide pH range. Moreover, it was anticipated that the silica plane of kaolinite would exhibit a negative charge. Thus, having a kaolinite particle interact with a positively charged single crystal, it would attach via the silica basal plane to the single crystal. Consequently, it would expose its gibbsite plane to the AFM probe, allowing to measure the distinct properties of the kaolinite-gibbsite plane. Applying the same approach but using a glass substrate as a support with a low IEP<sup>3</sup> (below pH 3), which makes it negative over a wide pH range, would allow to fix the gibbsite plane of the kaolinite particles to the supporting surface and thus expose the silica plane to the solution. The AFM probe was a conventional silicon nitride tip with widely known properties. Measurements were made in a fluid cell.

The outcome of the measurements with the distinct planes was that the gibbsite plane had an IEP from force measurements that corresponded to pH 6, whereas that of the silica plane was below pH 4.

These measurements can be compared to independent measurements or predictions. Gibbsite has been separately investigated in various studies. In particular, a similar AFM study on the basal plane of gibbsite particles was carried out. The various surfaces on kaolinite and their relations to gibbsite and silica as well as the situations for the force measurements (which typically involve a silica probe) are shown in Figure 2a. The results of the separate force studies are shown on Figure 2b.

Clearly, all data sets show positive potentials at pH < 6. This disagrees with predictions for the protonation constants of the doubly coordinated hydroxyl groups that occur on this surface both by MUSIC [16] and by advanced theoretical calculations [51]. However, it should be noted that the potentials are quite low, in particular for the gibbsite study, which would imply low surface charge. Likewise interesting is that (i) the positive potential differs significantly from each other (those obtained on kaolinite are much larger in one case) and (ii) there is a charge reversal on kaolinite, whereas, on the gibbsite basal plane, there is none in the pH range investigated. The kaolinite data differ among themselves as well, although the same material

---

<sup>3</sup> The IEP in our notation corresponds to the pH at which the zeta-potential or the DLVO potential is zero. DLVO potentials are interfacial potentials at the head end of the diffuse layer.

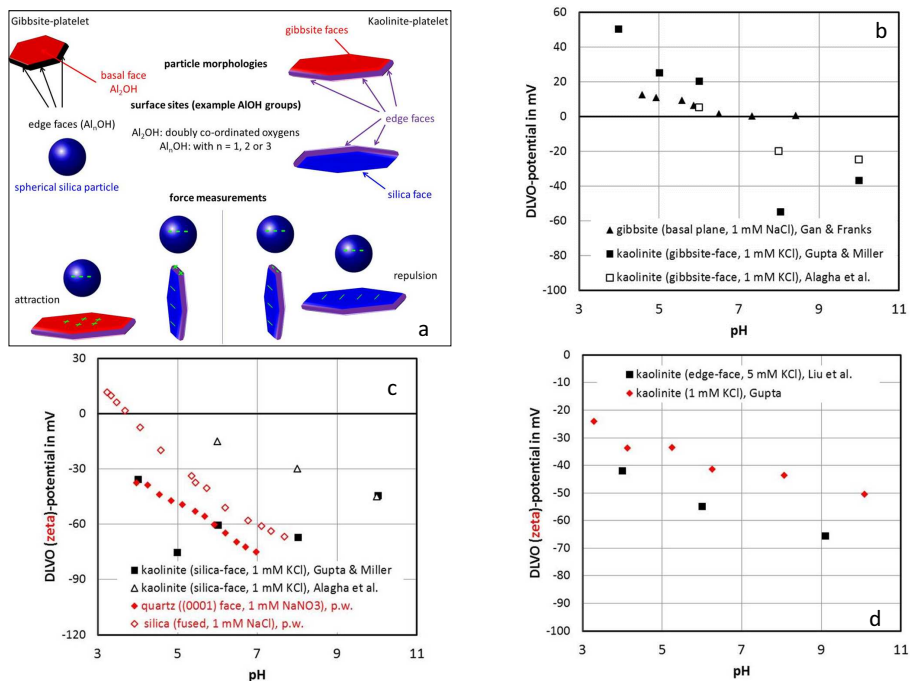


**Figure 2.** (a) Faces on kaolinite and their relations to oxide minerals and typical situations for force curves. (b) DLVO potential measured by AFM force distance curves on the gibbsite plane of kaolinite [42, 49] and on the basal plane of gibbsite [14]. (c) DLVO potentials (full black squares and open triangles) measured by AFM force distance curves on the silica plane of kaolinite [42, 49] and zeta-potentials (diamonds, red symbols) on the (0001) plane of quartz and fused silica (present work). (d) DLVO potential (black squares) of kaolinite edge surfaces in 5 mM KCl [44] and zeta-potentials (red diamonds) of the same kaolinite particles in 1 mM KCl [50].

was used. Note that electrolyte concentrations are equal in both cases, in KCl (kaolinite) and NaCl (gibbsite).

The disagreement on both experimental data and interpretation of the gibbsite basal plane has been ongoing for some time. The origin of the discrepancies in the experimental data has been discussed in some detail, but the issue is still not solved [13, 52, 53]. Adsorption on the gibbsite plane of either dissolved aluminum [17, 52, 54, 55] or background electrolyte [40] ions has been put forward or inferred from experimental data. Interpretation obviously is linked to the experimental data basis, and likewise, no agreement has been achieved.

The silica basal plane of kaolinite shows the expected results if one assumes that silica is usually negatively charged above pH 2. This is exemplified on Figure 2c by data series for the 0001 plane of quartz obtained by streaming potential measurements in 1 mM  $\text{NaNO}_3$ . Streaming potential measurements with a fused silica sample in 1 mM NaCl yield absolute zeta-potential values that are slightly lower than those of the quartz sample. Clearly, the data are in agreement in that they remain negative for nearly all measurements carried out. At the lower pH range, they

match very well. Independent data by Alagha et al. [49] on the same system are different and only coincide at pH 10.

### 2.1.2. Edge plane studies

For the determination of the IEP of the edge surfaces, samples of well-ordered kaolinite edge surfaces were prepared as an epoxy resin sandwich structure having layered kaolinite particles in the center of the epoxy resin sandwich [44]. The resulting samples always showed negative diffuse layer potentials (less than -40 mV in 5 mM NaCl solutions as shown in Figure 2d), which is rather surprising given that the points of zero net proton charge<sup>4</sup> based on potentiometric titrations as recently summarized by Liu et al. [56] were assumed to be between pH 5 and 6. Additional zeta-potential data from Gupta [50] do support an overall low IEP for the very same particles.

The important point to realize here is that potentiometric titrations at best yield relative surface charges, but these also include potential contributions from both basal planes, and a precise procedure of calculating the overall charge is not known. To put the data on an absolute scale, various approaches can be taken. On oxide minerals, a common intersection point of such relative charging curves occurs and typically coincides with an independent determination of the IEP and then the pristine point of zero charge emerges. Furthermore, referring again to Figure 3, the zeta-potentials in lower salt content measured for the metal oxide particles exhibit lower absolute values than the DLVO potentials of the edges in the more concentrated salt solution. Even if one might still argue that the DLVO potentials can be higher than the zeta-potentials [57], the observation could suggest that the pH dependence and absolute values for the kaolinite particles here originate from the edges only.

Including Figures 2b and 2c, this would mean that the basal planes should neutralize each other from a simple point of view, although they could still cause a finite zeta-potential [58]. This, in turn, would contradict the point of zero salt effect<sup>5</sup> of kaolinite determined by Gupta [50] in KCl, which is at pH 4.5. The assignment of a clear point of zero net proton charge based on the data shown in Figure 3 is not as simple with clays, as it usually is the case with oxides. First, the apparent zero level shifts with both the electrolyte concentration and the amount of kaolinite titrated. Second, a common intersection may occur at pH 7. If only the edge surfaces were responsible for the pH-dependent charging, the point of zero net proton charge would be clearly below pH 4, whereas the salt titration and the relative zero level would suggest it to be at pH 4.5.

For clays as discussed in detail above, there are several contributions to the overall charge and a common intersection point does not give the point of zero net proton charge. The charging curves are affected by the net charge that influences given surface functional groups. The distinct behavior of the different planes in terms of diffuse layer potentials is shown in

<sup>4</sup> For the five samples with generic sites, we calculate a mean of 5.7 with a standard deviation of 0.7 (the maximum being 6.8 and minimum being 5.0).

<sup>5</sup> The point of zero salt effect is the pH at which the addition of salt does not cause a change in surface charge density. This is likely to happen at zero surface charge for well-behaved particles.

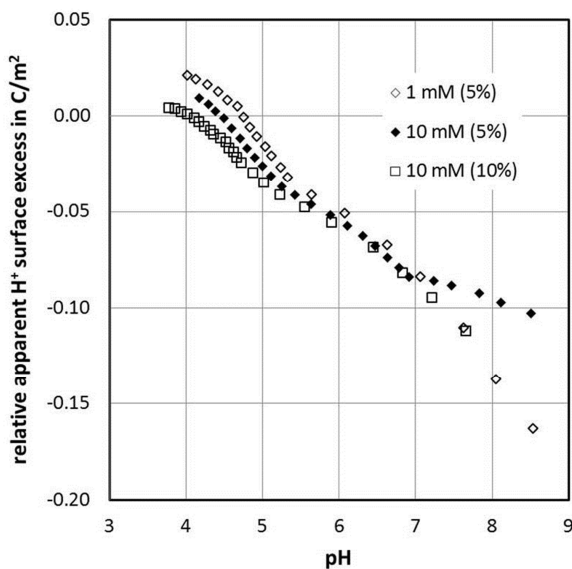


Figure 3. Titration of the kaolinite sample used for the AFM force distance measurements shown in Figures 1 and 2 [50]. The percentage refers to the weight of kaolinite in the titrated suspension. Salt was KCl.

Figure 4. Surprisingly, the silica basal plane and the edge plane are very similar, in particular with respect to the zero-potential condition. This could mean that the silica groups at the edge surface are dominating. The traditional view is that both alumina and silica groups are present and that the point of zero net proton charge of edges should be higher than reported here.

In summary, it is clear that both the gibbsite and the silica basal plane exhibit pH-dependent behavior, suggesting proton uptake and/or release from the surface functional groups on the two planes. This is surprising because the expected surface functional groups are usually expected to be inert towards the reactions of protons within the normal pH range. The lack of agreement on this issue for the gibbsite basal plane has been mentioned above. Based on the available data, the overall charging behavior is difficult to estimate because investigations on the basal planes were done in 1 mM NaCl media. The obtained diffuse layer potentials would be larger in value than in 5 mM NaCl, which was the medium in the experiments dealing with the edge faces. An overall estimate would be possible using the estimated diffuse layer charge densities and the respective areas to calculate an overall diffuse layer charge density on the particle. From this, one may estimate a new diffuse layer potential for comparison with the independent measure of zeta-potential for the particles, where the measurement device yields data that are in an unknown fashion obtained from the anisotropic particles. We also would like to mention here that similar studies are available in terms of pH dependencies on other clay materials [59, 60]. Without going into further details of this pH-dependent study, we turn the attention to the effect of electrolyte concentration at constant pH.

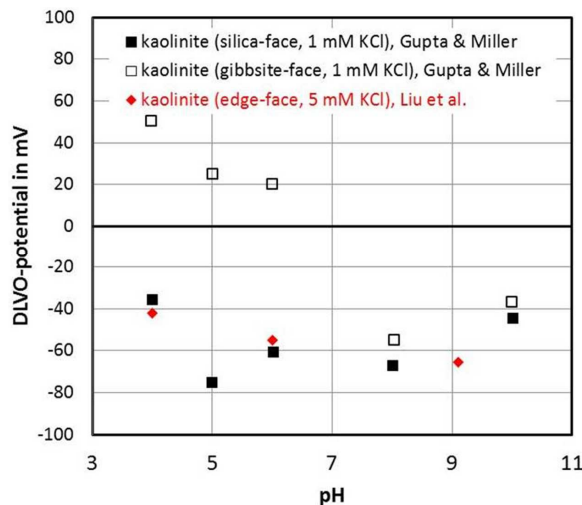
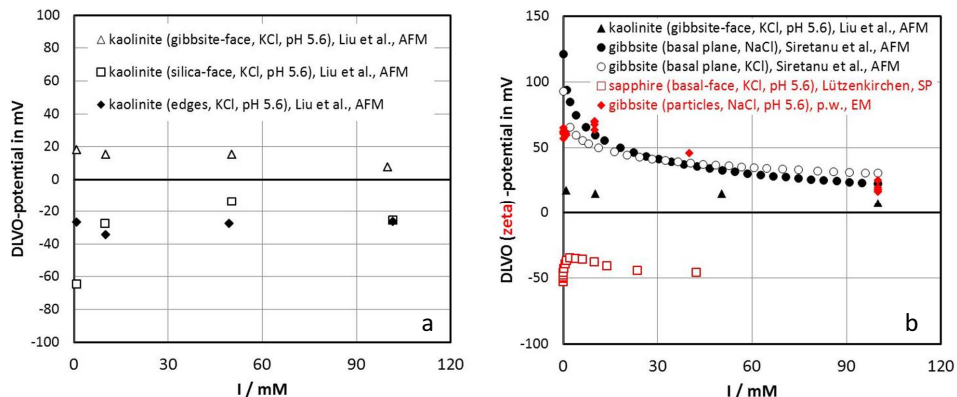


Figure 4. Comparison of the potentials on the different faces of kaolinite as a function of pH [42, 44].

## 2.2. Effect of ionic strength

A similar series of experiments as the one described above for the effect of pH has been carried out at a given pH for a variation of the electrolyte concentration. As a first step, a proof of principle has shown the consistency between diffuse layer and zeta-potentials among probe and a supporting surface [44]. The zeta-potentials were found to be smaller in magnitude than the diffuse layer potentials, suggesting that the zeta-potentials pertain to a location slightly shifted towards the solution side of the particle in agreement with independent work [16, 57]. The AFM force distance curve-based diffuse layer potential is at the head end of the diffuse layer and is attenuated towards the solution due to screening by the background electrolyte. For silica particles, the data follow the same trend but are just shifted, the shift decreasing with increasing ionic strength. For the kaolinite study at pH 5.6 [44], the results are shown in Figure 5a.

The data can be summarized as follows. The diffuse layer potential on the gibbsite plane is positive, remains roughly constant, and only decreases at the highest salt concentration. On the silica plane, the negative potential becomes less negative with increasing salt content and then remains approximately constant. The value for the edges is roughly constant and negative. The potentials on the gibbsite and the silica and edge planes are 20 and -30 mV, respectively, with little salt dependence in the range of ionic strength that was studied (except for the silica plane at very low salt content). As pointed out before, the overall zeta-potential estimation requires a recalculation of the diffuse layer charge densities from the measured potentials and area-weighted summation of the contribution. With the assumption that the gibbsite and silica planes have roughly the same area and within the experimental errors given, the charge from those two planes cancel each other at approximately 10 mM. Then, the edges would be solely contributing to the overall charge, resulting in a charge density (referred to as



In the following, we will use in the figure legends the abbreviations AFM (atomic force microscopy), SP (streaming potential), EM (electrophoretic mobility), SFA (surface force apparatus), PIT (plane interface technique), and p.w. (previously unpublished data from the present authors).

**Figure 5.** (a) Salt dependence of DLVO potentials of the different kaolinite faces. Data from Liu et al. [61] were all determined by AFM force distance measurements. (b) Interfacial potential for gibbsite basal plane-related surfaces at pH 5.6 as a function of salt concentration (given as ionic strength). Data are for the gibbsite face of kaolinite from Liu et al. [61], for the gibbsite basal plane from Siretanu et al. [40], and for the sapphire basal face from Lützenkirchen [62].

the edge area) of approximately  $-10 \text{ mC/m}^2$ . Scaled to as the overall surface, this would be much lower resulting in an overall diffuse layer potential below  $-20 \text{ mV}$  in  $10 \text{ mM}$  salt. The zeta-potential measurement under these conditions is not available for the very same sample. For  $1 \text{ mM}$  background electrolyte concentration, a value between  $-30$  and  $-40 \text{ mV}$  can be inferred from the thesis of Gupta [50]. Therefore, the range appears reasonable, although a self-consistent comparison again is not possible for lack of data. At  $50 \text{ mV}$ , the situation for the gibbsite and silica basal planes is similar [44] and the resulting reported charge density (scaled to as the edge area) yields a value of  $-15 \text{ mC/m}^2$ . Nothing can be further inferred from this result though. Finally, it has also to be acknowledged that the recalculation of diffuse layer potentials from overall charges involves geometry. The same is true for the calculation of zeta-potentials from electrophoretic mobility. Consequently, much can be done to improve the present attempts to gain insight in the effect of crystal plane-specific charging on overall charge. Interestingly, the silica and the edge planes are very similar again.

The salt dependencies of the two basal planes are compared to related surfaces in Figure 5b (gibbsite face) and Figure 7 (silica face). We first discuss the gibbsite face and some additional data on pure gibbsite particles.

Figure 5b shows that there is quite close agreement between gibbsite samples for pH approximately 5.6. True gibbsite particles that are dominated by the basal plane exhibit high zeta-potentials and a characteristic maximum at millimolar concentration. This is reminiscent of published AFM charge data on the basal plane of gibbsite [40]<sup>6</sup> and is also retrieved on sapphire single crystals [62], though displaced to negative values. It has been pointed out previously that the gibbsite basal plane appears to be rather complex when exposed to aqueous solutions.

As a further example of the complexity, we present data that show the evolution of the conductance of the gibbsite particles corresponding to the data in Figure 6a in MilliQ water with time (Figure 6b) as well as the concomitant sample zeta-potential (Figure 6c). The conductance increases with time. This could be caused by two effects. One would be a leakage of KCl from the glass electrode. Alternatively, Al could dissolve from the gibbsite and (partially) re-adsorb as has been speculated previously [17, 52, 54]. Figure 6c shows that the zeta-potential remains high and does not show the decrease that is found when adding NaCl (Figure 5).

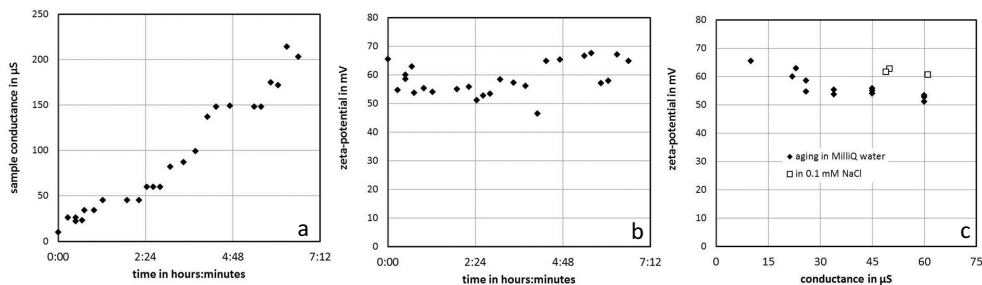


**Figure 6.** (a) Conductance of a gibbsite suspension in MilliQ water at pH 5.6 as a function of time. (b) Zeta-potential of a gibbsite suspension in MilliQ water at pH 5.6. (c) Zeta-potential of a gibbsite sample in MilliQ water when aged as a function of the conductance in comparison to a sample in 0.1 mM NaCl yielding a conductance in the relevant range.

Figure 6c shows a comparison between data at the lower end of conductance and compares the trend to a suspension freshly prepared in 0.1 mM NaCl, which gives rise to a similar conductance. Clearly, the zeta-potential is higher in the case of NaCl addition, supporting the idea that the increase in conductivity arises from dissolution of gibbsite. The overall trend in zeta-potential of the particles shown in Figure 5b appears to be more difficult to understand and would be the consequence of the various processes that occur. In themselves, these processes involving dissolution, re-adsorption, or even re-precipitation are complex, and these processes and the effect of added salt could also cause changes in pH.

The situation with respect to the silanol face is shown in Figure 7. Interfacial potentials are negative, but the range can vary widely. The data in Figure 7 are by no means exhaustive. There is a wealth of data available both from force curves<sup>7</sup> or zeta-potentials.

### 2.3. Summary of the kaolinite study

Despite the huge step forward to characterizing individual surface planes of distinct particles in terms of charging, there is ample space for improving the experimental data basis. Also, the kaolinite study has opened a plethora of new questions, one being why the observed kaolinite

<sup>6</sup> We note that it is not possible to directly compare the trends in the charges and potentials. In the cited work, the potentials were not reported. We obtained the DLVO potentials from Igor Siretanu (University of Enschede).

<sup>7</sup> Silica is a popular tip material in AFM force distance studies either directly or as a consequence of Si<sub>3</sub>N<sub>4</sub> oxidation.

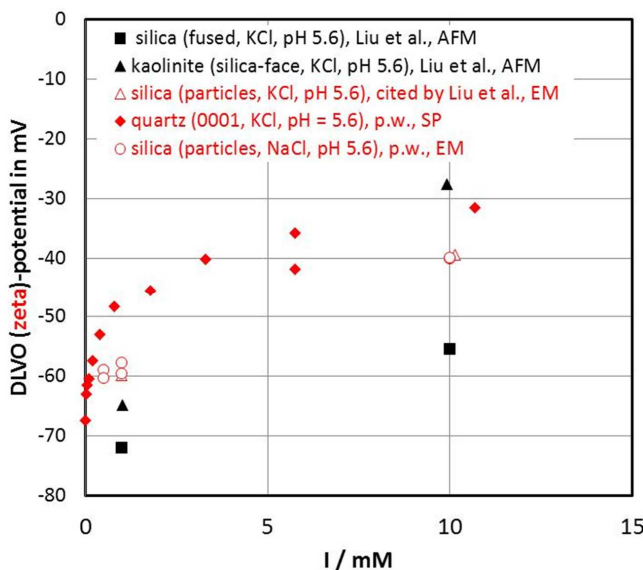


**Figure 7.** Interfacial potentials of silica relevant to the kaolinite silica plane as a function of salt concentration (equivalent to ionic strength in the case of the monovalent salts) at pH 5.6. Kaolinite and fused silica data are from Liu et al. [61]. Data for silica (AFM tip) are from Siretanu et al. [40]. Data for silica particles are those cited by Liu et al. [61] from previous literature.

edge surface chemistry with an IEP below pH 4 disagrees with all previous estimates of the point of zero net proton charge of above pH 5. It also disagrees with the theoretical estimates which suggest a pK of 5.7 [56]. Noteworthy, the determination of the edge face IEP was done by excluding the basal planes. The same could be said about the determination of the properties of the basal planes themselves, in which case, however, the edge planes were not excluded. Ideally measurements were made sufficiently far from the edges. The study of different sizes of the otherwise identical particles could shed light on possible surface potential effects.

### 3. Further direct evidence for the anisotropy of other clay minerals

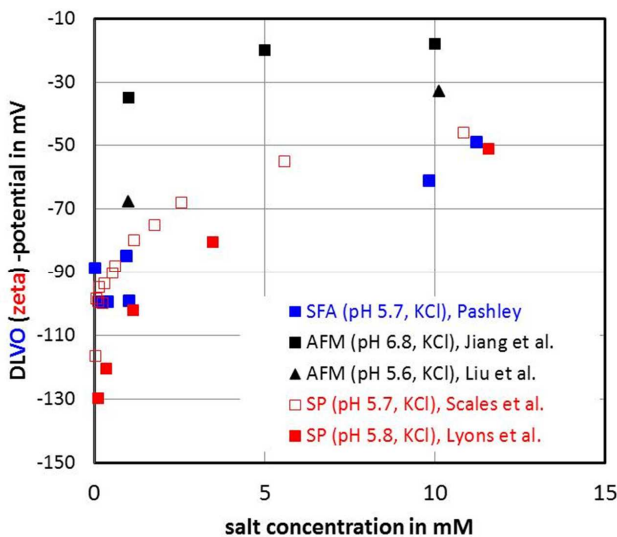
#### 3.1. Mica

##### 3.1.1. Mica basal plane

The mica basal plane is probably one of the most frequently studied single crystal surfaces. Because it can be prepared as an atomically flat sample, it is suitable for a range of sophisticated methods that are not applicable to rougher surfaces, including X-ray reflectivity [38, 39, 63], high-resolution AFM that is able to show hydration layers [64], or ions on mica [65] or nano-ultrasonics [66], to name a few such approaches. The literature on macroscopic data on mica

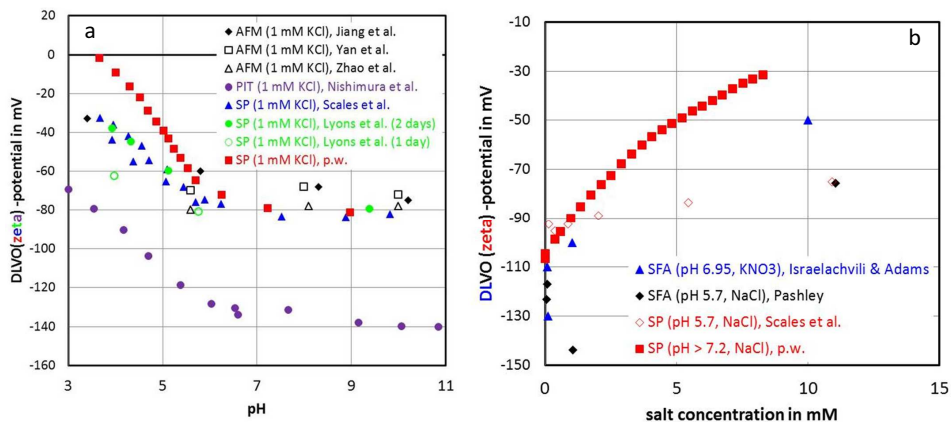
is also abundant. The present work is therefore not citing all the available work and comparing all available data.

Figure 12 shows data for mica at constant pH for variable salt levels of KCl. The data for the higher pH deviate, whereas the remainder of the data is in a common cloud independent of the method. Similar data are shown for a constant salt level and pH variation in Figure 9a. There is clear agreement about the level of the interfacial potential at pH >5.5, except for the data obtained using the plane interface technique (PIT). An important difference occurs at the lower pH range, where the IEP would be obtained. Depending on the source, the slope of the interfacial potential with decreasing pH differs a lot, resulting in different IEPs for the samples under investigation. Additional data on ionic strength dependence are shown in Figure 9b involving different salts.



**Figure 8.** Zeta-potentials (red) and DLVO potentials of mica as a function of salt concentration at near-neutral pH in KCl solutions. SFA data are from Pashley [67]. AFM data are from Jiang et al. [59] and Liu et al. [61]. Streaming potential data are from Scales et al. [68] and Lyons et al. [69].

The possible origins of the differences include aging according to Lyons et al. [69] as shown in Figure 10a for mica particles and for freshly cleaved mica basal planes that were subsequently aged. Clearly, aging in both cases strongly increases the IEP. Figure 10b also shows that freshly cleaved basal planes do not necessarily yield unique IEPs. There is significant scatter, and there is some discussion in the literature about how to prepare these surfaces. Figure 10c shows similar results for uncleaved mica basal planes. Again, there is clear scatter for mica samples from the same source. Also, the IEP is higher than for the freshly cleaved surfaces. This is consistent with the results obtained on aging of freshly cleaved samples. Overall, aging (whether on freshly cleaved samples or simply due to the use of aged samples) results in the deviation from the consistency that was noted in Figures 8 and 9a for pH >5.5. Besides these



**Figure 9.** Zeta-potentials (colored) and DLVO potentials of mica as a function of pH in 1 mM KCl solutions (a) and in other monovalent salts (b). Data in Figure 9a are from Jiang et al. [59], Yan et al. [70], Zhao et al. [60], Nishimura et al. [71], Scales et al. [68], and Lyons et al. [69]. Data in Figure 9b are from Pashley [67], Israelachvili and Adams [72], and Scales et al. [68].

preparation-related differences, the origin of the mica itself has also been shown to affect the results as discussed in some detail by Lyons et al. [69]. Therefore, mica data should best be compared if the source of the sample and the preparation of the surface under investigation were identical.

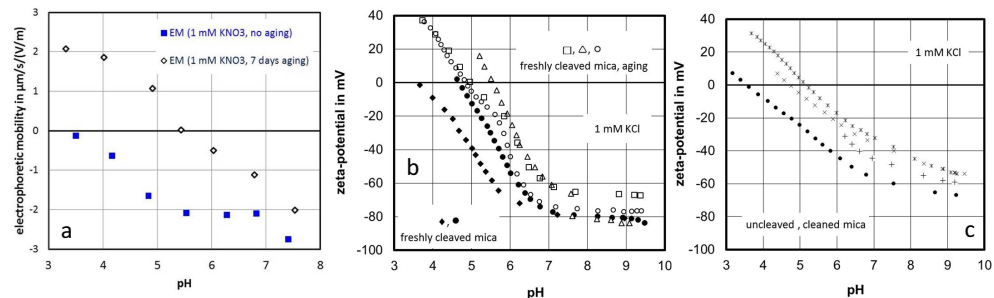


**Figure 10.** (a) Electrophoretic mobilities of mica particles at different aging times from Lyons et al. [69]. (b) Streaming potential data for mica basal planes in 1 mM KCl, freshly cleaved and aged. (c) Streaming potential data for uncleaved mica basal planes in 1 mM KCl.

The following comparison between the action of ions of different charge on the mica basal plane is restricted to measurements at pH > 5.5 and to samples that show strongly negative interfacial potentials. Figure 11a shows a comparison for results from SFA measurements. The cations are chosen such that no aqueous hydrolysis species occur, keeping the speciation simple and avoiding solution reactions that would also affect the pH. Clearly, the surface remains negative for the mono- and divalent salts. With the SFA, it was reported that measurements above 10 mM cation concentration resulted in too weak forces to measure. At very

high concentration, measurements show very interesting features that are related to hydration forces (triggered by the hydration shells of adsorbed cations). The divalent cations [here Ca, but the results are generic according to Pashley and Israelachvili for [73] alkaline earth elements, except Be, which strongly hydrolyzes and was not studied] generate less negative interfacial potentials than the monovalent cations. For the trivalent cation La, there is charge reversal. The surface turns positive at submillimolar concentrations. Figure 11b shows that the same kind of results has been independently obtained by zeta-potential measurements.

Figure 11c finally shows a direct comparison for the divalent cations (here Ca) in chloride solutions, now including also results from AFM-based experiments for which data on  $\text{La}^{3+}$  could not be found in our literature search. The comparison shows good agreement.

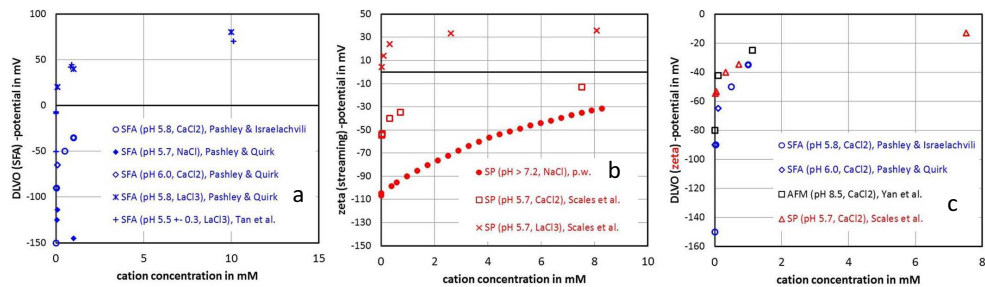


**Figure 11.** DLVO potentials from SFA experiments (a) and zeta-potentials from streaming potential measurements (b) of mica basal planes as a function of cation concentration at near-neutral pH for mono-, di-, and trivalent cations in chloride solutions. Data are from Pashley and Israelachvili [73], Pashley and Quirk [74], and Yan et al. [75] for Figure 11a and Scales et al. [68] for Figure 11b. (c) DLVO potentials from SFA and AFM experiments and zeta-potentials from streaming potential measurements of mica basal planes as a function of cation concentration at near-neutral pH for divalent cations in chloride solutions. Data are from Pashley and Israelachvili [73], Pashley and Quirk [74], Yan et al. [76], and Scales et al. [68].

The conclusion to be drawn from the above discussion of available data (note that we do not claim that the compilation of data is complete, nor do we claim that we have covered all available sources of measurements) is that tendencies are well retrieved for comparable samples and that even a quantitative agreement is probably achieved in particular for the divalent and trivalent cations at near-neutral pH.

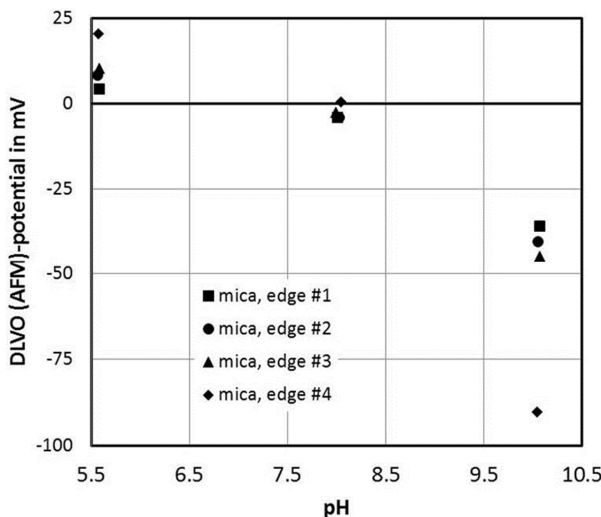
The data also clearly prove that the valence of the cations strongly affects the interfacial potentials. This will be further discussed in Chapter 4 in the context of electrolyte titrations.

Despite the good agreement in some cases, caution is required when studying mica basal planes because widely varying results can be obtained depending on sample pre-treatment, mica origin (i.e. composition), and aging (i.e. duration of exposure to aqueous solution) as was shown in specific work devoted to these issues [77-79].

### 3.1.2. Basal plane versus edge faces

For mica, some data sets exist showing that the IEP of the edge plane is at pH approximately 8. Figure 12 shows such data for different runs. As pointed out before, the measurements on

the edge planes are difficult. However, the absolute values away from the IEP may strongly differ for data taken at different locations (thus varying in roughness in particular).



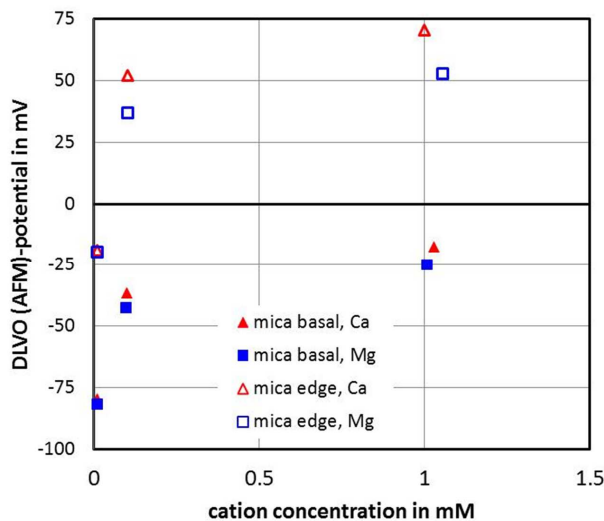
**Figure 12.** DLVO potentials from AFM experiments on mica edges as a function of salt concentration at pH 8.5 [60]; data sets 1 to 4 are taken at different spots and vary in surface roughness.

Figure 13 shows that even the action of divalent cations at pH 8.5 (i.e. where both basal plane and edge surfaces are intrinsically negative) will have very different effects. The data from Yan et al. show that [76], although the basal planes remain negative, the divalent cations are able to invert the charge on the edges. This clearly will generate anisotropy, and for the overall particle, it will require electrostatic (charge) regulation. It is not clear whether and how pH will be affected by such regulation.

### 3.2. Talc

Various data sets on talc are available from the literature. Zeta-potential measurements by Nalaskowski et al. [80] suggest IEPs for the edges and basal planes at pH approximately 3. The streaming potential measurements are in qualitative agreement with force distance curves by the same authors while showing distinct differences between the behavior of the edge and basal planes. The zeta-potential curves of the two planes are likewise not identical, so that the data appear self-consistent. These data sets, however, are in conflict with force measurements reported by Yan et al. [75] that are shown in Figure 14.

Figure 14a illustrates that the IEP of the basal plane is below pH 3 (i.e. at pH 5, the surface is still clearly negative), whereas that of the edges is at pH approximately 8. The origin of the differences is not clear. The latter study shows the anisotropy, which is further supported by data for divalent cations at pH 8.5 by [76] as shown in Figure 14b.



**Figure 13.** DLVO potentials from AFM experiments on mica basal plane and edge surfaces as a function of pH for 1 mM KCl solutions [76].

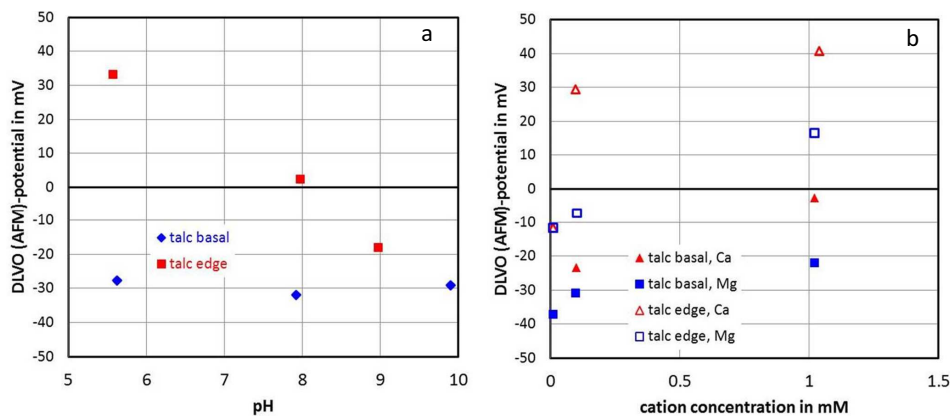


**Figure 14.** (a) DLVO potentials from AFM experiments on talc basal plane and edge surfaces as a function of pH for 1 mM KCl solutions [75]. (b) DLVO potentials from AFM experiments on talc basal plane and edge surfaces as a function of pH for 1 mM KCl solutions [76].

The results are similar to those obtained with mica shown in Figure 12. Again, the edge planes may change sign, whereas the basal plane remains negative. Similarly data for chlorite also exist and confirm the data sets discussed here, in general, and clearly exhibit anisotropy [70].

Overall, the examples shown in this part again suggest very complex situations when basal and edge surfaces are present simultaneously. Such situations are discussed in the following section, where first we discuss the amount of solid clay particles is buffering a suspension with

respect to pH yielding the overall point of zero net proton condition for the clay particles, whereupon, in the second step, the action of adding electrolyte to the buffered system can be investigated.

For the interpretation of such systems, assuming a full data set from force measurements or distinct measurements on specific planes were available, it would be very important to know whether there is a strong pH effect on the charge of a given plane or not. This is not always clear and may depend on many things as has been discussed in much detail for mica basal planes.

#### 4. Surface properties of well-defined clay samples

As already discussed in the introduction, the macroscopic measurements that are applied to investigate the charging behavior have mainly involved electrokinetic methods, force measurements, and all kinds of titrations. The outcome of these measurements needs to be associated further with the properties of the EIL (electric interfacial layer). The relation of the measurements to the interfacial potentials has been described in detail elsewhere [12] and will only be shortly summarized here.

- Electrokinetic methods probe the overall charge within the so-called shear plane, which is at the head end of the immobile part of the EIL. In classical electrophoretic mobility experiments, where the velocity of a particle in an applied electric field is measured, the resulting interfacial potential (the so-called zeta-potentials) is the result of the interfacial species that are present within the immobile part (i.e. the particle and the water layer that is moving with the particle). The zeta-potential is unspecific in the sense that it gives the overall result from a multitude of processes that may occur on complex particles as would be the case for clays. Electrokinetic potentials of clay particles are typically negative over the full pH range investigated. The isoelectric point (IEP, at which the electrokinetic mobility is zero) is usually at low pH, sometimes not accessible to measurement. This result suggests that the negative, permanent charge is controlling the overall electrokinetic behavior of the clays. The application of the method has become standard and many experimental set-ups are available to determine the electrokinetic properties of particles.
- Titration methods may probe specific kinds of interactions. Potentiometric acid-base titrations [19, 81] will include all those interactions that involve reactions of the complete system with protons and hydroxide ions<sup>8</sup>. In the case of clays, it may include reactions with surface functional groups on basal planes, edge surfaces, ion-exchange sites as well as secondary phenomena (such as dissolution and subsequent reactions such as hydrolysis or complex formation), re-precipitation, or adsorption of species that were released during

---

<sup>8</sup> This also includes dissolved carbon dioxide, which is a substantial complication due to the aqueous-phase reactions but also because carbon dioxide-related species can adsorb on surfaces. In all these reactions, protons are typically involved, which is why titrations are usually carried out in an inert atmosphere (such as purified argon). With natural clays, it is conceivable that calcite is present as a secondary mineral contained in a given sample, which makes the performance of reasonable acid-base titrations more or less senseless.

dissolution. It is probably impossible to disentangle contributions from the different phenomena in the analysis of a usual potentiometric acid-base titration. The method itself, though seemingly simple being an offspring of classical acid-base titrations, becomes quite complicated with surfaces. This is why often such titrations are carried out in the "fast" mode to limit the reactions to surface phenomena. However, if true equilibria involving dissolution and re-adsorption were to be considered, the approach would require substantial resources and analyses even for well-behaved oxide minerals.

- Mass titrations are a variant of potentiometric titrations [21, 23, 82]. They involve adding a known amount of solid to a solution of known composition and follow the evolution of the pH with increasing solid content. At a sufficient amount of solid in the system, the surface acid-base reactions buffer the system yielding the point of zero net proton charge for pure oxide systems. In such systems, the end point also coincides with the isoelectric point from electrokinetics. In the case of clays again, the situation is more complex.
- Yet, a further development of this technique is electrolyte titration [10]. From the effect of adding electrolyte to a surface buffered system on the resulting pH, the specific role of the electrolyte can be inferred. For well-behaved oxides, usually no effect is observed if inert electrolytes such as  $\text{NaClO}_4$  are used. For clays as pointed out earlier, there are multiple effects of electrolyte ions that could play a role in such measurements. One would be the ion-exchange part, which could lead to reactions not related to classical acid-base equilibria, but yet they might cause interactions. For example, when a Ca-clay is interacting with high concentrations of a monovalent electrolyte, Ca will be released and the interactions of divalent ions in an electrostatic sense are much more pronounced than those of monovalent cations.
- Complications in these measurements arise from the suspension effect [83-86]. In the present case, this will be neglected as is the case in all other studies of this kind that we are aware of. Further problems occur in solutions of high electrolyte concentration, where specific interactions of electrolyte ions with the glass electrode perturb the measurements [87].

Potentiometric mass and electrolyte titrations were carried out to examine surface properties of artificial clay samples (Na-, Ca-, and Mg-montmorillonite). The use of such a synthetic sample has the advantage that no pre-treatment is required as is the case for natural samples where accessory minerals have to be extracted. A wide variety of salts was used and it was found that the different electrolytes had different effects on the end point of mass titrations. A synthetic Na-montmorillonite (SM) was used for the experimental work [88]. It has the formula  $(\text{Si}_{3.8}\text{Al}_{0.2})/\text{Al}_{1.67}\text{Mg}_{0.33}\text{O}_{10}(\text{OH}_{1.9}\text{F}_{0.1})\text{Na}_{1.06}$  [88]. The external surface area was measured to be approximately  $100 \text{ m}^2/\text{g}$  (encompassing edges and basal plane surfaces), whereas the internal surface area was estimated to be approximately  $700 \text{ m}^2/\text{g}$ .

The clay was first used in its original Na-form. For additional experiments, it was transformed to Mg and Ca forms. For this purpose, the original Na-form was exposed to concentrated Mg or Ca solutions ( $0.1 \text{ mol/L}$ ) for 2 days to allow the ion exchange. After prolonged exposure to the concentrated Mg/Ca solutions, the transformed particles were separated from the supernatant by freeze-drying and reducing the surrounding pressure. For each sample, the proce-

dure was repeated three times, and we expect that most of the sodium was removed. The remainders of sodium would not interfere, because the starting conditions for the subsequent experiments were still the same, as all experiments with the three distinct forms were carried out from identical subsamples.

#### 4.1. Potentiometric mass titrations of clay samples

Potentiometric mass titrations were used to determine the effect of solid content on the pH of suspension. According to theory [21-23, 82], the suspension pH will increase (or decrease) with solid content until a constant pH is finally reached that no longer depends on solid content. For samples without acid or base impurities, this plateau pH corresponds to the  $pH_{pznc}$ . The surface of the particles is then buffering the pH of the suspension.

The known masses of the respective clay samples were added to an aqueous solution of  $pH_{in}$  in subsequent portions. After each addition and equilibration (at least 2 minutes under ultrasound and additional 10 minutes of stirring; the pH was found to remain constant after this procedure), the pH was recorded. The mass concentration beyond which the pH did not depend on solid mass content was approximately 35 g/dm<sup>3</sup>. In these mass titrations, ionic strength ( $I_c=10^{-3}$  mol/dm<sup>3</sup>;  $10^{-2}$  mol/dm<sup>3</sup>;  $10^{-1}$  mol/dm<sup>3</sup>) was controlled by the addition of electrolyte (NaCl in the case of Na-form and CaCl<sub>2</sub> in the case of Ca-form of montmorillonite).

The results from the potentiometric mass titrations were used to determine the effect of ionic strength on  $pH_{pznc}$  of the clays and to evaluate the proton-related surface charge densities.

Figures 15 and 16 show the results from mass titrations for the clay in its Na and Ca forms, respectively. Data for various starting values of pH and different electrolyte concentrations were obtained. The end points from the different starting points clearly converge with increasing solid concentration for a given ionic strength. With increasing salt content, it appears that the plateau can be reached at lower mass contents. For metal oxides [22], it had been observed that the plateau would be reached at lower mass concentration for higher ionic strength and if initial  $pH_{in}$  is close to  $pH_{pznc}$ . One reason for this difference could be that the slope of the  $pH(\gamma)$  function corresponds to the surface charge density, which is steeper for the higher ionic strength. Accordingly, proton-related surface charge density functions  $\sigma_{0,H^+}(pH)$  for clays are shifted with salt content (without any cross-point) and are nearly parallel [89]. The resulting end points (obtained or interpolated) are  $7.1 \pm 0.1$  (for  $10^{-3}$  mol/dm<sup>3</sup> NaCl),  $6.9 \pm 0.1$  (for  $10^{-2}$  mol/dm<sup>3</sup> NaCl), and  $6.6 \pm 0.1$  (for  $10^{-1}$  mol/dm<sup>3</sup> NaCl). Despite the experimental error, there is a clear trend for the end points to decrease with increasing ionic strength. This is expected based on the reported parallel shift of proton surface charge data as a function of ionic strength. For the Ca-form, as for the sodium form, the average plateau pH decreases with increasing salt content.

From the mass titration data, the specific surface charge densities (related to proton and hydroxide adsorption) can be calculated [22, 23]. The advantage of this method, compared to traditional acid-base potentiometric titrations, is that experiments can be performed at one ionic strength and also at very low electrolyte concentrations. Moreover, a comparison of the dispersion with blank titration is not required. The surface charge of an oxide in an aqueous

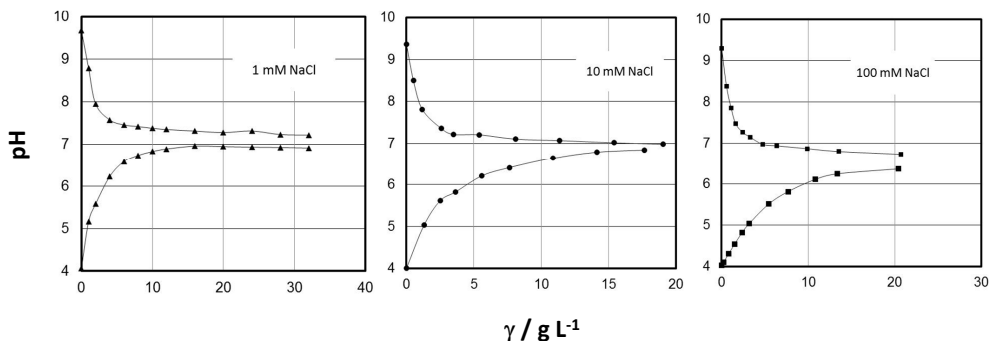


**Figure 15.** Potentiometric mass titrations of ACF2944 (Na-form) at different ionic strengths:  $I_c$  (mol/dm<sup>3</sup>): 0.001 ( $\blacktriangle$ ), 0.01 ( $\bullet$ ), and 0.1 ( $\blacksquare$ ) NaCl;  $t=20^\circ\text{C}$ . Shown are the values of the end points of mass titrations ( $\text{pH}_{\text{pZpc}}$ ) for the synthetic clay in its Na-form.

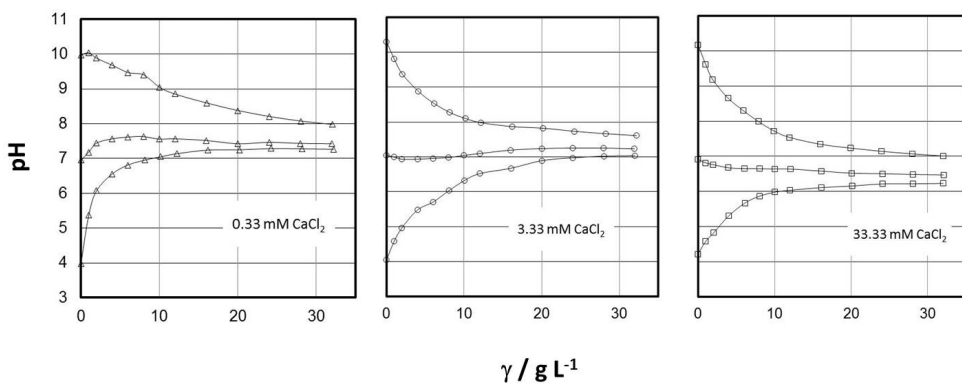


**Figure 16.** Potentiometric mass titrations of ACF2944 (Ca-form) at different ionic strengths:  $I_c$  (mol/dm<sup>3</sup>): 0.001 ( $\Delta$ ), 0.01 ( $\circ$ ), and 0.1 ( $\square$ ). Ionic strength was controlled by CaCl<sub>2</sub>;  $t=20^\circ\text{C}$ .

environment is the result of surface reactions (protonation, de-protonation, and counter-ion association). In the course of mass titration, when a solid metal oxide powder is added to an aqueous electrolyte solution, the amounts (and concentrations) of H<sup>+</sup> and OH<sup>-</sup> ions in the bulk of the solution are changing due to surface reactions but also due to the possible neutralization of H<sup>+</sup> and OH<sup>-</sup> ions in the bulk of the solutions. In the case of a pure sample (without acid or base impurities), the surface charge density in the 0-plane equals [23]:

$$\sigma_{0,\text{H}^+} = -\frac{F}{\gamma} \frac{c^\circ}{\bar{y}_\pm} \left( 10^{-\text{pH}_\gamma} - 10^{-\text{pH}_{\text{in}}} - 10^{\text{pH}_\gamma - \text{pK}_W^\circ} + 10^{\text{pH}_{\text{in}} - \text{pK}_W^\circ} \right) \quad (1)$$

where  $\gamma$  is the mass concentration of solid particles,  $\bar{\gamma}_{\pm}$  is the mean activity coefficient calculated from the Debye-Hückel equation, and  $K_W^{\circ}$  is the thermodynamic equilibrium constant of water ionization. Furthermore,  $pH_{in}$  is the initial pH,  $pH_{\gamma}$  is the pH of suspension at mass concentration  $\gamma$ ,  $c^{\circ}$  is the standard concentration ( $1 \text{ mol}/\text{dm}^3$ ), and  $F$  is the Faraday constant. To cover both acidic and basic pH ranges, at least two experiments should be performed, one with low and another with high initial pH.

Figure 17 presents the proton-related surface charge densities obtained from the potentiometric mass titration data according to a previously described procedure [23] for different concentrations of NaCl and CaCl<sub>2</sub>. As expected, a CIP of titration curves as a function of electrolyte concentration is not obtained. The PZNPC is shifted towards lower pH values with increasing electrolyte concentration. For the range between  $10^{-3}$  and  $10^{-1} \text{ mol}/\text{dm}^3$  concentration of NaCl, we obtain, on average, a difference of  $\Delta pH_{pznpc} = 0.9$  for CaCl<sub>2</sub>.

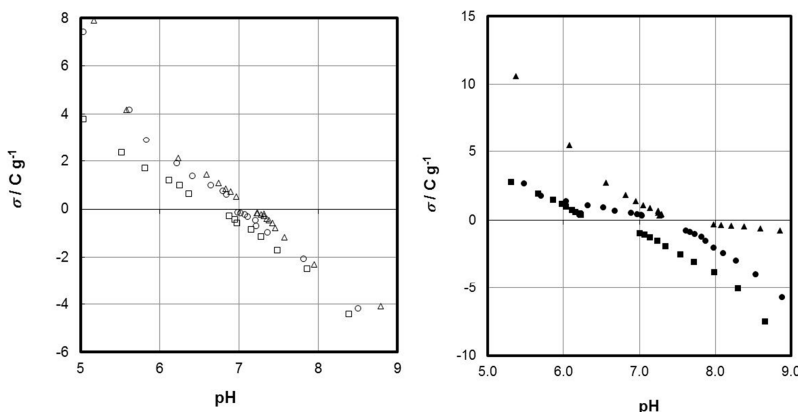


**Figure 17.** (a) Surface charge density of ACF2944 (Na-form) (calculated from mass titration data shown on Figure 15) at different ionic strength:  $I_c$  ( $\text{mol}/\text{dm}^3$ ): 0.001 ( $\Delta$ ), 0.01 ( $\circ$ ), and 0.1 ( $\square$ ); NaCl;  $t=20^\circ\text{C}$ . (b) Surface charge density of ACF2944 (Ca-form) (calculated from mass titration data shown on Figure 16) at different ionic strength:  $I_c$  ( $\text{mol}/\text{dm}^3$ ): 0.00033 ( $\blacktriangle$ ), 0.0033 ( $\bullet$ ), and 0.033 ( $\blacksquare$ ). Ionic strength was controlled by CaCl<sub>2</sub>;  $t=20^\circ\text{C}$ .

#### 4.2. Potentiometric electrolyte concentrations of clay samples

In the potentiometric electrolyte titrations, an initial clay suspension was prepared by adding the amount of powder to pure water that is sufficient to obtain the plateau pH. The standard value  $\gamma \approx 35 \text{ g}/\text{dm}^3$  had been previously determined in the mass titrations (see above). Subsequently, known aliquots of dry salt [NaCl, CsCl, CaCl<sub>2</sub>, LiNO<sub>3</sub>, NaNO<sub>3</sub>, or Ca(NO<sub>3</sub>)<sub>2</sub>] were added to the initial dispersion to scan a range of salt concentrations from  $10^{-5}$  to  $0.5 \text{ mol}/\text{dm}^3$ . The pH values of the dispersion obtained after each salt addition were measured after equilibration (at least 2 minutes under ultrasound and 10 minutes of stirring).

The results from electrolyte titrations results from electrolyte titrations for this sample are shown are shown in Figure 18 for three salts (NaCl, CsCl, and LiNO<sub>3</sub>) at a mass concentration

of 35 g/l Na-montmorillonite. In Figure 18, we also include the independent results from the direct mass titrations with the experimental errors based on the end-point values shown in Figure 16. A satisfactory agreement is found considering that the solid concentrations in the two experiments are not identical. This shows that the procedure is reliable. The lower solid concentrations in the continuous (pH) titrations tend to generate stronger effects based on the results in Figure 15a. The results of the electrolyte and mass titrations show that the effect of salt concentration is weak or absent at salt concentrations below approximately 1 mM. Above this value, however, a significant decrease of the mass titration end-points occurs in the electrolyte titrations for all salts tested.

A comparison between the different salts suggests that CsCl has a much stronger effect than NaCl, in agreement with the known strong affinity of Cs for clays [90, 91]. LiNO<sub>3</sub> has the weakest effect among the salts shown. The data sets indicate that different cations will have different effects on proton uptake on this clay, an observation that needs to be taken into account in comprehensive models to describe the charging of clays via ion-specific parameters.

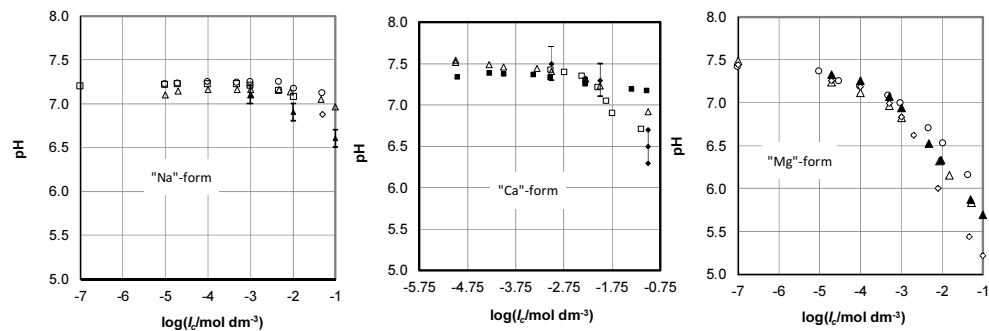


**Figure 18.** Potentiometric electrolyte titrations of ACF2944. (a) Na-form with NaCl ( $\Delta$ ), LiNO<sub>3</sub> ( $\circ$ ), and CsCl ( $\diamond$ ) and end points of mass titration ( $\blacktriangle$  with error bars); (b) Ca-form with NaCl ( $\Delta$ ), Ca(NO<sub>3</sub>)<sub>2</sub> ( $\blacksquare$ ), and CaCl<sub>2</sub> ( $\square$ ) and end points of mass titration ( $\blacklozenge$  with error bars); and (c) Mg-form with NaCl ( $\Delta$ ), NaNO<sub>3</sub> ( $\blacktriangle$ ), LiNO<sub>3</sub> ( $\circ$ ), and CsCl ( $\diamond$ ).

Figure 18 shows the results of the electrolyte titrations with Ca-montmorillonite. First, it becomes apparent that the variation of the pH values is much more pronounced than in the case of the Na-montmorillonite. The drop in pH again starts at approximately 1 mM concentration as for the Na-clay. The sequence is somewhat surprising in the sense that Ca(NO<sub>3</sub>)<sub>2</sub> has a much weaker effect than does CaCl<sub>2</sub>, given that the cation was to be the most relevant compound for the negatively charged surface.

For the Mg-form (Figure 18c), the effect of the electrolyte ions on the mass titration end-points starts at significantly lower concentration compared to the Na-form. The effect appears to be unspecific, however, up to approximately 1 mM concentration. Unlike in the previous example for Ca salts on Ca-montmorillonite, we did not observe a noticeable difference between NaCl and NaNO<sub>3</sub> systems, indicating that the nature of the anions tested in this case does not affect the results in a significant way. The order in which the cations affect the results is the same as for the Na-form of the clay, but the extent of the changes is much more pronounced for the Mg-form.

## 5. Reconciliation of results

The literature survey has shown that the understanding of clay surfaces in electrolyte solutions still has some space to improve. One important question is to what extent the aging of samples should be studied. Even if the aging steps and their consequences are not well studied and probably difficult to understand due to the complexity and the interdependencies of the process involved, natural samples will have undergone such aging. Simple aging in water can have significant effects on the interfacial potentials of relevant minerals as has been shown in the preceding text. Aging will make the surfaces more complex with adsorbed ions, and surely it will make them different from the ideal surfaces that can be obtained experimentally for sufficiently small times and conditions that would conserve the ideality and from those that have been used in computer codes to extract pK values.

Thus, a dual procedure is required to come to a full understanding:

- Comprehensive studies on the ideal systems involving the full monitoring of all potentially important features (solution composition, surface states, etc.) to gain insight in processes.
- Studies on the aging process and on aged samples to allow the transfer of the fundamental studies to the natural samples.

The wide range of reported values for isoelectric points or points of zero (net proton) charge of clay samples have to be considered with care in light of the aging processes and the potential effects of exposure to low or high pH conditions. This has been discussed in some detail for mica. We could add here that titrations of cleaved mica [92] have resulted in a pK value of 2.9, in strong contrast with the AFM data shown in Figure 12 for mica edges (always taking the general view that the basal plane is not proton sensitive and that consequently the proton reactions occur at the edges). As stated in the discussions about the techniques, such proton titrations will yield relative values, which may be overshadowed by permanent charge. The authors of the latter paper actually do conclude that the charge from deprotonation reactions is small compared to the permanent charge. In terms of published parameter, this all generates yet another set of contradictions given that the pK based on the AFM data would be 8 [60] and that the zeta-potential of freshly cleaved basal planes is pH sensitive as apparent from Figure 9a in particular for the low pH. Thus, the reported pK value from titrations could also stem from proton reactions at the basal plane. These could either occur at surface functional groups or be due to unconventional reactions of hydroxide ions on smooth surfaces.

We may continue by comparing the results of anions on the mica basal plane to the unexpected observations discussed in the electrolyte titrations in the previous section. Figure 19 illustrates that such effects are retrieved on the mica basal plane as well.

Both for monovalent Li solutions and for divalent Ca solutions, there is a difference between chloride and nitrate solutions. However, the effects are not the same: whereas, in the Li case, there is a strong decrease in the DLVO potential (an increase in absolute potential), in the Ca case, the opposite occurs. A study on ion-specific effects on sapphire-c has shown similar effects of nitrate versus chloride [62]. The co-adsorption of chloride as postulated for the

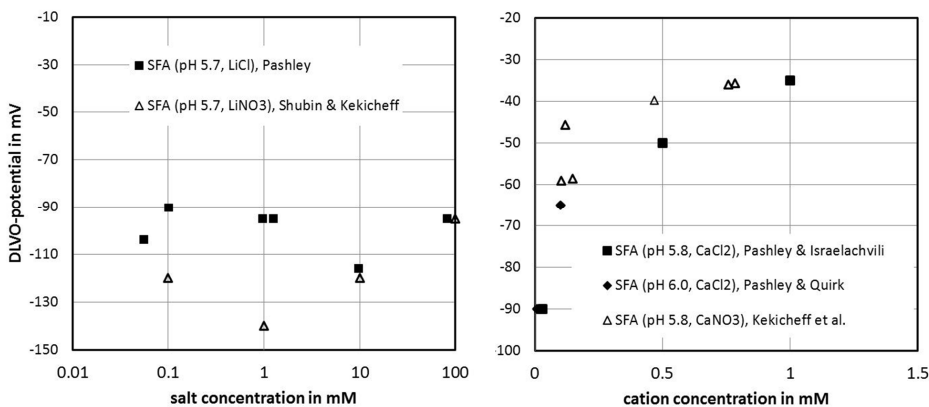


**Figure 19.** DLVO potentials of mica basal planes in chloride versus nitrate solutions. Left: Li solutions, data are from Pashley [67] and Shubin and Kekicoff [93]. Right: Ca solutions, data are from Pashley and Israelachvili [73], Pashley and Quirk [74], and Kekicoff et al. [94].

gibbsite basal plane [40] in Ca solutions could also explain the observation on sapphire-c. The pH dependence of and thus potential effects on the solution pH caused by such correlative interactions is not known at all but might explain the effect observed in the electrolyte titrations shown in Figure 18. The larger effect of the chloride would imply a stronger release of protons or co-adsorption of hydroxide ions in chloride solutions compared to nitrate solutions. This would keep the DLVO potentials higher in absolute values in the chloride systems, which is observed for the mica case (Figure 19) and concurs with the observations on sapphire-c as well. Such comparisons generate circumstantial evidence for the actions of hydroxide ions (or protons). The combining issue could be flat surfaces (for mica and sapphire-c, this is obvious; for the clay particles, it would mean that the reactions are happening on the basal planes). However, it would need to be a collective action of chloride and hydroxide ions (or protons) to explain the overall effect (i.e. causing changes in pH and the interfacial potential in the observed directions). It can be seen that, for the monovalent Li system on mica, this explanation cannot be sustained. However, the trend for the chloride system is also present, whereas the disagreeing observation for nitrate occurs in the very low concentration range.

To address the aging problem, we draw attention to a completely different field of research. In a recent study on mica as an active ice nucleation clay mineral, the structuring of water molecules at the surface of mica upon cooling using second harmonic generation (SHG) spectroscopy was measured [95]. Freshly cleaved mica induced the local ordering of the first water layer in contact with the surface, which was termed pre-activation of ice nucleation. This local ordering was recorded as the enhancement of the SHG upon cooling. Interestingly, small variations were observed from run to run for freshly cleaved samples. This is similar to what was discussed for mica in the previous sections. In the ice nucleation study, samples that were kept in contact with water for a longer time clearly exhibited an aging effect. Figure 20 reports additional results that only focus on the aging effect on the water/mica surface interaction.

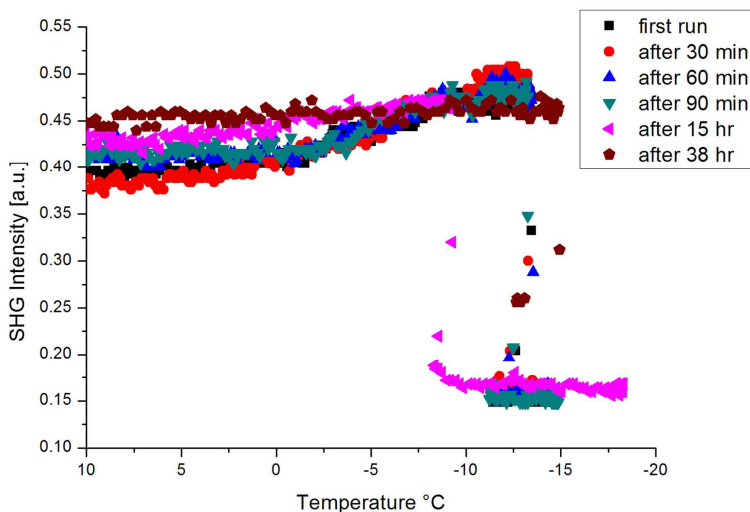


**Figure 20.** Second harmonic generation signals recorded in ice nucleation studies on a mica sample at different times.

Figure 20 shows the SHG signal at water-mica interface for the same sample after different aging periods. Measurements done within a few hours after the cleavage showed water ordering under cooling, and small variations were observed at high temperatures. Measurements carried out after 15 hours showed weaker ordering with cooling. Measurements carried out after 38 hours showed an almost temperature-independent signal in the liquid phase. In all measurements, the level of signal was different, particularly at high temperatures. For both the aqueous electrolyte mica interface and the ice nucleation study, the question will be what is the relevant surface to study. For most environmental applications, it will be an aged surface, although probably for fundamental studies aimed at process understanding fresh surfaces that are well defined should be preferable.

The anisotropy of the clay particles has relevance in many respects. The aggregation of the particles is highly affected by it as is the migration of clay particles. The spillover effects are complex and only few efforts have been dedicated to this issue. The effects become even more complex at points where more than just two surface planes meet (for example, two different edge planes and two different basal planes could be very close on kaolinite). The currently available experimental observations on the clay edges are still confusing in the sense that, for kaolinite, the edge surface data suggest a low point of zero charge contrary to expectations based on a previous experimental work. Interestingly, theoretical work does show the pK value for aluminols on kaolinite to be lower than in other cases [i.e. 5.7 for kaolinite versus 8.3 for montmorillonite [56] or 7.6 for pyrophyllite [47]]. Calculations also show that the pK values may differ between these extremes for a given solid depending on which edge surface is considered [96]. For talc and mica instead, the experimental points of zero charge (isoelectric points) determined for edges are in the expected range and in reasonable agreement with predicted pK values from advanced theoretical work [47, 56, 96] but disagree, for example,

with the above-mentioned titrations [92]. One has to keep in mind that the titrations (that also have been used in the cited theoretical work for comparison) may be misleading. Titrations yield relative changes, whereas the models used to extract pK values in surface complexation models will require absolute values (of charge of protons adsorbed or whatever quantity is used to fit surface complexation parameters). These absolute values are typically not available for clays. Furthermore, the shape of the titration curve or the relative charges versus pH cannot help because electrostatic factors may shift apparent pK values by many pH units from the intrinsic values (i.e. at zero surface potential).

As a consequence, it is probably necessary to improve the experimental data basis to come to more profound conclusions. In particular, a study on different clay edge surfaces could be important, but this is a significant experimental challenge. If the preparative issue was solved, one could test spillover effects at points where two edge surfaces meet for example. For the calculation work, it could turn out to be useful to report estimates for site densities of the sites that were studied as well as formal charges of the surface species. Furthermore, for comparison with experimental data and to scan the range of reported points of zero charge, it might turn out to be useful to explore the role of adsorbed ions (such as aluminum). It is noteworthy that some steps into such a direction have been taken by including potential composite ions such as Mg, Fe, or others in the calculations [56, 97].

Overall, a comprehensive study involving a multitude of experimental and theoretical approaches, with close collaboration to exactly mimic the experimental surfaces in the calculations, would be highly beneficial. This conclusion has also been drawn for seemingly simpler systems such as metal oxide surfaces.

Although the advances in the detailed understanding and the possibilities with modern experimental and computational techniques are breathtaking, much can be expected to surprise us in the future when taking an even closer look at mineral-electrolyte solution interfaces.

## Acknowledgements

The authors express their gratitude to Dr. Igor Siretanu (University of Enschede) for providing the potentials from the force measurements that were originally published in terms of charge densities. Professor Thomas Leisner (Karlsruhe Institute of Technology, IMK-AAF) is gratefully acknowledged for the support with the SHG study.

## Author details

Tajana Preocanin<sup>1</sup>, Ahmed Abdelmonem<sup>2</sup>, Gilles Montavon<sup>3</sup> and Johannes Luetzenkirchen<sup>4\*</sup>

\*Address all correspondence to: johannes@ine.fzk.de

1 Laboratory of Physical Chemistry, Department of Chemistry, Faculty of Science, University of Zagreb, Zagreb, Croatia

2 Institute of Meteorology and Climate Research-Atmospheric Aerosol Research (IMK-AAF), Karlsruhe Institute of Technology (KIT), Germany

3 Subatech, UMR 6457 (Ecole des Mines/CNRS-IN<sub>2</sub>P<sub>3</sub>/Nantes University), Nantes, France

4 Institut für Nukleare Entsorgung (INE), Karlsruhe Institute of Technology (KIT), Germany

## References

- [1] Lützenkirchen J. Determination of points of zero charge of minerals, experimental and computational approaches. *Current Topics in Colloid & Interface Science*. 2002;5:125 - 39.
- [2] Sposito G. On points of zero charge. *Environmental Science & Technology*. [Article]. 1998 Oct;32(19):2815-9.
- [3] Sposito G. On Points of Zero Charge. *Environmental Science & Technology*. 1999 1999/01/01;33(1):208-.
- [4] Kosmulski M. *Chemical Properties of Material Surfaces*: CRC Press; 2001.
- [5] Kosmulski M. *Surface Charging and Points of Zero Charge*: CRC Press; 2009.
- [6] Venema P, Hiemstra T, Weidler PG, van Riemsdijk WH. Intrinsic Proton Affinity of Reactive Surface Groups of Metal (Hydr)oxides: Application to Iron (Hydr)oxides. *Journal of Colloid and Interface Science*. 1998;198(2):282-95.
- [7] Hiemstra T, Van Riemsdijk WH. On the relationship between charge distribution, surface hydration, and the structure of the interface of metal hydroxides. *Journal of Colloid and Interface Science*. 2006;301(1):1-18.
- [8] Rahnemaie R, Hiemstra T, van Riemsdijk WH. A new surface structural approach to ion adsorption: Tracing the location of electrolyte ions. *Journal of Colloid and Interface Science*. 2006;293(2):312-21.
- [9] Bradbury MH, Baeyens B. Sorption modelling on illite Part I: Titration measurements and the sorption of Ni, Co, Eu and Sn. *Geochimica et Cosmochimica Acta*. 2009;73(4): 990-1003.
- [10] Lützenkirchen J, Preočanin T, Bauer A, Metz V, Sjöberg S. Net surface proton excess of smectites obtained from a combination of potentiometric acid–base, mass and electrolyte titrations. *Colloids and Surfaces A: Physicochemical and Engineering Aspects*. 2012;412:11-9.

- [11] Bradbury MH, Baeyens B. Sorption of Eu on Na- and Ca-montmorillonites: experimental investigations and modelling with cation exchange and surface complexation. *Geochimica et Cosmochimica Acta*. 2002;66(13):2325-34.
- [12] Kallay N, Preočanin T, Kovačević D, Lützenkirchen J, Chibowski E. Electrostatic potentials at solid/liquid interfaces. *Croatica chemica acta*. 2010;83(3):357-70.
- [13] Lützenkirchen J. Summary of studies on (ad) sorption as a “well-established” process within FUNMIG activities. *Applied Geochemistry*. 2012;27(2):427-43.
- [14] Gan Y, Franks GV. Charging behavior of the gibbsite basal (001) surface in NaCl solution investigated by AFM colloidal probe technique. *Langmuir*. 2006;22(14):6087-92.
- [15] Liu X, Cheng J, Sprik M, Lu X, Wang R. Understanding surface acidity of gibbsite with first principles molecular dynamics simulations. *Geochimica et Cosmochimica Acta*. 2013;120:487-95.
- [16] Hiemstra T, Yong H, Van Riemsdijk W. Interfacial charging phenomena of aluminum (hydr) oxides. *Langmuir*. 1999;15(18):5942-55.
- [17] Lützenkirchen J, Abdelmonem A, Weerasooriya R, Heberling F, Metz V, Marsac R. Adsorption of dissolved aluminum on sapphire-c and kaolinite: implications for points of zero charge of clay minerals. *Geochemical transactions*. 2014;15(1):9.
- [18] Lützenkirchen J, Zimmermann R, Preocanin T, Filby A, Kupcik T, Kuttner D, et al. An attempt to explain bimodal behaviour of the sapphire c-plane electrolyte interface. *Adv Colloid Interfac*. 2010 Jun 14;157(1-2):61-74.
- [19] Lützenkirchen J, Preočanin T, Kovačević D, Tomišić V, Lövgren L, Kallay N. Potentiometric titrations as a tool for surface charge determination. *Croatica chemica acta*. 2012;85(4):391-417.
- [20] Delgado AV, Gonzalez-Caballero F, Hunter RJ, Koopal LK, Lyklema J. Measurement and interpretation of electrokinetic phenomena. *Journal of Colloid and Interface Science*. [Article; Proceedings Paper]. 2007 May;309(2):194-224.
- [21] Noh JS, Schwarz JA. Estimation of the point of zero charge of simple oxides by mass titration. *Journal of Colloid and Interface Science*. 1989;130(1):157-64.
- [22] Preocanin T, Kallay N. Point of zero charge and surface charge density of TiO<sub>2</sub> in aqueous electrolyte solution as obtained by potentiometric mass titration. *Croatica chemica acta*. 2006 Mar;79(1):95-106.
- [23] Preočanin T, Kallay N. Application of» Mass Titration «to Determination of Surface Charge of Metal Oxides. *Croatica chemica acta*. 1998;71(4):1117-25.
- [24] Trasatti S, Doubova LM. Crystal-face specificity of electrical double-layer parameters at metal/solution interfaces. *Journal of the Chemical Society, Faraday Transactions*. [10.1039/FT9959103311]. 1995;91(19):3311-25.

- [25] Hiemstra T, De Wit JCM, Van Riemsdijk WH. Multisite proton adsorption modeling at the solid/solution interface of (hydr)oxides: A new approach: II. Application to various important (hydr)oxides. *Journal of Colloid and Interface Science*. 1989;133(1):105-17.
- [26] Lützenkirchen J, Behra P. A new approach for modelling potential effects in cation adsorption onto binary (hydr) oxides. *Journal of contaminant hydrology*. 1997;26(1):257-68.
- [27] Secor RB, Radke CJ. Spillover of the diffuse double layer on montmorillonite particles. *Journal of Colloid and Interface Science*. 1985;103(1):237-44.
- [28] Chang F-RC, Sposito G. The Electrical Double Layer of a Disk-Shaped Clay Mineral Particle: Effects of Electrolyte Properties and Surface Charge Density. *Journal of Colloid and Interface Science*. 1996;178(2):555-64.
- [29] Bourg IC, Sposito G, Bourg ACM. Modeling the acid-base surface chemistry of montmorillonite. *Journal of Colloid and Interface Science*. 2007;312(2):297-310.
- [30] Tournassat C, Grangeon S, Leroy P, Giffaut E. Modeling Specific pH Dependent Sorption of Divalent Metals on Montmorillonite Surfaces. A Review of Pitfalls, Recent Achievements and Current Challenges. *Am J Sci. [Article]*. 2013 May;313(5):395-451.
- [31] Lützenkirchen J, Preočanin T, Stipić F, Heberling F, Rosenqvist J, Kallay N. Surface potential at the hematite (001) crystal plane in aqueous environments and the effects of prolonged aging in water. *Geochimica et Cosmochimica Acta*. 2013;120:479-86.
- [32] Yanina SV, Rosso KM. Linked Reactivity at Mineral-Water Interfaces Through Bulk Crystal Conduction. *Science*. 2008;320(5873):218-22.
- [33] Luetzenkirchen J, Zimmermann R, Preocanin T, Filby A, Kupcik T, Kuettner D, et al. An attempt to explain bimodal behaviour of the sapphire c-plane electrolyte interface. *Advances in Colloid and Interface Science*. 2010 Jun 14;157(1-2):61-74.
- [34] Kallay N, Preocanin T, Selmani A, Kovacevic D, Luetzenkirchen J, Nakahara H, et al. Thermodynamic Model of Charging the Gas/Water Interface. *Journal of Physical Chemistry C*. 2015 Jan 15;119(2):997-1007.
- [35] Anderson JL. Effect of Nonuniform Zeta Potential on Particle Movement in Electric-Fields. *Journal of Colloid and Interface Science*. 1985 1985;105(1):45-54.
- [36] Franks GV, Gan Y. Charging behavior at the alumina–water interface and implications for ceramic processing. *Journal of the American Ceramic Society*. 2007;90(11):3373-88.
- [37] Catalano JG. Weak interfacial water ordering on isostructural hematite and corundum (0 0 1) surfaces. *Geochimica et Cosmochimica Acta*. 2011;75(8):2062-71.

- [38] Park C, Fenter PA, Nagy KL, Sturchio NC. Hydration and distribution of ions at the mica-water interface. *Physical review letters*. 2006;97(1):016101.
- [39] Schlegel ML, Nagy KL, Fenter P, Cheng L, Sturchio NC, Jacobsen SD. Cation sorption on the muscovite (001) surface in chloride solutions using high-resolution X-ray reflectivity. *Geochimica et Cosmochimica Acta*. 2006;70(14):3549-65.
- [40] Siretanu I, Ebeling D, Andersson MP, Stipp SLS, Philipse A, Stuart MC, et al. Direct observation of ionic structure at solid-liquid interfaces: a deep look into the Stern Layer. *Sci Rep. [Article]*. 2014;4.
- [41] Gupta V, Hampton MA, Stokes JR, Nguyen AV, Miller JD. Particle interactions in kaolinite suspensions and corresponding aggregate structures. *Journal of Colloid and Interface Science*. 2011;359(1):95-103.
- [42] Gupta V, Miller JD. Surface force measurements at the basal planes of ordered kaolinite particles. *Journal of Colloid and Interface Science*. 2010;344(2):362-71.
- [43] Yin X, Miller J. Wettability of kaolinite basal planes based on surface force measurements using atomic force microscopy. *Minerals and Metallurgical Processing*. 2012;29(1):13-9.
- [44] Liu J, Sandaklie-Nikolova L, Wang X, Miller JD. Surface force measurements at kaolinite edge surfaces using atomic force microscopy. *Journal of Colloid and Interface Science*. 2014;420:35-40.
- [45] Williams DJA, Williams KP. Electrophoresis and Zeta Potential of Kaolinite. *Journal of Colloid and Interface Science*. 1978 1978;65(1):79-87.
- [46] Zhou ZH, Gunter WD. The Nature of the Surface-Charge of Kaolinite. *Clay Clay Min.* 1992 Jun;40(3):365-8.
- [47] Tazi S, Rotenberg B, Salanne M, Sprik M, Sulpizi M. Absolute acidity of clay edge sites from ab-initio simulations. *Geochimica et Cosmochimica Acta. [Article]*. 2012 Oct;94:1-11.
- [48] Miller JD, Nalaskowski J, Abdul B, Du H. Surface characteristics of kaolinite and other selected two layer silicate minerals. *The Canadian Journal of Chemical Engineering*. 2007;85(5):617-24.
- [49] Alagha L, Wang S, Yan L, Xu Z, Masliyah J. Probing Adsorption of Polyacrylamide-Based Polymers on Anisotropic Basal Planes of Kaolinite Using Quartz Crystal Microbalance. *Langmuir*. 2013 2013/03/26;29(12):3989-98.
- [50] Gupta V. Surface charge features of kaolinite particles and their interactions: The University of Utah; 2011.
- [51] Liu XD, Cheng J, Sprik M, Lu XC, Wang RC. Understanding surface acidity of gibbsite with first principles molecular dynamics simulations. *Geochimica et Cosmochimica Acta. [Article]*. 2013 Nov;120:487-95.

- [52] Adekola F, Fedoroff M, Geckes H, Kupcik T, Lefevre G, Lutzenkirchen J, et al. Characterization of acid-base properties of two gibbsite samples in the context of literature results. *J Colloid Interf Sci.* 2011 Feb 1;354(1):306-17.
- [53] Rosenqvist J, Persson P, Sjoberg S. Protonation and charging of nanosized gibbsite ( $\text{Al(OH)}_3$ ) particles in aqueous suspension. *Langmuir.* [Article]. 2002 Jun; 18(12):4598-604.
- [54] Lutzenkirchen J, Kupcik T, Fuss M, Walther C, Sarpola A, Sundman O. Adsorption of Al-13-Keggin clusters to sapphire c-plane single crystals: Kinetic observations by streaming current measurements. *Appl Surf Sci.* 2010 Jun 15;256(17):5406-11.
- [55] Lutzenkirchen J, Marsac R, Casey WH, Furrer G, Kupcik T, Lindqvist-Reis P. The Effect of Monovalent Electrolytes on the Deprotonation of  $\text{MAl}_12$  Keggin Ions. *Aquat Geochem.* 2015 Jul;21(2-4):81-97.
- [56] Liu XD, Lu XC, Sprik M, Cheng J, Meijer EJ, Wang RC. Acidity of edge surface sites of montmorillonite and kaolinite. *Geochimica et Cosmochimica Acta.* [Article]. 2013 Sep;117:180-90.
- [57] Lutzenkirchen J, Preocanin T, Kallay N. A macroscopic water structure based model for describing charging phenomena at inert hydrophobic surfaces in aqueous electrolyte solutions. *Phys Chem Chem Phys.* 2008;10(32):4946-55.
- [58] Anderson JL. Electrokinetic transport of colloidal particles with heterogeneous surfaces. *Journal of Electrostatics.* 1995;34(2-3):189-203.
- [59] Jiang H, Xie Z, Liu GR, Yu YW, Zhang D. Interaction forces between muscovite and silica surfaces in electrolyte solutions measured with AFM. *Transactions of Nonferrous Metals Society of China.* 2013 Jun;23(6):1783-8.
- [60] Zhao HY, Bhattacharjee S, Chow R, Wallace D, Masliyah JH, Xu ZH. Probing Surface Charge Potentials of Clay Basal Planes and Edges by Direct Force Measurements. *Langmuir.* [Article]. 2008 Nov;24(22):12899-910.
- [61] Liu J, Miller JD, Yin X, Gupta V, Wang X. Influence of ionic strength on the surface charge and interaction of layered silicate particles. *Journal of Colloid and Interface Science.* 2014 Oct 15;432:270-7.
- [62] Lutzenkirchen J. Specific Ion Effects at Two Single-Crystal Planes of Sapphire. *Langmuir.* 2013 Jun 25;29(25):7726-34.
- [63] Cheng L, Fenter P, Nagy KL, Schlegel ML, Sturchio NC. Molecular-Scale Density Oscillations in Water Adjacent to a Mica Surface. *Physical review letters.* 2001;87(15): 156103.
- [64] Kobayashi K, Oyabu N, Kimura K, Ido S, Suzuki K, Imai T, et al. Visualization of hydration layers on muscovite mica in aqueous solution by frequency-modulation atomic force microscopy. *The Journal of Chemical Physics.* 2013;138(18):184704.

- [65] Loh SH, Jarvis SP. Visualization of Ion Distribution at the Mica-Electrolyte Interface. *Langmuir*. 2010 Jun 15;26(12):9176-8.
- [66] Mante P-A, Chen C-C, Wen Y-C, Chen H-Y, Yang S-C, Huang Y-R, et al. Probing Hydrophilic Interface of Solid/Liquid-Water by Nanoultrasonics. *Sci Rep. [Article]*. 2014;4:6249.
- [67] Pashley RM. DLVO and Hydration Forces between Mica Surfaces in Li<sup>+</sup>, Na<sup>+</sup>, K<sup>+</sup>, and Cs<sup>+</sup> Electrolyte-Solutions - a Correlation of Double-Layer and Hydration Forces with Surface Cation-Exchange Properties. *Journal of Colloid and Interface Science*. 1981;83(2):531-46.
- [68] Scales PJ, Grieser F, Healy TW. Electrokinetics of the muscovite mica-aqueous solution interface. *Langmuir*. 1990 1990/03/01;6(3):582-9.
- [69] Lyons JS, Furlong DN, Healy TW. The Electrical Double-Layer Properties of the Mica (Muscovite)-Aqueous Electrolyte Interface. *Aust J Chem*. 1981;34(6):1177-87.
- [70] Yin XH, Yan LJ, Liu J, Xu ZH, Miller JD. Anisotropic Surface Charging of Chlorite Surfaces. *Clay Clay Min*. 2013 Feb-Apr;61(1-2):152-64.
- [71] Nishimura S, Tateyama H, Tsunematsu K, Jinnai K. Zeta-Potential Measurement of Muscovite Mica Basal-Plane Aqueous-Solution Interface By Means of Plane Interface Technique. *Journal of Colloid and Interface Science. [Article]*. 1992 Sep;152(2):359-67.
- [72] Israelachvili JN, Adams GE. Direct Measurement of Long-Range Forces between 2 Mica Surfaces in Aqueous KNO<sub>3</sub> Solutions. *Nature*. 1976;262(5571):773-6.
- [73] Pashley RM, Israelachvili JN. DLVO and Hydration Forces between Mica Surfaces in Mg-2+, Ca-2+, Sr-2+, and Ba-2+ Chloride Solutions. *Journal of Colloid and Interface Science*. 1984;97(2):446-55.
- [74] Pashley RM, Quirk JP. The Effect of Cation Valency on DLVO and Hydration Forces between Macroscopic Sheets of Muscovite Mica in Relation to Clay Swelling. *Colloid Surface*. 1984;9(1):1-17.
- [75] Yan LJ, Masliyah JH, Xu ZH. Understanding suspension rheology of anisotropically-charged platy minerals from direct interaction force measurement using AFM. *Current Opinion in Colloid & Interface Science*. 2013 Apr;18(2):149-56.
- [76] Yan L, Masliyah JH, Xu Z. Interaction of divalent cations with basal planes and edge surfaces of phyllosilicate minerals: Muscovite and talc. *Journal of Colloid and Interface Science*. 2013 Aug 15;404:183-91.
- [77] Balmer TE, Christenson HK, Spencer ND, Heuberger M. The effect of surface ions on water adsorption to mica. *Langmuir*. 2008 Feb 19;24(4):1566-9.
- [78] Perkin S, Chai L, Kampf N, Raviv U, Briscoe W, Dunlop I, et al. Forces between mica surfaces, prepared in different ways, across aqueous and nonaqueous liquids confined to molecularly thin films. *Langmuir*. 2006 Jul 4;22(14):6142-52.

- [79] Israelachvili JN, Alcantar NA, Maeda N, Mates TE, Ruths M. Preparing contamination-free mica substrates for surface characterization, force measurements, and imaging. *Langmuir*. 2004 Apr 27;20(9):3616-22.
- [80] Nalaskowski J, Abdul B, Du H, Miller JD. Anisotropic character of talc surfaces as revealed by streaming potential measurements, atomic force microscopy, molecular dynamics simulations and contact angle measurements. *Can Metall Q. [Article; Proceedings Paper]*. 2007 Jul;46(3):227-35.
- [81] Sjöberg S, Lövgren L. The application of potentiometric techniques to study complexation reactions at the mineral/water interface. *Aquatic Sciences*. 1993;55(4):324-35.
- [82] Zalac S, Kallay N. Application of mass titration to the point of zero charge determination. *Journal of Colloid and Interface Science*. 1992;149(1):233-40.
- [83] Brezinski DP. INFLUENCE OF COLLOIDAL CHARGE ON RESPONSE OF PH AND REFERENCE ELECTRODES - THE SUSPENSION EFFECT. *Talanta*. [Article]. 1983;30(5):347-54.
- [84] Oman S. A step to a uniform definition and interpretation of the suspension effect. *Talanta*. 2000;51(1):21-31.
- [85] Oman SF. On the seventieth anniversary of the "Suspension Effect": A review of its investigations and interpretations. *Acta Chim Slov*. [Article]. 2000;47(4):519-34.
- [86] Oman SF, Camoes MF, Powell KJ, Rajagopalan R, Spitzer P. Guidelines for potentiometric measurements in suspensions. Part A. The suspension effect (IUPAC Technical Report). *Pure and Applied Chemistry*. [Article]. 2007 Jan;79(1):67-79.
- [87] Schnurr A, Marsac R, Rabung T, Lutzenkirchen J, Geckeis H. Sorption of Cm(III) and Eu(III) onto clay minerals under saline conditions: Batch adsorption, laser-fluorescence spectroscopy and modeling. *Geochim Cosmochim Ac*. 2015 Feb 15;151:192-202.
- [88] Reinholdt M, Miehe-Brendle J, Delmotte L, Le Dred R, Tuilier MH. Synthesis and characterization of montmorillonite-type phyllosilicates in a fluoride medium. *Clay Min*. 2005 Jun;40(2):177-90.
- [89] Tombacz E, Szekeres M. Colloidal behavior of aqueous montmorillonite suspensions: the specific role of pH in the presence of indifferent electrolytes. *Appl Clay Sci*. [Article]. 2004 Oct;27(1-2):75-94.
- [90] Seliman AF, Lasheen YF, Youssief MAE, Abo-Aly MM, Shehata FA. Removal of some radionuclides from contaminated solution using natural clay: bentonite. *J Radianal Nucl Ch*. 2014 Jun;300(3):969-79.
- [91] Okumura M, Nakamura H, Machida M. Mechanism of Strong Affinity of Clay Minerals to Radioactive Cesium: First-Principles Calculation Study for Adsorption of Cesium at Frayed Edge Sites in Muscovite. *J Phys Soc Jpn*. 2013 Mar;82(3).

- [92] Maslova MV, Gerasimova LG, Forsling W. Surface Properties of Cleaved Mica. *Colloid Journal.* 2004 2004/05/01;66(3):322-8.
- [93] Shubin VE, Kekicheff P. Electrical Double-Layer Structure Revisited Via a Surface Force Apparatus - Mica Interfaces in Lithium-Nitrate Solutions. *Journal of Colloid and Interface Science.* 1993 Jan;155(1):108-23.
- [94] Kekicheff P, Marcelja S, Senden TJ, Shubin VE. Charge Reversal Seen in Electrical Double-Layer Interaction of Surfaces Immersed in 2-1 Calcium Electrolyte. *J Chem Phys.* 1993 Oct 15;99(8):6098-113.
- [95] Abdelmonem A, Lutzenkirchen J, Leisner T. Probing ice-nucleation processes on the molecular level using second harmonic generation spectroscopy. *Atmos Meas Tech.* 2015;8(8):3519-26.
- [96] Liu XD, Cheng J, Sprik M, Lu XC, Wang RC. Surface acidity of 2:1-type dioctahedral clay minerals from first principles molecular dynamics simulations. *Geochimica et Cosmochimica Acta.* [Article]. 2014 Sep;140:410-7.
- [97] Liu XD, Cheng J, Sprik M, Lu XC, Wang RC. Interfacial structures and acidity of edge surfaces of ferruginous smectites. *Geochimica et Cosmochimica Acta.* 2015 Nov; 168:293-301.

---

## Adsorption of Industrial Pollutants by Natural and Modified Aluminosilicates

---

Liudmila Novikova and Larisa Belchinskaya

Additional information is available at the end of the chapter

<http://dx.doi.org/10.5772/61678>

---

### Abstract

The adsorption ability of natural clay minerals and zeolites is a structurally caused distinguished feature, which determines their physical-chemical properties and almost each area of application. The type of surface active sites responsible for adsorption behavior differs for various structural types of aluminosilicates and varies under modifying agents. The present chapter illustrates the effect of the acid and base modification of natural aluminosilicates on their adsorption behavior in respect to a number of pollutants present in aqueous media. For this, the change of adsorption-structural characteristics of natural clay samples containing representatives of the main groups of clay minerals under activation is considered. Further, the chapter focuses on characterization of surface active sites by means of a new method of a catalytic conversion of 2-methylbut-3-yn-2-ol. The presence of both acid and basic sites on the aluminosilicates surface as well as variations of surface acidity and basicity for different structural types of aluminosilicates under varying conditions of modification is discussed. The third highlight of the chapter encompasses adsorption processes taking place in aqueous solutions of formaldehyde, acetic acid, and ammonium chloride on the surface of natural and activated aluminosilicates. The activating effect of a number of inorganic acids and bases on adsorption equilibrium is compared. The considered mechanism of the adsorption of electrolytes and polar molecules from aqueous media may comprise hydrogen bonding, chemisorptions, or ion-exchange reactions.

**Keywords:** Clay minerals, zeolites, acid and base activation, surfaceactive sites, methylbutynol conversion, adsorption

---

### 1. Introduction

The adsorption ability of natural aluminosilicates, e.g., clay minerals and zeolites, is inseparable from humans from the times of their first existence till the present days. The use of clays

for making ceramic wares and their use in households, industry, engineering, and in creating the art articles, etc., is based on the unique properties of their surfaces to absorb/adsorb molecules of water, organic substances, inorganic cations, and anions, leading to a partial or complete swelling of the layered structure of minerals followed by a sliding of clay layers relative to each other. Nowadays, ceramic materials, both traditional and advanced, are of extreme significance in the fields of electronics, communications, optics, transportation, medicine, energy conversion and pollution control, aerospace, construction, and recreation [1, 2]. Each of the specified fields of application exploits some single or several distinguished properties of ceramic materials, but despite this, the general feature of all these areas is the phenomenon of adsorption (lat. *sorbeo*—capture or uptake), which, in the nature of the case, is realized by the contact of two or more different phases. The adsorption properties of materials are determined by the state and chemical activity of surface, porosity, and external conditions; they assign the conditions for material production and further exploitations.

The present chapter considers adsorption phenomena and physical–chemical properties of surface of natural aluminosilicates, which are the base of traditional ceramic materials, in natural state and under effect of reagent treatment (acid and alkaline activation). Noteworthy, that natural aluminosilicate samples are always a mixture of different phases, i.e., clay and nonclay minerals, mixed phases, oxides, organic matter, etc., formed under varied geological conditions. Depending on the application field, one may employ separation and purification of natural polymineral phases in order to enrich the content of a definite mineral phase or to eliminate admixtures. Nevertheless, under no specific treatment or purification, raw aluminosilicate samples are confirmed to comprise enhanced physical–chemical characteristics and, hence, significant adsorption, ion-exchange, or catalytic ability, which are proportional to the content of a rock forming clay mineral or a zeolite in the natural sample [3–6]. Hereinafter, physical–chemical behavior of raw aluminosilicate samples is considered with the aim of further application as low cost and effective adsorbents of industrial pollutants.

The first part of the chapter illustrates the effect of a chemical exposure (acid and base activation) on the chemical composition of aluminosilicates and their surface properties (porosity and specific surface area), including chemical reactions of aluminosilicates during activation.

The second part is focused on a new characterization method for identification of the type and activity of surfaceactive sites by means of catalytic reaction of 2-methylbut-3-yn-2-ol (MBOH) conversion. It is shown hereinafter that depending on the crystal structure of a mineral present in natural raw sample, as well as on the chemical modification applied, the acidity and basicity of the surface is changed, providing various sites to be active in adsorption or catalytic process.

The possibility of a diverse adsorption mechanism (physical, chemical adsorption, and ion-exchange) realized during uptake of various substances from aqueous media will be illustrated for formaldehyde, acetic acid, and ammonia chloride solutions in the third part of the chapter.

The background considered in this chapter will be a correlation of the structural type and physical–chemical properties of the surface of natural aluminosilicates to the type of activating effect of an inorganic modifier and to the mechanism of adsorption process in systems with

industrial toxicants. The examined information will improve the knowledge and understanding of the professionals on the specific properties of natural aluminosilicates used in ceramics, as well as on the methods of their investigation and application for elaboration of environmentally safe materials and technologies.

## 2. Surface properties of natural aluminosilicates and their modification

### 2.1. Structural features and classification of natural aluminosilicates

Among a rich variety of natural aluminosilicates, the most remarkable adsorption properties are typical for clay minerals and zeolites owing to the features of their structure and chemical composition.

Clay minerals are a group of hydrous aluminum, magnesium, and iron silicates that form the bases of clays and soils. Most of clay minerals have layered or semilayered structure. The main structural elements of the most natural aluminosilicates are tetrahedra of  $\text{SiO}_4$  (T) and/or octahedra of  $\text{AlO}_6$  (O) joint by the vertices and forming the planar sheets, i.e., tetrahedral and octahedral sheets, respectively. A combination of T- and O-sheets constitutes an elementary layer and attributes a mineral to a specific structural type or a group according to the last recommendations of the nomenclature committee of AIPEA (International Association for the Study of Clays) [7]. For instance, as for planar phyllosilicates, a combination of T- and O-sheets (Fig. 1a) forms the elementary layer of 1:1 mineral type (kaolinite, dickite, etc.), whereas in the extensive 2:1 mineral type (talc, montmorillonite, vermiculite, etc.), an octahedral sheet is sandwiched between two T-sheets (T-O-T layer, Fig. 1b). The type of interlayer material, i.e., water molecules, exchangeable cations of alkali/alkaline earth metals, and hydroxides (Fig. 1c), and the layer charge ( $x = 0\sim2$ ) allow further subdivision of minerals into subgroups. Additionally, there is a group of nonplanar minerals, previously named “quasi-layered silicates,” observing a modulated structure (strips, islands, ribbons, etc). Unlike the planar ones, discontinuous chains of T-sheets are inverted, linking adjacent 1:1 or 2:1 sheets (Fig. 1d) and producing the zeolites like channels [8].

The layers are combined into elementary packages, the aggregate of which forms a mineral particle with the size finer than 4  $\mu\text{m}$ . The isomorphic substitutions of  $\text{Si}^{4+}$  for  $\text{Al}^{3+}$  in T-sheets and  $\text{Al}^{3+}$  for  $\text{Fe}^{2+}/\text{Fe}^{3+}$  in O-sheets impart a negative charge of aluminosilicate framework, which is balanced by cations from the surrounding environment and explains cation-exchange properties of aluminosilicates. The most remarkable cation-exchange capacity (CEC) is typical for clay minerals of 2:1 group, layered-chain minerals (sepiolite, palygorskite), whereas members of kaolinite group possess the lowest CEC as well as low swelling due to weak isomorphic substitutions.

Apart from layered minerals, the high CEC and adsorption ability is a characteristic feature of natural zeolites, aluminosilicates with a three-dimensional hard-sphere framework structure. The structural elements of zeolites are  $\text{SiO}_4$  and  $\text{AlO}_4$  tetrahedra joint by vertices in the way that cavities and channels are formed, in which hydrated cations, water, and other molecules may diffuse.

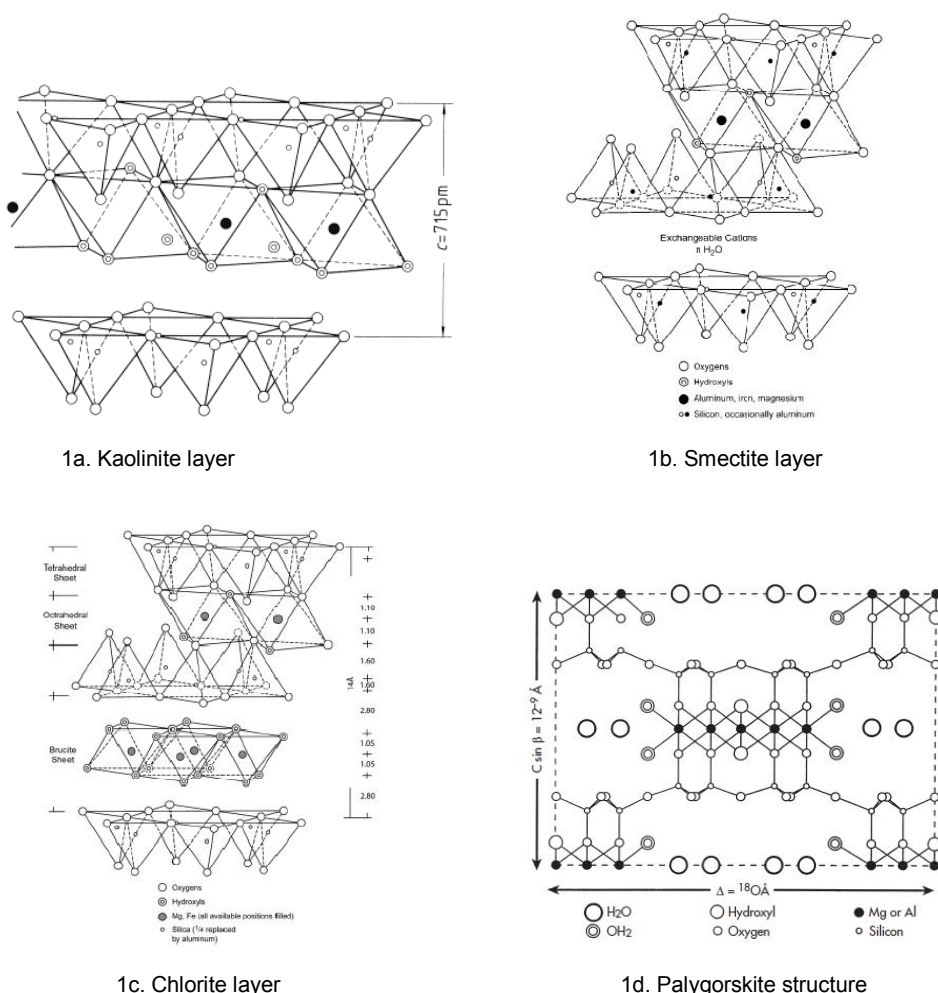


**Figure 1.** Structural types of planar (a–c) and nonplanar silicates (d): (a) 1:1 mineral group [9], (b) 2:1 mineral group (exchangeable cations and water in the interlayer) [10], (c) 2:1 mineral group (chlorite and hydroxides in the interlayer) [10], and (d) 2:1 nonplanar (modulated) silicate (palygorskite) [11].

Numerous investigations in the field of chemistry of aluminosilicates specify that the structure of clay minerals as well as their chemical composition, approximately expressed by the formula  $M_{2/n}O Al_2O_3 ySiO_2 zH_2O$ , determines the following active sites, which will be responsible for the adsorption behavior of natural clay minerals or zeolites: (i) exchangeable cations ( $K^+$ ,  $Na^+$ , and/or  $Ca^{2+}$ ); (ii) hydroxyls of acid/basic character ( $SiOH$ ,  $SiO(H^+)Al$ ,  $Al-OH$ , and  $OH$  or  $Mg-OH$ ); (iii) coordinatively unsaturated ions of  $Al^{3+}$ ,  $Mg^{2+}$ , and/or  $Fe^{3+}$ ; and (iv) oxygen anions  $O^-$ . Such reactivity of the surface and structural elements of silicates is obviously realized in their ability to physical adsorption, realized by van der Waals interactions or hydrogen

bonding with surface OH groups, coordinately unsaturated cations, oxygen anions, etc. Additionally, there is a good and proved opportunity for chemisorptions due to a stronger interaction between the surface and the molecules followed by formation of chemical bonds [12, 13]. Of course, ion-exchange reactions (involving exchangeable cations or OH groups) are important and will readily contribute to the adsorption process, as well as catalytic ability in specific processes and conditions [14]. However, to be competitive to the other commercial materials and adsorbents, clay minerals should meet the same requirements as for other adsorbents (Table 1).

Requirement	Characteristic of clay mineral	Compliance
High specific surface area and porosity	Mesoporous, $S = 20\text{--}150 \text{ m}^2/\text{g}$	+ Activation needed
Chemical affinity to adsorbates	Polar, hydrophilic surface of clay minerals—affinity toward polar substances	+ Modification needed
Chemical and thermal stability	Low chemical and thermal stability in natural form	Modification needed
Ability to regeneration	Possible	Modification needed
Availability	Widely available	+

**Table 1.** Compliance of natural aluminosilicates to general requirements for industrial adsorbents

As shown in Table 1, porosity, surface area, and surface physical–chemical affinity of natural aluminosilicates need to be improved to meet general requirements. For this, various methods of activation and modification have been applied

## 2.2. Chemical modification of clay minerals and its influence on surface properties

Natural aluminosilicates are able to interact easily with chemical reagents, modifying through this their surface and structural properties and, as a sequence, their physical–chemical activity. Along with the chemical exposure, aluminosilicates can significantly vary their properties under mechanical, thermal, and recently under physical exposure of magnetic field of different types (ultrahigh frequency (UHF), weak pulse field) [15, 16]. This behavior enables scientist unlimited opportunities in varying and targeting the properties of materials, produced based on or involving clay minerals and other silicates.

Despite the manifold means applied and being currently improved for the activation or modification of aluminosilicates properties, it is still possible to consider the following general groups of methods for clay minerals activation: mechanical (grinding of kaolinite), thermal, chemical (acid, alkali, salt, etc.), and physical (exposure of magnetic field) activations or a combination of them, e.g., mechanochemical and thermochemical activation.

For *mechanical and/or mechanochemical activation*, different types of mills have been applied, i.e., planetary ball-mill, vertical jet (compressed air), cryogenic mills, etc. [17]. Grinding usually

starts from a reduction of particle size, promoting the deformation of crystal structure of minerals mainly along the *c*-axis, and a disruption of Si-OH, Al-OH, Al-O-Si, and Si-O bonds. Depending on the milling conditions, surface characteristics and colloid properties of clay minerals are changed [18]. In the first grinding stages, a decrease of particle sizes and an increase in clay surface area are observed, including variations of their porosity. Further grinding causes adhesion of the particles, followed by a decline of the specific surface area, amorphization of the structure, and change in plastic and dispersion properties of clays [19, 20]. Mechanical exposure is accompanied by the new active sites appearing at the boundaries of the particles faults and an increase in cation-exchange capacity of the mineral, as often observed for kaolinite and other clay minerals.

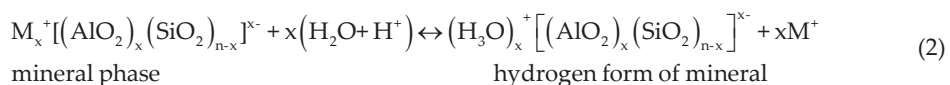
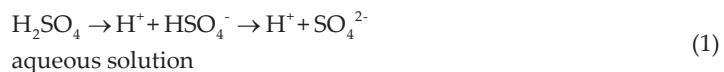
Severe changes of the structure and properties of minerals are reached by mechanochemical treatment in a definite chemical media (water, acid, alkaline solutions, and other substances) [21–23]. It is frequently used to enhance their catalytic activities, acid dissolution, or for the higher leaching of aluminum.

*Thermal activation* of clay minerals is based on the thermal treatment of natural clay sample at an elevated temperature resulting in desorption of adsorbed gases and water molecules and evolution of free surface. However, at rather high temperatures, which are different for each mineral type, crystal structure can undergo partial damage or entire structure collapse followed by a decrement of surface activity.

*Chemical activation or modification* usually provides the strongest effect on the structure and properties of materials due to chemical interactions of a modifying agent and the surface of material [24]. Despite numerous modifying agents exploited in recent decades for altering the properties of aluminosilicates, the activation by acid and alkaline solutions remains as the most frequently used in industrial or laboratory processing of clays [8, 25, 26].

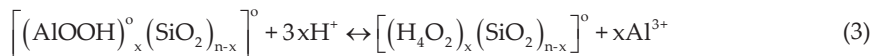
For acid activation or acid leaching, generally mineral acids (sulfuric or hydrochloric acids) are used [27–29]. The application of organic acids, e.g., acetic, formic acids, and oxalic, is rarer as their effect is weaker due to their low strength [30, 31].

The following chemical reactions take place during the contact of an aluminosilicate and acid solution. First, as most of the clay minerals possess ion-exchange ability, the ion-exchange reactions will occur. The exchangeable cations, usually cations of alkaline or alkaline earth elements, e.g.,  $\text{Na}^+$ ,  $\text{K}^+$ , or  $\text{Ca}^{2+}$ , located in the interlayer space will be substituted (cation-exchange) for protons resulted from dissociation of an acid:

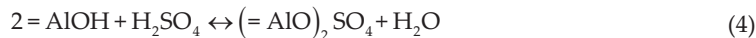


where  $M_x^+ = Na^+, K^+, Ca^{2+}, Mg^{2+}$ .

Along with the Ion-exchange reactions, there is an acid attack of the layered structure. Protons of the acid easily penetrate into the interlayer space and react mainly with cations of the octahedral sheet. This process is known as "dealumination" as it comprises substitution of octahedral  $Al^{3+}$  or  $Fe^{2+}/Fe^{3+}$  ions by protons and formation of additional Si-OH groups in the tetrahedral sheet:



In addition, one may expect anion-exchange reactions (Eq. (4)) between AlOH groups of basic character and  $SO_4^{2-}$  anions with the formation of sulfates:



The occurrence of these reactions of decationating and dealumination is confirmed by changes in the chemical composition of natural aluminosilicate samples (Table 2). Raw clay samples from several deposits in Russia, which phase composition involved presence of clay minerals of different layer type (1:1; 2:1 layered and 2:1 nonplanar), were crushed and sieved into grain fraction <0.25 mm and further subjected to acid activation by 2M  $H_2SO_4$  solution at 100°C for 6 h [4].

Aluminosilicate sample, deposit	Structural components	Chemical composition, %								Loss on ignition	SiO <sub>2</sub> /Al <sub>2</sub> O <sub>3</sub>
		SiO <sub>2</sub>	Al <sub>2</sub> O <sub>3</sub>	Fe <sub>2</sub> O <sub>3</sub>	FeO	MgO	CaO	Na <sub>2</sub> O+K <sub>2</sub> O	H <sub>2</sub> O		
Palygorskite (Pal), Cherkassy, Russia	Palygorskite ~50%, quartz, zeolites, mica, feldspar	53,25 70,33	9,84 5,46	7,68 1,98	0,61 0,16	7,95 2,15	3,62 0,92	0,86 0,61	10,00 10,28	4,83 7,31	98,64 99,20
Kaolinite (Kaol), Voronezh, Russia	Kaolinite ~60% mica ~30% montmorillonite ~10%	50,48 69,83	18,21 7,43	6,84 2,23	0,27 0,08	1,80 0,42	1,96 0,11	0,35 0,24	0,23 0,24	3,20 9,10	99,34 99,85
Mixed samples (HdmCK), Voronezh, Russia	Hydromica ~30-35%, clinoptilolite e ~5%, kaolinite ~5% quartz, mica – traces	48,54 71,43	11,24 8,93	0,86 0,74	-	1,10 0,38	9,78 0,62	4,12 0,96	-	13,86 16,78	99,93 99,74
											5,41 12,88

**Table 2.** Chemical composition of natural aluminosilicate samples before and after acid activation by 2M  $H_2SO_4$  at 100°C for 6 h [4]; size fraction of grains<0.25 mm

It follows from Table 2 that the content of metal oxides was markedly reduced after acid activation, namely,  $\text{Al}_2\text{O}_3$  (by 1.3–2.5 times),  $\text{Fe}_2\text{O}_3$  (1.2–3.8 times),  $\text{FeO}$  (3.4–3.8),  $\text{MgO}$  (2.9–4.3 times),  $\text{CaO}$  (3.9–17.8 times),  $\text{Na}_2\text{O}$ , and  $\text{K}_2\text{O}$  (1.4–4.0 times), except for  $\text{SiO}_2$ . This fact clearly testifies to the occurrence of the Cation-exchange reactions (Eqs. (2) and (3)) during acid leaching. As a result, the content of silica oxides as well as silica module ( $\text{SiO}_2/\text{Al}_2\text{O}_3$ ) was increased.

Moreover, due to changes of the chemical composition caused by acid treatment, serious variations of surface and structural characteristics of minerals have been observed [32, 33], which also strongly depend on the acid solution concentration and duration of the treatment. At shorter acid leaching times, mainly Ion-exchange reactions take place along with a slight destruction of the layered structure. This is followed by an increase in pore size of aluminosilicates, transformations of the micro pores into mesopores, and rise of specific surface area of the mineral [34]. However, by durable acid treatment, the crystal structure of minerals is more profoundly damaged, which finally lead to the falling of surface area as well as the adsorption capacity of aluminosilicates.

Fig. 2 illustrates  $\text{N}_2$  adsorption/desorption isotherms obtained to characterize surface properties of porous materials applying the BET method [4]. Here, the S-shape forms of  $\text{N}_2$  adsorption and desorption isotherms for natural and 2M  $\text{H}_2\text{SO}_4$ -treated samples, containing palygorskite (Pal) and kaolinite (Kaol) as major components, and hysteresis loops arose due to polymolecular adsorption and a capillary condensation of  $\text{N}_2$  molecules in the pores of adsorbent. According to the IUPAC classification, this isotherm type is attributed to mesoporous materials having pore diameter of 2–50 nm.

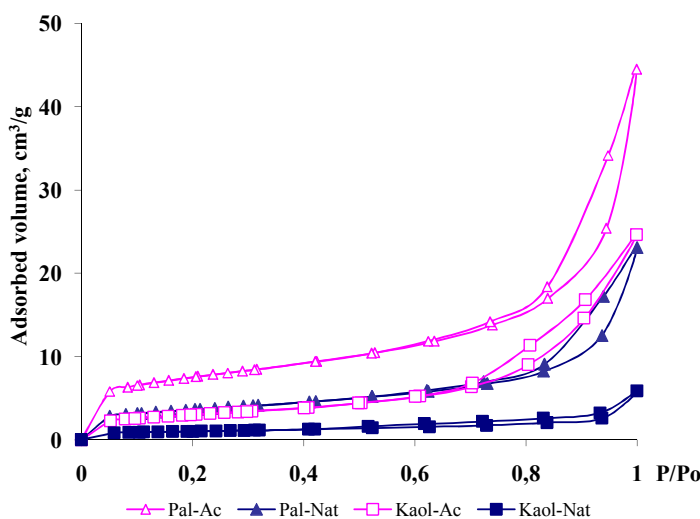


**Figure 2.** BET  $\text{N}_2$  adsorption isotherms for natural (Nat) and treated by 2M  $\text{H}_2\text{SO}_4$ (Ac) palygorskite (Pal) and kaolinite (Kaol).

The volumes of nitrogen adsorbed by Pal were higher than that for Kaol samples. Acid treatment of natural samples increased  $N_2$  adsorbed volume in two times that testified to development of additional free surface area and free pores volume of adsorbents. It follows from pore size distribution (Fig. 3) that pore diameters of investigated clay samples varied within 3–4 nm.

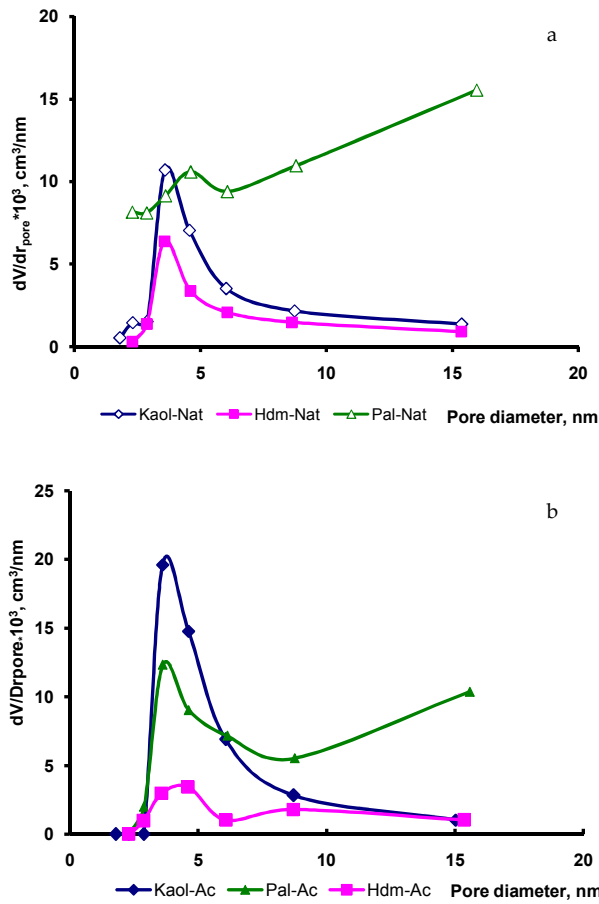


Figure 3. Pore size distribution of natural aluminosilicate samples before (a) and after (b) modification by 2M  $H_2SO_4$  [4].

It is remarkable that acid treatment practically did not change the pore diameters of clay samples, whereas the pore volume rose by two orders owing to additional formation/opening of mesopores (Fig. 3b). The highest growth of mesopores fraction observed for Kaol sample (Fig. 3b) testifies to the strongest acid attack of its structure (1:1 layer type), obviously due to easy accessible for protons octahedral sheet and octahedral cations of  $Al^{3+}$ . The crystal structure of palygorskite or illite minerals present in other natural samples, apparently more resistant

to acid as in their structure the octahedral sheet, is hidden between tetrahedral sheets as well as the stronger interactions between the layers occurs in mica/illite.

Experimental isotherms of N<sub>2</sub> adsorption provide information on values of specific surface area of investigated clay samples (Table 3). The phase composition of natural samples (Table 2) along with the features of their structure determined the order in which specific surface area of samples decreased: Pal > Kaol > HdmCK.

Sample	S, m <sup>2</sup> /g		$S_{\text{acid}}/S_{\text{nat}}$
	Natural	Acid treated	
Pal	146	262	1.8
Kaol	27	64	2.4
HdmCK	24	31	1.3

**Table 3.** Specific surface area of natural and modified by 2M H<sub>2</sub>SO<sub>4</sub> aluminosilicate samples

The application of acid treatment for the modification of natural aluminosilicates increased their specific surface area in 1.3–2.4 times. The ratio of  $S_{\text{acid}}/S_{\text{nat}}$  pointed out that the effect of acid treatment on surface characteristics of investigated aluminosilicate samples, containing various structural components, weakened in the order Kaol > Pal > HdmCK.

*Alkaline or soda activation* is often used for industrial processing of clays applied as drilling muds. Different substances have been used as an activating agent, i.e., alkalis (NaOH, KOH, and LiOH), salts of alkaline (Na<sub>2</sub>SiO<sub>3</sub>, Na<sub>2</sub>CO<sub>3</sub>) or alkaline earth metals (CaSO<sub>4</sub>), and oxides (MgO) of about 2–4 mass%. The most significant parameter, which affects the dispersing and rheological properties, is the Na<sup>+</sup> content. As a result, the viscosities, swelling indices, and filtration losses of clay suspensions significantly vary until they fulfill the drilling mud standards or satisfy the requirements of paint industry [35], ceramic production [36], etc.

The alkaline activation of natural mineral sorbent M<sub>45</sub>C<sub>20</sub> (grain size < 0.25 mm) with the following phase composition: montmorillonite (45%), clinoptilolite (20%), goethite (10%), illite (15%), and calcite (10%) from Sokirnitsa deposit, Ukraine, was carried out by 2M solutions of NaOH or NH<sub>4</sub>OH for 6 h at 100°C, followed by washing of the sample till neutral pH. The observed changes in the chemical composition of the aluminosilicate were mainly due to the reduction of SiO<sub>2</sub> (6%) and MgO (1%) oxides and an increase in content of Na<sub>2</sub>O (Table 4).

Sorbent	Content (% per absolutely dry sample)								SiO <sub>2</sub> /R <sub>2</sub> O <sub>3</sub>	
	SiO <sub>2</sub>	Al <sub>2</sub> O <sub>3</sub>	Fe <sub>2</sub> O <sub>3</sub>	CaO	MgO	Na <sub>2</sub> O	K <sub>2</sub> O	TiO <sub>2</sub>		
MCNat	56.65	14.32	7.03	8.12	1.62	0.79	2.78	0.63	7.9	2.74
MC-Alk	50.72	15.50	8.13	8.79	0.55	5.32	2.8	0.7	7.3	2.14

Note: R—Al, Fe; MCN—natural aluminosilicates M<sub>45</sub>C<sub>20</sub>; MC-Alk—aluminosilicates M<sub>45</sub>C<sub>20</sub> treated with a 2M NaOH solution.

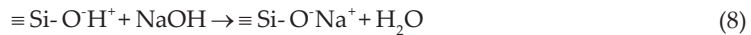
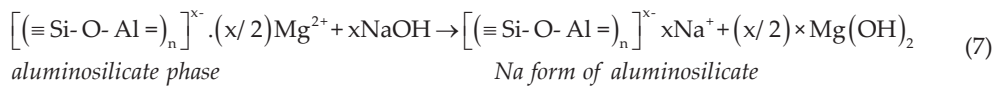
**Table 4.** Chemical composition of natural mineral sorbent M<sub>45</sub>C<sub>20</sub> treated by 2M NaOH [37]

Apart from the acid treatment, which affect to the most to octahedral cations, alkaline treatment selectively influences the tetrahedral sheets by means of the chemical dissolution of  $\text{SiO}_2$  and  $\text{Al}_2\text{O}_3$  in the alkali forming sodium silicates and sodium aluminate, respectively [38]:

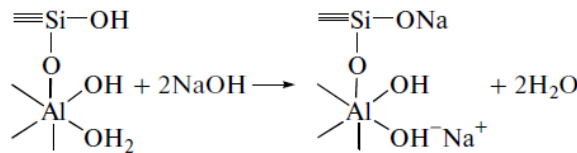


In the alkaline medium, the Si–O–Si bond is less stable than the Si–O–Al bond [39]; therefore,  $\text{Si}^{4+}$  easily transfers from aluminosilicate structure into the solution in comparison with  $\text{Al}^{3+}$ . This is evidenced by a decrease in  $\text{SiO}_2$  content, whereas that for  $\text{Al}_2\text{O}_3$  remained almost unchanged (Table 4).

Meanwhile, the Na<sub>2</sub>O content increased abruptly (by a factor of 6.7), which along with a threefold decrease of MgO content, illustrated the occurrence of several ion-exchange reactions, involving (i) Mg<sup>2+</sup> (or Ca<sup>2+</sup>) from the interlayer space or octahedral positions (7) and (ii) silanol groups (8) and Na<sup>+</sup> ions from the external solution:

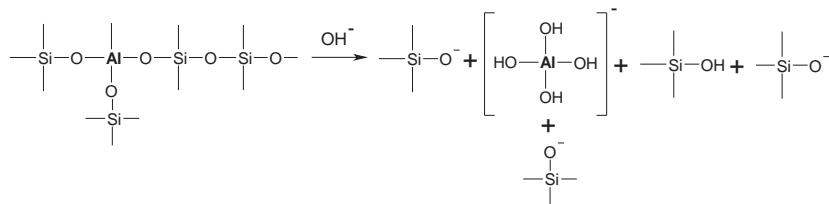
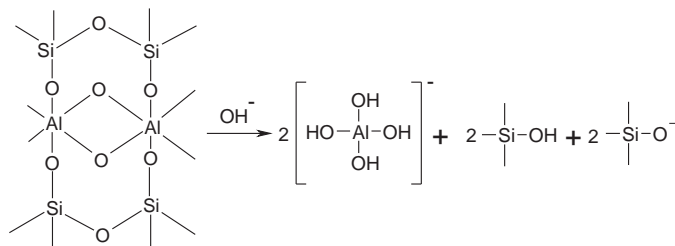


In the case of montmorillonite,  $\text{Na}^+$  ions can be exchanged for  $\text{H}^+$  ions of hydroxyl groups bound to aluminum atoms at the boundaries of the octahedral layer [37]:



**Scheme 1** Exchange of Na<sup>+</sup> for H<sup>+</sup> ions of protonated Al-OH groups

All in all, the action of NaOH solution is destructive for silicon skeleton of aluminosilicate via the disruption of -Si-O-Si-, -Si-O-Al-, and -Al-O-Al- bonds followed by formation of low polymeric aluminate and silicate anions, and anions of silicon acids. Schemes 2 and 3 demonstrate this action of alkali on clinoptilolite and montmorillonite structural components, respectively:

**Scheme 2.** Transformations of the aluminosilicate structure of the clinoptilolite component under alkaline conditions**Scheme 3** Transformations of the aluminosilicate structure of the montmorillonite component under alkaline conditions

As aluminate and silicate are accumulated in the alkaline medium, the polycondensation reaction is likely to occur between aluminate and silicate ions, either yielding an amorphous aluminosilicate phase or followed by the crystallization of the amorphous phase and formation of new zeolite phases [37, 40, 41]. This reaction is the basic one for the production of geopolymers by means of alkaline activation of natural clays that have been frequently used for manufacturing the building materials [42].

For the case of a combined aluminosilicate sorbent  $M_{45}C_{20}$ , the alkali activation contributed to transformation of the original aluminosilicate structure into a zeolite structure of heulandites [37]. The surface characteristics of aluminosilicates, including  $M_{45}C_{20}$ , were significantly changed after alkaline exposure (Table 5). Porosity, pore diameter, and specific surface area raised in about 1.5 times. Fig. 4 testified that total pore volume increased by a factor of 2.2 mainly due to a significant increase in mesopore volume (by a factor of 2.6).

Sample	Porosity, %	Average pore diameter, $D_{av}$ , nm	Adsorption capacity of monolayer, $am(H_2O)$ , mmol/g	Specific surface area, $S$ , $m^2/g$
$M_{45}C_{20}$ -Nat	36,0	2,6	2,55	197
$M_{45}C_{20}$ -Alk	48,8	3,9	3,77	297

**Table 5.** Surface characteristics of the natural (Nat) and alkali-treated (Alk) sorbent  $M_{45}C_{20}$

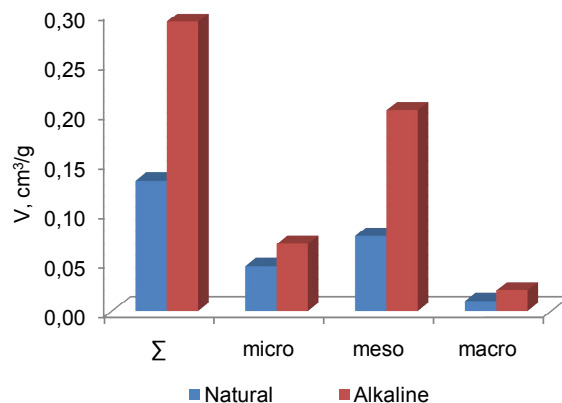


**Figure 4.** Pore volumes of natural (Nat) and alkali-treated (Alk) sorbent  $M_{45}C_{20}$ . (Adopted from Belchinskaya et al. [43].)

Summarizing this section, one should emphasize that the extent of acid/alkaline modification of aluminosilicates chemical composition, and hence, their surface properties depends strongly on (i) structural features of the major aluminosilicate phase in the sample and (ii) type of modifying agent and conditions. Octahedral sheets of 1:1 layer type mineral phase are easily accessible for acid attack as compared to 2:1 planar (montmorillonite and illite) or 2:1 nonplanar (palygorskite) mineral phases. Tetrahedral sheets of all mineral types undergo chemical interaction with alkaline solution yielding either an amorphous or crystalline aluminosilicate phase.

Variations in chemical composition as well as in the structure of modified aluminosilicate samples affect the activity of the surface. In the next section, one will consider the nature of surfaceactive sites of natural aluminosilicate samples and the effect of surface modification by acid and basic solutions on their distribution and the strength. It is of high importance to characterize the surfaceactive centers, which impart the material adsorption, catalytic, or other surface activity.

### 3. Characterization of surfaceactive sites of natural aluminosilicates by catalytic conversion of methylbutynol

Surface acid-base properties of solid materials are essential for almost each of their application. The use of aluminosilicates as adsorbents, binders, fillers, ion-exchangers, emulsifiers, catalysts or catalysts supports, etc., requires knowledge of their surface activity. To this belongs surface ability to donate/accept a proton (Broensted sites) or an electron pair (Lewis sites). Natural clay minerals and other aluminosilicates, like no other materials, comprise both Broensted acid (protons of polarized SiOH groups or water molecules, bridge hydroxyls  $Si-O(H^+)-Al$ ), Broensted basic sites (hydroxyls of structural MeOH groups,

OH groups of polarized water molecules), Lewis acid (exchangeable cations, coordinative nonsaturated ions  $\text{Al}^{3+}$ ,  $\text{Mg}^{2+}$ ,  $\text{Fe}^{3+}$  ions), and Lewis basic sites (oxygen anions of tetrahedral or octahedral sheets). Usually the number and the type of surface sites of different solids, including aluminosilicates, are determined by using the probe molecules. The nonreactive probe molecule is adsorbed on the surface and studied then by different physical-chemical methods (titration and spectroscopic techniques (FTIR, XPS, NMR), temperature-programmed desorption (TPD) of  $\text{NH}_3$  and  $\text{CO}_2$ , microcalorimetry, thermal analysis, etc.). On the other hand, in a number of catalytic reactions, reactive probe molecules have been applied, i.e., iso-propanol, cumene, benzene, etc., to characterize surface sites based on their reactivity under conditions close to real operation [44–46].

One of the catalytic test reactions, the catalytic conversion of 2-methylbut-3-yn-2-ol(MBOH), was recently applied for characterization of surface active sites of natural clay minerals and nonclay aluminosilicates [4, 5, 47, 48]. A distinguished feature of this method is that it allows unambiguous determination of acidic, basic, and coordinatively unsaturated (amphoteric) sites, which can be present simultaneously on the surface of the adsorbent or catalyst.

A substrate (probe) molecule of methylbutynol is converted into various reaction products depending on the type of active site (Fig. 5). Acidic sites are responsible for formation of 3-methyl-3-buten-1-yne (MBYNE) or 3-methyl-2-buten-1-al (Prenal), whereas basic sites generate acetone and acetylene [49].

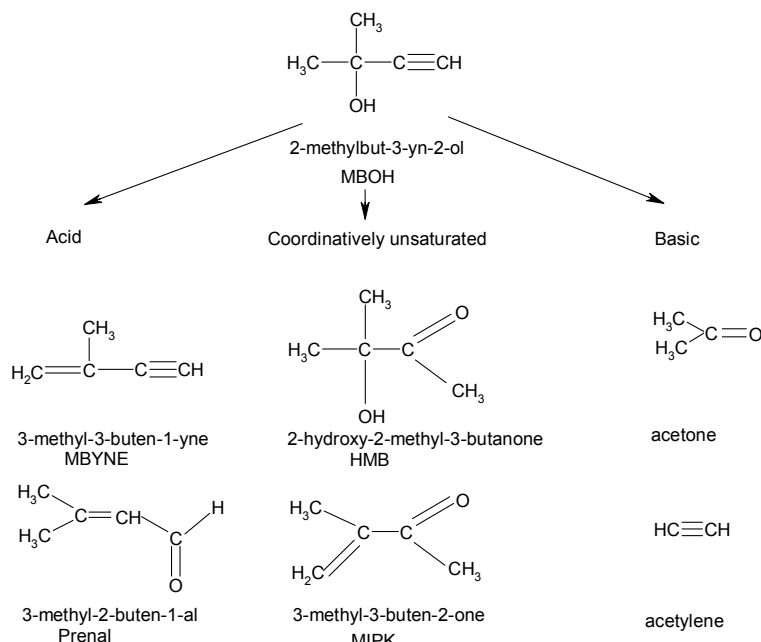


Figure 5. Scheme of methylbutynol conversion.

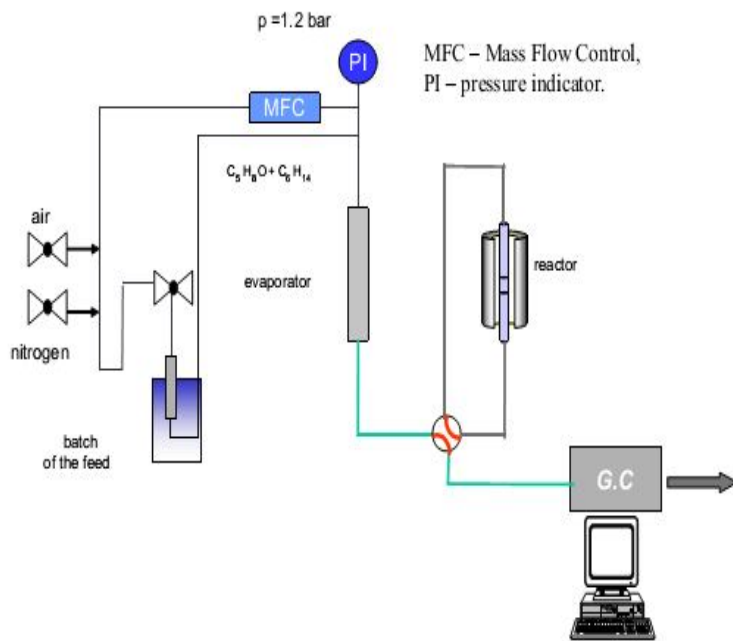


Figure 6. Experimental setup for test reaction of methylbutynol conversion [50].

The experimental setup for MBOH conversion is shown in Fig. 6. The reaction mixture of 95% of methylbutynol and 5% of toluene is fed applying static nitrogen pressure of 202.65 kPa into the evaporator and then into the reactor where 0.2 g of catalyst is placed. Prior to the reaction, the catalyst was sieved in to 215–300  $\mu\text{m}$  fraction and activated in a stream of nitrogen at 500°C during 4 h in order to remove water and  $\text{CO}_2$  from the surface. The catalytic conversion of MBOH is carried out at 120°C applying GC method for on-line product analysis.

Fig. 7 displays conversions of MBOH over natural and acid modified aluminosilicate samples discussed in Section 2.1–2.2.

The highest conversion of MBOH was observed for palygorskite-containing sample (Pal), and the lowest for hydromica (HdmCK) and a synthetic zeolite ZSM-5 ( $\text{SiO}_2/\text{Al}_2\text{O}_3 = 45$ ) used as a reference. The gradual decrease of MBOH conversion on time testifies to deactivation of the catalyst, especially in the case of HdmCK and zeolite ZSM-5, which underwent the strongest deactivation from the initial stage of reaction, apparently, due to its microporous structure and irreversible adsorption of reaction products [50].

The catalytic activity of natural aluminosilicate samples for the conversion of MBOH under applied conditions declined in the order Pal > Kaol > HdmCK, which is in accordance to their specific surface area changed as 146, 35, and 24  $\text{m}^2/\text{g}$ , correspondingly [5]. It is essential to note that proportion of clay mineral in a raw clay sample directly affects its catalytic activity in the conversion of MBOH. For instance, the conversion of MBOH over samples with content of

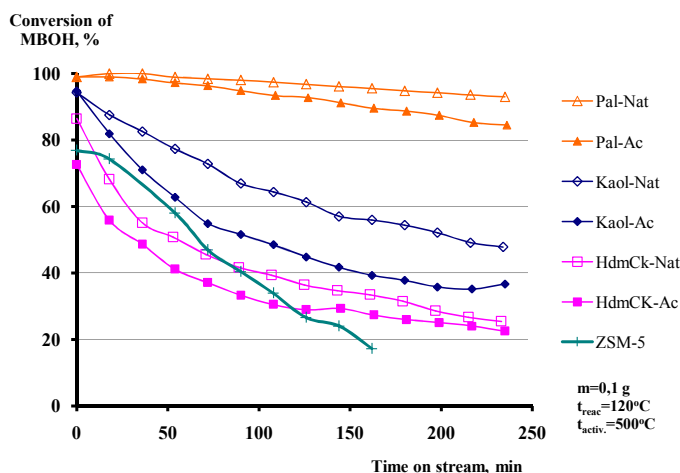


Figure 7. Conversion of MBOH over natural (Nat) and treated by  $2\text{M}\text{H}_2\text{SO}_4$  (Ac) aluminosilicate samples.

montmorillonite varied as 10%, 30%, 60%, and 80% amounted respectively to 52%, 85%, 87%, and 95% after 200 min of reaction [5]. Hereby, an increasing contribution of both acidic and basic sites into the conversion of MBOH was observed at higher proportions of the mineral in the raw sample.

After acid treatment of these aluminosilicate samples by 2M solution of  $\text{H}_2\text{SO}_4$ , the conversion of MBOH was lower than that in the case of natural minerals. This was caused by the changes of the chemical composition of aluminosilicates, considered above in Section 2.2, resulted in the dissolution of Al and Fe oxides followed by the weakening of silanol groups Si-OH polarization and reduction of a number of bridge hydroxyls Si-O(H<sup>+</sup>)-Al acting as Broensted acid sites.

To identify the types of surface-active sites, one should address to the yields of reaction products shown in Fig. 8.

The typical products of MBOH conversion over natural aluminosilicate samples were MBYNE and Prenal formed via acid pathway of the reaction as well as acetone and acetylene, confirming the presence of basic centers on the surface. Indeed, many authors [51–53] proved there is no clay having only acidic or basic properties because both types of sites are present on the surface and transforms to each other under definite conditions such as water content, pH, etc.

The ratio between the acidic and basic products differs from the type of major aluminosilicate component in the sample. Thus, yields of MBYNE and Prenal exceed yield of acetylene and acetone during the MBOH conversion over Pal, Kaol, and H-ZSM-5 (entirely acidic products). This fact shows, apparently, that the number or the strength of acid centers on the surface of given aluminosilicates exceeds the number/strength of basic centers. However, the contribution of basic centers to the general concentration of surface centers is essential. Additionally, TPD-NH<sub>3</sub> and CO<sub>2</sub> studies of acidity and basicity distribution for natural and ion-exchanged

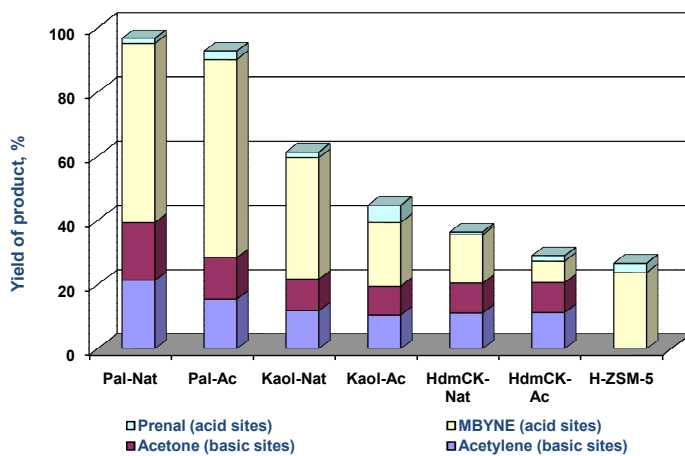


Figure 8. Yields of products formed during MBOH conversion over natural and acid-treated aluminosilicate samples.

montmorillonites revealed that acidity level is 2–3 times higher than that for basicity, regardless to the cation introduced on the clay surface [52]. Alkaline cations confer to clays low acidity and weak acid strength, in comparison with alkaline earths.

In the case of kaolinite-rich sample (Kaol), the contribution of acidic and basic sites should be comparable due to its weak natural structural acidity caused by low isomorphic substitution of low valence cations for higher valence cations mainly in the tetrahedral sheet. AIOH groups of basic character located at side edges of crystals cover about 45% of total kaolinite surface [51] resulting in its ability to adsorb both acidic and basic molecules almost equally [53]. However, the presence of montmorillonite (10%) and mica (30%), as referred to in Table 1, in the natural sample containing kaolinite explains higher yield of acidic products.

In the case of the sample containing natural hydromica (HdmCK), the yields of acid and basic products were practically identical that evidenced of comparable concentration or the strength of acid and basic sites on its surface. Natural hydromicas, as nonexpanding clay minerals, possess low Broensted acidity due to absence or very low hydration of interlayer exchangeable cations. Its catalytic activity originates from cation sites on the external basal surfaces [54] as well as from surface sites of clinoptilolite and montmorillonite present in the samples.

The origin of basic properties of natural clay minerals, for which acidic properties are more characteristic, is related to formation of Lewis basic sites during dehydroxylation process taking place at catalyst activation at 500°C. Upon heating, silanol groups Si-OH transform into siloxane one Si-O-Si, in which O<sup>-</sup> ions are able to act as Lewis bases. Other reactions, such as carbonates decomposition, take place as well, yielding MgO and CaO and providing additional basic sites.

Acid treatment of samples containing kaolinite and hydromica resulted in a reduced yield of acid products. This was mainly due to the dissolution of metal oxides, loss of cations from the

interlayer space ( $\text{Ca}^{2+}$ ,  $\text{Na}^+$ ) and from octahedral positions ( $\text{Al}^{3+}$ ,  $\text{Mg}^{2+}$ ) that provided lower polarization of structural Si-OH groups and/or water molecules in hydrated shells, and consequently weaker surface acidity. Nevertheless, the yields of basic products for MBOH conversion over Kaol-Ac and Hdm-Ac were almost not affected, indicating the same basicity of the surface before and after acid activation.

On the contrary, the higher basicity of the sample containing natural palygorskite caused by its higher content of  $\text{MgOH}$  and  $\text{AlOH}$  groups was markedly reduced after acid treatment, obviously on the same reason (dissolution of octahedral cations of  $\text{Mg}^{2+}$  and  $\text{Al}^{3+}$ ), providing higher yields of acidic products at the same time.

In the case of alkaline treatment of natural aluminosilicates, different effects were observed depending on the base used as a modifying agent. Fig. 9 illustrates yields of products for MBOH conversion over natural clinoptilolite sample (C95, 95% of clinoptilolite, 5% illite; grain size, 215–300  $\mu\text{m}$ ) treated by 2M solutions of  $\text{NaOH}$  and  $\text{NH}_4\text{OH}$ .

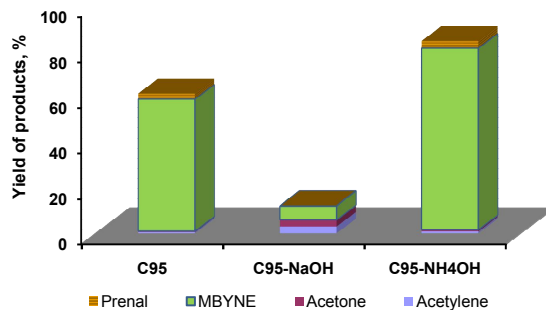


**Figure 9.** Yields of products formed during MBOH conversion over natural clinoptilolite (C95), treated by 2M  $\text{NaOH}$  (C95-NaOH) and  $\text{NH}_4\text{OH}$  (C95-NH<sub>4</sub>OH) solutions.

The treatment of clinoptilolite sample by a  $\text{NaOH}$  solution strongly inhibited the conversion of MBOH, providing higher basicity and scarce acidity of the surface. Considering variations in chemical composition and porosity [37,43] by alkaline modification, the possibility of both rising and falling specific surface area, and the low stability of Si-O-Al bond in the alkaline media, it is obvious that not only the surface-active sites but also the structure and textural properties were changed [55].

The effect of  $\text{NH}_4\text{OH}$  treatment on surface activity of clinoptilolite was completely different. The catalytic activity of C95-NH<sub>4</sub>OH for the conversion of MBOH was significantly higher as for natural one, mainly due to high surface acidity, which arises from the dissociation of  $\text{NH}_4^+$  ions by thermal effect under reaction conditions. The  $\text{NH}_4^+$  ions adsorbed during  $\text{NH}_4\text{OH}$  treatment acted as strong proton donors (Broensted acid sites) upon the reaction.

In addition to the above-considered application of the MBOH conversion method for characterization of surface-active sites of aluminosilicates, it is necessary to illustrate the ability of

this method to assess the strength of surface-active sites attracting other independent method (TPD-NH<sub>3</sub> technique) for surface acidity/basicity analysis. For the series of natural aluminosilicate samples originated from several deposits in Jordan (J) and Russia (R), it was possible to compare the acidity/basicity of the surface. The phase compositions of investigated aluminosilicate samples are given in Table 6. Experimental yields of products from MBOH conversion and surface acidity determined by TPD-NH<sub>3</sub> for various natural aluminosilicate samples are summarized in Table 7. To compare the surface activity of the investigated samples, the values of A<sub>s</sub> and B<sub>s</sub> (Table 7) were introduced as yields of products normalized by specific surface area (S<sub>BET</sub>) or by surface acidity of aluminosilicates.

Sample	Phase composition	Chemical composition (mass%)								
		SiO <sub>2</sub>	Al <sub>2</sub> O <sub>3</sub>	Fe <sub>2</sub> O <sub>3</sub>	FeO	MgO	CaO	Na <sub>2</sub> O	K <sub>2</sub> O	TiO <sub>2</sub>
Zeolite, Tell Rmah, Jordan (Zeol-J)	(Major—phillipsite, chabazite, faujasite)	42.0	12.8	12.1	-	10.1	8.5	4.0	0.8	0
Bentonite, Al-Azraq, Jordan (Bent-J)	Smectite 10%, illite, feldspar, quartz	55.7	20.1	1.5	-	3.5	2.1	0.1	2.4	2.5
White kaolinite, Al-Azraq, Jordan (W-Kaol-J)	(Minor—quartz, mica, feldspar, gypsum)	48.0	36.3	1.0	-	0.3	0.1	0.1	1.8	0
Red kaolinite, Batn el Ghoul, Jordan (R-Kaol-J)	(Minor—quartz, mica, feldspar, gypsum)	47.6	24.9	6.1	-	1.0	0.5	0.8	2.3	0.7
Diatomite, Al-Azraq, Jordan (Diat-J)	Traces of kaolinite, illite, and quartz	72.0	11.8	5.8	-	1.5	7.2	0	0	0
Palygorskite, Cherkassy, Russia (Pal-R)	Plg-R~50%, quartz, zeolite, mica, feldspar	53.2	9.8	7.7	0.6	7.9	3.6	$\frac{\text{Na}_2\text{O}+\text{K}_2\text{O}}{0.9}$		0
Kaolinite-R, Voronezh, Russia (Kaol-R)	Kaolinite ~60%, hydromica ~30%, montmorillonite ~10%	50.5	18.2	6.8	0.3	1.8	1.9	0.3	0	
Hydromica-R, Voronezh, Russia (Hdm-R)	Hydromica ~30–35%, clinoptilolite ~5%, kaolin ~5%, quartz, mica –traces	48.5	11.2	0.9	-	1.1	9.8	4.1	0	

**Table 6.** Chemical and phase composition of the aluminosilicate samples from deposits in Jordan (J) and Russia (R)

As shown in Table 7, the highest acidity per unit area was observed for kaolinite sample (Kaol-R). For the other aluminosilicate samples, the acidity of unit surface area varied in the following order: Kaol-R > Hdm-R > Bent-J = R-Kaol-J > Zeol-J = Pal-R > W-Kaol-J > H-ZSM-5 = Diat-J. This

is in agreement with the confirmed fact of an extremely high acidity of thermally treated Kaol, acidic surface of which at 0% moisture is equivalent in acidity to a solution of 90% sulfuric acid [14]. Additionally, as confirmed by Liu et al. [56], the major acidic sites on the edges of minerals particles are  $\equiv\text{Si}-\text{OH}$  and  $\equiv\text{Al}-\text{OH}_2\text{OH}$  groups, which had  $pK_a$ s of 6.9 and 5.7 for kaolinite and  $pK_a$ s of 7.0 and 8.3 for montmorillonite (Mt), respectively.

Regarding the surface sites of other clay minerals samples, Voronchak et al. [57] confirmed that 48% of surface sites of Pal were weak acid sites, whereas that for Bent was only 21%.

According to the values of  $A_m$  (Table 7), the strength of acid sites available after 116 min of the MBOH conversion was distributed among the studied samples in a following way: Kaol-R > Pal-R > Bent-J > R-Kaol-J > W-Kaol-J > Zeol-J > Diat-J > H-ZSM-5.

Catalyst	$S_{\text{BET}}$ , $\text{m}^2/\text{g}$	Acidity, $\mu\text{mol/g}$	$S_{\text{BET}}$ , $\mu\text{mol}/\text{m}^2$	Yields of reaction products, mol%				$A_s$ , mol ( $\text{m}^2/\text{g}$ )	$B_s$ , mol ( $\text{m}^2/\text{g}$ )	$R_{a/b}$ , mol/m	$A_m$ , mol (mmol/g)				
				Acid sites ( $Y_{a.s.}$ )		Basic sites ( $Y_{b.s.}$ )									
				MBYNE	Prenal	Acetone	Acetylene								
Zeol-J	96 [43]	130.0 [43]	1.3	42.5	1.1	6.5	5.9	0.4	0.1	6.7	336				
Bent-J	70 [43]	59.4 [43]	0.8	33.9	0.0	15.2	5.6	0.5	0.2	2.2	571				
R-Kaol-J	45 [43]	56.9 [43]	1.3	17.9	5.2	4.5	4.2	0.5	0.1	5.1	407				
W-Kaol-J	41 [43]	14.1 [43]	0.3	10.0	0.0	11.2	1.1	0.2	0.3	0.9	346				
Diat-J	39 [43]	29.0 [43]	0.7	1.4	1.2	4.5	4.4	0.1	0.1	0.6	186				
Pal-R	146 [27]	73.0	0.5	55.8	1.6	18.0	21.3	0.4	0.1	3.2	786				
Kaol-R	27 [27]	48.0	1.8	37.9	1.7	9.9	11.8	1.5	0.4	4.0	825				
Hdm-R	24 [27]	-	-	15.1	0.8	9.4	11.1	0.7	0.4	1.9	-				
H-ZSM-5 (t.o.s.= 116 min)	370 [27]	240.0	0.6	23.8	2.8	0.0	0.0	0.1	-	-	111				
H-ZSM-5 (t.o.s.= 17 min)				73.1	0.0	0.0	0.0	0.2	-	-	304				

$A_s$ —yield of products formed on acid sites normalized to  $S_{\text{BET}}$ , mol%/ $(\text{m}^2/\text{g})$ ;  $B_s$ —yield of products formed on basic sites normalized to  $S_{\text{BET}}$ , mol%/ $(\text{m}^2/\text{g})$ ;  $R_{a/b}$  =  $A_s/B_s$  mol/mol;  $A_m$ —yield of products formed on acidic sites normalized to surface acidity,  $A_m = Y_{a.s.}/C_{a.s.}$ , mol%/ $(\text{mmol/g})$ ;  $C_{a.s.}$ —surface acidity (TPD-NH<sub>3</sub>), mmol/g; t.o.s.—time on stream.

**Table 7.** Yields of reaction products in MBOH conversion over natural aluminosilicates (t.o.s. = 116 min)

The evidence of a strong and fast deactivation of H-ZSM-5 follows from its values of  $A_m$  at early (17 min) and late (116 min) stages of reaction (Table 7). At the same time, it is obvious that the strength of active sites for natural Zeol and H-ZSM-5 is comparable, while the latter undergoes significant deactivation due to its microporous structure.

The values of  $B_s$ , characterizing the basicity of unit surface area of aluminosilicate samples, changed in the following order: Kaol-R > Hdm-R > W-Kaol-J > Bent-J > Pal-R > Zeol-J > Diat-J. It follows that for Kaol-R and Hdm-R samples, the higher basicity of unit area of surface is typical despite the high values of surface acidity  $A_s$ . As shown Alsawalha et al. [50], the energy of activation for the basic pathway was slightly higher than that for the acidic one ( $E_A = 79.4 \text{ kJ/mol}$  and  $E_A = 45.8 \text{ kJ/mol}$ , respectively) as calculated for the conversion of MBOH on silica-alumina and hydrotalcite. The reaction mechanism considered in detail by the same authors indicated that SiOH groups were the acidic centers and oxygen anions O<sup>-</sup> were the basic centers on the surface of the catalyst. As expected from the structure of zeolite H-ZSM-5 and from its high value of  $\text{SiO}_2/\text{Al}_2\text{O}_3$  ratio, equal to 45, only products of the acidic pathway were formed. In the case of clay minerals, the Broensted acid sites are mainly represented by the water molecules polarized by interlayer cations during an activation procedure.

The lowest conversion and product yields were observed for Diat-J, probably due to its low acidity [47] as a result of partial condensation of surface silanols to siloxane groups during the thermal treatment [58].

Thus, it was proved by the MBOH conversion method that surface of natural aluminosilicate samples comprise both acidic and basic sites, which can be responsible for the catalytic or adsorption ability of the material surface. The application of acid or alkaline modification changes not only the structure but also the texture and surface sites activity and a ratio between various active sites. Surprisingly, the highest surface acidity of kaolinite-containing samples was proved by several methods, although this mineral has the lowest isomorphic substitution and cation-exchange ability.

In the next paragraph, the adsorption ability of natural aluminosilicate samples is considered, which developed in aqueous solutions of various substances considered as industrial toxicants.

## 4. Adsorption of industrial pollutants by natural and modified aluminosilicates

### 4.1. Natural and acid/base-treated clay minerals and zeolite as adsorbents of formaldehyde from aqueous solutions

Formaldehyde is an organic substance (the simplest aliphatic aldehyde), a colorless gas with a pungent odor, soluble in water, alcohols, and polar solvents. It causes a negative impact on the genetic material, reproductive organs, respiratory tract, eyes, and skin, as well as seriously affects the central nervous system and has been considered and officially proved as a potentially carcinogenic to humans and living organisms by the Hygienic Standards of Russian Ministry of Health and the International Agency for Research on Cancer. However, for the last decades, such materials and goods as resins, plastics, paints, textiles, disinfectants, and preservatives were manufactured using formaldehyde and its derivatives. Among them are urea-formaldehyde resins frequently used as a base for adhesives and gluing mixtures for manufacturing of the furniture, lacquers, building paints, gluing materials, composites, etc.

By the production of urea-formaldehyde resins (UFR), polycondensation reaction between urea and formaldehyde is not usually brought to the end in order to get the resin in liquid form and vary the structure of the polymer resin. As a result, there is always free formaldehyde in the end-product of UFR synthesis, which is released into the atmosphere of the working zone during synthesis, preparation of gluing composition, gluing and drying of wood products (cheap boards, furniture, etc.), and washing of the gluing equipment, while exploiting the new furniture itself.

The amount of formaldehyde in wastewater coming from washing of gluing equipment may reach 500 mg/L [3, 16], which is 10 times higher than the concentration of formaldehyde in wastewater taken for treatment and 10,000 times higher than the MPC of water ( $0.05 \text{ mg/dm}^3$ ). To eliminate formaldehyde pollution, modern water treatment technologies combine various physical-chemical methods, among which adsorption is the major one and the development of effective, low cost, recyclable, and environmentally benign adsorbent is of current interest.

Natural clay minerals and zeolites revealed high adsorption capability toward formaldehyde both from aqueous and from gaseous phases [3], which can be further increased by applying acid treatment or physical (thermal, electromagnetic field exposure) activation. The activation effect of mineral acids (Fig. 10) on adsorption capacity toward formaldehyde of natural bentonite samples decreased in the order  $\text{H}_2\text{SO}_4 > \text{HCl} > \text{HNO}_3 > \text{H}_3\text{PO}_4$ , which did not fully matched the change of mineral acid dissociation constants.

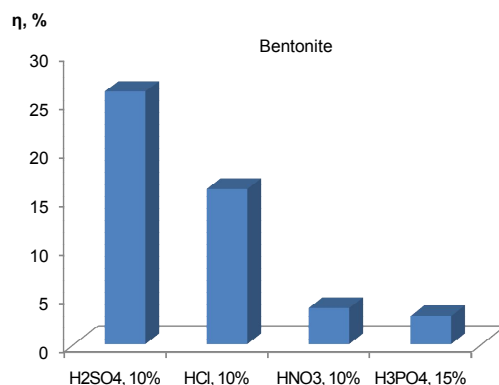


**Figure 10.** The rate of purification of model wastewater containing formaldehyde by acid-treated bentonite (deposit from Voronezh area, Russia).

As shown in Fig. 10, hydrochloric acid, as a stronger electrolyte compared with  $\text{H}_2\text{SO}_4$ , caused lower activating effect on bentonite adsorption capacity. However, one should consider the more severe structural and surface changes caused by HCl and expect, therefore, the shorter times needed to enhance the surface and adsorption characteristic of minerals.

In the case of clinoptilolite-rich sample containing C95 (95% of clinoptilolite), the activating effect observed for various mineral acids and bases was in a strict compliance with their

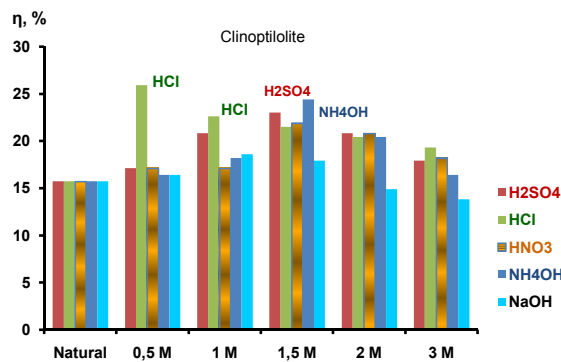


**Figure 11.** The rate of purification of model wastewater containing formaldehyde by clinoptilolite C95 (95% of clinoptilolite, Slovak deposit) treated by varied concentrations of mineral acids and bases.

strength determined by the dissociation constants (Fig. 11). The adsorption capacity of clinoptilolite activated by mineral acids decreased in the order  $\text{HCl} > \text{H}_2\text{SO}_4 > \text{HNO}_3$  [29], which is the order for the decrease of their  $K_d$  values. Moreover, the weaker the acid, the higher the concentration necessary to activate the sample and reach the same adsorption capacity as for the sample treated by a stronger mineral acid. The activation effect of acids observes a maximum, when at lower and moderate concentrations there is a rise of surface characteristics (specific surface area, porosity, and adsorption capacity) and then, at higher concentrations, a decline due to severe destruction of the mineral structure.

Adsorption isotherms of formaldehyde from aqueous solutions by natural and acid-treated samples containing kaolinite, hydromica, and palygorskite are shown in Fig. 12.

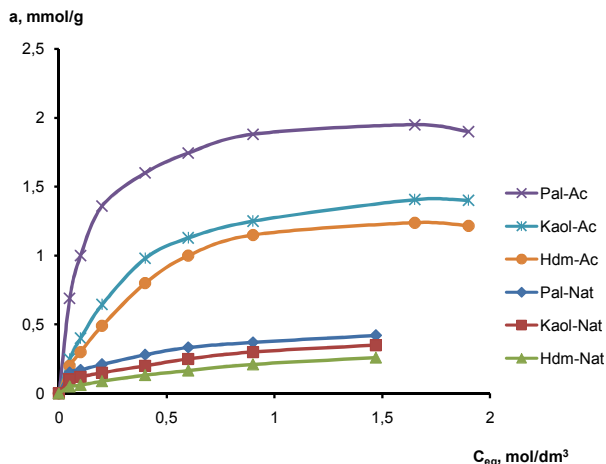


**Figure 12.** Isotherms of formaldehyde adsorption from aqueous solutions by natural (Nat) and acid-treated (Ac) aluminosilicate samples rich in palygorskite (Pal); kaolinite (Kaol), and hydromica (Hdm).

The obtained adsorption isotherms have a convex shape, which is similar to isotherms of the Langmuir's type. The isotherms for acid-treated samples lie much higher than that for natural ones, specifying the activation effect of acid. The highest adsorption ability was observed for Pal, and the lowest for Hdm, obviously, due to the changes of their specific surface area and porosity considered earlier (Table 3).

The adsorption parameters (Table 8) obtained from the isotherms were satisfactorily described applying the Langmuir equation (Eq. 9):

$$a = a_{\max} \frac{K_{ads} \cdot C_{eq}}{1 + K_{ads} \cdot C_{eq}} \quad (9)$$

$$\text{or } \frac{1}{a} = \frac{1}{a_{\max}} + \frac{1}{a_{\max} \cdot K_{ads} \cdot C_{eq}},$$

where  $a$  is the adsorption ability of a sorbent, mmol/g;  $a_{\max}$  is the maximal adsorption ability of a sorbent, mmol/g;  $K_{ads}$  is the constant of adsorption equilibrium; and  $C_{eq}$  is the equilibrium concentration of a substance in solution, mol/dm<sup>3</sup>.

Sample	$a_{\max}$ , mmol/g		$\frac{a_{\max}(Ac)}{a_{\max}(Nat)}$	$K_{ads}$		$\frac{K_{ads}(Ac)}{K_{ads}(Nat)}$	$R^2$	$-\Delta G_{293K}$ , kJ/mol	
	Nat	Ac		Nat	Ac			Nat	Ac
Pal	0.67	2.36	3.5	3.60	11.70	3.25	0.999 0.961	2.94	5.98
Kaol	0.37	1.60	4.3	2.20	5.90	2.70	0.998 0.986	1.92	4.32
Hdm	0.39	1.10	2.8	1.70	7.40	4.35	0.987 0.913	1.29	4.87

$R^2$ —correlation coefficient; numerator—natural; denominator—activated by H<sub>2</sub>SO<sub>4</sub>.

**Table 8.** Adsorption characteristics of natural (Nat) and modified by 2M H<sub>2</sub>SO<sub>4</sub> (Ac) clay minerals samples

The equilibrium parameters ( $a_{\max}$  and  $K_{ads}$ ) were maximal for both natural and activated Pal sample, owing to its well-developed surface, porosity, and high activity of surface sites. Acid treatment enhanced the adsorption capacity of aluminosilicates more than 3 times (Table 8), having the most significant effect on Kaol sample, containing kaolinite, illite, and montmorillonite (Table 2). Apparently, this was the feature of the layered structure of the Kaol components, which was less stable against acid attack, unlike that for Pal and Hdm.

The adsorption equilibrium constants ( $K_{ads}$ ) were also maximal for Pal, changing in the order Pal > Kaol > Hdm for adsorption on natural samples and as Pal > Hdm > Kaol for adsorption on acid-activated samples. Evidently, the acid activation caused not only the surface area and porosity variations but also the type and/or the strength of active sites. As a result, the highest

value of  $\frac{K_{\text{ads}}(\text{Ac})}{K_{\text{ads}}(\text{Nat})}$  found for Hdm sample (4.35) indicated the strongest shift of the adsorption equilibrium toward adsorption products due to more significant changes in the surface sites activity. The ratio of Gibbs free energy,  $\Delta G$  (thermodynamic potential), calculated as  $\Delta G = -R T \ln K_{\text{ads}}$ , was the highest for Pal samples as well. However, the ratio of  $\Delta G$  before and after acid treatment was the highest for Hdm, which means that the higher energy gain was obtained due to increased activity of surface sites of Hdm. To explain this fact, the adsorption parameters from Table 8 were normalized per unit of surface area of the samples (Table 9).

Sample	$a'_{\max}$ mmol/m <sup>2</sup>		$\frac{a'_{\max}(\text{Ac})}{a'_{\max}(\text{Nat})}$	$-\Delta G'_{293K}$ kJ/mol/m <sup>2</sup>	
	Nat	Ac		Nat	Ac
Pal	0.0045	0.009	2.0	0.02	0.022
Kaol	0.013	0.025	1.9	0.071	0.067
Hdm	0.0162	0.035	2.1	0.053	0.157

**Table 9.** Adsorption parameters of aluminosilicate samples normalized per unit area

As shown in Table 9, there is an inverted order of adsorption capacity for investigated aluminosilicate samples: Hdm > Kaol > Pal. The maximal adsorption occurs on the unit surface of Hdm sample, while the minimum one occurs on the unit surface of Pal. Apparently, it points at the higher number and/or the stronger active sites on the surface of Hdm sample, and the weaker one or in a fewer amount on the surface of Pal.

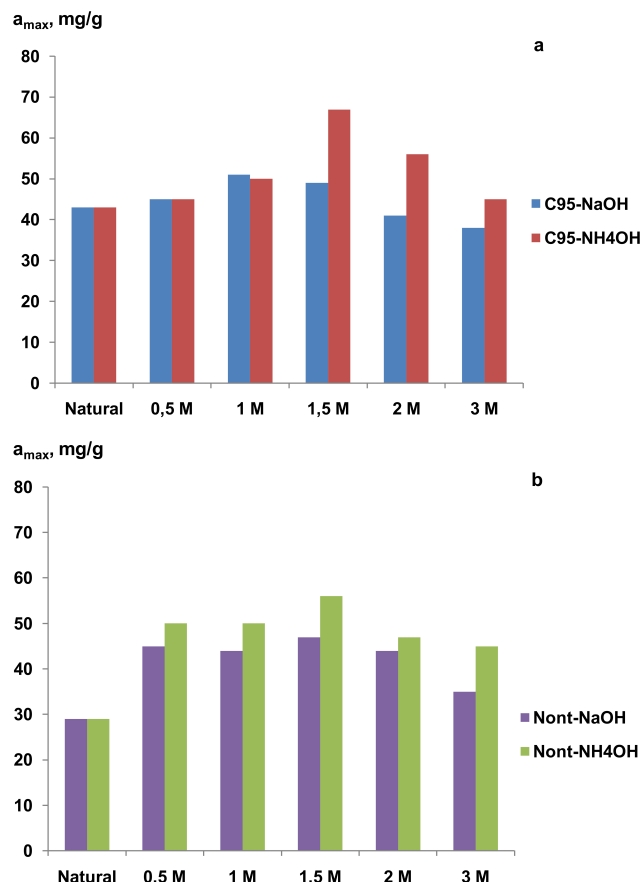
According to the ratio of  $a'_{\max}$  before and after acid treatment, this type of activation almost equally influenced the surface properties of investigated aluminosilicates and caused a twofold increase in their adsorption capacity.

Higher values of Gibbs free energy for adsorption per unit area were obtained for Hdm, and the lowest values were for Pal. Therefore, one may assume the stronger adsorption interaction on Hdm surface than on other minerals that is apparently related to the strength of the adsorption sites and in good agreement with MBOH characterization data considered in Section 3.

The effect of alkaline activation of the adsorption capacity of natural aluminosilicates was weaker in the case of NaOH solutions compared with NH<sub>4</sub>OH (Fig. 13a and b) or mineral acids solutions (Fig. 12).

As confirmed in Fig. 13 for natural samples rich in clinoptilolite (C95, 95%) and nontronite (Nont; 58% nontronite, 7% kaolinite, 15% illite, and 20% quartz), treatment by NaOH (6 h, 100°C) brought up to 15% and 38% gain in adsorption capacity, respectively, while acid treatment gave 32–65% excess in formaldehyde adsorption for C95 and more than twofold excess for Nont treated by 2M H<sub>2</sub>SO<sub>4</sub>.

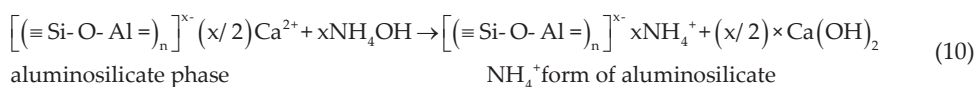
The use of NH<sub>4</sub>OH solutions as activation agent was more effective than NaOH, providing 35–50% rise in formaldehyde adsorption by C95 and Nont samples. Moreover, the effect of

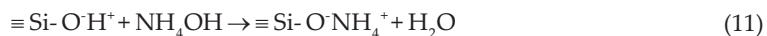


**Figure 13.** Adsorption capacity of samples containing natural clinoptilolite (C95,(13a)) and nontronite (Nont, (13b)), modified by varied bases ( $\text{NaOH}$ ,  $\text{NH}_4\text{OH}$ ) concentrations, determined in aqueous solutions of formaldehyde.

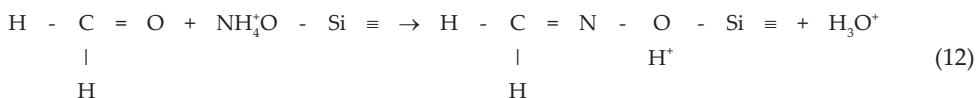
$\text{NH}_4\text{OH}$  treatment was comparable to that for mineral acids or even higher than the treatment with 2–3M  $\text{H}_2\text{SO}_4$ ,  $\text{HCl}$ , and  $\text{HNO}_3$ .

The treatment of aluminosilicates with  $\text{NH}_4\text{OH}$  solution comprises the occurrence of ion-exchange reactions (Eqs. (7) and (8)) considered above for the case of  $\text{NaOH}$  treatment:





Also, there is a possible adsorption of  $\text{NH}_4\text{OH}$  molecules due to H-bonding to the surface polar groups. The consequences of such enrichment of the silicate surface with ammonia ions is a possibility of chemisorptions of formaldehyde molecules due to their interaction with  $\text{NH}_4^+$  ions resulting in formation of imine



The occurrence of this reaction was observed and confirmed for the amine-functionalized mesoporous silica [59]. Thus, reaction (12) concerns one of the possible mechanisms of formaldehyde adsorption, which is likely to occur via surface functional amine groups.

Nevertheless, the surface of acid and alkali-treated aluminosilicate samples supposes another adsorption mechanism, comprising the most likely allocation of the formaldehyde molecules (associates) on the adsorbent surface. The FTIR spectroscopy applied to elucidate the mechanism of adsorption from the aqueous phase met some obstacles. Under the competitive adsorption of water molecules on the highly hydrophilic and hydroxylated surface of aluminosilicate, the main changes observed are the intensities of the absorption bands of the hydroxyl groups of water, whereas the absorption bands of carbonyl group C = O are superimposed on the oscillations of OH group and was hard to determine unambiguously the presence of formaldehyde in the spectra. In this regard, the following adsorption mechanism for formaldehyde molecules was suggested (Fig. 14). The molecules of formaldehyde, which exist in the form of hydrates ( $\text{HO-CH}_2\text{-OH}$ ) in aqueous solutions, are bound to the surface, mainly via hydrogen bonding. Various active sites, e.g., Broensted ( $\text{Si-OH}$ ,  $\text{Si-O}(\text{H}^+)$ -Al,  $\text{AlO}\text{H}_2^+$ ) and Lewis (exchangeable and structural cations, oxygen anions of the lattice) sites, are expected to contribute to H-bonding of formaldehyde.

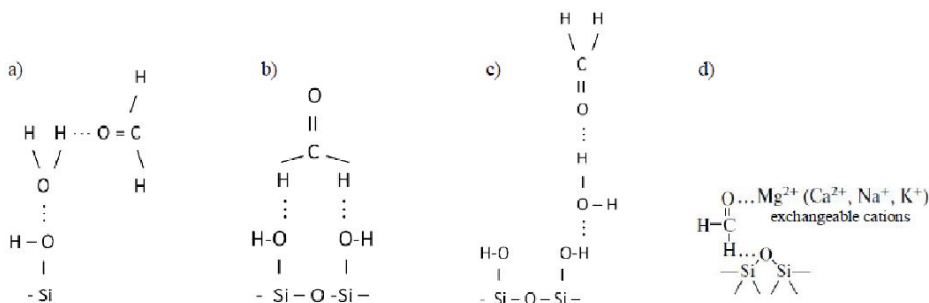


**Figure 14.** Adsorption of formaldehyde on the surface of aluminosilicates [3, 29].

Additionally, it is necessary to take into account that formaldehyde molecules are highly reactive; they easily oxidize and polymerize, undergoing hydrolysis in an acidic media to the starting monomer formaldehyde, whereas in alkaline media, the reaction of Kannitsarro may take place.

Thereby, the above-mentioned behavior of the aluminosilicate samples allows one to conclude that, depending on the structure of clay minerals or a zeolite presenting in the investigated natural samples, the adsorption of formaldehyde may occur (i) on the surface and in the interlayer space of layered aluminosilicates (montmorillonite and other clay minerals), (ii) on the lateral facets of clay mineral crystals, (iii) inside and outside of zeolite channels of clinoptilolite, and (iv) in the transport channels of palygorskite.

#### 4.2. Base-treated natural aluminosilicate as adsorbents of acetic acid from aqueous solutions

Acetic acid along with formic and other organic acids comes into the wastewater of wood-working industry on the stages of the hot steam treatment of wood before the production of plywood and fiber boards. Cellulose and hemicelluloses undergo hydrolysis yielding these acids and other organic substances, which are released then into the atmosphere and get into wastewater amounting up to 3000 mg/L for acetic and up to 500 mg/L for formic acids. Anaerobic wastewater treatment allows reducing organic acid content to 100 mg/dm<sup>3</sup>, whereas the maximal permissible concentration (MPC) for acetic acid in water is 0.01 mg/dm<sup>3</sup>.

The adsorption of acetic acid on acid-treated clay minerals do not occur [60], whereas natural and alkali-activated clay minerals proved adsorption ability toward acetic acid.

The isotherms of the adsorption of acetic acid by natural and alkali (2M NaOH)-treated sample of montmorillonite M95 (95% of montmorillonite) had typical form of the Langmuir type isotherms, indicating at monolayer adsorption within the chosen concentration interval (0.1–2.0 mol/dm<sup>3</sup>). The equilibrium parameters of adsorption assessed applying Langmuir equation are given in Table 10.

Adsorbent	$a_{\max}$ , mmol/g	$K_{\text{ads}}$	$R^2$	$-\Delta G$ , kJ/mol
Mont-Nat	2.1	3.0	0.989	12.5
Mont-Alk	2.9	6.5	0.999	14.3

Table 10. Adsorption parameters of natural and alkali-treated montmorillonite M95

Alkaline treatment increased the maximal adsorption capacity of montmorillonite in 1.4 times, obviously, due to additional hydroxylation of the aluminosilicate surface, which contributed to a higher adsorption of acetic acid molecules. The increase in adsorption equilibrium constant,  $K_{\text{ads}}$ , and the change of thermodynamic potential testify to a higher thermodynamic probability and a higher energy gain for the adsorption process on alkali-treated clay mineral.

The FTIR spectra of natural and alkali-activated montmorillonite (Fig. 15) allowed the elucidation of the mechanism of the adsorption of acetic acid.

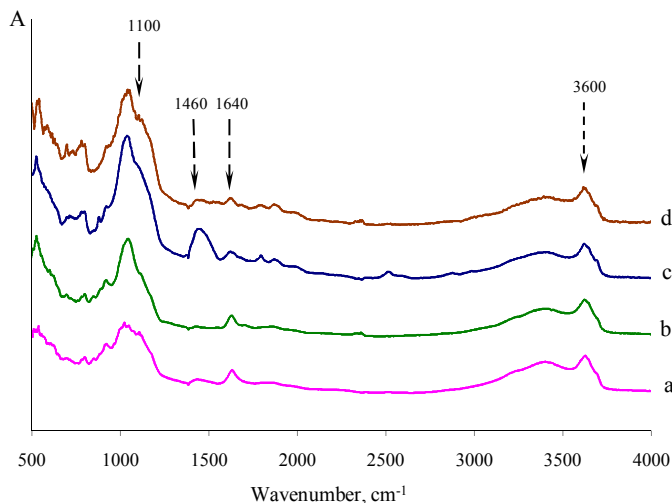


**Figure 15.** FTIR spectra of montmorillonite (M95) before and after the adsorption of acetic acid: (a) natural montmorillonite (MM), (b) natural MM after the adsorption of acetic acid, (c) alkali-treated MM, and (d) alkali-treated MM after the adsorption of acetic acid.

As shown in Fig. 15, all the spectra comprise the bands of the aluminosilicate lattice, i.e., Si-O (1050 cm<sup>-1</sup>), Si-O-Si (804 cm<sup>-1</sup>), O-Si-O (540 cm<sup>-1</sup>), and Si-O-Al (1100 cm<sup>-1</sup>) [61, 62]. Under alkaline exposure, there was partial change of montmorillonite structure evidenced by the broadening of the 1050–1110 cm<sup>-1</sup> band in spectra c and d (Fig. 15). This has likely facilitated the access of hydroxyls to lattice Mg<sup>2+</sup> and Al<sup>3+</sup> ions and resulted, therefore, in a significant absorption at 1460 cm<sup>-1</sup> (overtones of Mg-OH and Al-OH groups [62]). The band about 1640 cm<sup>-1</sup> was caused by adsorbed water molecules and practically did not change the intensity. Also, the stretching vibrations of OH groups (3600 cm<sup>-1</sup>) as well as a band at 3400 cm<sup>-1</sup> due to hydroxyls of interlayer water did not change from samples to sample.

After the adsorption of acetic acid, the FTIR spectra observed no bands corresponding to neutral or ionized carboxylic group as well as bands of methyl group of acetic acid. However, the absorption band at 1460 cm<sup>-1</sup> was found to substantially reduce its intensity for the case of alkali-activated montmorillonite and almost completely disappeared from the spectrum of natural sample. This fact allows one to conclude that hydroxyl groups of Al-OH and Mg-OH were involved in the binding of acetic acid. Adsorptive interaction may be due to the hydrogen bonding between the hydroxyl groups of montmorillonite (=SiOH,-MgOH,-AlOH) and the carboxyl group of acetic acid. The mechanism of acetic acid adsorption on the surface of montmorillonite shown in Fig. 16 was proposed after Tanaka et al. [61], who confirmed it for the adsorption of acetic acid on hydroxyapatite.

Furthermore, the reaction of neutralization is possible between hydroxyl groups of montmorillonite and molecules of acetic acid.

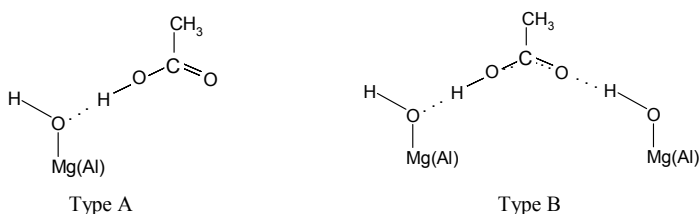


**Figure 16.** Mechanism of the adsorption of acetic acid [61].

Thus, the above-mentioned examples of alkaline and ammonium hydroxide activation illustrated that depending on the nature of the activating agent and the chemical nature of the adsorbate, the adsorption phenomenon may occur via various interactions, e.g., hydrogen bonding, chemical reaction (chemisorption), and/or ion-exchange.

#### 4.3. Contribution of ion-exchange reactions to the adsorption of ammonia ions

In solutions of electrolytes, the substances that dissociate into ions by dissolution, ion-exchange processes significantly contribute to the adsorption process if the adsorbent exhibits ion-exchange ability. This is illustrated hereinafter, on the features of ammonium ions adsorption, which is a major toxicant of industrial, domestic, and agricultural wastewater. For the treatment of wastewater from ammonium ions, adsorbents on the base of natural and synthetic zeolites as well as other aluminosilicates are frequently used.

The main mechanism for  $\text{NH}_4^+$  sorption by zeolites is ion-exchange. Extra framework cations  $\text{K}^+$ ,  $\text{Na}^+$ ,  $\text{Ca}^{2+}$ , and  $\text{Mg}^{2+}$ , balancing the negative charge of the framework, are being replaced stoichiometrically for  $\text{NH}_4^+$  ions [64–66] in the order of selectivities for clinoptilolite  $\text{K}^+ > \text{NH}_4^+ > \text{Na}^+ > \text{Ca}^{2+}, \text{Mg}^{2+}$  [64]. The  $\text{NH}_4^+$  sorption capacities of zeolites vary about 6.8–7.2 mmol/g.

Similarly, the ion-exchange sorption of  $\text{NH}_4^+$  ions from aqueous solutions occurs on natural clays [67–69]. Both exchangeable cations and pH-influenced hydrolyzed Si-OH or AlOH groups from the edges of clay particles contribute to cation-exchange for  $\text{NH}_4^+$  ions, mainly in dilute solutions. The CEC of natural clays for  $\text{NH}_4^+$  is lower compared with zeolites, varying within 1–2 mmol/g. The  $\text{Na}^+$  form of natural clays enhances the adsorption of  $\text{NH}_4^+$  ions, the process of which obeys Langmuir-type adsorption. At high  $\text{NH}_4^+$  content, the retaining capacity of natural adsorbent materials decreases, providing contribution of the nonion-exchange sorption of  $\text{NH}_4^+$  ions.

In more detail, the contribution of ion-exchange reactions as major processes related to ammonium ions adsorption as well as the effect of acid/alkaline modification were studied for the mixed natural silica-alumina sorbent  $\text{M}_{45}\text{C}_{20}$  (45% of montmorillonite and 20% clinoptilolite) [63]. The isotherms of  $\text{NH}_4^+$  ions adsorption were obtained for natural and activated

$M_{45}C_{20}$  sorbent from 0.0025 to 0.2 M solutions of  $NH_4Cl$  at 295 K with an equilibration time of 3 h (Fig. 17).

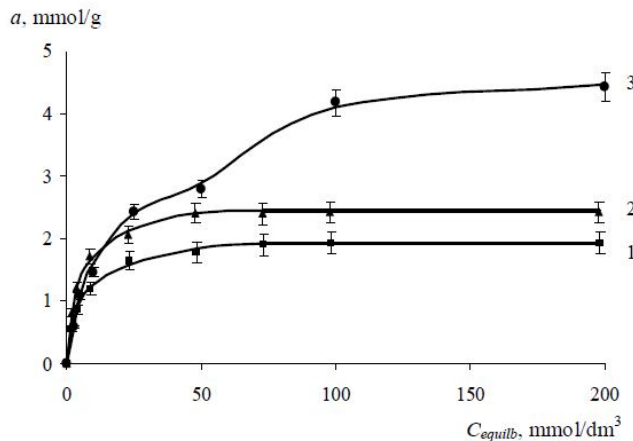


Figure 17. Isotherms of  $NH_4^+$  ions sorption on natural (1), acid-treated (2), and alkali-treated (3)  $M_{45}C_{20}$  sorbent.

The obtained isotherms have a convex shape with a saturation region that was satisfactorily described by the Langmuir equation. The adsorption capacity ( $a_{max}$ , mmol/g) of natural and activated  $M_{45}C_{20}$  sorbent increased in the order MCN (1.9) < MCAC (2.4) < MCAlk (4.1) observing the highest value for alkali-activated sample.

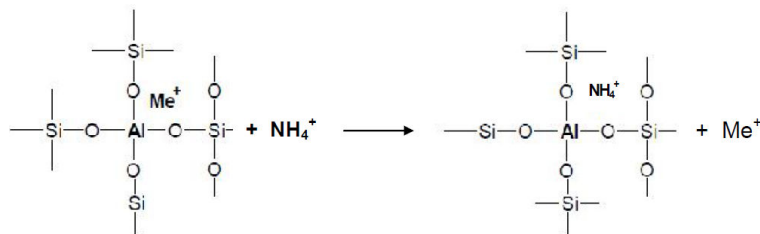
The quantities of exchangeable cations of  $Na^+$ ,  $K^+$ ,  $Ca^{2+}$ , and  $Mg^{2+}$  displaced by  $NH_4^+$  ions during sorption process are summarized in Table 11.

$C_{eq}(NH_4^+)$ , mmol/dm <sup>3</sup>	Quantity of desorbed cations, mmol/g				$\sum Na^+, K^+, Ca^{2+}, Mg^{2+}$ , mmol/g	$a_{NH_4^+}$ , mmol/g	CEC, <sup>a</sup> mmol/g	CEC/ $a_{NH_4^+}$
	$Na^+$	$K^+$	$Ca^{2+}$	$Mg^{2+}$				
1.950	0.085	0.020	0.370	0.092	0.567	0.550	1.029	1.9
4.143	0.115	0.025	0.481	0.208	0.829	0.857	1.518	1.8
8.806	0.134	0.029	0.741	0.301	1.207	1.194	2.249	1.9
23.363	0.154	0.035	0.952	0.395	1.536	1.637	2.883	1.8
48.228	0.160	0.039	1.105	0.453	1.757	1.772	3.315	1.9
73.108	0.170	0.041	1.180	0.509	1.901	1.892	3.590	1.9
98.076	0.170	0.041	1.180	0.509	1.901	1.924	3.590	1.9

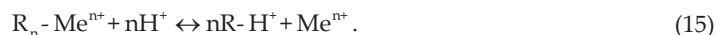
<sup>a</sup>CEC assessed as total amount of exchangeable 1<sup>+</sup> cations considering equivalent exchange of bi- and monocharged cations.

Table 11. Quantity of exchangeable cations desorbed from natural  $M_{45}C_{20}$  (MCN) sorbent by sorption of  $NH_4^+$  ions (changed after Belchinskaya et al. [63])

It is seen from Table 11 that the total number of displaced exchangeable cations was almost equal to the amount of absorbed  $\text{NH}_4^+$  ions on natural sorbent in the whole range of external solution concentration. This fact testifies to cation-exchange reactions (Scheme 4) (and (Eq. 13)) taking place between the  $\text{NH}_4^+$  ions in aqueous solution and exchangeable cations ( $\text{Me}^{n+} = \text{Ca}^{2+}, \text{Mg}^{2+}, \text{Na}^+, \text{K}^+$ ;  $R_n$  is the framework of a silicate with a charge “n.”) in the sorbent phase. Moreover, the hydrolysis reaction (Eq. (14)) of  $\text{NH}_4\text{Cl}$  in aqueous solution should be considered, resulting in a significant contribution of protons to cation-exchange reactions (Eq. (15)).



**Scheme 4.** Cation-exchange reaction between  $\text{NH}_4^+$ -ions in solution and exchangeable cations in sorbent phases



The intensity of  $\text{NH}_4^+$  ions exchange for cations decreased in the order  $\text{Ca}^{2+} > \text{Mg}^{2+} > \text{Na}^+ > \text{K}^+$ , which was mainly determined by the chemical content of respective metal oxide except for  $\text{K}^+$  ions. However, despite the higher  $\text{K}_2\text{O}$  content in the mineral phase, the exchange of  $\text{K}^+$  for  $\text{NH}_4^+/\text{H}^+$  was weaker compared with  $\text{Na}^+$ , although it had lower amount of  $\text{Na}_2\text{O}$ .

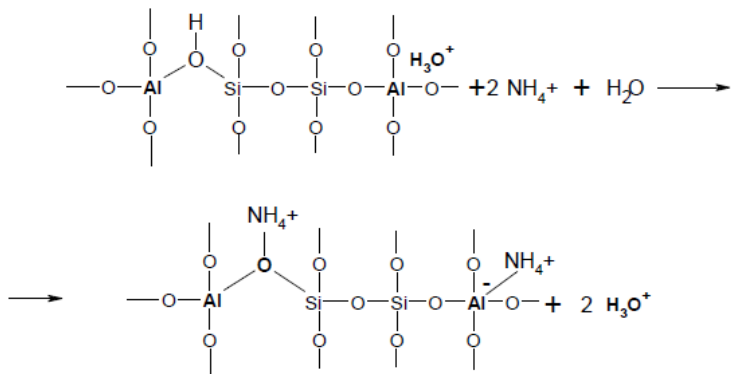
Taking into account the equivalent ion-exchange between 2+ and 1+ ions, the values of sorbent CEC available for  $\text{NH}_4^+$  capturing confirmed the significant contribution of protons ion-exchange (Eq. (15)) to the adsorption of  $\text{NH}_4^+$  ions by natural  $\text{M}_{45}\text{C}_{20}$  sorbent. As a consequence, the ratio of CEC/ $a_{\text{NH}_4^+}$  (Table 11) was twice as amount of ammonia adsorbed.

As shown in Table 12, the amount of  $\text{NH}_4^+$  ions adsorbed by acid-activated samples MCAC exceeds about twice the total amount of desorbed cations  $\text{Na}^+, \text{K}^+, \text{Ca}^{2+}$ , and  $\text{Mg}^{2+}$ . This is explained by the transition of natural sorbent into  $\text{H}^+$  form by the acid treatment. As a result, the composition of the cation-exchange complex of MCAC to a greater extent was determined by the exchanged protons (or hydronium ions  $\text{H}_3\text{O}^+$ ), which has a quantity of ~0.79 mmol/g, as estimated from a difference in the amount of desorbed cations from MCN and MCAC samples during the  $\text{NH}_4^+$  adsorption.

$C_{eq}(\text{NH}_4^+)$ , mmol/dm <sup>3</sup>	Quantity of desorbed cations, mmol/g				$\sum \text{Na}^+, \text{K}^+,$ $\text{Ca}^{2+}, \text{Mg}^{2+}$ , mmol/g	$a_{\text{NH}_4^+}$ , mmol/g	CEC, mmol/g	CEC/ $a_{\text{NH}_4^+}$
	Na <sup>+</sup>	K <sup>+</sup>	Ca <sup>2+</sup>	Mg <sup>2+</sup>				
1.695	0.029	0.013	0.504	0.036	0.581	0.805	1.121	1.4
3.787	0.040	0.015	0.677	0.058	0.790	1.213	1.525	1.2
8.288	0.048	0.017	0.909	0.071	1.046	1.712	2.186	1.3
22.951	0.053	0.017	0.949	0.093	1.112	2.049	2.578	1.2
47.607	0.053	0.019	0.949	0.093	1.113	2.393	2.800	1.2
72.592	0.053	0.019	0.949	0.093	1.113	2.408	2.944	1.2
97.589	0.053	0.019	0.949	0.093	1.113	2.411	2.944	1.2

**Table 12.** Quantity of exchangeable cations desorbed from acidly treated  $\text{M}_{45}\text{C}_{20}$  (MCAC) sorbent by sorption of  $\text{NH}_4^+$  ions (changed after Belchinskaya et al. [63])

Therefore, the main ion-exchange reactions that took place were (i) ion-exchange of  $\text{NH}_4^+$  for exchangeable cations including  $\text{Ca}^{2+}$  и  $\text{Mg}^{2+}$  according to Eqs. (13) and (15), (ii) ion-exchange of  $\text{NH}_4^+$  for exchangeable protons, and (iii) exchange between  $\text{NH}_4^+$  and hydronium ions as well as protons of Si-OH groups located close to three-coordinated aluminum atoms, formed after acid treatment according to Scheme 5.



**Scheme 5.** Ion-exchange reaction between  $\text{NH}_4^+$ -ions and protons

In the case of alkali-treated aluminosilicate  $\text{M}_{45}\text{C}_{20}$  (Table 13), which was converted mainly in to  $\text{Na}^+$  form during treatment, the main adsorption mechanism was provided by ion-exchange of  $\text{Na}^+$  for  $\text{NH}_4^+/\text{H}^+$  ions from external  $\text{NH}_4\text{Cl}$  solution:

$$\text{R}_n - \text{Na}^+ + n\text{NH}_4^+ \leftrightarrow n\text{R}-\text{NH}_4^+ + n\text{Na}^+. \quad (16)$$

$C_{eq}(\text{NH}_4^+)$ , mmol/dm <sup>3</sup>	Quantity of desorbed cations, mmol/g				$\sum \text{Na}^+, \text{K}^+$ , $\text{Ca}^{2+}, \text{Mg}^{2+}$ , mmol/g	$a_{\text{NH}_4^+}$ , mmol/g	CEC, mmol/g	CEC/ $a_{\text{NH}_4^+}$
	Na <sup>+</sup>	K <sup>+</sup>	Ca <sup>2+</sup>	Mg <sup>2+</sup>				
1.915	0.397	0.018	0.351	0.052	0.817	0.585	1.22	2.1
3.916	0.554	0.024	0.521	0.096	1.195	1.084	1.812	1.7
8.545	0.773	0.029	0.721	0.166	1.690	1.455	2.577	1.8
22.579	0.923	0.034	0.994	0.209	2.160	2.421	3.363	1.4
47.213	1.202	0.041	1.061	0.223	2.524	2.787	3.808	1.4
95.831	1.260	0.042	1.204	0.250	2.782	4.169	4.236	1.0
195.580	1.291	0.042	1.202	0.265	2.797	4.420	4.264	1.0

**Table 13.** Quantity of exchangeable cations desorbed from alkali-treated  $\text{M}_{45}\text{C}_{20}$  (MCAlk) sorbent by sorption of  $\text{NH}_4^+$  ions (changed after Belchinskaya et al. [63])

The ratio CEC/ $a_{\text{NH}_4^+}$  (Table 13) illustrated that the joint ion-exchange of  $\text{NH}_4^+/\text{H}^+$  ions from external solution for exchangeable cations of mineral phase occurred till the higher concentrations. Starting from 95 mmol/dm<sup>3</sup> of  $\text{NH}_4\text{Cl}$ , the ion-exchange was determined mainly by  $\text{NH}_4^+$  ions providing CEC/ $a_{\text{NH}_4^+} = 1$ .

## 5. Conclusion

The physical–chemical properties of natural aluminosilicate samples containing mineral phases of various structural types (layered planar and nonplanar silicates, zeolites) and considered in this chapter illustrated that the structure of the natural aluminosilicate phases in the sample determined its surface characteristics and surface activity toward a modifying agent and adsorbate molecules, namely, higher content of kaolinite phase (1:1 layer type mineral with a lack of isomorphic substitutions) in the natural sample comprised lower surface parameters (specific surface area, porosity) and weaker population of the surface with active sites, according to its activity in MBOH conversion. Despite this, the surface of the sample containing kaolinite underwent severe changes under acid modification due to its higher reactivity, which results, obviously, from the easier access of the modifier to octahedral sheets in the 1:1 layer type of mineral structure. Moreover, as confirmed here by the method of MBOH conversion and that is in agreement with the observations done by other physical–chemical methods, including the quantum modeling, the surface of the sample containing kaolinite (Kaol) is characterized by the strongest acid sites along with the highest basicity of the unit area of the surface.

For the cases of palygorskite (Pal) or hydromica (Hdm)-rich natural samples, the effect of acid treatment on their surface parameters was weaker, which obviously referred to a higher resistance of the structure against acid attack resulting from the features of 2:1 layer type in both planar and nonplanar silicates. The well-developed surface of the sample containing

palygorskite, although it is populated by the weaker acid and basic sites, is another sequence of its structure.

Despite the variations in surface activity observed for different aluminosilicate types, one must underline the general mechanism of the adsorption of electrolytes and polar molecules by the surface of natural aluminosilicates. Owing to the similarity of the building elements of the considered natural silicates (tetrahedral/octahedral sheets), isomorphic substitutions, and a negative layer charge, they possess similar surface-active sites, involving OH groups, exchangeable cations, coordinately unsaturated cations, and surface oxygen anions. This allows natural aluminosilicates revealing similar adsorption behavior and the occurrence of the following several mechanisms of adsorption: hydrogen bonding, ion-exchange, or chemisorptions. The physical-chemical nature of the adsorbate is a determining factor for the contribution of a specific mechanism of sorption.

## Acknowledgements

The authors would like to acknowledge the Coordinator of Erasmus Mundus program for the International Master in Advanced Clay Sciences, IMACS, Mrs. Patricia Patrier, for affording the opportunity to present the material of this chapter to IMACS students, the University of Poitiers, France, for the financial support of the teaching and research stay, and the German Academic Exchange Service, DAAD, and Russian Ministry of Education and Science, for offering research grants under "Mikhail Lomonosov" program.

## Author details

Liudmila Novikova\* and Larisa Belchinskaya

\*Address all correspondence to: novikov-la@yandex.ru

Department of Chemistry, Voronezh State University of Forestry and Technologies,  
Voronezh, Russian Federation

## References

- [1] Richerson D, Richerson DW, Lee WE. Modern Ceramic Engineering: Properties, Processing, and Use in Design. 3rd ed. CRC Press; 2006. 728 p.
- [2] Feng S, editor. Ceramic Materials—Progress in Modern Ceramics. Rijeika: InTech; 2012.

- [3] Belchinskaya LI. Environment Protecting Technologies for Treatment and Utilization of Wastes From Woodworking Industries. Voronezh: Voronezh State Academy of Forestry and Technologies; 2002.
- [4] Novikova LA, Belchinskaya LI, Roessner F. Effect of treatment with acids on the state of the surface of natural clay minerals. Russ. J. Phys. Chem. 2006; 80(1): S185–S188.
- [5] Novikova L, Belchinskaya L, Roessner F, Alsawalha M. Characterization of surface acidity and catalytic ability of natural clay minerals by means of test catalytic reaction. Acta Geodyn. Geomater. 2013; 10(4): 475–484.
- [6] Amirianshoja T, Junin R, Kamal Idris A, Rahmani O. A comparative study of surfactant adsorption by clay minerals. J. Petrol. Sci. Eng. 2013; 101: 21–27.
- [7] Giggenheim S, Adams JM, Bain DC, Bergaya F, Brigatti MF, Drits VA, Formoso ML, Galan E, Kogure T, Sranek H. Summary of recommendations of nomenclature committees relevant to clay mineralogy: report of the Association Internationale pour l'Etude des Argiles (AIPEA) Nomenclature Committee for 2006. Clay Minerals. 2006; 41: 863–877.
- [8] Bergaya F, Lagaly G, editors. Handbook of Clay Science. Developments in Clay Science 5. 2nd ed. Amsterdam: Elsevier; 2013. 787 p.
- [9] Murray H. Applied clay mineralogy today and tomorrow. Clay Minerals. 1999; 34: 39–49.
- [10] Murray H. Applied Clay Mineralogy: Occurrences, Processing and Applications of Kaolins, Bentonites, Palygorskite-Sepiolite, and Common Clays. Amsterdam: Elsevier; 2006. 188 p.
- [11] Murray HH, Zhou H. Palygorskite and sepiolite (Hormites). In: Kogel JL, Trivedi NC, Barker JM, Krukowski ST, editors. Industrial Minerals and Rocks. 7th ed. Littleton, Colorado: Society for Mining, Metallurgy and Exploration; 2006, pp. 401–406.
- [12] Delle Site A. Factors affecting sorption of organic compounds in natural sorbent–water systems and sorption coefficients for selected pollutants. A review. J. Phys. Chem. Ref. Data; 2001, 30(1): 187–439.
- [13] Ramírez-Moreno MJ, Romero-Ibarra IC, Ortiz-Landeros J, Pfeiffer H. Alkaline and alkaline-earth ceramic oxides for  $\text{CO}_2$  capture, separation and subsequent catalytic chemical conversion. In: Vaz Morgado CR, Esteves V, editors.  $\text{CO}_2$  Sequestration and Valorization. InTech; 2014, pp. 403–441. DOI: 10.5772/57034470.
- [14] Solomon DH, Murray HH. Acid–base interactions and the properties of kaolinite in non-aqueous media. Clays Clay Miner. 1972; 20: 135–141.
- [15] Belchinskaya LI, Khodosova NA, Bityutskaya LA. Adsorption of formaldehyde at mineral nanoporous sorbents exposed to a pulse magnetic field. Prot. Met. Phys. Chem. Surf. 2009; 45 (2): 203–206. DOI: 10.1134/S2070205109020130.

- [16] Belchinskaya LI, Khodosova NA, Tkacheva OA, Strelnikova OYu, Novikova LA. Physical methods of adsorption activation of natural aluminosilicates nanomaterials. Voronezh, FGBOU VPO "Voronezh State Academy of Forestry and Technologies"; 2012. 155 p., deposited in VINITI 14.09.2012, No. 373-V 2012.
- [17] Valaskova M, Barabaszova K, Hundakova M, Ritz M, Plevova E. Effect of brief milling and acid treatment on two ordered and disordered kaolinites structure. *Appl. Clay Sci.* 2011; 54(1): 70–76.
- [18] Fernandez M, Albab MD, Torres Sanchez RM. Effects of thermal and mechanical treatments on montmorillonite homoionized with mono- and polyvalent cations: insight into the surface and structural changes. *Colloids Surf. A. Physicochem. Eng. Asp.* 2013; 423: 1–10.
- [19] Mitrovic A, Zdujic M. Mechanochemical treatment of Serbian kaolin clay to obtain a highly reactive pozzolana. *J. Serb. Chem. Soc.* 2013; 78(4): 579–590.
- [20] Horvath E, Frost RL, Makoc E, Kristof J, Cseh T. Thermal treatment of mechanochemically activated kaolinite. *Thermochimica Acta.* 2003; 404: 227–234.
- [21] Yariv S, Lapides I. The effect of mechanochemical treatments on clay minerals and the mechanochemical adsorption of organic materials onto clay minerals. *J. Mat. Synth. Process.* 2000; 8(3–4): 223–233.
- [22] Akimkhan AM. Structural and Ion-Exchange Properties of Natural Zeolite in Ion-Exchange Technologies. InTech; 2012, pp. 261–282.
- [23] Zdralkova J, Valaskova M, Studentova S. Talc properties after acid treatment and mechanical procedures. Proceedings of the 5th International Conference on Nanomaterials, NANOCON-2013; 2013 Oct 16–18; Brno, Czech Republic, EU.
- [24] Valaskova M, Martynkova GS, Matejka V, Kratosova G. Chemically activated kaolinites after de-intercalation of formamide. *Ceramics-silikaty.* 2007; 51(1): 24–29.
- [25] Kokuneshoskia M, Shaponjich A, Maksimovich V, Stankovich M, Pavlovich M, Pantich J, Majstorovich J. Preparation and characterization of clay-based porous ceramics with boric acid as additive. *Ceram. Int.* 2014; 40: 14191–14196.
- [26] Jozefaciuk G. Effect of acid and alkali treatments on surface-charge properties of selected minerals. *Clays Clay Miner.* 2002; 50(5): 647–656.
- [27] Vlasova M, Dominguez-Patino G, Kakazey N, Dominguez-Patino M, Juarez-Romero D, Enriquez Mendez Y. Structural-phase transformations in bentonite after acid treatment. *Sci. Sinter.* 2003; 35: 155–166.
- [28] Temuujina J, Jadambaab Ts, Burmaaa G, Erdenechimegb Sh, Amarsanaab J, MacKenzie KJD. Characterisation of acid activated montmorillonite clay from Tuulant (Mongolia). *Ceram. Int.* 2004; 30: 251–255.

- [29] Belchinskaya LI, Khodosova NA, Strelnikova OYu, Petukhova GA, Ciganda L. Regulation of sorption processes on natural nanoporous aluminosilicates. I. Acidic and basic modifications. *Prot. Met. Phys. Chem. Surf.* 2015; 51(5): 779–786.
- [30] Terrazas Calderón GD, Ibarra Rodríguez J, Ortiz-Méndez U, Torres-Martínez LM. Iron leaching of a Mexican clay of industrial interest by oxalic acid. *Adv. Technol. Mat. Mat. Process.* 2005; 7(2): 161–166.
- [31] Kong M, Huang L, Li L, Zhang Z, Zheng S, Kuang Wang M. Effect of oxalate and citric acids on three clay minerals after incubation. *Appl. Clay Sci.* 2014; 99: 207–214.
- [32] Tomich ZP, Antich Mladenovich SB, Babich BM, Poharc Logar VA, Dordevich AR, B. Cupach SB. Modification of smectite structure by sulfuric acid and characteristics of the modified smectite. *J. Agric. Sci.* 2011; 56(1): 25–35.
- [33] Biesekia L, Bertellab F, Treichelc H, Penhad FG, Perghera SBC. Acid treatments of montmorillonite-rich clay for Fe removal using a factorial design method. *Mater. Res.* 2013; 16(5): 1122–1127.
- [34] Chmielarz L, Rutkowska M, Jablonska M, Wegrzyn A, Kowalczyk A, Boron P, Piwowarska Z, Matusiewicz A. Acid-treated vermiculite as effective catalysts of high-temperature N<sub>2</sub>O decomposition. *Appl. Clay Sci.* 2014; 101: 237–245.
- [35] Karagüzel C, Çetinel T, Boylu F, Çinku K, Çelik MS. Activation of (Na, Ca)-bentonites with soda and MgO and their utilization as drilling mud. *Appl. Clay Sci.* 2010; 48: 398–404.
- [36] Manfredini T, Pellacani GC, Pozzi P. Preparation of a ceramic floor tile body containing pure bentonite as strengthening agent. *Bol. Soc. Esp. Ceram. Vidr.* 1991; 30(1): 5–9.
- [37] Belchinskaya LI, Khokhlov VYu, Ly Tkhi Y, Petukhova GA, Voishcheva OV, Zhabin AV. The influence of alkaline treatment on the chemical composition and adsorption-structural characteristics of mineral nanoporous sorbent M45K20. *Prot. Met. Phys. Chem. Surf.* 2012; 48(3): 322–327.
- [38] Komarov VS. Adsorbenty: Poluchenie, Struktura, Svoistva (Production, Structure and Properties of Adsorbents). Minsk: Belarus. Navuka; 2009.
- [39] Zhdanov SP, Egorova EN. *Khimiya tseolitov* (Zeolite Chemistry). Leningrad: Nauka; 1968.
- [40] Ma H, Yao Q, Fu Y, Ma C, Dong X. Synthesis of Zeolite of Type A from Bentonite by Alkali Fusion Activation Using Na<sub>2</sub>CO<sub>3</sub>. *Ind. Eng. Chem. Res.* 2010; 49: 454–458.
- [41] Slaty F, Khoury H, Wastiels J, Rahier H. Characterization of alkali activated kaolinitic clay. *Appl. Clay Sci.* 2013; 75–76: 120–125.
- [42] Slaty F, Khoury H, Rahier H, Wastiels J. Durability of alkali activated cement produced from kaolinitic clay. *Appl. Clay Sci.* 2015; 104: 229–237.

- [43] Belchinskaya LI, Novikova LA, Khokhlov VYu, Lu Tkhi J, Kartel MT. Surface chemistry and porosity of natural and activated aluminosilicate from montmorillonite and clinoptyllolite. *Chem. Phys. Technol. Surface (Ukraine)*. 2013; 4(4): 358–365.
- [44] Trombetta M, Busca G, Lenarda M, Storano L, Ganzerla R, Piovesan L, Lopez AJ, Alcantara-Rodriduez M, Rodriguez-Castellon E. Solid acid catalysts from clays: evaluation of surface acidity of mono- and bi-pillared smectites by FT-IR spectroscopy measurements, NH<sub>3</sub>-TPD and catalytic tests. *Appl. Catal. A. Gen.* 2000; 193: 55–69.
- [45] Pushpalettha P, Rugmini S, Lalithambika M. Correlation between surface properties and catalytic activity of clay catalysts. *Appl. Clay Sci.* 2005; 30(3–4): 141–153.
- [46] Lauron-Pernot H. Evaluation of surface acido-basic properties of inorganic-based solids by model catalytic alcohol reaction networks. *Catal. Rev.* 2006; 48: 315–361.
- [47] AlSawalha M, Roessner F, Novikova L, Belchinskaya L. Acidity of different Jordanian clays characterized by TPD-NH<sub>3</sub> and MBOH conversion. *World Acad. Sci. Eng. Technol.* 2011; 79: 417–421.
- [48] Novikova LA, Roessner F, Belchinskaya LI, Alsawalha M, Krupskaya VV. Study of surface acid–base properties of natural clays and zeolites by conversion of 2-methylbut-3-yn-2-ol. *Appl. Clay Sci.* 2014; 101: 229–236.
- [49] Lauron-Pernot M, Luck F, Popa JM. Methylbutynol: a new and simple diagnostic tool for acidic and basic sites of solids. *Appl. Catal.* 1991; 78: 213–225.
- [50] Alsawalha M, Roessner F. Insight in to the reaction mechanism of the conversion of methylbutynol on silica-alumina. *React. Kinet. Catal. Lett.* 2008; 94 (1): 63–69.
- [51] Tarasevich YuI. Structure and Chemistry of Surface of Layered Silicates (in Russian). Kiev: Naukova Dumka; 1988.
- [52] Azzouz A, Niquette P, Asaftei S, Monette F, Hausler R, Nistor D, Miron D. Acid–base properties of montmorillonite and interactions with enzymes through REM investigations. *Sci. Technol. A.* 2004; 22: 89–96.
- [53] Kaya A. Characterization of clay particle surfaces for contaminant sorption in soil barriers using flow microcalorimetry. *J. Environ. Eng.* 2004; 130. Special issue: waste containment barrier materials, 918–921.
- [54] Zhabin AV, Sharov VA. Micro- and macroelements in the glauconite of Eocene from the south-west of the Voronezh anticline—the indicators of formation conditions. *Annals of Voronezh State University. Geology.* 2005; 1: 18–32.
- [55] Jozefaciuk G, Slawinski C, Vrzhashch E. Changes in textural properties of selected minerals under acid and alkali treatment from mercury intrusion porosimetry. *Appl. Clay Sci.* 2009; 43: 63–68.
- [56] Liu X, Lu X, Sprik M, Cheng J, Meijer EJ, Wang R. Acidity of edge surface sites of montmorillonite and kaolinite. *Geochim. Cosmochim. Acta.* 2013; 117: 180–190.

- [57] Voronchak T, Nykulysyn I, Pikh Z, Rypka A. Activated palygorskite and activated bentonite clays as the catalysts of the process of co-oligomers obtaining from ethylene productions byproducts. *Chem. Chem. Technol.* 2012; 6: 189–198.
- [58] Fubini B, Bolis V, Cavenago A, Volantel M. Physicochemical properties of crystalline silica dusts and their possible implication in various biological responses. *Scand. J. Work. Environ. Health.* 1995; 21: 9–14.
- [59] Saeung S, Boonamnuayvitaya V. Adsorption of formaldehyde vapor by amine-functionalized mesoporous silica materials. *J. Environ. Sci.* 2008; 20: 379–384.
- [60] Novikova LA, Belchinskaya LI, Roessner F. Adsorption of acetic acid on natural and alkali activated montmorillonite. *Sorption and Chromatographic Processes.* 2007; 7(5): 741–745.
- [61] Tanaka H, Watanabe T, Chikazawa M. FTIR and TPD studies on the adsorption of pyridine, n-butylamine and acetic acid on calcium hydroxyapatite. *J. Chem. Soc. Faraday Trans.* 1997; 93(24): 4377–4381.
- [62] Hofmeister AM, Bowey JE. Quantitative infrared spectra of hydrosilicates and related minerals. *Mon. Not. R. Astron. Soc.* 2006; 367: 577–591.
- [63] Belchinskaya L, Khokhlov V, Novikova L, Ly Tkhi J. Contribution of ion-exchange and non-ion-exchange reactions to sorption of ammonium ions by natural and activated aluminosilicate sorbent. *J. Appl. Chem. Hindawi Publishing Corporation.* 2013; 1–9.
- [64] Kithome M, Paul JW, Lavkulich LM, Bomke AA. Kinetics of ammonium adsorption and desorption by the natural zeolite clinoptilolite. *Soil Sci. Soc. Am. J.* 1998; 62: 622–629.
- [65] Franus W, Wdowin M. Removal of ammonium ions by selected natural and synthetic zeolites. *Gospodarka Surowcami Mineralnymi.* 2010; 6(4): 133–147.
- [66] Wen D, Ho YS, Tang X. Comparative sorption kinetic studies of ammonium onto zeolite. *J. Hazard. Mater.* 2006; B133: 252–256.
- [67] Copcia V, Hristodor C, Luchian C, Bilba N, Sandu I. Ammonium nitrogen removal from aqueous solutions by natural clay. *Rev. Chim.* 2010; 61(12): 1192–1196.
- [68] Rozic M, Cerjan-Stefanovich S, Kurajica S, Vanchina V, Hodzic E. Ammoniacal nitrogen removal from water by treatment with clays and zeolites. *Water Res.* 2000; 34(14): 3675–3681.
- [69] Ismadji S, Soetaredjo FE, Ayucitra A. *Clay Materials for Environmental Remediation. SpringerBriefs in Green Chemistry for Sustainability;* 2015.

# **Structural and Electrochemical Properties of Cementitious and Hybrid Materials Based on Nacrite**

---

Nouha Jaafar, Hafisia Ben Rhaiem and Abdesslem Ben Haj Amara

Additional information is available at the end of the chapter

<http://dx.doi.org/10.5772/61594>

---

## **Abstract**

This chapter gives possible valorization of a well-crystallized Tunisian nacrite as an interesting clay mineral belonging to the kaolin group: The first part of the chapter aims to produce a new synthetic material labeled “metanacrite”. Metanacrite is a supplementary cementitious material originated by heating a raw Tunisian nacrite at 823 K. The structure of the amorphous synthetic product was corroborated by X-ray diffraction (XRD) and infrared spectroscopy (IR). The decomposition of the silicate framework was confirmed by transmission electron microscope (TEM). The obtained metanacrite was also examined by electrochemical impedance spectroscopy (EIS). Accordingly, a semiconductor behavior of the novel synthetic material is evidenced. The second part of this chapter deals with the intercalation of lithium chloride salt between the planar layers of this Tunisian nacrite. The intercalation leads to a stable hybrid material that after calcination under inert atmosphere at 723–873 K induces an amorphous hybrid. The structural identification of the obtained nacrite–LiCl hybrid was determined by means of XRD, IR, TGA, and EIS. Finally, the resulting amorphous hybrid shows a superionic behavior with high ionic conductivity up to  $10^{-2}$  S.m<sup>-1</sup>, good electrochemical stability, and can be used as an innovative solid electrolyte in lithium batteries and other electrochemical devices.

**Keywords:** Nacrite, Clay Mineral, Metanacrite, Hybrid, Lithium-Ion Battery

---

## **1. Introduction**

Clay minerals are abundant in soil and important to a wide variety of disciplines such as environmental chemistry, astrophysics, geology, and the ceramics industry [1]. One of the most

used clay minerals is **kaolin**, which is a 1:1 dioctahedral layered aluminosilicate produced of advanced weathering processes [2]. Kaolin clays include kaolin-group minerals, of which the most common are kaolinite, dickite, nacrite, and halloysite [3]. Kaolin is white or near white color with pseudo-hexagonal crystal along with plates, some larger books, and vermicular stacks [4]. The structural formula of kaolin is  $[Al_2Si_2O_5(OH)_4]$  per half unit cell with Si/Al ratio  $\sim 1$ . One layer of the mineral consists of an alumina octahedral sheet and a silica tetrahedral sheet that share a common plane of oxygen atoms and repeating layers of the mineral are hydrogen bonded together [2,5]. Quantitative estimates indicate that the cohesive energy between kaolinite layers is primarily electrostatic [6]. There is also a certain degree of van der Waals attraction between the hydroxyl groups of the gibbsite sheet and the oxygen atoms of the adjoining silica sheet [7, 8].

Consequently, wide applications based on virgin as well as treated (heat treatment, functionalization, etc.) kaolinite were developed:

1. Clay minerals in soil play an important role in the environment by acting as a natural scavenger of pollutants from water through adsorption mechanism [9]. For example, China clay can confiscate cadmium from hazardous waste [10]. Use of kaolinite for the removal of copper, nickel, cobalt, and manganese is also studied [11].
2. Conversion of kaolin to metakaolin by firing above the dehydroxylation temperature activates the clay and improves its properties [12]. The heating process drives off water from the mineral ( $Al_2O_3 \cdot 2SiO_2 \cdot 2H_2O$ ), the main constituent of kaolin clay, and collapses the material structure, resulting in an amorphous aluminosilicate ( $Al_2O_3 \cdot 2SiO_2$ ), metakaolin. Metakaolin (MK) had 99.9% particles  $<16 \mu m$  with a mean particle size of about 3  $\mu m$  ([www.metakaolin.com](http://www.metakaolin.com)). Therefore, there is an ongoing interest to apply metakaolin in the construction industry as a raw material for the production of white cement clinker and as an artificial pozzolanic additive for concrete to produce blended cement [4]. The use of by-products like metakaolin in cement and concrete has gained significant importance because of the requirements of environmental protection and sustainable construction in the future [13].
3. The ability to modify clay minerals by insertion of inorganic and/or organic guest species into the interlamellar region opens up a range of potential uses for these materials. The resultant hybrid materials combine the features of the clay and the guest species. These complexes have the potential to be used as adsorbents, as catalyst support, and in chromatographic columns and ion exchangers [14].

In this regard, Tunisian nacrite has been employed as a natural clay mineral in the development of new materials with high functionalities and unique properties. Therefore, the first part of this study herein describes the structural and electrochemical characteristics of a novel material, commonly named "*metanacrite*". This chapter allows us to achieve better applicability of the calcined nacrite, as a supplementary cementitious material (SCM) that can be used to replace part of the clinker in a cement or cement in a concrete mixture. The second part of this work deals with the control of the evolution of the nacrite structure during the intercalation process and the study of the structural and electrochemical properties of the novel synthesized material labeled "*nacrite–LiCl nanohybrid*".

## 2. Tunisian nacrite: Starting clay mineral

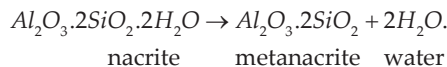
Well-crystallized Tunisian nacrite from North Tunisia (Jbel Slata, Kef) was used in this work as a starting clay mineral economically viable and technically efficient [15]. This layered aluminosilicate material contributes large particle size and high chemical stability and has been previously characterized in the work of Ben Haj Amara and co-workers [15–21]. Bailey [22] described nacrite by a 2M stacking mode which crystallized in the monoclinic lattice with a Cc space group. The structural parameters of nacrite are  $a = 0.8906$  nm,  $b = 0.5146$  nm,  $c = 1.5669$  nm, and  $\beta = 113.58^\circ$  with a main basal distance  $d_{002} = c \sin \beta/2 = 0.72$  nm [15, 19].

## 3. Dehydroxylation of nacrite: Metanacrite

Recently, several studies focused on the physicochemical characteristics of *metakaolin* (MK) materials derived from dehydroxylation of *kaolin* at 823 K. This phenomenon is accompanied by loss of water and decomposition into a disordered metastate [23], which undergoes massive structural changes of the octahedral layer: aluminium changes its coordination from six to four and five [24–26]. In Tunisia, particular attention is given to the exploitation of clays which are abundant in the country and may present potential pozzolanic activity, if they are appropriately calcined at relatively low temperatures [27, 28].

### 3.1. Calcination procedure

The sample of about 20 g was heat treated in the “Nabertherm GmbH” laboratory furnace. The optimal calcination parameters, for which complete dehydroxylation of the material was achieved, are temperature of 823 K and heating time of 120 min. The dehydroxylation process may be presented by the following simple equation [29]:



### 3.2. Structural Properties of Tunisian Metanacrite

#### 3.2.1. X-Ray Diffraction

The experimental X-ray diffraction patterns of both nacrite and metanacrite are reported in Figures 1(a) and 1(b), respectively. Results show a broad characteristic reflection extending from approximately 17 to 39° $2\theta$  attributed to the overlapping of the 00l reflections of the well-crystallized natural nacrite [15–21]. The XRD analysis illustrates then the amorphous structure of the obtained metanacrite synthetic phase [29].

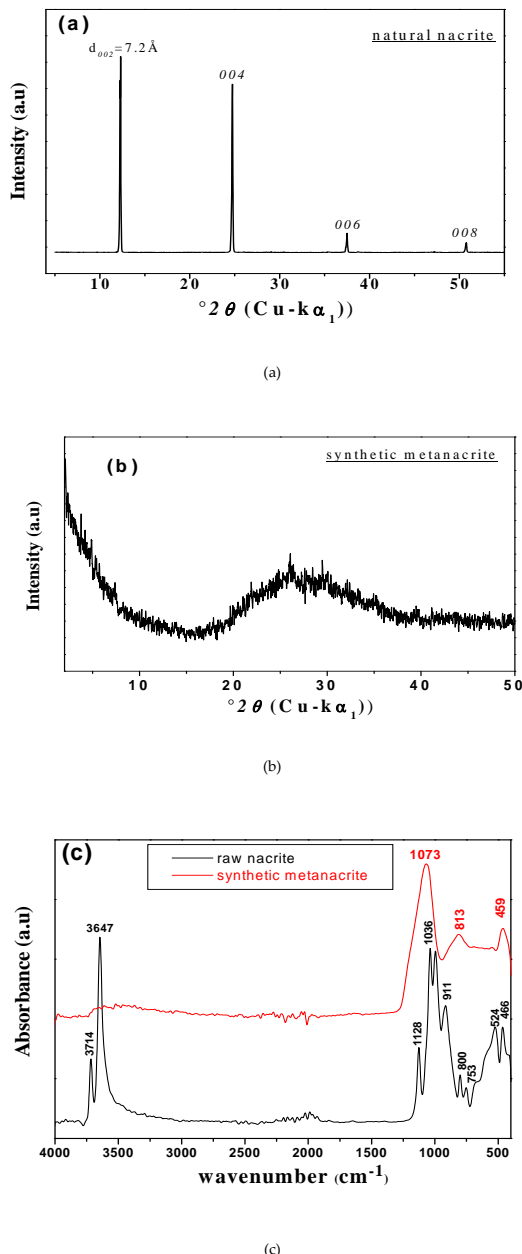


**Figure 1.** (a) Experimental X-ray pattern of nacrite raw-clay material [29]. (b) Experimental X-ray pattern of metanacrite synthetic material [29]. (c) Infrared spectra in the 4000–400  $\text{cm}^{-1}$  region for nacrite and metanacrite samples [29].

### 3.2.2. IR Spectroscopy

By comparing the IR spectra of metanacrite and nacrite recorded in Figure 1(c), it is possible to follow the modifications of the stretching and deformation vibrations obtained after heating nacrite above 823 K: they shift from their positions in the spectrum of untreated nacrite, and their shapes change. Indeed, at high frequencies, it should be mentioned that no bands were detected in the infrared spectrum of metanacrite, indicating the disappearance of the OH lattice stretching band since it is located in the envelope of water band corresponding to natural nacrite at 3714 and 3647  $\text{cm}^{-1}$  [15, 17–21]. Figure 1(c) reveals that, at low frequencies, the Si–O stretching vibrations  $\nu(\text{Si–O})$  located at 1073  $\text{cm}^{-1}$  and the Si–O deformation vibrations located at 459  $\text{cm}^{-1}$  are commonly present with a slight change in their shape and intensity, while the Al–O deformation vibrations are shifted to high frequencies from 524 to 813  $\text{cm}^{-1}$  and the Al–OH deformation vibrations placed at 753, 800, and 911  $\text{cm}^{-1}$  in the spectrum of nacrite are omitted in the spectrum of metanacrite. All these changes in the infrared spectrum between metanacrite and nacrite imply that the starting aluminosilicate loses water during calcinations. The layered structure is then destroyed and transformed into a disordered metanacrite phase possessing amorphous structure very different from the nacrite matrix [29].

### 3.2.3. TEM and EDXS

The morphology, size, and composition of the synthesized sample were characterized via local chemical microanalysis performed using energy dispersive X-ray spectroscopy (EDXS) coupled to the transmission electron microscope (TEM). Figure 2 provides the TEM observations micrographs of Tunisian metanacrite. At first glance, the studied sample exhibits a disordered granular structure with various shapes and sizes. We note the presence of defects, mostly dislocations, which are generated by the distortion around the particle. The contributions of defects, grain size, distribution, and morphology confirm that the amorphous behavior dominates the whole structural composition of metanacrite synthetic material. Such defects seem to be produced during the heating of the starting nacrite clay material and play an important role in the second part of this paper. The larger the number of defects and disorder, the higher the mobility of the free charge carriers, which results in an improvement of the conduction behavior. In order to obtain more detailed information about the microstructure and the chemical composition of metanacrite, we performed TEM coupled with EDXS analysis. The obtained spectra show the presence of Si and Al atoms with a major proportion, constituting the fundamental elements of the metanacrite phase, with a minor contribution of Fe and Cu atoms corresponding to the presence of a trace amount of impurities in the metanacrite material. However, the presence of Ni atoms belongs to the membrane on which the sample is placed. The preliminary physicochemical analysis of metanacrite reveals that the sample is mainly in high amorphous aluminosilicate phase with a disordered polymerized silicon/aluminum framework which allows its applicability as a new synthetic source of pozzolan for producing composite building materials [29].

## 3.3. Electrochemical properties of Tunisian Metanacrite

In order to investigate the role of the microstructure of the resultant amorphous synthetic material in the transport properties, we carried out electrochemical impedance spectroscopy

(EIS). The impedance measurements were taken in an open circuit in the frequency range from 10 Hz to 13 MHz, with an applied potential of 50 mV at different temperatures. The metanacrite sample was ground to fine powder and pressed into a pellet. Platinum electrodes were deposited by sputtering on both parallel faces of the pellet to form a symmetrical cell. The cell was then placed inside a programmable oven coupled with a temperature controller [29, 30].

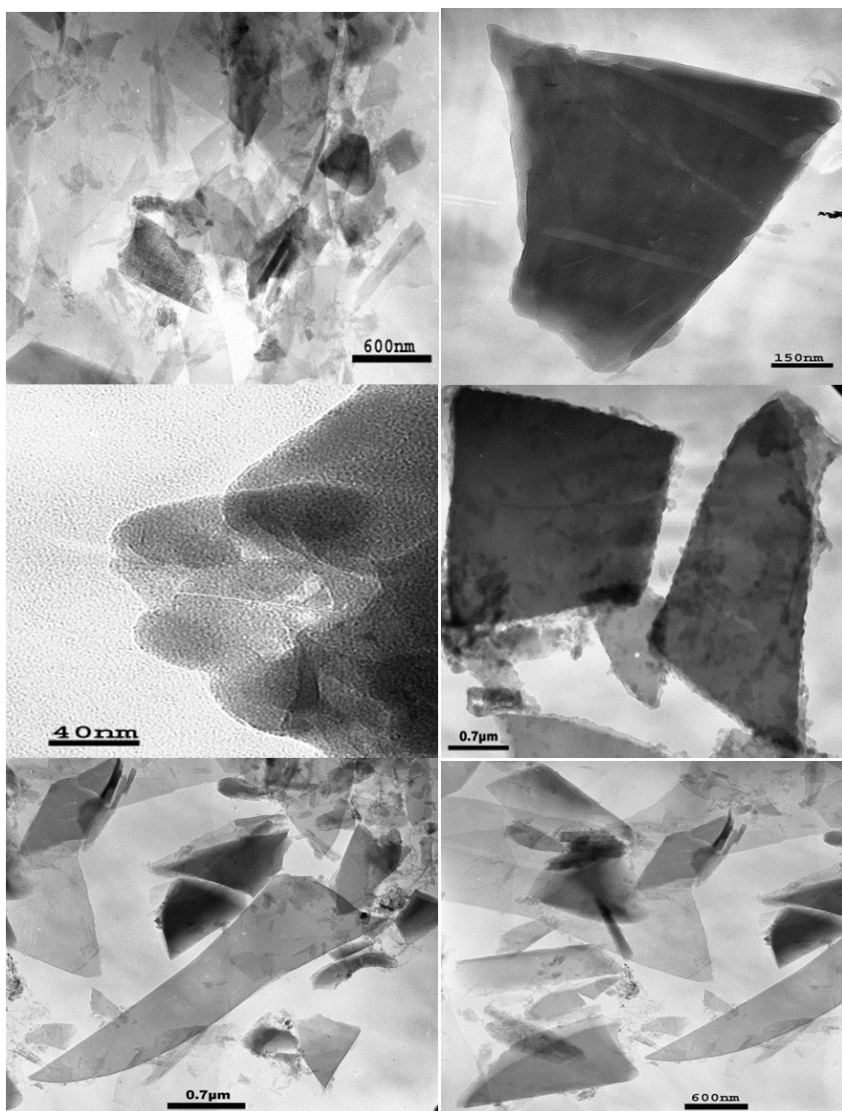
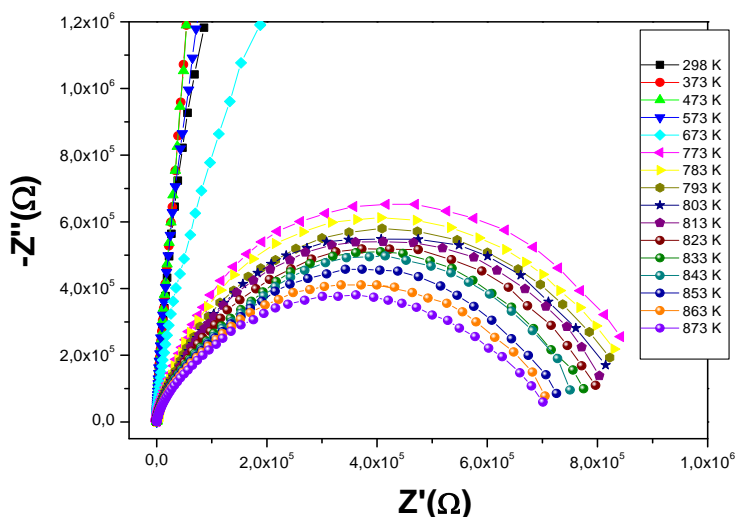


Figure 2. TEM micrographs of metanacrite synthetic material [29].

### 3.3.1. Impedance Analysis

In this section, we will discover the influence of the heat treatment of metanacrite from room temperature to 873 K on the enhancement of the electrical conductivity. Accordingly, the complex impedance plots of metanacrite in the temperature range 298–873 K are displayed in Figure 3.



**Figure 3.** Nyquist diagram of metanacrite at the temperature range from 298 to 873 K [29].

The Nyquist plots describe the transport properties which are strongly affected by the microstructure. From Figure 3, two domains are identified: the first one is observed at low temperature (298–673 K) describing the insulator behavior and the second one is detected at high temperature (673–873 K) for which a significant increase in conductivity is observed. The increase of the electrical conductivity may be attributed to an increase of the disorder degree as well as defects density in the sample [29].

### 3.3.2. Electrical conductivity

Different models have been proposed to describe and draw the ac conduction model corresponding to metanacrite such as quantum mechanical tunneling (Q.M.T.) [31,32], non-overlapping small-polaron tunneling (N.S.P.T.), overlapping large-polaron tunneling (O.L.P.T.), and the correlated barrier hopping (C.B.H.) [31–36]. All these models were deemed to be in disagreement with our results. Therefore, the experimental data will be discussed in the frame of the C.B.H. model. Thus, the conduction occurs via the hopping carriers over a potential barrier between two different valence states. The ac conductivity and frequency exponent expressions due to the C.B.H. model are given by the following equations:

$$s_{ac}(\omega) = \left( \frac{1}{24} \right) \pi^3 \epsilon' N^2 \epsilon_0 \omega R^6 \quad (1)$$

$$s = 1 - \left\{ \frac{6kT}{W_M + k_B T \ln(1/\omega\tau_0)} \right\} \quad (2)$$

where  $\sigma_{ac}$  is the ac conductivity,  $\epsilon_0$  is the free-space dielectric permittivity,  $\epsilon'$  is the dielectric constant,  $N$  is the density of states at Fermi level,  $R_\omega$  is the hopping length at frequency  $\omega$ ,  $W_M$  is the maximum barrier height,  $\tau_0$  the atomic vibration period,  $s$  is the frequency exponent, and  $k_B$  is the Boltzmann constant.

Equation (2) predicts that  $s$  decreases with increasing temperature. Therefore, the C.B.H. is the involved conduction mechanism for the investigated metanacrite sample [37, 38].

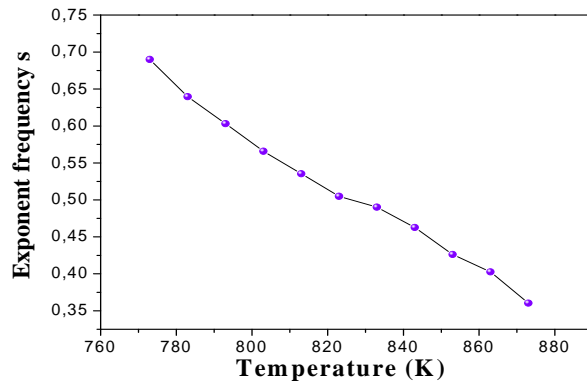


Figure 4. Temperature dependence of frequency exponent(s) for metanacrite sample [29].

Concerning the ac conductivity of metanacrite, it is found to obey the universal Arrhenius power law [39]:

$$\sigma_{ac} = \sigma_0 \exp\left(\frac{-E_{a(ac)}}{k_B T}\right) \quad (3)$$

where  $\sigma_0$  is the pre-exponential factor,  $k_B$  is the Boltzmann constant,  $T$  is the temperature, and  $E_{a(ac)}$  is the activation energy that controls the jump of charge carriers from one site to another neighboring site. The (ac) values have been calculated at four fixed frequencies [29]. Indeed, the activation energy varies between  $0.24 \pm 0.01$  eV (at low frequencies) and  $0.17 \pm 0.01$  eV (at high frequencies). These results are specific to the temperature range 773–873 K. Thus, the increase of the applied frequency enhances the electronic jumps between the localized states.

Consequently, the activation energy decreases with increasing frequency. Moreover, at high frequency, the ac activation energies are found to be lower than those found at low frequency regions [29]. Therefore, at high frequencies the mobility of charge carriers over short distances needs lower energy than that necessary for mobility over longer distances at low frequencies.

The ac conductivity increases as a function of frequency at a fixed temperature (773 K) from  $3.40 \cdot 10^{-6} \text{ S} \cdot \text{m}^{-1}$  at  $f = 100 \text{ Hz}$  to  $1.27 \cdot 10^{-2} \text{ S} \cdot \text{m}^{-1}$  at  $f = 10 \text{ MHz}$  [29]. Besides the ac conductivity increases as a function of temperature at a fixed frequency ( $f = 10 \text{ MHz}$ ), it increases from  $1.27 \cdot 10^{-2} \text{ S} \cdot \text{m}^{-1}$  at  $T = 773 \text{ K}$  to  $1.98 \cdot 10^{-2} \text{ S} \cdot \text{m}^{-1}$  at  $T = 873 \text{ K}$ . The small values of the ac activation energy  $E_{a(\text{ac})}$  and the increase of ac conductivity  $\sigma_{ac}$  with the increase of frequency confirm the dominant hopping conduction mechanism.

The conductivity is thermally activated; therefore, the electrical conduction follows a process in which the electron or hole hops from one localized site to another. The electron resides at one site; when it is thermally activated, it migrates to another site. Moreover, we demonstrated in the first part of this chapter that the defects constitute the active sites in the conduction process. Therefore, the electron or hole tends to associate with local defects, so the activation energy for charge transport may also include the energy of freeing the hole from its position next to the defect [40]. Otherwise, the electronic conduction takes place by hopping between two charge-defect states over the barrier separating them.

As mentioned above, the ac conductivity increases with increasing both temperature and frequency. Simultaneously, the dc conductivity increases with increasing temperature (Figure 5). Indeed, the dc conductivity ( $\sigma_{dc}$ ) fits the well-known Arrhenius relation [39]. We found  $E_{a(\text{dc})} = 0.24 \pm 0.01 \text{ eV}$  (Figure 5):

$$\sigma_{dc} = \frac{\sigma_0}{T} \exp\left(\frac{-E_{a(dc)}}{k_B T}\right) \quad (4)$$

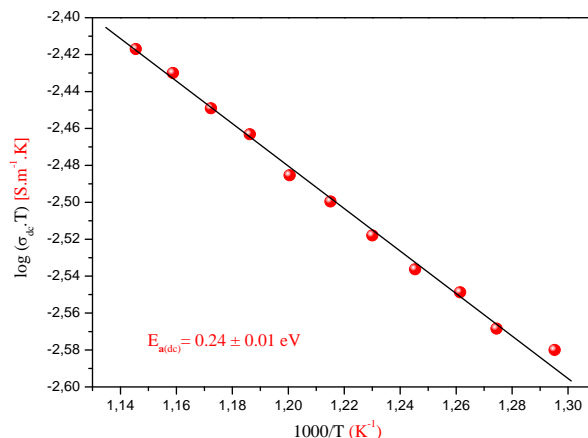


Figure 5. Evolution of the dc conductivity of metanacrite between 773 K and 873 K [29].

where  $\sigma_0$  is the pre-exponential factor,  $E_{a(ac)}$  is the activation energy,  $T$  is the temperature, and  $k_B$  is the Boltzmann constant. As a consequence of the increased dc conductivity with temperature for small activation energies, we conclude that the amorphous metanacrite sample behaves like a semiconductor material [29].

From these results, we deduce a correlation between the electrochemical impedance spectroscopy and the structural properties of amorphous Tunisian metanacrite synthetic material.

#### 4. Functionalization of Nacrite: Nacrite–LiCl Nanohybrid

Intercalation of kaolin nanoclay minerals with inorganic and organic compounds has wide potential for scientific and industrial applications [41]. Indeed, intercalation is eventually accompanied by substantial modifications of the kaolin surface due to the expansion of the interlamellar space [42,43]. The resulting hybrid materials have attracted much interest from researchers, since they frequently show unexpected and remarkable improvements in the rheological, mechanical, thermal, optical, and electrical properties compared to the unmodified aluminosilicate clay mineral.

However, due to the hydrogen-bonding between the layers of kaolinite, only a limited number of small and highly polar organic compounds such as dimethyl-sulfoxide, deuterated dimethyl-sulfoxide [44], formamide [45], N-methylformamide (NMF), dimethylformamide, acetamide, pyridine N-oxide, potassium acetate, and methanol can directly be intercalated [46, 47]. Thus, these kaolinite intercalation compounds were used as precursors, because intercalation reactions of kaolinite have been extended by a guest displacement method in which a new guest can be intercalated by displacing previously intercalated species [48]. Additionally, three intercalation modes of alkali halides into the kaolin subgroup can be distinguished [49]: Mode A includes those species that are directly intercalated [50, 51]. Mode B includes those species which can enter the interlayer space by means of an “entraining agent” such as hydrazine or ammonium acetates [52]. Mode C includes those species which can only be intercalated into the interlayer space by the displacement of a previously intercalated compound such as dimethylsulfoxide “DMSO” [52].

In the case of Tunisian nacrite-polytype, the intercalation process of several inorganic salts and dipolar organic molecules are well documented and numerous publications are available [16, 21, 49, 53, 54]. In this study, we focus eventually on the intercalation of LiCl alkali halide in the interlayer space of nacrite. Mode B has been adopted, firstly, due to hydrogen bonds between the oxygen atoms on the surface of the tetrahedral sheet of one layer and adjacent hydroxyl groups on the surface of the octahedral sheet of the next layer [55]. Secondly, this process ensures the fast intercalation of the alkali halide without destruction of the kaolinite framework and complications of the kaolinite/alkali halide interactions compared to Mode A. Finally, the protocol of synthesis followed in Mode B is much easier in comparison to that in Mode C. For these reasons, potassium acetate “KAc” was selected as a precursor for the expansion of nacrite [15, 49, 52]. The resulting KAc complex is characterized by a basal distance equal to 1.4 nm; it is then washed with water and air dried leading to a stable hydrate (0.84

nm), which constituted the starting material for the next step of the synthesis of the new hybrid material [15, 17, 20, 49].

#### 4.1. The Intercalation Process of Lithium Chloride Alkali Halide in the Interlamellar Space of Nacrite

The inorganic salt employed during the course of this work was imposed by the literature data [52, 56], since the intercalation of lithium chloride alkali halide into kaolinite, in the previous cases, has failed due to the hygroscopic properties of the salt–clay mixture [57]. Thus, this research has been the first to intercalate LiCl in the interlamellar space of nacrite. Experiments based on the use of water as a solvent induces an unaccomplished intercalation of  $\text{Li}^+$  cations. For this reason, different organic solvents (acetone, methanol, ethanol, glycerol, and ethylene glycol) were tried until an intercalation of 0.82 g of LiCl was reached in the presence of 20 ml of acetone at room temperature [49]. Indeed, acetone is considered as the best solvent for nacrite intercalation after 3 days of mechanical shaking under a magnetic stirrer. The final hybrid product was obtained and labeled: nacrite–LiCl [49].

#### 4.2. Structural Characterization of Nacrite–LiCl Nanohybrid Material

The intercalation process is characterized via X-ray diffraction analysis, thermogravimetric analysis, infrared spectroscopy, and electrochemical impedance spectroscopy. In the following sections, the structural properties of nacrite–LiCl hybrid will be detailed starting with X-ray diffraction analysis.

##### 4.2.1. X-ray Measurements

###### 4.2.1.1. Qualitative XRD Analysis

By examining the  $00l$  reflections of the XRD pattern related to the stable nacrite–LiCl hybrid, Figure 6, we note a main reflection situated at  $7.724^\circ 2\theta$ , with  $d_{002}=1.143\pm 0.002$  nm basal spacing value attributed to an expansion of the interlamellar space of nacrite by  $\sim 0.423$  nm along the  $c^*$  axis. This result is probably due to the insertion of lithium chloride salt accompanied by one water sheet into the nacrite matrix [49]. The exploitation of the CV coefficient and the rationality series confirm the homogenous sample character [49].

However, the high  $FWHM$  value at around  $0.846^\circ 2\theta$  of the first reflection is interpreted as a contradictory result. This is traduced by the fact that the  $FWHM$  could be notably affected by stress, strain, and interstratifications [49]. The extent of intercalation was determined using integrated areas of the reflections [58]:

$$\text{Intercalation ratio} = \left[ \frac{I_{002} \text{ hybrid}}{I_{002} \text{ hybrid} + I_{002} \text{ nacrite}} \right] \times 100\% \quad (5)$$

where  $I_{002}\text{hybrid}$  and  $I_{002}\text{nacrite}$  represent the main basal peak intensity of the hybrid and of the unexpanded nacrite component ( $d_{002} \sim 0.72$  nm), respectively. The intercalation ratio value is equal to 86% for nacrite–LiCl and remained unchanged even for long time reaction.

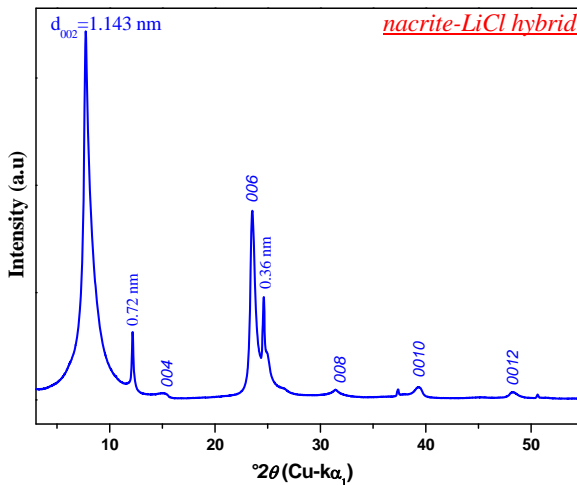


Figure 6. Experimental XRD pattern of the nacrite–LiCl hybrid [49].

#### 4.2.1.2. Quantitative XRD Analysis

Simulations of the  $00l$  reflections seem to be a dominant path to gain an accurate picture about the fine structure of the nacrite–LiCl hybrid including the number and positions of the intercalated species in the interlayer space of nacrite. For that, an XRD-modeling computer program designed to carry out intensity calculations was used: The quantitative XRD analysis is based essentially on comparison between the experimental XRD pattern with the theoretical one [49].

However, the tiny atomic scattering factor of  $\text{Li}^+(2)$  prevents the location of this cation with good preciseness in the interlamellar space of nacrite. So, we dressed a series of models with different positions of  $\text{Li}^+$  cation [49]. It was therefore interesting to handle the unweighted  $R_p$  factor of each model as an indication of the effectiveness of fit [59]:

$$R_p = \sqrt{\frac{\sum [I(2\theta_i)_{obs} - I(2\theta_i)_{calc}]^2}{\sqrt{[I(2\theta_i)_{obs}]^2}}} \quad (6)$$

where,  $I(2\theta_i)_{obs}$  and  $I(2\theta_i)_{calc}$  represent measured and calculated intensities, respectively, at the  $2\theta_i$  position, the subscript  $i$  running over all points in the refined angular range.  $R_p$  is mainly influenced by the most intense diffraction maxima, such as the  $00l$  reflections, which contains essential information on the proportions of the different layer types and layer thickness [49].

The best model belongs to the smallest  $R_p$  factor (6.20%) [49]. This model suggests the presence of a hydrated salt and is in agreement with the qualitative analysis. It allows then a more

accurate determination of the structural parameters of the stable nacrite–LiCl hybrid per half unit-cell: The z coordinates of intercalated Li<sup>+</sup> and Cl<sup>-</sup> cations, taken from the oxygen surface oxygen along the normal to the layer, are respectively, 0.96 ± 0.01 nm and 0.64 ± 0.01 nm along c\* axis. Finally, one intercalated water molecule situated at z = 0.79 ± 0.01 nm is sandwiched between the cation and the anion [49].

To summarize, the intercalated species stand vertically in the interlayer space of nacrite, where the cations are located close to the ditrigonal holes of the tetrahedral layers and the anions are located close to the inner-surface hydroxyls of the octahedral layer of the subsequent sheet [49]. Moreover, the quantitative study of the nacrite–LiCl hybrid clearly showed an interstratified stacking characterized by a segregation tendency consisting of a total demixion of two types of layers: Layer A related to a minor fraction (14%) of the unexpanded 0.72 nm clay and Layer B attributed to a major fraction (86%) of the intercalated nacrite {W<sub>A</sub> = 0.86, W<sub>B</sub> = 0.14, P<sub>AA</sub> = 1, P<sub>AB</sub> = 0, P<sub>BA</sub> = 0, P<sub>BB</sub> = 1} [49]. The structural formula of the studied hybrid at room temperature was then determined as {(1- $\alpha$ )[Si<sub>2</sub>Al<sub>2</sub>O<sub>5</sub>(OH)<sub>4</sub>LiCl.H<sub>2</sub>O] +  $\alpha$ [Si<sub>2</sub>Al<sub>2</sub>O<sub>5</sub>(OH)<sub>4</sub>] } per half unit cell, where “ $\alpha$ ” is equal to 0.14 and corresponds to the unexpanded nacrite fraction [49].

#### 4.3. IR Spectroscopy

By comparing the spectrum of nacrite intercalated with lithium chloride to the spectrum of the untreated nacrite, it is possible to follow the modification of the stretching and deformation vibrations: they shift from their positions and their shapes change. These effects are a consequence of several factors, such as the intercalated entities, the degree of intercalation, and the degree of hydration [60].

These modifications are manifested in the recorded spectrum of the nacrite–LiCl hybrid [49].

Finally, IR spectroscopy proved that the intercalating species overcome the strong interactions between the nacrite-like layers and form hydrogen bonds with components of the TO layer [49]:

1. The Cl<sup>-</sup> halide anion interacts with the inner surface hydroxyls through hydrogen-bonding;
2. The intercalated water molecule only interacts with the Cl<sup>-</sup> and Li<sup>+</sup> ions;
3. The Li<sup>+</sup> alkali cation, located near the basal oxygens of the nacrite layer, interacts electrostatically with the negatively charged oxygens of the inner-surface oxygen.

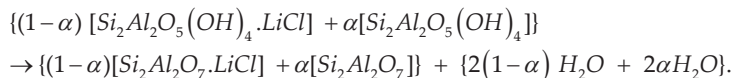
These results are in concordance with those suggested by [50, 51, 60–62].

#### 4.4. Thermal Analysis: Decomposition Process of the Nacrite–LiCl Nanohybrid During Heat Treatment

Thermogravimetric analysis of the nacrite–LiCl hybrid reveals that the sample gradually loses weight from room temperature to 800°C (Scheme 1) [49]:

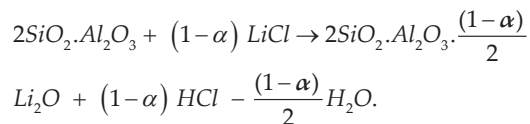
1. The first remarkable weight loss was observed between 298 and 423 K and is mostly attributed to the drying process by which the water molecules that are confined to the clay mineral pores are released.

2. The second weight loss (3.62%) occurred between 673 and 773 K and belongs to the removal of the intercalated water molecule. This temperature range is also characterized by the beginning of the dehydroxylation of the hybrid at around 723 K. The chemical decomposition reaction of the hybrid per half unit cell can be expressed as follows:



The product formed at the commencement of the dehydroxylation of the hybrid is called “metanacrite–LiCl hybrid”: {  $Si_2Al_2O_7.(1-\alpha)LiCl$  }, ( $\alpha = 0.14$ ), and is amorphous.

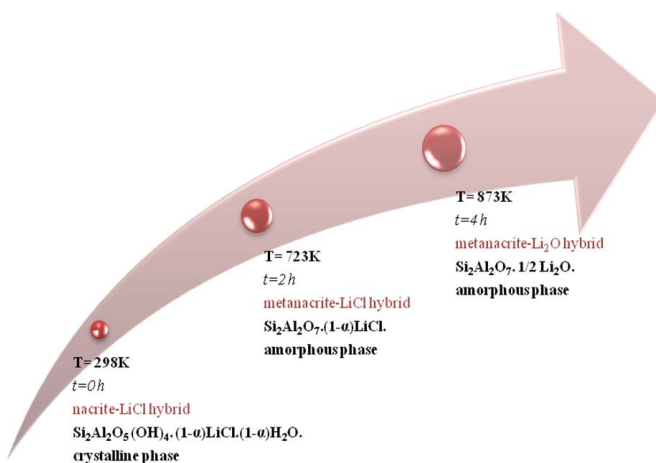
3. The third weight loss was centered on 873 K (9.23%) and was due to the removal of two structural water  $\{2(1-\alpha) H_2O + 2\alpha H_2O\} = \{2 H_2O\}$  during the calcination process. This step was ultimately accompanied by the evolution of the hydrogen halide which results from the following thermal hydrolysis [63, 64]:



On the clay surface, a liberated water molecule associates with  $Cl^-$  to form volatile  $HCl$ . The volatilization of  $HCl$  is responsible for a great amount of thermal mass loss of the examined hybrid. This phenomenon causes the trapping of the alkali metal oxide  $Li_2O$  within the metanacrite matrix. The amorphous hybrid phase formed during this step has the following chemical formula:  $[Si_2Al_2O_7.(1-\alpha) / 2Li_2O]$ . Knowing that  $(1-\alpha)/2$  coefficient is equal to 0.43 ~ 0.5, we can simplify this chemical formula and express our “metanacrite– $Li_2O$  hybrid” by the following formula  $[Si_2Al_2O_7. 1 / 2Li_2O]$  [49].

#### 4.5. Electrochemical Characterization of Nacrite–LiCl Nanohybrid Material

Over the past three decades, much attention has been paid to solid electrolytes instead of liquid electrolytes because of their potential use in the electrochemical power sources (batteries, lithium ion cells, lithium batteries, fuel cells, electrochemical sensors, etc.) [65]. The advantages of solid electrolytes include longer life, high energy density, and no possibility of leak, etc. They are suitable in compact power batteries used in pace-makers, mobile telephones, and laptops [66]. In order to improve the bulk properties of solid electrolytes, a good number of researchers are interested in the synthesis and characterization of lithium-ion conductors based on different classes of materials such as ceramics, polymers, glasses, and so on [65, 30]. They are motivated by the small ionic radius of  $Li^+$  cation, its low weight, ease of motion, and its appliance in high energy density batteries [67–71]. Therefore, we are proposing to innovate a new class of conductors based on nacrite-polytype clay [30].



**Scheme 1.** Schematic representation of the thermal transformations of heat-treated nacrite–LiCl hybrid from room temperature to 873K [30].

#### 4.5.1. Impedance Analysis

With the  $(-\text{Z}''')$  versus  $\text{Z}'$  representations (Figure 7), we observed the existence of semicircles in the complex plane from 548 K to 873 K. At high temperature, these semi-arcs shift toward higher frequencies with a significant reduction of their size. We point out that nacrite–LiCl hybrid becomes more conductive at high temperature. We think that this phenomenon is attributed to the existence of a deformation (destruction) of some physical characteristics of the host clay material framework and to some chemical characteristics of LiCl alkali halide [30].

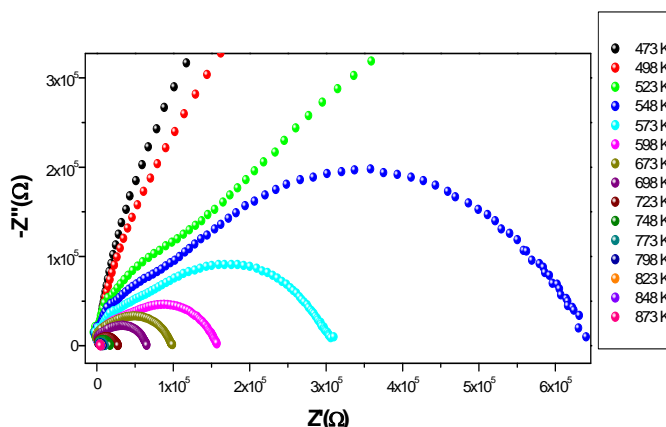


**Figure 7.** Nyquist diagram of nacrite–LiCl hybrid at a temperature range from 473 to 873 K [30].

#### 4.5.2. Electrical Conductivity

The  $\sigma_{dc}$  of nacrite–LiCl hybrid increases from  $(4.02 \cdot 10^{-6} \text{ S.m}^{-1})$  at 523 K to the  $(0.11 \cdot 10^{-2} \text{ S.m}^{-1})$  at 873 K. An Arrhenius behavior was observed for the hybrid. The  $E_{a(dc)}$  was determined from the slope of  $\log(\sigma_{dc} \cdot T)$  versus  $(1000 / T)$  and was found to be 0.84 eV and 0.82 eV, respectively, below and above 673 K [30]. The obtained values suggest an ionic conduction process. The  $\sigma_{ac}$  conductivity measurements at high frequencies (1 MHz) show that  $\sigma_{ac}$  increases from  $1.22 \cdot 10^{-4} \text{ S.m}^{-1}$  at 523 K to  $0.13 \cdot 10^{-2} \text{ S.m}^{-1}$  at 873 K. This remarkable increase is also related to the increase of the number of free ions in the hybrid matrix in terms of temperature [30]. The  $E_{a(ac)}$ , calculated in agreement with (Eq.(3)), corresponds to the free energy barrier that an ion has to overcome for a successful jump from one site to another. These values designate that the ionic transport mechanism can be interpreted by the thermally activated hopping process [72].

According to these experimental results, we deduce that the disordered hybrid bears easier motion than the ordered one [30]. We conclude that contribution of disorder and defects in the hybrid framework are responsible for the motion of charge carriers; this result is in agreement with the previous publication of Kumar and Yashonath [66, 30].

Furthermore,  $\text{Li}^+$  is known as an excellent current carrying ion in superionic solids motivated by its small ionic radius of 0.076 nm, lower weight, and ease of motion [66], but  $\text{Cl}^-$  anion appears to be rather less mobile than the cation due to its great ionic radius equal to 0.181 nm [66].

To conclude,  $\text{Li}^+$  is the common current carrier via hopping from one site to the next for both “metanacrite–LiCl hybrid” and “metanacrite– $\text{Li}_2\text{O}$  hybrid”. Since the “metanacrite– $\text{Li}_2\text{O}$  hybrid” phase is more amorphous than the “metanacrite–LiCl hybrid” phase, therefore it produces greater ionic conductivity. This shows that the conductivity was preferably affected by the amorphicity of the metanacrite framework through which mobile lithium ions may migrate.

$\text{Si}_2\text{Al}_2\text{O}_7 \cdot \frac{1}{2} \cdot L \text{ i}_2\text{O}$  hybrid's high conductivity ( $\sigma_{ac} \sim 10^{-2} \text{ S.m}^{-1}$ ) makes it an excellent candidate as electrolyte solid for lithium-ion batteries. Furthermore, this amorphous-type Li-ion conductor offers several advantages such as low cost and ease of handling. Its use instead of the conventional superionic conductors can drastically improve the safety aspects of lithium batteries [30].

## 5. Concluding Remarks

The structural and electrical properties of metanacrite synthesized from Tunisian nacrite were investigated in the first part of this work. The amorphous character of metanacrite was identified using XRD, IR, TEM, and EDXS analysis. Results of the electrochemical impedance spectroscopy show that the amorphous sample behaves like a semiconductor material. The present work gives possible valorization of Tunisian metanacrite as an interesting precursor to produce a new class of cementitious materials [29]. In the second part, structural experiments have been conducted in order to characterize the salt intercalation process between the nacrite

layers. The stable intercalated material has been characterized by XRD, TG, and IR analyses. The XRD pattern showed basal spacing at  $1.143 \pm 0.002$  nm with integral series of  $00l$  reflections, indicating an ordered structure of parallel 1:1 layers. The quantitative XRD analysis showed that best agreement between the observed and simulated patterns ( $R_p = 6.20\%$ ) was obtained with one  $\text{Cl}^-$  ion at  $z = 0.64 \pm 0.01$  nm, one  $\text{Li}^+$  ion at  $z = 0.96 \pm 0.01$  nm and one  $\text{H}_2\text{O}$  at  $z = 0.79 \pm 0.01$  nm in the interlamellar space of nacrite (per half-unit cell). The  $\text{Li}^+$  cation was located near the oxygen atom plane while the  $\text{Cl}^-$  anion was near the hydroxyl groups of the adjacent layer. The TG analysis of the hybrid produced showed a loss of water between 723 and 873 K, the weight loss (1 molecule per half unit cell) corresponding to the interlamellar water, in agreement with that showed by XRD. The positions of the  $\text{H}_2\text{O}$  molecules,  $\text{Li}^+$  and  $\text{Cl}^-$ , suggest an interaction between  $\text{Li}^+$  and the basal oxygen on one side and  $\text{Cl}^-$  and the surface hydroxyls on the other side. The  $\text{H}_2\text{O}$  can establish binding either with  $\text{Li}^+$  cation or  $\text{Cl}^-$  ions [49]. The investigation of the *ac* and *dc* conductivity of nacrite– $\text{LiCl}$  hybrid suggests that the suppression in the degree of crystallinity of the elaborated hybrid improves dramatically the ionic conduction, which is about ten orders of magnitude larger than the low temperature conductivity value. The activation energies for conduction measured at different temperatures indicate that the conduction mechanism is driven by hopping of  $\text{Li}^+$  ions from one site to the neighboring one [30].

Finally, Tunisian nacrite is a candidate for the production of metanacrite as a supplementary cementitious material and as a host material of nanohybrid owing to its high crystallinity and unique structure. Further studies are in progress to point out the use of nacrite to synthesize other materials for a wide range of applications.

## Author details

Nouha Jaafar\*, Hafisia Ben Rhaiem and Abdesslem Ben Haj Amara

\*Address all correspondence to: nouhajaafar@yahoo.fr

Laboratory of Physics of Lamellar Hybrid Materials and Nanomaterials, Department of Physics, Faculty of Sciences, Bizerte, University of Carthage, Tunis, Tunisia

## References

- [1] Hu XL, Michaelides A. The kaolinite (001) polar basal plane. *Surf Sci* 2010;604:111–7.
- [2] Miranda-Trevino JC, Coles CA. Kaolinite properties, structure and influence of metal retention on pH. *Appl Clay Sci* 2003;23:133–9.
- [3] Newman ACD. Chemistry of clays and clay minerals, Mineral. Soc. Engl. Monogr. Longman, Essex, England. p. 6. 1987.

- [4] Liew YM, Kamarudin H, Mustafa Al Bakri AM, Luqman M, Khairul Nizar I, Ruzaidi CM, Heah CY. Processing and characterization of calcined kaolin cement powder. *Construct Build Mater* 2012;30:794–802.
- [5] Bear FE. Chemistry of the Soil, 2nd edn. Reinhold Publishing, New York. 1965.
- [6] Cruz M, Jacobs J, Fripiat JJ. International Clay Conference Madrid. 1972;1:59.
- [7] Giese RF. *Clays Clay Miner* 1973;21:145.
- [8] Wolfe RW, Giese RF. *Clays Clay Miner* 1974;22:139.
- [9] Gupta SS, Krishna GB. Removal of Cd(II) from aqueous solution by kaolinite, montmorillonite and their poly(oxo zirconium) and tetrabutylammonium derivatives. *J Hazard Mater* 2006;128:247–57.
- [10] Sarma YC, Prasad C, Rupainwar DC. *J Ind Assoc Environ Manage* 1991;18:100.
- [11] Yavuz O, Altunkaynak Y, Guzel F. Removal of copper, nickel, cobalt and manganese from aqueous solution by kaolinite. *Water Res* 2003;37:948–52.
- [12] Heller-Kallai L, Lapides I. Reactions of kaolinites and metakaolinites with NaOH-comparison of different samples (Part 1). *Appl Clay Sci* 2007;35:99–107.
- [13] Siddique R, Klaus J. Influence of metakaolin on the properties of mortar and concrete: a review. *Appl Clay Sci* 2009;43:392–400.
- [14] Gardolinski JE, Peralta-Zamora P, Wypch FJ. *Colloid Interface Sci* 1999;211:137.
- [15] Ben Haj Amara A. X-ray diffraction, infrared and TGA/DTG analysis of hydrated nacrite. *Clay Miner* 1997;32:463–70.
- [16] Ben Haj Amara A, Ben Brahim J, Besson G, Pons CH. Study of intercalated nacrite with dimethylsulfoxide and n-methylacetamide. *Clay Miner* 1995;30:295–306.
- [17] Ben Haj Amara A, Ben Brahim J, Ben Ayed N, Ben Rhaiem H. Occurrence of nacrite in old Pb-Zn deposits from northern Tunisia. *Clay Miner* 1996;31:127–30.
- [18] Ben Haj Amara A, Ben Brahim J, Plançon A, Ben Rhaiem H, Besson G. Etude Structurale d'une Nacrite Tunisienne. *J Appl Crystallography* 1997;30:338–44.
- [19] Ben Haj Amara A, Plançon A, Ben Brahim J, Ben Rhaiem H. XRD Study of the stacking mode in natural and hydrated nacrite. *Mater Sci Forum* 1998a;278–81:809–13.
- [20] Ben Haj Amara A, Ben Brahim J, Plançon A, Ben Rhaiem H. X-Ray Diffraction study of the stacking modes of hydrated and dehydrated nacrite. *J Appl Crystallography* 1998b;31:654–62.
- [21] Ben Haj Amara A, Ben Rhaiem H, Plançon, A. Structural evolution of nacrite as a function of the nature of the intercalated organic molecules. *J Appl Crystallography* 2000;33:1351–9.

- [22] Bailey SW. Polymorphism of the kaolin minerals. *Am Mineralog* 1963;48:1197–209.
- [23] Leluk K, Orzechowski K, Jerie K, Baranowski A, Słonka T, Głowinski J. Dielectric permittivity of kaolinite heated to high temperatures. *J Phys Chem Solids* 2010;71:827–31.
- [24] Anthony GD, Garn PD. Kinetics of kaolinite dehydroxylation. *J Am Ceramic Soc* 1974;57:132–5.
- [25] McManus J, Ashbrook SE, MacKenzie KJD, Wimperis S.  $^{27}\text{Al}$  multiple-quantum MAS and  $^{27}\text{Al}^1\text{H}$  CPMAS NMR study of amorphous aluminosilicates. *J Non-Crystall Solids* 2001;282:278–90.
- [26] Sabir B, Wild S, Bai, J. Metakaolin and calcined clays as pozzolans for concrete: a review. *Cement Concrete Compos* 2001;23(6):441–54.
- [27] Mielenz RG, White LP, Glantz OJ. Effect of calcination on natural pozzolanas. *Am Soc Test Mater Special Technical Publication*. 1950;99:43–91.
- [28] Chakchouk A, Samet B, Mnif T. Study on the potential use of Tunisian clays as pozzolanic material. *Appl Clay Sci* 2006;33:79–88.
- [29] Jaafar N, Ben Rhaiem H, Ben Haj Amara A. Correlation between electrochemical impedance spectroscopy and structural properties of amorphous Tunisian metanacrite synthetic material. *Adv Mater Sci Eng* 2014a;1–10. Article ID: 469871. <http://dx.doi.org/10.1155/2014/469871>
- [30] Jaafar N, Naamen S, Ben Rhaiem H, Ben Haj Amara A. Elaboration of amorphous-clay hybrid:  $(\text{Al}_2\text{Si}_2\text{O}_7 \cdot 1/2 \text{Li}_2\text{O})$  designed as a single ion conducting solid electrolyte for Li-ion batteries. *Am J Anal Chem* 2014b;5:1261–72. <http://dx.doi.org/10.4236/ajac.2014.517132>
- [31] Austin IG, and Mott NF. Polarons in crystalline and noncrystalline materials. *Adv Phys* 1969;18:41–102.
- [32] Pollak M. On the frequency dependence of conductivity in amorphous solids. *Philos Magaz* 1971;23(183):519–42.
- [33] Pike GE. AC conductivity of scandium oxide and a new hopping model for conductivity. *Phys Rev B* 1972;6(4):1572–80.
- [34] Elliott SR. A theory of A.C. conduction in chalcogenide glasses. *Philos Magaz* 1977;36:1291–304.
- [35] Elliott SR. A.C. conduction in amorphous chalcogenide and pnictide semiconductors. *Adv Phys* 1987;36:135–218.
- [36] Springett, BE. AC conductivity of  $4.5 \text{ TiO}_2-x \text{ 2P}_2\text{O}_5$ . *J Non-Crystall Solids* 1974;15:179–90.

- [37] Giuntini JC, Deroide B, Belougne P, Zanchetta JV. Numerical approach of the correlated barrier hopping model. *Solid State Commun* 1987;62:739–42.
- [38] Bensimon Y, Giuntini, JC, Belougne, P, Deroide, B, Zanchetta JV. An example of A.C. conduction by correlated barrier hopping in amorphous molybdenum sulphides. *Solid State Commun* 1988;68:189–92.
- [39] Hummel RE. *Electronic Properties of Materials*, Springer, New York, NY, USA.1993.
- [40] Nefzi H, Sediri F, Hamzaoui H, Gharbi N. Dielectric properties and electrical conductivity of the hybrid organic-inorganic polyvanadates  $(H_3N(CH_2)_4NH_3)[V_6O_{14}]$ . *J Solid State Chem* 2012;190:150–6.
- [41] Deng Y, Norman White G, Dixon J. Effect of structural stress on the intercalation rate of kaolinite. *J Colloid Interface Sci* 2002;250(2):379–93.
- [42] Vagvolgyi V, Kovacs J, Horvath E, Kristof J, Mako E. Investigation of mechanochemically modified kaolinite surfaces by thermoanalytical and spectroscopic methods. *J Colloid Interface Sci* 2008;317:523–9.
- [43] Michaelian KH, Lapidés I, Lahav N, Yariv, Brodsky I. Infrared study of the intercalation of kaolinite by caesium bromide and caesium iodide. *J Colloid Interface Sci* 1998;204:389–93.
- [44] Martens WN, Frost RL, Kristof J, Horvath E. Modification of kaolinite surfaces through intercalation with deuterated dimethylsulfoxide. *J Phys Chem B* 2002;106(16):4162–71.
- [45] Horvath E, Kristof J, Frost RL, Mako E, Jakab E, Rédey A. Identification of super-active centers in thermally treated formamide intercalated kaolinite. *J Colloid Interface Sci* 2005;289:132–8.
- [46] Frost RL, Kristof J, Horvath E, Kloprogge JT. *J Colloid Interface Sci* 1999;214:109.
- [47] Komori Y, Sugahara Y, Kuroda K. A Kaolinite-NMF-methanol intercalation compound as a versatile intermediate for further intercalation reaction of kaolinite. *J Mater Res* 1998;13:930–4.
- [48] Zhang B, Li Y, Pan X, Jia X, Wang X. Intercalation of acrylic acid and sodium acrylate into kaolinite and their in situ polymerization. *J Phys Chem Solids* 2007;68(2):135–42.
- [49] Jaafar N, Naamen S, Ben Rhaiem H, Ben Haj Amara A. Functionalization and structural characterization of a novel nacrite-LiCl nanohybrid material. *Am J Anal Chem (Special Issue on X-Ray Diffraction)*. 2015;6:202–15. <http://dx.doi.org/10.4236/ajac.2015.63019>
- [50] Michaelian KH, Yariv S, Nasser A. Study of the interactions between caesium bromide and kaolinite by photoacoustic and diffuse reflectance infrared spectroscopy. *Can J Chem* 1991a;69:749–54.

- [51] Michaelian KH, Friesen WI, Yariv S, Nasser A. Diffuse reflectance infrared spectra of kaolinite and kaolinite/alkali halide mixtures. Curve-fitting of the OH stretching region. *Can J Chem* 1991b;69:1786–90.
- [52] Lapides I, Lahav N, Michaelian KH, Yariv S. X-ray study of the thermal intercalation of alkali halides into kaolinite. *J Thermal Analys* 1997;49:1423–32.
- [53] Naamen S, Ben Rhaiem H, Ben Haj Amara, A. XRD study of the nacrite/CsCl/H<sub>2</sub>O intercalation complex. *Mater Sci Forum* 2004a;443–444:59–64.
- [54] Naamen S, Ben Rhaiem H, Karmous, MS, Ben Haj Amara A. XRD study of the stacking mode of the nacrite/alkali halides complexes. *Mater Struct* 2004b;11.
- [55] Giese RF. Interlayer bonding in kaolinite, dickite and nacrite. *Clays Clay Miner* Pergamon Press. Printed in Great Britain. 1973;21:145–9.
- [56] Weiss A, Thielepape W, Orth H. Neue Kaolinit-Einlagerungsverbindungen. In: Rosenquist, T. and Graff-Petterson, P. (Eds.) *Proc Int Clay Conf* Israel University Press, Jerusalem. 1966;1:277–93.
- [57] Garrett WG, Walker GF. The cation-exchange capacity of hydrated halloysite and the formation of halloysite-salt complexes. *Clay Miner* 1959;4:75–80.
- [58] Wiewióra A, Brindley GW. Potassium acetate intercalation in kaolinites and its removal: effect of material characteristics. In Heller L. (Ed.) *Proc Int Clay Conf*, Israel University Press, Jerusalem. 1969;1723–33.
- [59] Howard SA, Preston KD. Profile fitting of powder diffraction patterns. In: Bish DL, Post JE. (Eds.) *Modern Powder Diffraction: Reviews in Mineralogy*. Mineralogical Society of America, Washington DC. 1989, pp. 217–275.
- [60] Yariv S, Lapides I, Michaelian KH, Lahav N. Thermal intercalation of alkali halides into kaolinite. *J Thermal Analys Calorimet* 1999;56:865–84.
- [61] Yariv S. Interactions of minerals of the kaolin group with cesium chloride and deuteration of the complexes. *Int J Trop Agri* 1986;5:310–22.
- [62] Frost RL, Kristof J, Horvath E, Kloprogge JT. *Spectrochim Acta A* 2000;56:1191.
- [63] Heller-Kallai L. Reactions of salts with kaolinite at elevated temperatures. *Clay Miner* 1978;13:221–35.
- [64] Gabor M, Poepl L, Koeros E. Effect of ambient atmosphere on solid state reaction of kaolin-salt mixtures. *Clays Clay Miner* 1986;34:529–33.
- [65] Minami T, Tatsumisago M, Iwakura C, Kohjiya S, Tanaka I. *Solid State Ionics for Batteries*. Springer, Berlin, 2005.
- [66] Kumar PP, Yashonath S. Ionic conduction in the solid state. *J Chem Sci* 2006;118:135–54.

- [67] Ghosh A, Kofinas P. PEO based block copolymer as solid state lithium battery electrolyte. *ECS Transac* 2008;11:131–7.
- [68] Wang M, Zhao F, Guo Z, Dong S. Poly(vinylidene fluoride-hexafluoropropylene)/organo-montmorillonite clays nanocomposite lithium polymer electrolytes. *Electrochim Acta* 2004;49:3595–602.
- [69] Morenoa M, Quijada R, Anaa MAS, Benaventea E, Romeroe PG, González G. Electrical and mechanical properties of poly(ethylene oxide)/intercalated clay polymer electrolyte. *Electrochim Acta* 2011;58:112–8.
- [70] He P, Chen B, Wang Y, Xie Z, Dong F. Preparation and characterization of a novel organophilic vermiculite/poly(methyl methacrylate)/1-butyl-3-methylimidazolium hexafluorophosphate composite gel polymer electrolyte. *Electrochim Acta* 2013;111:108 –13.
- [71] Prasanth R, Shubha N, Hng HH, Srinivasan M. Effect of nano-clay on ionic conductivity and electrochemical properties of poly(vinylidene fluoride) based nanocomposite porous polymer membranes and their application as polymer electrolyte in lithium ion batteries. *Eur Polymer J* 2013;49:307–18.
- [72] Réau JM, Rossignol S, TanguyB, Rojo JM, Herrero P, Rojas RM, Sanz J. Conductivity relaxation parameters of some  $\text{Ag}^+$  conducting tellurite glasses containing  $\text{AgI}$  or the  $(\text{AgI})_{0.75}(\text{TlI})_{0.25}$  eutectic mixture. *Solid State Ionics* 1994;74:65–73.

---

# **Clay/Biopolymer Composite and Electrorheological Properties**

---

Mehmet Cabuk

Additional information is available at the end of the chapter

<http://dx.doi.org/10.5772/62270>

---

## **Abstract**

The combination of clays with polymers having different characteristics opens a way to new composite materials showing novel properties. Electrorheological (ER) fluids show phase transition from a liquid to a solid-like state between the electrodes of a rheometer due to the interactions of polarized particles. Composite systems comprising biodegradable chitosan (CS) and natural bentonite (BNT) are important in ER applications. In this study, BNT/CS composites were synthesized by the *in situ* method. The structure and morphology of the synthesized composites were characterized using X-ray diffraction (XRD), thermo-gravimetric analysis (TGA), and scanning electron microscopy (SEM) techniques. Thermal stability was observed to increase with the presence of BNT clay. Conductivity of the composites was found the suitable range for ER measurements. According to ER results, BNT/CS composites were found to be sensitive to external electric field strength, exhibiting a typical shear thinning non-Newtonian viscoelastic behavior.

**Keywords:** Bentonite, clay/biopolymer composite, electrorheology, viscoelastic material

---

## **1. Introduction**

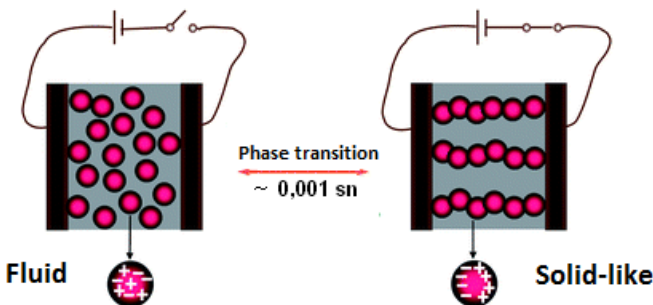
The combination of clays with polymers having different characteristics opens a way to new composite materials showing novel properties [1]. The clay component of the composites provides a potential for high carrier mobility; band gap tunability; a range of electric, magnetic, and dielectric properties; and thermal/mechanical stabilities. On the other hand, polymer component of the composites offers structural flexibility, convenient processing, and tunable electrical and electronic properties. A major attraction of such research activities is to combine these desired advanced properties in the organic/inorganic hybrid materials, which can even be improved in comparison with the intrinsic properties of each component. Various polymer/clay composites can be synthesized via different preparation methods, including polymer

intercalation into the layers of clays, in which clay minerals are offered various advantages such as high thermal stability, enhanced reinforcement, small particle size, layer expanding capabilities, and insolubility [2].

Bentonite (BNT) clays are largely composed of the mineral montmorillonite. It is constructed from octahedral alumina sheets sandwiched between two tetrahedral silicate sheets, which exhibit a net negative charge on the surface and can adsorb positive charges. BNT dispersions are widely used in industrial processes because of their exceptional rheological behavior. Compatibility with various polymers is accomplished by modifying the layers of BNT with surfactants via an ion-exchange reaction. When the BNT clay is exchanged with  $\text{Na}^+$  ion, it possesses an excellent swelling behavior in water, and interlayer spacing becomes large enough for the penetration of polymer chains [3].

## 2. Electrorheological fluids

Electrorheological (ER) fluids are heterogeneous colloidal suspensions whose properties strongly depend on an externally applied electric field [4]. Commonly, these kinds of fluids are suspensions containing polarizable solid particles (dispersed phase) and non-conducting oils (continuous phase). When an electric field is imposed, suspended particles in the suspension are polarized due to the mismatches of electrical conductivity and dielectric permittivity between the dispersed particles and the continuous phase. The ER fluid shows phase transition from a liquid to a solid-like state between the electrodes of a rheometer due to the interactions of polarized particles (Scheme 1). This solid-like fibrillation of particles is due to the electric field-induced increase in the apparent viscosity of suspensions [5].



**Scheme 1.** ER response of clay/biopolymer composite particles dispersed in silicone oil.

According to chemical contents of ER suspensions, dispersed phase can be composed of organic (i.e. polymer) or inorganic (i.e. clay) particles [6]. Composite systems comprising natural materials such as chitosan (CS) and BNT are important in ER applications. In addition, the synthesis and ER properties of composites containing different clay groups (montmorillonite, silica, etc.) were reported in the literature [7, 8].

## 2.1. Synthesis of bentonite/chitosan composites

This study was aimed at synthesizing BNT/CS composites by the intercalation method [9]. A definite amount of BNT [ $\text{SiO}_2$  (54.82%),  $\text{Al}_2\text{O}_3$  (20.27%),  $\text{Fe}_2\text{O}_3$  (9.08%),  $\text{MgO}$  (3.02%),  $\text{CaO}$  (2.10%),  $\text{Na}_2\text{O}$  (1.31%),  $\text{TiO}_2$  (0.78%), and  $\text{K}_2\text{O}$  (0.06%)] was dispersed in 1 wt.% acetic acid and stirred for 2 h with the presence of 0.1 g cetyltrimethylammonium bromide (CTAB) cationic surfactant. Then, a definite amount of CS [medium molecular weight (i.e.  $M_w = 190,000\text{--}300,000 \text{ g mol}^{-1}$ ) with 75–85% deacetylation degree] that was dissolved in 1 wt.% acetic acid was added into the aqueous dispersions. The mixture was stirred for 12 h for the intercalation of CS chains between BNT layers. Then, the dispersion was transferred into a flask containing 0.5 M  $\text{NaOH}_{(\text{aq})}$  and stirred for 2 h for neutralization. It is known that CS is soluble in weak acids and insoluble in alkaline medium. The crude BNT/CS composite particles were recovered from  $\text{NaOH}_{(\text{aq})}$  solution and washed with distilled water until the particles were neutral. Finally, the BNT/CS composites obtained were dried in a vacuum oven at 60°C for 2 days. By this method, three different biodegradable BNT/CS composites were synthesized and coded as BNT/CS(1%), BNT/CS(5%), and BNT/CS(25%).

## 2.2. Electrorheological measurements

Silicone oil (SO) was used in a continuous phase ( $\rho = 0.965 \text{ g/cm}^3$ ,  $\eta = 1 \text{ Pa s}$ ,  $\varepsilon = 2.61$  at 25°C). The sample suspensions were prepared in SO at a series of concentrations ( $c = 5\text{--}25 \text{ wt.\%}$ ), dispersing definite amount of dispersed phase in calculated amount of continuous phase (SO) according to formula (1):

$$c = \left( \frac{m_{\text{dispersed phase}}}{m_{\text{dispersed phase}} + m_{\text{continuous phase}}} \right) \times 100 \quad (1)$$

ER properties of the suspensions were determined with a Thermo-Haake RS600 parallel plate torque electrorheometer (Germany). The gap between the parallel plates was 1.0 mm, and the diameters of the upper and lower plates were 35 mm. The voltage used in these experiments was supplied by a 0–12.5 kV (with 0.5 kV increments) direct current electric field generator (Fug Electronics, HCL 14, Germany), which enabled the creation of resistivity during the experiments.

## 3. Results and discussion

### 3.1. Characterization results

Average particle sizes, densities, and conductivities of the samples were given in Table 1. The diffraction pattern of BNT indicated the crystalline nature, whereas CS showed the amorphous nature. The XRD pattern of pure BNT has sharp peaks around  $2\theta = 8^\circ, 18^\circ, 21^\circ, 26^\circ$ , and  $28^\circ$  that are typical of BNT [10]. The XRD pattern of BNT/CS composites has peaks with relatively

lower intensities than that of BNT. This indicates that the amorphous structure of CS covers the crystalline structure of BNT, which confirms the more amorphous nature of the composites. According to the TGA curves of the samples in contrast to pure CS, the residual amounts of the composites increased with increasing BNT content as follows:  $(89\%)_{BNT} > (86\%)_{BNT/CS(1\%)} > (81\%)_{BNT/CS(5\%)} > (57\%)_{BNT/CS(25\%)} > (30\%)_{CS}$ . This tendency can be attributed to high thermal stability of the BNT component. These thermal stability results of BNT/CS composites are very suitable for potential and industrial applications as new ER materials [11]. According to the SEM results, CS chains not only intercalated inside the interlayer spaces of BNT but also settled on the surface of BNT layers (flocculated) [12]. The flocculated formation of the composites could be due to the hydroxylated edge–edge interaction of the silicate layers between the silicate hydroxylated edge groups and the CS chains.

Samples	Conductivity ( $S \text{ cm}^{-1}$ ) $\times 10^5$	Density ( $\text{g cm}^{-3}$ )	Average particle size ((m))
CS	5.88	1.035	65
BNT	1.51	1.245	11
BNT/CS(1%)	1.01	1.158	14
BNT/CS(5%)	1.71	1.122	23
BNT/CS(25%)	3.45	1.116	51

**Table 1.** Some physical properties of the samples.

### 3.2. Electrorheological properties

The electric field viscosities of BNT/CS/SO suspensions increased with increasing electric field strength and reached to 470, 980, 550, and 515 Pa s under  $E = 1 \text{ kV/mm}$ , respectively (Fig. 1). BNT/SO ER fluid exhibited to enhance ER effect with applied electric field to improve the particles' polarization ability and a typical shear thinning non-Newtonian viscoelastic behavior [13]. When  $E$  was applied to the ER suspension, the magnitude of the polarization forces between particles increased and the particles rapidly formed fibrillar structure perpendicular to the electrodes, which resulted in enhanced electric field–induced viscosity.

For the composites, the highest electric field viscosity (980 Pa s) was obtained for BNT/CS(1%)/SO suspension under  $E = 1 \text{ kV/mm}$ , whereas the lowest electric field viscosity (515 Pa s) was obtained for BNT/CS(25%)/SO suspension under the same field strength. This result may be attributed to a decrease in the mutual action between the particles due to increasing particle size or BNT content, which reduces the possibility of the formation of strong chains between the upper and lower electrodes. Shear stress is one of the critical design parameters in ER phenomenon. The change of electric field–induced shear stress ( $\tau_E$ ) of the suspensions increased with the increasing electric field strength as follows:  $(190 \text{ Pa})_{BNT/CS(1\%)} > (118 \text{ Pa})_{BNT/CS(5\%)} > (95 \text{ Pa})_{BNT/CS(25\%)} > (88 \text{ Pa})_{BNT}$  under  $E = 1 \text{ kV/mm}$ .

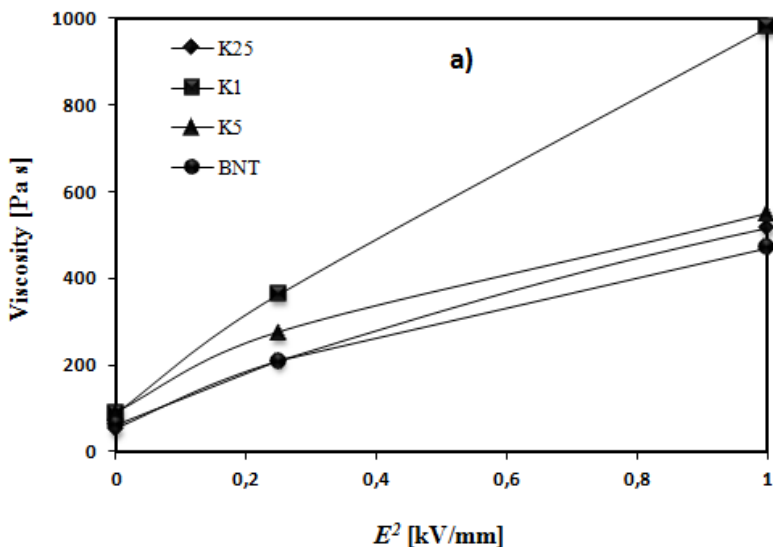


Figure 1. Effect of electric field strength on viscosity, K1: BNT/CS(1%), K5 : BNT/CS(5%), and K25 : BNT/CS(25%), ( $T = 25^\circ\text{C}$ ,  $c = 25$  wt.%, and  $\dot{\gamma} = 0.2 \text{ s}^{-1}$ ).

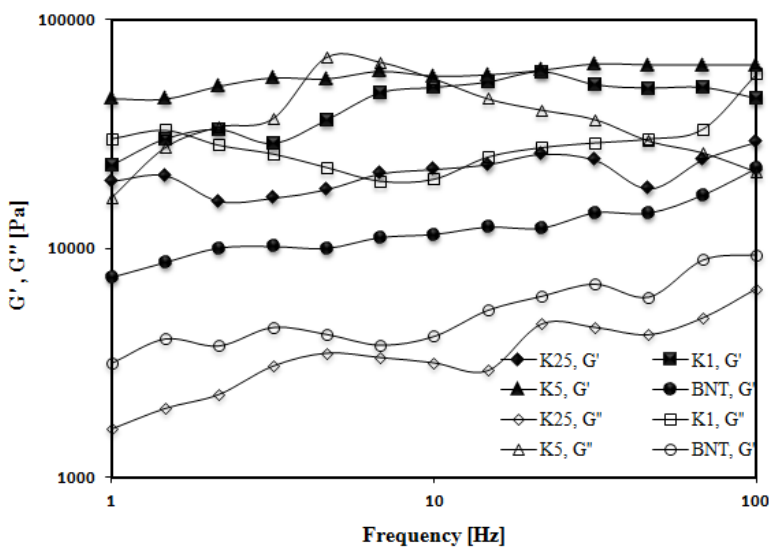


Figure 2. Change in  $G'$  and  $G''$  with frequency, K1: BNT/CS(1%), K5 : BNT/CS(5%), and K25 : BNT/CS(25%), ( $c = 25$  wt.%,  $T = 25^\circ\text{C}$ ,  $\tau = 10 \text{ Pa}$ , and  $E = 1 \text{ kV/mm}$ ).

The external frequency is an essential factor for characterizing the dynamic viscoelastic properties of ER fluids. Storage modulus ( $G'$ ) and loss modulus ( $G''$ ) values of CS/SO, BNT/SO and BNT/CS/SO suspensions slightly increased with increasing frequency (Fig. 2). These variations in  $G'$  and  $G''$  correspond to energy change occurring during dynamic shear process and are strongly dependent on the interactions between CS chains and BNT layer interphases in the suspension [14].

The  $G'$  values of the prepared suspensions are higher than  $G''$  values. According to this result, strong interactions were developed between CS and BNT interphases, which enhance the elastic properties of these composites.

In conclusion, characterization results confirmed the introduction of the CS side chains into the BNT layers. ER activities of the suspensions increased with increasing electric field strength, dispersing particle concentration, and decreasing shear rate. Viscoelastic properties of the suspensions enhanced due to the interactions between BNT and CS. BNT-based ER fluids with improved ER and viscoelastic behaviors could be a good candidate as a smart material for ER applications.

## Author details

Mehmet Cabuk\*

Address all correspondence to: mehmetcabuk@sdu.edu.tr; mhmtcbk@gmail.com

Department of Chemistry, Faculty of Arts and Sciences, Süleyman Demirel University, Isparta, Turkey

## References

- [1] Zhang A., Sun L., Xiang J., Hu S., Fu P., Su S. & Zhou Y. (2009) Removal of elemental mercury from coal combustion flue gas by bentonite–chitosan and their modifier, *Journal of Fuel Chemistry and Technology*, 37, 489–495.
- [2] Yilmaz K., Akgoz A., Cabuk M., Karaagac H., Karabulut O. & Yavuz M. (2011) Electrical transport, optical and thermal properties of polyaniline–pumice composites, *Materials Chemistry and Physics*, 130 (3), 956–961.
- [3] Brindley G.W. & Brown G. (1980) *Crystal Structures of Clay Minerals and Their X-ray Identification*. Mineralogical Society, London.
- [4] Jang W.H., Cho Y.H., Kim J.W., Choi H.J., Sohn J.I. & Jhon M.S. (2001) Electrorheological fluids based on chitosan particles, *Journal of Materials Science Letters*, 20, 1029–1031.

- [5] Wu S. & Shen J. (1996) Electrorheological properties of chitin suspensions, *Journal of Applied Polymer Science*, 60, 2159–2164.
- [6] Li H., Yunling J., Shuzhen M. & Fuhui L. (2007) Synthesis and electrorheological property of chitosan phosphate and its rare earth complex, *Journal of Rare Earths*, 25, 15–19.
- [7] Kim J.W., Noh H.M., Choi H.J., Lee D.C. & Jhon M.S. (2000) Synthesis and electro-rheological characteristics of SAN-clay composite suspensions, *Polymer*, 41, 1229–1231.
- [8] Park D.P., Sung J.H., Kim C.A., Choi H.J. & Jhon M.S. (2004) Synthesis and electro-rheology of potato starch phosphate, *Journal of Applied Polymer Science*, 91, 1770–1773.
- [9] Badawy M.E.I. & Rabea E.I. (2009) Potential of the biopolymer chitosan with different molecular weights to control postharvest gray mold of tomato fruit, *Postharvest Biology and Technology*, 51, 110–117.
- [10] Tilki T., Karabulut O., Yavuz M., Kaplan A., Cabuk M. & Takanoglu D. (2012) Irradiation effects on transport properties of polyaniline and polyaniline/bentonite composite, *Materials Chemistry and Physics*, 135 (2–3), 563–568.
- [11] Ksiezopolska A. & Pazur M. (2011) Surface properties of bentonite and illite complexes with humus acids, *Clay Minerals*, 46, 149–156.
- [12] Lee D., Char K., Lee S.W. & Park Y.W. (2003) Structural changes of polyaniline/montmorillonite nanocomposites and their effects on physical properties, *Journal of Materials Chemistry*, 13, 2942–2947.
- [13] Xiang L. & Zhao X. (2006) Preparation of montmorillonite/titania nanocomposite and enhanced electrorheological activity, *Journal of Colloid and Interface Science*, 296, 131–140.
- [14] Yavuz M. & Cabuk M. (2006) Electrorheological properties of pumice/silicone oil suspension, *Journal of Material Science*, 42, 2132–2137.



---

# Ceramic Materials Based on Clay Minerals in Cultural Heritage Study

---

Rodica-Mariana Ion, Radu-Claudiu Fierăscu, Sofia Teodorescu,  
Irina Fierăscu, Ioana-Raluca Bunghez, Daniela Țurcanu-Caruțiu and  
Mihaela-Lucia Ion

Additional information is available at the end of the chapter

<http://dx.doi.org/10.5772/61633>

---

## Abstract

The artifacts belonging to the ceramic heritage are mostly based on all clay types used by humans over the ages, because the sources of clays were easily available and people were interested to produce ceramics and pottery. This is the reason why the conservation of cultural heritage is of great concern. Ceramics (Greek κεράμιον Keramion) is a material obtained by shaping and firing clay. In the Romanian history, many ceramic pieces, of great diversity, have been discovered, and most of them are used in traditional households. Ceramic materials based on clay minerals in cultural heritage (ceramic heritage) involve techniques of characterization of raw materials and ceramic objects based on clays, discovered in different archaeological sites, leading to some results about the production technology, provenance, authentication, and historical appartenance on Romanian territory. The chemical composition of ancient ceramics and pigments decorating them, excavated from different Romanian archaeological sites, suggested a chemical composition of ceramic based on clay minerals (kaolinite, illite, and smectite), while the pigments belonging to them contained red pigments (hematite or ocher), manganese oxides (brown pigments), and magnetite or carbon of vegetable origin (black-pigmented layers).

**Keywords:** Cultural heritage, clays, pottery, ceramics, Transylvania tiles

---

## 1. Introduction

In ancient times, sources of clays were widely available, between them soils or surface sediments have been the proper sources for ceramics without further treatment, due to their natural mixture of plastic and nonplastic components [1]. Ceramics is an inorganic nonmetallic

material obtained through thermal processing of natural raw materials at relatively high temperature [2]. The raw materials are clays with finely divided quartz (sand) (0.02–0.04 mm) and feldspar, responsible for the rheology along the thermal processing. Clay is a group of minerals in earth that is granular; plastic, when mixed with a little water; or hard and brittle, if combusted. The clay is composed of hydrated aluminum silicates, with the addition of an appreciable amount of other elements: magnesium, iron, calcium, and potassium [3,4]. The clays retain fluid water (liquid) (from pores between clay particle aggregates) at low temperature, molecular water from the surface of particles or crystallites at medium temperature, and, sometimes, neutral molecules ( $H_2O$ ) or ionic hydroxyl groups ( $OH^-$ ) liberated at higher temperatures during thermal processing [5–7]. The production of ceramics was first implemented in the Neolithic period. The Greeks and Romans developed lime mortar cements, with a remarkable resistance, and some of these archaeological sites stand testimony to this day [8]. The Industrial Revolution of the eighteenth and nineteenth centuries registered significant improvements in the ceramic industry, while the twentieth century contributed to the scientific understanding of these materials. Conservation and restoration of cultural heritage has become one of the main concerns worldwide. In this respect, there is particular interest for investigations by nondestructive techniques some unique heritage ceramics for their subsequent preservation and restoration. These nondestructive analytical methods are able to provide information on composition/chemical nature of cultural artifacts, selected parts and materials in order to elucidate their origin, state of degradation (surface and/or internal) objects as a result of exposure over a period to environmental conditions, and the effects/effectiveness of strategies to conservation/restoration during their implementation.

### 1.1. Traditional ceramics

The traditional ceramics involve those materials that are derived from common, naturally occurring raw materials such as clay minerals and quartz sand. The traditional ceramics is manufactured from naturally occurring raw materials: silicates—compounds based on silica ( $SiO_2$ ) and unmodified or chemically modified aluminosilicates (alumina [ $Al_2O_3$ ] plus silica). In addition, the raw materials used in traditional ceramics could be classified into three groups: clay, silica, and feldspar [9].

Clay minerals such as kaolinite ( $Al_2[Si_2O_5][OH]_4$ ) generated either by the weathering of igneous rocks under the influence of water, dissolved carbon dioxide, and organic acids, or from feldspar ( $KAlSi_3O_8$ ) eroded from rocks such as granite and deposited in lake beds, which are aluminosilicates that contain sodium (Na), potassium (K), or calcium (Ca) with a composition from  $NaAlSi_3O_8$  and  $KAlSi_3O_8$  to  $CaAlSi_3O_8$ . Feldspar acts as fluxing agents to reduce the melting temperatures of the aluminosilicate phases where they are subsequently transformed into clay [10]. Except feldspar, silica, as the second major ingredient in refractories, is usually added as quartz sand, sandstone, or flint pebbles [11]. The role of silica is either to maintain the shape during firing (as filler) or to improve the final mechanical properties.

The behavior of ceramics depends on its chemical, physical, and mechanical properties [7]. In the ancient ceramics, the main minerals are gehlenite ( $Ca_2Al_2SiO_7$ ), anorthite ( $CaAl_2Si_2O_8$ ), quartz ( $SiO_2$ ), belite ( $\beta-Ca_2SiO_4$ ), and carbonates/calcite ( $CaCO_3$ ) and/or dolomite

(CaMg(CO<sub>3</sub>)<sub>2</sub>). For ceramics with limestone as raw material, the fired products may also contain akermanite (Ca<sub>2</sub>MgSi<sub>2</sub>O<sub>7</sub>), gehlenite (Ca<sub>2</sub>(Al,Fe,Mg)(Si,Al)<sub>2</sub>O<sub>7</sub>), and Mg-silicates (e.g., diopside and CaMgSi<sub>2</sub>O<sub>6</sub>) [12,13].

## 2. Background

### 2.1. Romanian history of ceramics

Ceramics, until the twentieth century, was essentially used for utilitarian purposes for ritual acts. At first, craftsmen did not know the potter's wheel, but they were very skilled at shaping and baking clay. Ceramic art painting in white, black and red, with models of great beauty and originality, was spread over a territory more extensive than present-day Romania and perfected for almost 2000 years [14]. The pottery techniques are extremely important for archaeologists as a source of results about cultural groups and their distribution areas. Through fragments of pottery, one can identify intercultural links or movements of populations in certain geographical areas [15]. For example, Romania's geographical region consists of Wallachia until Jiu Valley in Dobrogea, southwest Moldova and southeast Transylvania, and extending south to the Aegean Sea.

Some of the most relevant ceramic types specific to Romania are:

- **Cucuteni** (village in the county of Iași) **mankind ceramics**, 5000–6000 years ago, between the Carpathians and Dnieper, for nearly a millennium, a remarkable Neolithic culture flourished, known as the most relevant example of the relationship between man and clay. These ceramics are widespread in Moldova, northeast Muntenia, and southeast Transylvania, and Bessarabia site is characterized by a very high-quality ceramic that is technically rich with varied paintings [15, 16]. One of the most well-known Cucuteni ceramics, a representative of Romanian culture, is shown in Figure 1. This civilization is a representative of the Chalcolithic period from southeastern Europe and as a valuable source of data on the transformations of the human social evolution, pointing out the following aspects: social, cultural, and technological development, which played a significant role in generating an early form of ranked societies.
- **Monteoru ceramics**, one of the most well-researched Bronze Age times at the north of the Danube, is formed in parts of hilly north and northeast Muntenia and spread quickly in southern Moldova (including east of Prut) and points toward the Carpathian Mountains.
- **Culture Wietenberg** was developed in central Transylvania together with Coțofeni culture that take potteries decorated with mature style, with some Schneckenberg influences.
- **In Gumelnița culture**, the ceramics is especially black and sometimes brown (brick-red rare). Both are weathered, with various shapes and decorations, and the latter carved in relief and barbotined or graphite painted.
- **Hamangia culture** is the oldest Neolithic culture in Dobrogea with a long flowering period, which lasted until the birth of Pontic Gumelnița period.



Figure 1. Cucuteni ceramics

For ancient ceramics, the methodological exact sciences have their beginning in the sixth decade of twentieth century, when it was widely used in X-ray diffraction (XRD) technique [18], investigation of thermal expansion [19], and optical microscopy ceramic artifact analysis [20]. In the next decade, new analytical methods such as Mössbauer spectroscopy [21], differential thermal analysis [22,23], and electron microscopy [24, 25] were explored. Through improvements in the investigation methods in the last decade of the twentieth century, the characterization of such ceramics reached impressive new levels [26–28]. The eighth decade of the twentieth century coincided with the development of some methods based on SEM that currently dominates the studies about pottery. The use of these methods allowed for a better understanding of structural changes due to the different types of clay burning at different temperatures [14], which allowed the extraction of information, enabling economic and social outline of the communities that produced these artifacts. At present, the world can identify and understand the most stages of the technological process of making ceramics in different chronological periods and in different cultures.

It is important to use modern chemical analysis, both nondestructive (which can be in some cases fully noninvasive) methods and destructive methods of modern microanalysis, for small samples analysis [29–32]. They may be extremely valuable in the provenance investigation of an object, the origin of the materials used for its manufacture, in determining its degradation state and, finally, to choose the most suitable methods of restoration and conservation, the type of materials for conservation, and also in monitoring the progress of conservation processes, or to identify the fake art objects [33]. The main aspects of ceramic characterization are classification, production technology, and provenance through specific techniques for chemical and mineralogical characterization: spectroscopic techniques (FT-IR, Raman, XRD, EDXRF, and ICP-AES) and thermoanalytical techniques [34].

## 2.2. Analytical techniques for investigation

Modern chemical methods and measuring techniques can be used for archaeometric purposes. Some analytical techniques have been investigated with exemplification for different Romanian artifacts.

### 2.3. Methods and apparatus

**Thermal analysis** presented in the following chapter helped in the characterization of pottery in order to conclude about the chemical and phase composition, and it was recorded with a Mettler 4000 TA, TG 50 analyzer system at a rate of  $10^{\circ}\text{C min}^{-1}$  in a static air atmosphere; PerkinElmer thermoanalyzer TG S-2; and DTA 1700 at a rate of  $10^{\circ}\text{C min}^{-1}$ . A sample (15 mg) of finely ground stones were subjected to analysis in a Pt plate at a temperature range of 35–1000 oC ( $10^{\circ}\text{C min}^{-1}$ ). This concluded that the archaeological pottery was fired at relatively high temperatures.

**Energy-dispersive X-ray fluorescence (EDXRF)** analyses were performed with an PW4025 apparatus, type Minipal PANalytical, with a Si(PIN)-detector and an Rh tube with an acceleration voltage of 30 kV. Due to varying surface structures and inhomogeneities in the surface composition of the samples, the analyses are usually performed on both sides of the objects and a mean value is calculated, when the analysis must be completely nondestructive. When possible, the sample is powdered, so a representative homogenous sample can be obtained. An XRF is known as the first powerful, commercial, fast, nondestructive, and relatively accurate technique for qualitative as well as semiquantitative chemical analysis.

**Inductively coupled plasma—atomic emission spectrometry (ICP-AES)** was used to quantify minor and trace elements. Detection limit for major elements is under the ppm level and the analytical precision calculated from replicate analysis is  $\pm 1\%$ . For the ICP-AES measurements (usually with Varian equipments), the samples are finely powdered in an agate mortar and then mineralized with a microwave-assisted digestion oven with the use of high-pressure closed Teflon PFA vessels (with a mixture of 5 ml HF 40% and 5 ml  $\text{HNO}_3$  65%) and pressure and temperature control. Multielement matrix-matched standards were used for the quantitative determinations.

**X-ray diffraction (XRD)** patterns were recorded on a DRON UM1 diffractometer, operating at 32 kV and 25 mA, using  $\text{Co K}\alpha$  radiation ( $1.79021 \text{ \AA}$ ) with an iron filter. The diffractometer is connected to the PC, so the collected data can be analyzed and interpreted using either the dedicated program or other specific data analysis software.

**Fourier transform IR spectroscopy (FT-IR)** standard spectra were collected by using a PerkinElmer Spectrum GX spectrometer, for a range of 400–4000 scans and a spectral resolution of  $4 \text{ cm}^{-1}$ . It was possible to use the drift accessory with the powdered pure substance, thereby allowing for a better and easier analysis.

**The Raman spectroscopy** analysis performed with **Raman spectra** has been recorded with a First Guard Raman apparatus, BaySpec with two wavelengths (1,064 and 785 nm). The Raman system includes a “superhead” optic fiber for noncontact measurements, with a  $50\times$  long

working distance (LWD)-visible Olympus lens. The spectral data were processed with a software application dedicated to the file generation of Raman spectra. The spectral resolution was  $3\text{ cm}^{-1}$ . All the spectra were recorded in the  $200\text{--}3,400\text{ cm}^{-1}$  domain.

### 3. Case studies

#### 3.1. Ceramics from Schneckenberg culture (sixteenth century), Dealul Melcilor, Brașov, Romania

Sampling, reported in Table 1, was performed at the ruins of the Schneckenberg culture (sixteenth century), Dealul Melcilor, Brașov, Romania. Some examples of the investigated ceramic samples are shown in Figure 2.



Figure 2. Different ceramic samples

It is interesting that this region conserved many cultures (Vatina, Gârla Mare, Luciu de Sus, Wietenberg and Otomani). Eight differently fabricated contemporary pottery samples were selected for characterization, as shown in Table 1.

Clay minerals, as the main material for production of ceramics and pottery, show some characteristic reactions—dehydroxylation, decomposition, transformation—during the firing (heating effects,  $20\text{--}800^\circ\text{C}$ ), and several steps for reconstruction of former production conditions are identified, knowing that the temperature at which ancient ceramics and pottery were fired varies over a wide range ( $600\text{--}800^\circ\text{C}$ ) depending on the type of clay used. Thermogravimetric (TG) analysis and differential thermogravimetric (DTG) analysis are very important characterization methods used for the control of the reaction process and of the properties of the materials obtained [35–38]. The presence of some minerals is related to the ceramics firing process, giving information about the manufacture technology of the pottery. For a firing temperature higher than  $900^\circ\text{C}$  (observed for all the analyzed samples), a certain conclusion had been reached that the glazed ceramics was usually fired at temperatures ranging from

900°C to 950°C, mostly due to the reaction between quartz and carbonates when the temperature reaches 900°C.

No.	Sample	Color/location
1	Ceramic	Black/Dealul Melcilor
2	Ceramic	Grey/Dealul Melcilor
3	Ceramic	Red/Dealul Melcilor
4	Ceramic	White/Dealul Melcilor
5	Ceramic	Green/Dealul Melcilor
6	Ceramic	Brown/Dealul Melcilor
7	Ceramic	Brașov tile
8	Ceramic pot	Brașov medieval customs/Bran-Brașov

**Table 1.** The ceramic samples analyzed

Thermal analysis enables detection of exothermic and endothermic peaks (effects due to gain/loss of enthalpy) occurring in the sample when undergoing controlled heating and compares to an inert reference material [39–46]. The endothermic peak around 100°C is due to moisture water, whereas those appearing at about 200–250°C are attributed to “bound” water, or to “hydrated” interlayer cations (as in swelling clay minerals). The TG/DTG diagrams for different colored ceramics are shown in Figure 3.

Figure 4 shows the TG/DTG diagram for the Transylvania tile ceramics.

Some effects have been observed as follows:

- endothermic effects attributed to gypsum appear in the range 120–160°C [47];
- endothermic peak that could be attributed either to water lost from iron hydroxides, or to recrystallization of amorphous and/or crystallized Fe-oxy hydroxides appears at 300°C, through an exothermic peak in the range 300–350°C.
- some exothermic peaks in the range 550–650°C could be attributed to some organic matter (binder used in the preparation of the ceramic paste, or external coating).

In both cases, an abrupt increase in weight starts immediately at room temperature and lasts up to 200°C. To our knowledge, such thermoanalytical behavior of pottery samples has never been observed previously.

Usually, the ceramic heritage contains mostly the following clay types: kaolinites (kaolinite, dickite, nacrite, and halloysite), illites (illite, hydrous micas, phengite, glauconite, and celadonite), smectites (montmorillonite, beidellite, and saponite), vermiculites, and palygorskite (palygorskite and sepiolite). Some minerals, such as kaolinite, illite, and smectite, show strong endothermic peaks (in the range 550–650°C (higher for chlorite)), and some endothermic peaks are at 840°C (single peak)—for calcite and dубlets at 780°C and 860°C—for dolomite. They are

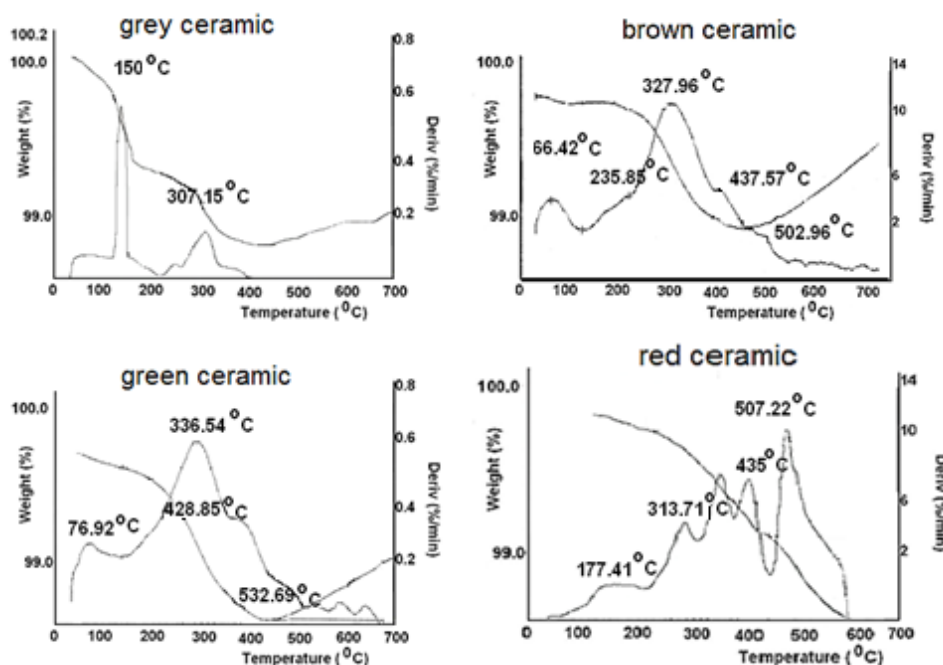


Figure 3. Thermal analyses of colored ceramics

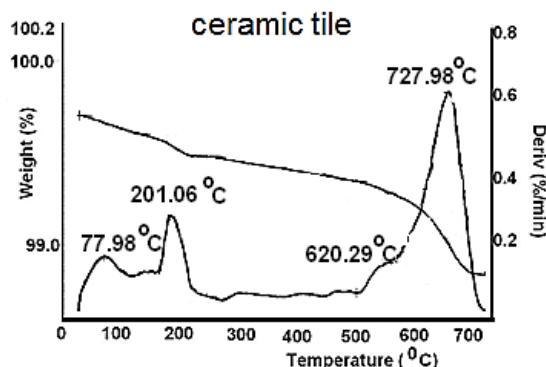


Figure 4. Thermal analyses of tile ceramics

due to the escape of CO during the breakdown of their structure (other carbonates are unusual in ancient ceramic materials). The presence of these characteristic thermal effects indicates that the primary minerals survived the firing processes required to destroy the structure of the minerals. The DTA curves of salts are complex, and their interpretation needs familiar

experience with the technique, and also information from other analytic techniques, such as XRD, XRF, ICP-AES, FT-IR [48], micro-chemical tests, and microanalyses (scanning electron microscopy and energy-dispersive X-ray microanalysis (SEM-EDX)).

The X-ray diffraction, as one of the most important techniques for potteries analysis, led to the identification of the following mineral phases: quartz, kaolinite, illite, gibbsite, goethite, feldspar, and mixed layers (smectite/illite). The presence of illite peak in X-ray diffraction patterns indicates the presence of calcite, too. We observe that quartz, kaolinite, and K-feldspar are common elements. These are basic constituents of the original clay matrix.

From profile of the DTG curves, the clays could be classified as Ca-rich and Ca-poor raw clays. **Ca-poor ceramics** include quartz, feldspar, and micas.

For them some processes could be observed:

- for calcite presence, which decomposes by oxidation at lower temperature than illite, generated CaO is visible until 800°C.
- hygroscopic water is visible at 80°C, and gypsum at 145°C.
- for almost all clay minerals, their decomposition is visible in the region 580–640°C [33,49–54].

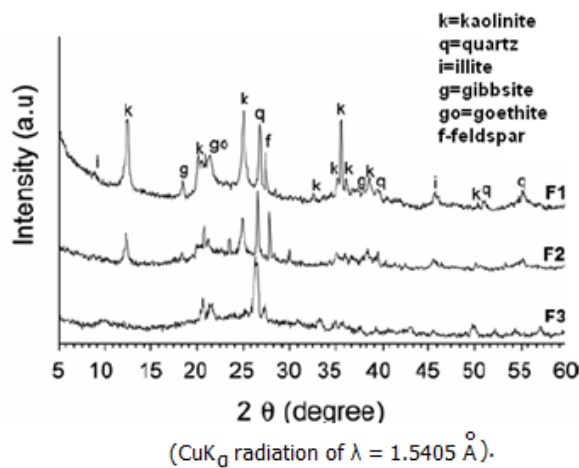
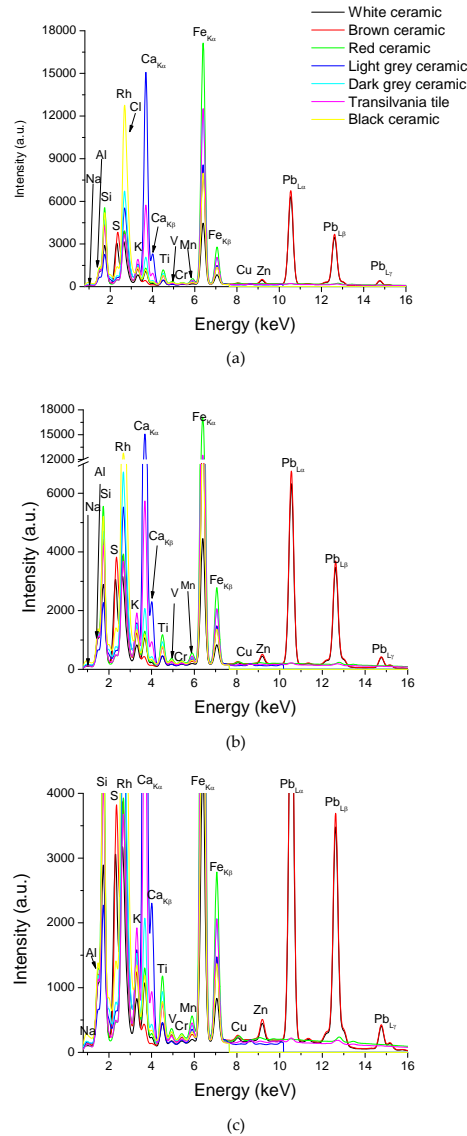


Figure 5. XRD diagram for tile (F1) and ceramics (green (F2) and brown (F3))

**The Ca-rich ceramics** (with CaO content >5%) include kaolinite, illite, and chlorite. They show peaks at about 640°C, where clay minerals decompose. The samples present very low firing temperatures (740°C), and CaO has an important role in the transformation process of the ceramic matrix. The red bricks show extensive vitrification with iron oxide phases dispersed almost homogeneously in the vitreous matrix (allocated to large hematite crystals surrounded by lepidolite) [55]. In the ceramics with higher percentage of CaO, calcium aluminosilicate microcrystalline is obtained, simultaneously with a color difference, due to the trapping of iron

in the augite lattice [56]. A denser, less porous, and more durable ceramics is observed for the red bricks, mostly due to a higher vitrification.



**Figure 6.** (a) XRF spectra of the analyzed samples. (b) XRF spectra of the analyzed samples: a break was inserted in order to observe the variation of the elements; the color codes are the same as for Figure 6 a. (c) XRF spectra of the analyzed samples: the intensity scale was modified in order to observe the variation of the minor elements; the color codes are the same as for Figure 6 a.

Quartz, feldspar, white mica, biotite-like mica, iron oxides, and calcite are the main phases present, but the archaic ceramics contain smaller amounts of detrital feldspar. Also, ilmenite, sphene, zircon, rutile, spinel, epidote, apatite, and monazite have been identified by EDXRF (Figure 6 a,b,c) and SEM in some samples [57]. Cs and Rb concentrations are influenced by the presence of K-feldspar and mica (Cs and Rb are substitute for K). This observation, coupled with their low K<sub>2</sub>O and Na<sub>2</sub>O content and high Al<sub>2</sub>O<sub>3</sub> content, suggests that during the preparation of the raw materials, the potters production followed a procedure, probably “levigation,” separating the less fine nonplastic particles such as K-feldspar and albite. Th and Sc are considered as proper sensors for ancient ceramics provenance due their insolubility and their reduced effects on metamorphism, weathering, and diagenesis [58,59].

Element	Ceramic	Enamel
Si	25.3%	5.56%
Ti	10.1%	15.3%
Al	3,34%	6.42%
Fe	3.05%	4.17%
K	1.21%	0,49%
Na	1.19%	2,97%
Ca	0.28%	0.93%
Ba	0.11%	2.27%
Mg	702 ppm	0.15%
Zr	147 ppm	0.056%
Mn	355 ppm	0.025%
Cr	85.3 ppm	84 ppm
Zn	71.2 ppm	97 ppm
Sr	46.4 ppm	0.026%
Li	24.9 ppm	41%
Ag	1.99 ppm	49 ppm
Pd	—	0.015%
Pb	—	26.2%
Cu	—	0.68%
Tl/Bi	—	26%
P	—	0.22%
Sb	—	0.17%
As	—	5.4 ppm
Au	—	55%

**Table 2.** Major and trace elements ICP-AES analytical results for ancient ceramics and raw material sample (in wt.% and ppm)

The presence of certain chemical elements in the composition of ceramic samples and in the composition of the enamel can provide interesting data on the types of materials used in the

medieval period. Some of these elements are found in the recipes used in painting [60–64]. The fact that the composition was found in zirconia ceramics is proof of the use of bentonite as raw material [15,33].

The degradation of the ceramic parts can be explained by the presence of potassium. Depending on environmental conditions, potassium becomes potassium hydroxide by artifact drying and then potassium carbonate by reacting with CO<sub>2</sub> from the atmosphere. The presence of KOH makes the area around the vessel to become alkaline, this being responsible for corrosion layer present only in enamel. This is the reason that it should be kept in a controlled humid environment to prevent the subsequent artifacts degradation [30].

Piesa/element	Green paint	Blue paint	White paint	Ceramics
Na <sub>2</sub> O	—	3	4.2	—
MgO	2	—	2.1	2.9
Al <sub>2</sub> O <sub>3</sub>	20.2	18.5	24.2	17.6
SiO <sub>2</sub>	30.2	36.9	36	52.6
SO <sub>3</sub>	12.1	—	—	0.63
Cl	5.46	3.4	5.79	2.1
K <sub>2</sub> O	2.23	3.89	1.67	3.45
CaO	2.16	2.2	3.27	9.66
TiO <sub>2</sub>	1.29	1.21	1.63	0.985
V <sub>2</sub> O <sub>5</sub>	0.02	0.03	0.03	—
Cr <sub>2</sub> O <sub>3</sub>	0.04	0.05	0.041	0.04
MnO	0.043	0.04	0.079	0.22
Fe <sub>2</sub> O <sub>3</sub>	1.53	2.17	1.96	9.17
Co <sub>3</sub> O <sub>4</sub>	0.070	0.24	0.02	0.069
NiO	0.1	0.36	0.02	—
CuO	0.047	0.064	0.042	0.02
As <sub>2</sub> O <sub>3</sub>	0.03	0.35	--	—
PbO	22.3	36.9	18.7	0.17
ZnO	—	—	—	0.03

**Table 3.** Chemical composition of artifacts detected by XRF and XRD

From Tables 2 and 3, similarities for different tempers can be observed, as a proof that most samples fall close, but the ceramic fragment containing sand and feldspar are less similar.

SiO<sub>2</sub> and Al<sub>2</sub>O<sub>3</sub> together comprise more than 50 wt.% of the ceramic chemical composition. The alkali oxides (K<sub>2</sub>O, Na<sub>2</sub>O, CaO, and MgO) constitute together less than 5 wt.% and Fe<sub>2</sub>O<sub>3</sub>

reaches 10 wt.% on average. A high H<sub>2</sub>O value (10 wt.% on average) is observed, which is too high for burned ceramic material. The Al<sub>2</sub>O<sub>3</sub> and H<sub>2</sub>O contents explain the great abundance of clay-derived minerals, and confirm the abundance of partial dehydroxylation of clay material derived from kaolinite (main mineral of the ceramics) [65].

The chemical and mineralogical data, as well as textural aspects, conclude that the main raw material for ceramic elaboration comes from fine-grained clay quartz-rich material. Some important conclusions could be reached:

- When SiO<sub>2</sub> concentration is high, the sample contains quartz sand.
- When the sample contains feldspar, the concentration of K, Na, Ca increases the firing temperature. Kaolinite is the main mineral of the ceramics [66].
- K<sub>2</sub>O, Na<sub>2</sub>O, MgO, and CaO build the feldspar (microcline and albite) and together indicate the presence of illite, hematite, maghemite, goethite, and anatase in the raw material.
- The extremely high SiO<sub>2</sub> contents correspond, besides clay-derived material and the abundance of quartz, to sand grains and rock fragments. The predominance of SiO<sub>2</sub> (61.2%), Al<sub>2</sub>O<sub>3</sub> (34%), Fe<sub>2</sub>O<sub>3</sub> (2%), CaO (<10%), MgO (<3%), and 1.3% loss on ignition confirm clay-derived minerals, quartz, and some iron oxyhydroxides as the main minerals of ceramic fragments. The chemical composition of high-quality refractory clays is as follows: silicon oxide, aluminum oxide, and 2% iron oxide.
- The P<sub>2</sub>O<sub>5</sub> contents relatively high for clay material normally are responsible for amorphous to criptocrystalline (Al,Fe) phosphate.
- The water contents are still high (5.6–8.9 wt.%) showing the rehydration of the ceramic vessel after their discharge and the formation of the soil with black earth.
- Barium, phosphorus, and even Pb seem to be the anomalous elements found in the ceramic fragments of Scheneckenberg. The anomalous values of Ba were frequently found in the ceramic fragments with temper.
- The iron contents represent hematite and goethite, and some maghemite, minerals also identified in the studied ceramic fragments. Maghemite is responsible for the red color of the potteries. This phase is formed by partial dehydroxylation of clay material (visible at 600 °C). These potteries are used for cooking. They contain elements such as Mg, Ca, Ba, Zn, Pb, Y, from aluminum phosphates and Ba-Mn oxyhydroxides.
- After breaking, these potteries in long contact with soil concentrate in P, Mg, Ca, Mn, Ba, Zn, and Pb. In this phase, hematite and maghemite rehydrate and form kaolinite and goethite, respectively.

### 3.2. Archaeometric investigation of medieval polychrome glazed pottery

The composition and origin of the tile sample taken from the Medieval Customs archaeological site, Bran region, Brașov County, dating back to the seventeenth and the eighteenth centuries, have been used at first for ceramic composition for making ceramics and for the composition

of paints used to decorate this tile. The chemical composition of ancient pigments is an important criterion for the identification of pottery preservation, decoration, and technology used. The study was focused on red, brown, and black pigments from a pre-Roman pottery—a Transylvania tile, Figure 7 [67].

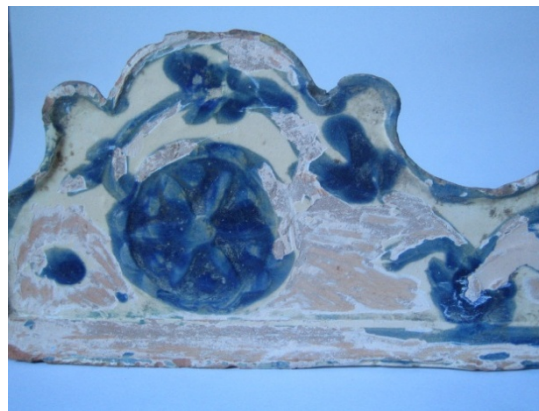


**Figure 7.** Transylvania tile

### 3.2.1. Historical aspects

It seems like ancient tiles appeared in Germany around 1300. The tiles were more advantageous than open fireplace due to storage of warmth and for elimination of smoke in the room. Their use is common in our country and quickly spread throughout Europe, thanks to their advantages. The oldest tile known to us dates from the early fifteenth century. These are unglazed and they represent biblical scenes, mythological strange mermaids with fish or snake tail and wing, real or fantastic animals, pictures knighthood, geometrical, and floral motifs. The tiles could be glazed and polychrome painted with cobalt blue, green, yellow, and brown pigment-based enamel. Besides functionality, tiles were always meticulously decorated in relief. They had to be not only stove plates, but beautiful objects, providing protection and comfort family space. We have too few studies about the representations that appear on Transylvania tiles, how they were chosen, who were favorite reasons, motivations, and their symbolism elections. It is interesting to follow the trail forms and reasons in the European recurrence in different cultures. It seems that often the choice of decoration for tiles was linked to beliefs and rituals apotropaic, popular superstitions. In this respect, chimney, hearth were considered passageways, as well as threshold or window. Transitional spaces were exposed to evil spirits, evil eye, magic outside. And inside the house, the stove was considered a dangerous object, which could cause fire and smoke poisoning of the occupants of the house. Hence the need for home care through icons and symbols apotropaic fireplace [68]. An analysis of the compositions of the Roman ceramics reveals that the latter tend to have lower concentrations in Cs, Rb, K<sub>2</sub>O, Na<sub>2</sub>O, and CaO and higher in Al<sub>2</sub>O<sub>3</sub>.

### 3.2.2. Ceramics support

Ceramic is a type of kaolin as hydrated aluminum silicate double, feldspar formed by the decomposition of igneous rocks and by the action of carbonic acid and water, under pressure, and subjected to high temperatures. The clays are some of the most common rocks from the earth, with smaller grains of 0.002 mm, composed of a complex mixture of clay minerals: kaolinite, illite, montmorillonite, etc. These are aluminum and magnesium silicate hydrate, made from altered feldspar and other silicates. They add muscovite, feldspar, heavy minerals (zircon, ilmenite, rutile, magnetite, garnets, etc.), fragments of shells, and other sulfide minerals as diagenetic, glauconite, calcite, and very fine particles of minerals from rock unspoiled page of complex colloidal silicate, hydrated, and the remnants of organic substances. The chemical composition of clays varies by minerals they contain. Ceramic clays and semi-acid clays are used in brick masonry construction, terracotta tiles, or cement. Semi-acid clays have a content of approximately 30%.  $\text{Al}_2\text{O}_3$  can be used for the extraction of alumina in the synthesis process; and strong base and basic clays (refractory clays) are used in the manufacture of refractory chamotte for the manufacture of fine ceramics. Clays always contain a greater or lesser amount of impurities, which reduce refractoriness [69].

### 3.2.3. Pigments for glazed tile

For aesthetic and for a consistent colored ceramic, pigments are used with metallic oxides and different salts. Pigments vary from green to blue-green to blue. They can be used as dyes in clay bodies and glazes, directly or mixed with water. The coating is constituted of lead-alkali glass with the addition of copper or iron ions as coloring agents.

The presence of the oxides is vital. For example, chrome oxide gives green color, but it may fume or volatilize. If tin is present in a white or pastel glaze, the chrome reacts with the tin to create a pink coloration. If zinc oxide is present in the glaze, a dirty-brown color will be obtained. For green color, cobalt-zinc-alumina-chromite blue-green pigment system could be used, where varying the amounts of cobalt and chrome oxides produces a green ceramic color. Many pigments have mineral origin with different colors; for example, ocher: red and yellow; cinnabar: bright red; azurite: blue; malachite: green; lime: white; carbonized bone: black. As organic pigments red madder and murex shell purple are used, and as binding media, egg, casein, and wax.

The chemical compositions of the ancient ceramics and pigments used are shown in Table 4.

Except all these techniques, FT-IR has been used for ceramic composition identification, including the assignment on the basis of the typical wavenumbers of the contributions to the FTIR absorbance spectra of minerals given in the Sadler database "Minerals and Clays" [70]. Making a distinction of clays present in the samples was also a difficult task: the contribution centered at  $\sim 1033 \text{ cm}^{-1}$  can be attributed both to illite and montmorillonite. Montmorillonite is visible at the peak from  $\sim 615 \text{ cm}^{-1}$ , while the band centered at  $\sim 1,633 \text{ cm}^{-1}$  could be attributed to illite spectrum. Montmorillonite could be derived from hydrolysis process occurring during the burial period of the findings [71]. Calcite, as clearly shown by the FT-IR spectrum in which the large band centered at about  $1444 \text{ cm}^{-1}$  and the contribution at about  $870 \text{ cm}^{-1}$ , typical of

this mineral, is present. The absorptions from the main quartz phase ( $\text{Si}-\text{O}$ ) could also be easily identified in the FTIR spectrum of ceramics and pigments used for glaze (Figure 8; 1163, 1083, 798, 778, 695, 514  $\text{cm}^{-1}$ ) [72]. The several intense bands in the range 800–550  $\text{cm}^{-1}$  (725, 646, 584  $\text{cm}^{-1}$ ) are characteristic of the metal–oxygen vibrations in the ceramic samples [73]. However, additionally the characteristic carbonate (calcite phase) vibrations at 1795, 1430, 876, 713  $\text{cm}^{-1}$  [74] and M–O vibrations at 725, 685, 642, 580, 531  $\text{cm}^{-1}$  could also be determined. Characteristic  $\text{Si}-\text{O}$ ,  $\text{C}-\text{O}$ , and M–O stretchings could be easily identified in all FT-IR spectra. Broadbands between 3700–3000  $\text{cm}^{-1}$  can be assigned to the adsorbed water (or water of crystallization) and O–H vibrations of glazed pottery. This could be associated with specific surface properties of pottery, which stimulate adsorption of moisture from atmosphere at ambient conditions.

Compound	Green pigment	Blue pigment	White pigment	Ceramic
$\text{Na}_2\text{O}$	—	3	4.2	—
$\text{MgO}$	2	—	2.1	2.9
$\text{Al}_2\text{O}_3$	20.2	18.5	24.2	17.6
$\text{SiO}_2$	30.2	36.9	36	52.6
$\text{SO}_3$	12.1	—	—	0.63
$\text{Cl}$	5.46	3.4	5.79	2.1
$\text{K}_2\text{O}$	2.23	3.89	1.67	3.45
$\text{CaO}$	2.16	2.2	3.27	9.66
$\text{TiO}_2$	1.29	1.21	1.63	0.985
$\text{V}_2\text{O}_5$	0.02	0.03	0.03	—
$\text{Cr}_2\text{O}_3$	0.04	0.05	0.041	0.04
$\text{MnO}$	0.043	0.04	0.079	0.22
$\text{Fe}_2\text{O}_3$	1.53	2.17	1.96	9.17
$\text{Co}_3\text{O}_4$	0.070	0.24	0.02	0.069
$\text{NiO}$	0.1	0.36	0.02	—
$\text{CuO}$	0.047	0.064	0.042	0.02
$\text{As}_2\text{O}_3$	0.03	0.35	—	—
$\text{PbO}$	22.3	36.9	18.7	0.17
$\text{ZnO}$	—	—	—	0.03

**Table 4.** Chemical composition of the Transylvania tile

The Raman spectra collected have to be compared with those obtained previously from reference materials. Published libraries of spectra are now widely available in the literature on historical pigments [75,76], enamel and glazing pigments [77], modern synthetic pigments [78],

modern inks [79], gums, waxes, varnishes, resins and other binders of historical and archaeological importance [80,89], minerals [70,90,91], and plant fibers [92]. As already mentioned, Raman scattering is a very weak phenomenon that requires an intense monochromatic light source to generate a readily detectable effect. Also, the use of lasers has allowed a wider choice of excitation lines, with wavelengths ranging from 351.1 nm to 1064 nm. In Raman spectra, the hematite ( $\alpha\text{-Fe}_2\text{O}_3$ ) bands are identified at 613 (s); 408 (s); 227 (m); 204 (w)  $\text{cm}^{-1}$ , whereas 663  $\text{cm}^{-1}$  band indicates the presence of magnetite ( $\text{Fe}_3\text{O}_4$ ) [94]. The 1329 $\text{cm}^{-1}$  band is also assigned to hematite. When the sample has been produced in an oxidizing atmosphere, the most important indicator is the hematite [90,93]. If magnetite is present, this is an indicator of its incomplete phase transformation into hematite [91].

The Raman spectrum of the tile ceramic is shown in Figure 9. The representative Raman band for beta-quartz is located at 462  $\text{cm}^{-1}$ , while the medium intense 507 $\text{cm}^{-1}$  band is assigned to albite (Na-feldspar). Specific bands appear here: 462, 401, 356  $\text{cm}^{-1}$ , all being attributed to quartz. The band from 506  $\text{cm}^{-1}$  together with the shoulder around 600  $\text{cm}^{-1}$  indicates the presence of hematite. All these are more pronounced for not-glazed face (red colored spectrum). The broadband around 1350–1500 $\text{cm}^{-1}$  is due to amorphous carbon, 461  $\text{cm}^{-1}$  band is assigned to  $\beta$ -quartz. Also, in the Raman spectrum of the ceramic supports, the medium intense –550  $\text{cm}^{-1}$ —band reveals the presence of hematite, as shown in Figure 10.

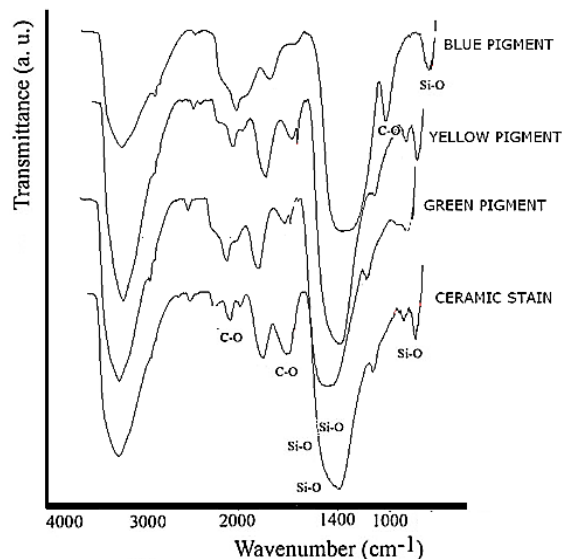


Figure 8. FT-IR spectra of the pigments

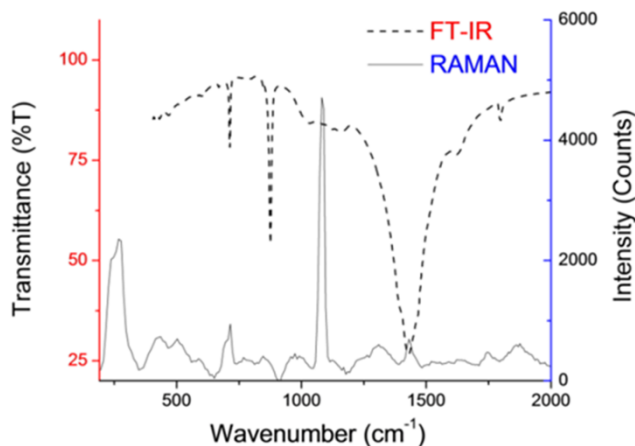


Figure 9. FT-IR and RAMAN spectra of calcite

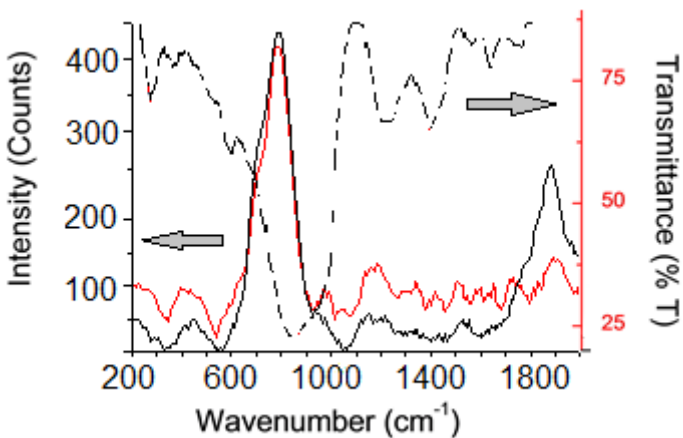


Figure 10. FT-IR and RAMAN spectra of the ceramic tile

#### 4. Conclusions

Many ceramic pieces known as ceramic heritage have been discovered, characterized by specific techniques of characterization either for raw materials or ceramic objects based on clays, discovered in different archaeological sites, leading to some results about the production technology, provenance, authentication, and historical appartenance. The chemical composi-

tion of ancient ceramics and pigments decorating them, excavated from different Romanian archaeological sites, suggested a chemical composition of ceramic based on clay minerals (kaolinite, illite, and smectite), while the pigments belonging to them contain hematite or ocher (a red pigment), manganese oxides (brown pigments), and magnetite or carbon of vegetable origin (black-pigmented layers).

## Acknowledgements

This paper received the financial support of the projects: PN 09.09.03.07, PNII 222/2012 and PNII project 261/2014.

## Author details

Rodica-Mariana Ion<sup>1,2\*</sup>, Radu-Claudiu Fierăscu<sup>1</sup>, Sofia Teodorescu<sup>3</sup>, Irina Fierăscu<sup>1</sup>, Ioana-Raluca Bunghez<sup>1</sup>, Daniela Turcanu-Caruțiu<sup>4</sup> and Mihaela-Lucia Ion<sup>5</sup>

\*Address all correspondence to: rodica\_ion2000@yahoo.co.uk

1 ICECHIM, Nanomedicine Research Group, Bucharest, Romania

2 Valahia University, Nanomaterials Research Center, Târgoviște, Romania

3 Valahia University, Multidisciplinary Science and Technology Research Institute of Valahia University of Târgoviste - ICSTM, Târgoviște, Romania

4 Ovidius University, Art Faculty, Constanța, Romania

5 Valahia University, History Faculty, Târgoviște, Romania

## References

- [1] Barden L., Sides G.R., (1970). *The engineering behavior of compacted clay*, Journal of the Soil Mechanics and Foundations Division, ASCE 96(SM4): 1171–1200.
- [2] Grim R.E., (1968). *Clay Mineralogy*, 2nd ed., McGraw-Hill Book Company, New York, NY.
- [3] Biot M.A., (1956). *General solutions of the equations of elasticity and consolidation for a porous material*, Journal of Applied Mechanics, Transactions of ASME 78: 91–96.

- [4] Campanella R.G., Mitchell J.K., (1968). *Influence of temperature variations on soil behavior*, Journal of the Soil Mechanics and Foundations Division, ASCE 94(SM3): 709–734.
- [5] Martin R.T., (1960). *Adsorbed water on clay: A review*, Clays and Clay Minerals 9(1): 28–70.
- [6] Martin R.T., (1962). *Adsorbed water on clay*, In: Swineford A. (ed.), Proceedings of the Ninth National Congress on Clays and Clay Minerals, Pergamon Press, New York, NY, pp. 28–70.
- [7] Grim R.E., (1959). *Physico-chemical properties of soils: Clay minerals*, Journal of the Soil Mechanics and Foundations Division, ASCE 85(SM2): (1959) 1–17.
- [8] Maniatis Y., (2009). *The Emergence of Ceramic Technology and Its Evolution as Revealed with the use of Scientific Techniques*, In: Shortland A.J., Freestone I., Rehren T., From Mine to Microscope: Advances in the Study of Ancient Technology, Oxford: Oxbow Books, Chapter 2, pp. 11–28.
- [9] Bergaya F., Lagaly G., (2000). *General introduction: Clays, clay minerals and clay science*, In: Bergaya F., Theng B.K.G., Lagaly G. (eds.), Handbook of Clay Science. Elsevier, Amsterdam, (2000) pp. 1–18.
- [10] Schofield R.K., Samson H.R., (1954). *Flocculation of kaolinite due to the attraction of oppositely charged crystal faces*, Faraday Society, London 18 (1954) 135–145.
- [11] Abercrombie H.J., Hutcheon I.E., Bloch J.D., de Caritat, P., (1994). *Silica activity and the smectite-illite reaction*, Geology 22 (1994) 539–542.
- [12] Guggenheim S., Martin R.T., (1995). *Definition of clay and clay mineral: Joint report of the aipea nomenclature and cms nomenclature committees*, Clays and Clay Minerals, 43(2), 257–259;
- [13] Stolman J.B., Burton J. H., Haas J., (1992). *Chemical and petrographic characterizations of ceramic pastes: Two perspectives on a single data set*, In: NeV H. (ed.), Chemical Characterization of Ceramic Pastes in Archaeology. Madison: Prehistory Press, pp. 85–92
- [14] Maniatis Y., Tite M.S., (1981). *Technological examination of Neolithic - Bronze Age pottery from central and southeast Europe and from the Near East*, Journal of Archaeological Science 8 (1981) 59–76.
- [15] Ion R.M., Ion M.L., Fierăscu R., Dumitriu I., Rugină F., Coșuleț St., Niculescu V.I.R., (2007), *Studii de arheometrie asupra unor artefakte ceramice din patrimoniul muzeal românesc – Analele Universitatii Valahia din Târgoviște – secțiunea Ingineria Materialelor și Mecatronica* 5, 62–68.
- [16] Dumitrescu V., (1985), *Prehistoric Art in Romania*. Meridiane Publishing House. (in Romanian)
- [17] Ellis L., (1980). *Analysis of Cucuteni-Tripolye and Kurgan pottery and the implications for ceramic technology*, Journal for Indo-European studies 8 (1985) 211–230.

- [18] Perinet G., (1960). *Contribution de la diffraction des rayons X à l'évaluation de la température de cuisson d'une céramique*, 7th International Ceramic Congress (1960) 370–376.
- [19] Cole W.F., Crook D.N., (1962). *A study of fired-clay bodies from Roman times*, Transition of the British Ceramic Society 61 (1962) 299–315.
- [20] Cowgill U.M., Hutchinson G.E., (1969). *A chemical and mineralogical examination of the ceramic sequence from Tikal, El Petén, Guatemala*, American Journal of Science 267 (1969) 465–477.
- [21] Bouchez R., Coey J.M.D., Coussemant R., Schmidt K.P., Rossum M.V., Aprahamian J., Deshayes J., (1974). *Möessbauer study of firing conditions used in the manufacture of the grey and red ware of Tureng-Tepe*, Journal de Physique 35 (1974) 540–546.
- [22] Kingery W.D., (1974). *A note on the determination of the differential thermal analysis of archaeological ceramics*, Archaeometry 16 (1974) 109–112.
- [23] Slager S., Plas L., Doesburg J.D.J., (1978). *Examination of LBK potsherds from Heienheim*, Analecta Praehistorica Leidensia XI (1978) 193–201.
- [24] Tite M.S., Maniatis Y., (1975). *Examination of ancient pottery using the scanning electron microscope*, Nature 257 (1975) 122–123.
- [25] Maniatis Y., Tite M.S., (1978/9). *Examination of Roman and Medieval Pottery Using the Scanning Electron Microscope*, Acta Praehistoria et Archaeologica 9/10 (1978/9) 125–130.
- [26] González García F., Romero Acosta V., García Ramos G., González Rodríguez M., (1990). *Firing transformations of mixtures of clays containing illite, kaolinite and calcium carbonate used by ornamental tile industries*, Applied Clay Science 5 (1990) 361–375.
- [27] Duminuco P., Messiga B., Riccardi M.P., (1998). *Firing process of natural clays. Some microtextures and related phase compositions*, Thermochimica Acta 321 (1998) 185–190.
- [28] Spataro M., (2011). *A comparison of chemical and petrographic analyses of Neolithic pottery from South-eastern Europe*, Journal of Archaeological Science 38 (2011) 255–269.
- [29] Fierăscu R.C., Dumitriu I., Ion M.L., Catangiu A., Ion R.-M., (2009). *Surface and analytical techniques study of Romanian coins*, European Journal of Science and Theology, 5(1) 17–28.
- [30] Dumitriu I., Fierăscu R.C., Catangiu A., Neață M., Ion R.M., Șomoghi R., (2011). *A synthetic approach into the restoration and conservation of metal artifacts (coins)*, Journal of Optoelectronics and Advanced Materials 13, 874–878.
- [31] Ion R.M., Radovici C., Fierăscu R.C., Fierăscu I., (2015). *Thermal and mineralogical investigations of iron archaeological materials*, Journal of Thermal Analysis and Calorimetry, DOI 10.1007/s10973-015-4659-0.

- [32] Dumitriu I., Fierăscu R.C., Ion R.M., (2011). *Analytical methods in archaeometry: Study of support material*, Scientific Study & Research, Chemistry & Chemical Engineering, Biotechnology, Food Industry 12, 17–24.
- [33] Ion R.M., Ion M.L., Fierăscu R.C., Serban S., Dumitriu I., Radovici C., Bauman I., Coșuleț S., Niculescu V.I.R., (2010). *Thermal analysis of Romania ancient ceramics*, Journal of Thermal Analysis and Calorimetry, 102, 393–398.
- [34] Salazar A., Vergara L., (2011), *ICA mixtures applied to ultrasonic nondestructive classification of archaeological ceramics*, Eurasip Journal on Advances in Signal Processing, Vol. 2010, 11 pages.
- [35] Cardiano P., Sergi S., De Stefano C., Ioppolo S., Piraino P., (2008). *Investigations on ancient mortars from the basilian monastery of Fragal*, Journal of Thermal Analysis and Calorimetry 91, 477–485.
- [36] Krapukaityte A., Tautkus S., Kareiva A., Zalieckiene E., (2008). *Thermal analysis—a powerful tool for the characterization of pottery*, Chemija 19, 4–8.
- [37] Franquelo M.L., Robador M.D., Ramirez-Valle V., Duran A., Jimenez de Haro M.C., Perez-Rodriguez J.L., (2008). *Roman ceramics of hydraulic mortars used to build the Mi-thraeum house of Merida (Spain)*, Journal of Thermal Analysis and Calorimetry 92, 331–335.
- [38] Ion R.M., Dumitriu I., Fierăscu R.C., Ion M.-L., Pop S.F., Radovici C., Bunghez R.I., Niculescu V.I.R., (2011). *Thermal and mineralogical investigations of historical ceramic: A case study*, Journal of Thermal Analysis and Calorimetry 104, 487–493.
- [39] Papadopoulou D.N., Zachariadis G.A., Anthemedis A.N., Tsirliganis N.C., Stratig J.A., (2004). *Microwave-assisted versus conventional decomposition procedures applied to a ceramic potsherd standard reference material by inductively coupled plasma atomic emission spectrometry*, Analytica Chimica Acta 505, 173–181.
- [40] Hein A., Tsolakidou A., Iliopoulos I., Mommsen H., Buxeda i Garrigos J., Montana G., Kilikoglou V., (2002). *Standardisation of elemental analytical techniques applied to provenance studies of archaeological ceramics: An inter laboratory calibration study*, Analyst 127, 542–553.
- [41] Mirti P., Gulmini M., Perardi A., Davit P., Elia D. (2004). *Technology of production of red figure pottery from Attic and southern Italian workshops*, Analytical and Bioanalytical Chemistry 380, 712–718.
- [42] Ghedini N., Sabbioni C., Pantani M., (2003). *Thermal analysis in cultural heritage safeguard: an application*, Termochimica Acta 406, 105–113.
- [43] Fessas D., Signorelli M., Schiraldi A., Kennedy C.J., Wess T.J., Hassel B., Nielsen K., (2006). *Thermal analysis on parchments I: DSC and TGA combined approach for heat damage assessment*, Termochimica Acta 447, 30–35.

- [44] Branda F., Luciani G., Costantini A., Piccioli C., (2003). *Interpretation of the thermogravimetric curves of ancient Pozzolanic concretes*, Archaeometry 43, 447–453.
- [45] Drebushchak V.A., Mylnikova L.N., Drebushchak T.N., Bodyrev V.V., (2005). *The investigation of ancient pottery—application of thermal analysis*, Journal of Thermal Analysis and Calorimetry 82, 617–626.
- [46] Drebushchak VA., Mylnikova LN., Drebushchak TN., (2011). *The mass-loss diagram for the ancient ceramics*, Journal of Thermal Analysis and Calorimetry 104(2), 459–466.
- [47] Shackelford F., Doremus RH., (2008). *Ceramic and Glass Materials: Structure, Properties and Processing* (2008), p.1.
- [48] Dumitriu I., Fierăscu R.C., Bunghez R.I., Pop S.F., Doncea S.M., Ion M.L., Ion R.M., (2011). *Analytical methods for artefacts complex analysis*, Revue Roumaine de Chimie 56, 931–940.
- [49] Shoval S., Beck P., (2005). *Thermo-FTIR spectroscopy analysis as a method of characterizing ancient ceramic technology*, Journal of Thermal Analysis and Calorimetry 82, 609–616.
- [50] Sondi I., Slovenec S., (2003). *The mineralogical characteristics of the Lamboglia 2 Roman-Age Amphorae from the Central Adriatic (Croatia)*, Archaeometry 45, 251–262.
- [51] Papadopoulou D., Sakalisa A., Merousis C.N., Tsirliganis N.C., (2007). Study of decorated archaeological ceramics by micro X-ray fluorescence spectroscopy, Nuclear Instruments and Methods in Physics Research 580, 743–746.
- [52] Papadopoulou D.N., Lalia-Kantouri M., Kantiranis N., Stratis J.A., (2006). *Thermal and mineralogical contribution to the ancient ceramics and natural clays characterization*, Journal of Thermal Analysis and Calorimetry 84, 39–45.
- [53] Mojumdar S.C., Sain M., Prasad R.C., Sun L., Venart J.E.S., (2007). *Selected thermoanalytical methods and their applications from medicine to construction, Part I*. Journal of Thermal Analysis and Calorimetry 90, 653–662.
- [54] Mothe C.G., Ambrosio R.M.C., (2007). *Processes occurring during the sintering of porous ceramic materials by TG/DSC*, Journal of Thermal Analysis and Calorimetry 87, 819–822.
- [55] Ion R.M., Dumitriu I., Boroş D., Isac D., Ion M.L., Fierăscu R.C., Catangiu A., (2008). *Characterization of corrosion products on roman mirror*, Metalurgia International 8, 43–46.
- [56] Ion R.M., Boroş D., Ion M.L., Dumitriu I., Fierăscu R.C., Radovici C., Florea G., Bercu C. (2008). *Combined spectral analysis (EDXRF, ICP-AES, XRD, FTIR) for characterization of bronze roman mirror*, Metalurgia International 5, 61–65
- [57] Rathossi C., Tsolis-Katagas P.C., Katagas C., (2004). *Technology and composition of Roman pottery in northwestern Peloponnese, Greece*, Applied Clay Science 24, 313–326.

- [58] Cullers R.L., Basu A., Suttner L.J., (1988). *Geochemical signature of provenance in sand-size material in soils and stream sediments near the Tobacco Root Batholith, Montana, U.S.A.* Chemical Geology 70 (1988) 335–348.
- [59] Nesbitt H.W., Markovics G., Price R.C., (1980). *Chemical processes affecting alkalis and alkaline earths during continental weathering*, Geochimica et Cosmochimica Acta 44 (1980) 1659–1666.
- [60] Niculescu G., Coltoș C., Popovici D., (1982). *Determinarea pigmentilor utilizati la decorația ceramicii cucuteniene*, Cercetari de Restaurare si Conservare 2, 205–206 (in Romanian).
- [61] Ståhl K., (2000). *The Huber G670 imaging-plate Guinier camera tested on beamline I711 at the MAXII synchrotron*, Journal of Applied Crystallography 33, 394–396.
- [62] Stosgale Z., Rook E., (1981). *Analysis of Pigments Used for Decorations of Neolithic Pottery from Bilcze Złote, Ukraine*, BritishMuseum–Occasionalpaper 19, 155–161.
- [63] Tang C.C., Maclean E.J., Roberts M.A., Clarke D.T., Praga J.N.W., Pantos E., (2001). *The study of Attic black glosses herds using Synchrotron X-RayDiffraction*, Journal of Archaeological Science 2, 1015–1024.
- [64] Uda M., Sassa S., Yoshimura S., Kondo J., Nakamura M., Ban Y., Adachi H., (2000). *Yellow, red and blue pigments from ancient Egyptian palace painted walls*, Nuclear Instruments and Methods in Physics Research B 161–163, 758–761.
- [65] da Costa M.L., Kern D.C., Pinto A.H.E., da Trindade Souza J.R. (2004), *The ceramic artifacts in archaeological black earth (terra preta) from Lower Amazon Region, Brazil: chemistry and geochemical evolution*, Acta Amazonia 34(3) 375–386.
- [66] da Costa M.L., Rios G.M., Carvalho da Silva M.M., da Silva G.J., Molano-Valdes U., (2011). *Mineralogy and chemistry of archaeological ceramic fragments from archaeological Dark Earth site in Colombian Amazon*, Rem: Revista Escola de Minas 64, 17–23.
- [67] Dumitriu I., Ion R.M., Fierăscu R.C., (2011). *Archeometry of support materials (In Romanian: Arheometria materialelor support)*, 1st ed. Târgoviște (ed.), Transversal, p. 178.
- [68] González-García F., Romero-Acosta V., García-Ramos G., González-Rodríguez M., (1990). *Firing transformations of mixtures of clays containing illite, kaolinite and calcium carbonate used by ornamental tile industries*, Applied Clay Science 5, 361–375.
- [69] Salazar A., (ed.), *Cultural Heritage Applications: Archaeological Ceramics and Building Restoration* (2013). In: On Statistical Pattern Recognition in Independent Component Analysis Mixture Modelling, Springer Theses, Vol. 4, Springer-Verlag, Berlin, Heidelberg, pp. 129–153.
- [70] Coleyshaw E.E., Griffith W.P., Bowell R.J., (1994). *Fourier-transform Raman spectroscopy of minerals*, Spectrochimica Acta A 50, 1909–1918.

- [71] Murray H.H. (1991). *Overview - clay mineral application*, Applied Clay Science 5, 379–395
- [72] De Benedetto G.E., Laviano R., Sabbatini L., Zambonin P.G., (2002). *Infrared spectroscopy in the mineralogical characterization of ancient pottery*, Journal of Cultural Heritage 3, 177–186,
- [73] Westin G., Nygren M., (1994). *Synthesis and Characterization of Ni<sub>2</sub>Sb<sub>4</sub>(OEt)<sub>16</sub> and its Hydrolysis Products*, Journal of Materials Chemistry 4, 1275–1282.
- [74] Nakamoto K., (1986). *Infrared and Raman spectra of inorganic and coordination compounds*, John Wiley and Sons, New York.
- [75] Bell I.M., Clark R.J.H., Gibbs P.J., (1997). *Raman Spectroscopic Library of Natural and Synthetic Pigments (pre-1850 AD)*, Spectrochimica Acta Part A 53, 2159–2179.
- [76] Burgio L., Clark R.J.H., (2001). *Library of FT-Raman Spectra of Pigments, Minerals, Pigment Media and Varnishes, and Supplement to Existing Library of Raman Spectra of Pigments with Visible Excitation*, Spectrochimica Acta Part A 57, 1491–1521.
- [77] Colombar P., Sagon G., Faurel X. (2001). *Differentiation of antique ceramics from the Raman spectra of their coloured glazes and paintings*. Journal of Raman Spectroscopy 32, 351–360.
- [78] Vandenabeele P., Moens L., Edwards H.G.M., Dams R. (2000), *Raman spectroscopic database of azopigments and application to modern art studies*, Journal of Raman Spectroscopy 31, 509–517.
- [79] Claybourn M., Ansell M., (2000). *Using Raman spectroscopy to solve crime: inks, questioned documents and fraud*, Science and Justice 40, 261–271.
- [80] Edwards H., Chalmers J.M., (2005). *Raman Spectroscopy in Archaeology and Art History*, Cambridge: The Royal Society of Chemistry.
- [81] Edwards H.G.M., Drummond L., Russ J., (1999). *Fourier-Transform Raman spectroscopic study of prehistoric rock paintings from the Big Bend Region, Texas*, Journal of Raman Spectroscopy 30, 421–428.
- [82] Edwards H.G.M., Drummond L., Russ J., (1998). *Fourier-Transform Raman spectroscopic study of pigments in native American Indian rock art: Seminole Canyon*, Spectrochimica Acta A 54, 1849–1856.
- [83] Edwards H.G.M., Falk, M.J.P., (1997). *Fourier-Transform Raman spectroscopic study of unsaturated and saturated waxes*, Spectrochimica Acta A 53, 2685–2694;
- [84] Edwards H.G.M., Falk D.W., Sibley M.G., Alvarez-Benedi J., Rull F., (1998). *FT-Raman spectroscopy of gums of technological significance*, Spectrochimica Acta A 54, 903–920.
- [85] Edwards H.G.M., Farwell D.W., Daffner L., (1996). *Fourier-transform Raman spectroscopic study of natural waxes and resins*. Spectrochimica Acta A 52, 1639–1648.

- [86] Edwards H.G.M., Farwell D.W., Perez F.R., Villar S.J., (1999). *Spanish mediaeval frescoes at Basconcillos del Tozo: A Fourier-Transform Raman spectroscopic study*, Journal of Raman Spectroscopy 30, 307–311.
- [87] Edwards H.G.M., Farwell D.W., Rozenberg S., (1999). *Raman spectroscopic study of red pigment and fresco fragments from King Herod's Palace at Jericho*, Journal of Raman Spectroscopy 30, 361–366;
- [88] Edwards H.G.M., Gwyer E.R., Tait J.K.F., (1997). *Fourier-transform Raman analysis of paint fragments from biodeteriorated Renaissance frescoes*, Journal of Raman Spectroscopy 28, 677–684;
- [89] Edwards H.G.M., Newton E.M., Russ J., (2000). *Raman spectroscopic analysis of pigments and substrata in prehistoric rock art*, Journal of Molecular Structure 550–551, 245–256.
- [90] Griffith W.P., (1987). *Advances in Raman and infrared spectroscopy of minerals*, In: Clark R.J.H., Hester R.E (eds.), Spectroscopy of Inorganic-Based Materials, Wiley, Chichester.
- [91] De Faria D.L.A., Silva V., de Oliveira M.T., (1997). *Raman microspectroscopy of some iron oxides and oxyhydroxides*, Journal of Raman Spectroscopy 28, 873–878.
- [92] Edwards H.G.M., Farwell D.W., Webster D., (1997). *FT Raman microscopy of untreated natural plant fibres*, Spectrochimica Acta A 53, 2383–2392.
- [93] Clark R.J.H., (2002). *Applications of Raman spectroscopy to the identification and conservation of pigments on art objects*, In: Handbook of Vibrational Spectroscopy Volume 4: Applications of Vibrational Spectroscopy in Industry, Materials and the Physical Sciences, John Wiley & Sons Ltd, Chichester.
- [94] Smith G.D., Clark R.J.H., (2001). *Raman microscopy in art history and conservation science*, Reviews in Conservation 2, 96–110.